

Die approbierte Originalversion dieser
Dissertation ist in der Hauptbibliothek der
Technischen Universität Wien aufgestellt und
zugänglich.

<http://www.ub.tuwien.ac.at>



The approved original version of this thesis is
available at the main library of the Vienna
University of Technology.

<http://www.ub.tuwien.ac.at/eng>

Dissertation

Multi-Dimensional modeling of the ionospheric parameters, using space geodetic techniques

ausgeführt zum Zwecke der Erlangung des akademischen Grades einer Doktors der
technischen Wissenschaften unter der Leitung von

o.Univ.-Prof. Dr.-Ing. Dr. h.c. Harald Schuh

Höhere Geodäsie (E120-4)

Department für Geodäsie und Geoinformation

eingereicht an der Technischen Universität Wien

Fakultät für Mathematik und Geoinformation

von

MSc. Mohamad Mahdi Alizadeh Elizei

Rudolf-Zeller gasse 69/12/8, 1230 Wien

Matr.-Nr.: 0628056

Wien, February 2013

Supervisors

o.Univ.-Prof. Dr.-Ing. Dr. h.c. Harald Schuh

Advanced Geodesy Research Group (E120-4)

Department of Geodesy and Geoinformation

Vienna University of Technology

Vienna, Austria

apl. Prof. Dr.-Ing. habil. Michael Schmidt

Deutsches Geodätisches Forschungsinstitut

(DGFI)

Munich, Germany

Assessors

o.Univ.-Prof. Dr.-Ing. Dr. h.c. Harald Schuh*

Advanced Geodesy Research Group (E120-4)
Department of Geodesy and Geoinformation
Vienna University of Technology
Vienna, Austria

apl. Prof. Dr.-Ing. habil. Michael Schmidt*

Deutsches Geodätisches Forschungsinstitut
(DGFI)
Munich, Germany

Univ. Prof. Dr. Manuel Hernández Pajares*

Research group of Astronomy and GEomatics (gAGE)
Technical University of Catalonia (UPC)
Barcelona, Spain

Ao. Prof. Dipl.-Ing. Dr.techn. Robert Weber*

Advanced Geodesy Research Group (E120-4)
Department of Geodesy and Geoinformation
Vienna University of Technology
Vienna, Austria

* See Examiners page (IV) for more details.

Dedicated to my beloved parents,
and to my loving wife.

Abstract

The rapid development of new technological systems for navigation, telecommunication, and space missions which transmit signals through the Earth's upper atmosphere - the ionosphere - makes the prediction of the meteorological conditions of space around the Earth more essential. For space geodetic techniques, operating in microwave band, ionosphere is a dispersive medium; thus signals traveling through this medium are in the first approximation, affected proportional to inverse of the square of their frequencies. This effect allows gaining information about the parameters of the ionosphere in terms of Total Electron Content (TEC) or the electron density (Ne). Making use of this phenomenon, space geodetic techniques have turned into a capable tool for studying the ionosphere in the last decades. The classical data for obtaining ionospheric parameters from space geodetic techniques are the Global Navigation Satellite Systems (GNSS) dual-frequency observations. However, due to the fact that the GNSS ground stations are in-homogeneously distributed in globe and have a poor coverage over the oceans, the precision of TEC maps are rather low in these areas. On the other hand dual-frequency satellite altimetry missions (such as Jason-1 and 2) provide direct TEC values exactly over the oceans, and furthermore the six Formosat-3/COSMIC (F/C) spacecraft provide about 2500 globally distributed occultation measurements per day, which can be used for obtaining TEC values. Integrating these data with the ground-based data improves the accuracy and reliability of the ionospheric maps. This study aims at developing a global multi-dimensional model of the TEC and electron density, using measurements from several space geodetic techniques. In the case of 2D model, TEC is represented using a spherical harmonic expansion. However, due to the fact that 2D models of TEC provide information about the integral of the whole electron content along the vertical or slant ray-path, when information about the ionosphere at different altitudes is needed, these maps are not useful. Besides the geodetic applications, 3D modeling approach can include geophysical parameters like maximum electron density, and its corresponding height. High resolution modeling of these parameters, allow an improved geophysical interpretation. In the case of 3D model, electron density is represented using two sets of spherical harmonic expansions. The 3D models represent the height-dependency of the electron density by a multi-layered Chapman function for the bottom-side and topside ionosphere, and an appropriate base-function for the plasmaspheric contribution. To conclude, due to several developments and modifications of conceptual approaches, this study can be considered as a pioneer in the field of modeling the upper atmosphere, using space geodetic techniques.

Kurzfassung

Die Ionosphäre ist ein dispersives Medium für die Signale der geodätischen Weltraumverfahren, die den Mikrowellenbereich nutzen; dadurch werden Signale in diesem Medium in erster Näherung invers proportional zum Quadrat der Frequenzen beeinflusst. Dieser Effekt ermöglicht die Bestimmung von ionosphärischen Parametern in Form von Total Electron Content (TEC) Werten oder Elektronendichten (N_e). TEC Werte oder Elektronendichten können mit Kugelfunktionen beschrieben werden, um daraus globale Ionosphärenkarten (Global Ionosphere Maps, GIM) abzuleiten. Üblicherweise stammt der Input für die Entwicklung von GIM von Zweifrequenz-Beobachtungen auf Global Navigation Satellite Systems (GNSS) Stationen. Jedoch sind GNSS Stationen inhomogen über die gesamte Erde verteilt, mit großen Lücken über den Ozeanen; dadurch wird die Genauigkeit der GIM über diesen Gebieten verringert. Andererseits liefern Satellitenaltimetriemissionen auf zwei Frequenzen wie Topex/Poseidon (T/P) oder Jason-1 präzise Informationen zur Ionosphäre über den Ozeanen; weiters erlauben Low Earth Orbiting (LEO) Satelliten, wie Formosat-3/COSMIC (F/C) global gut verteilte Ionosphärenmessungen. Diese Dissertation behandelt die globale Modellierung von TEC durch die Kombination von GNSS Beobachtungen mit Satellitenaltimetrie und auch mit globalen TEC Daten aus Okkultationsmessungen der F/C Mission. Die Untersuchungen konzentrierten sich auf die Dauer zwischen dem letzten solarem Minimum (2006) und einigen Jahren danach (bis 2010). An einigen ausgewählten Tagen wurde die Kombination durchgeführt, und die kombinierten GIM von vertikalem TEC (VTEC) zeigen eine maximale Abweichung von ungefähr 1.5 TEC Units ($TECU$) bezogen auf das ausschließlich aus GNSS-Beobachtungen ermittelte GIM. Die RMS (root mean square) Fehlerkarten der kombinierten Lösung zeigen eine Verbesserung während des ganzen Tages. Die Verringerung des RMS erreicht 0.5 $TECU$ in Gebieten, wo nur wenige GNSS Beobachtungen aber eine große Zahl an F/C Beobachtungen zur Verfügung stehen. Das bestätigt, dass die kombinierten GIM eine homogenere globale Verteilung haben als Ergebnisse von einer Technik alleine. Somit kann die Schlussfolgerung gezogen werden, dass die Kombination von Satellitenaltimetrie und auch F/C mit GNSS Beobachtungen für die globale Modellierung der Ionosphäre die Genauigkeit und Zuverlässigkeit der GIMs signifikant verbessert, besonders wenn eine große Anzahl an Okkultationsmessungen zur Verfügung steht. Alle Vergleiche und Validierungen in dieser Studie liefern wichtige Informationen bezüglich der Kombination und Integration der verschiedenen Beobachtungsverfahren im Global Geodetic Observing System (GGOS) der International Association of Geodesy (IAG).

Contents

Abstract	v
Kurzfassung	vii
Acronyms	xiii
1 Introduction and motivation	1
I Basic Concepts	7
2 Basics of the ionosphere	9
2.1 Ionization and recombination	9
2.2 Chapman layer profile	11
2.3 Variations in the ionosphere	12
2.3.1 Spatial variations	14
2.3.1.1 Height dependent	14
2.3.1.2 Latitude dependent	17
2.3.2 Temporal variations	18
2.3.2.1 Regular variations	18
2.3.2.2 Irregular variations	20
2.4 Ionospheric effects on microwave signals	21
2.4.1 Group and phase velocity	21
2.4.2 Ionosphere refractive index	24
2.4.3 Ionospheric delay	26
3 Ionosphere and space geodetic observation techniques	33
3.1 GNSS	33
3.1.1 General concepts	33
3.1.2 Observables	36
3.1.2.1 Fundamental observation equation	36
3.1.2.2 Pseudo-range smoothing	37

3.1.3	Ionosphere-related combination of observables	37
3.1.3.1	Ionosphere-free linear combination	37
3.1.3.2	Geometry-free linear combination	40
3.2	Satellite altimetry	42
3.2.1	General concepts	42
3.2.2	TEC from dual-frequency altimetry measurements	43
3.3	LEO satellites	45
3.3.1	General concepts	45
3.3.2	Formosat-3/COSMIC	45
3.3.3	CHAMP	46
3.3.4	GRACE	46
3.4	VLBI	47
3.4.1	General concepts	47
3.4.2	TEC from VLBI data	47
3.5	DORIS	48
II	Modeling Theory	49
4	Ionosphere Models	51
4.1	Physical models	51
4.1.1	GAIM	51
4.1.2	PIM	52
4.2	Empirical models	53
4.2.1	Klobuchar	53
4.2.2	IRI	54
4.2.3	NeQuick	55
4.2.4	MIDAS	57
4.2.5	NTCM	57
4.3	Mathematical models	58
4.3.1	Global TEC representation using spherical harmonics	58
4.3.1.1	Parametrization of VTEC	59
4.3.1.2	VTEC interpolation	60
4.3.1.3	Ionosphere Working Group at IGS	60
4.3.2	Regional TEC representation using B-splines	61
5	New ionosphere reconstructing approaches	65
5.1	Basics of data analysis and estimation	65
5.1.1	Least-Squares adjustment	65
5.1.2	Constrained Least-Squares	68
5.1.3	Assigning appropriate base-function	69

5.1.4	Accuracy of the estimated parameters	69
5.2	Two-dimensional modeling of VTEC	72
5.2.1	Combined global maps	72
5.2.2	Inter-technique combination	72
5.2.3	Relative weighting of different techniques	73
5.3	Three-dimensional modeling of the electron density	75
5.3.1	Chapman profile function	75
5.3.1.1	Simple Chapman profile function	76
5.3.1.2	Multi-layer Chapman profile function	78
5.3.1.3	Electron density representation in topside ionosphere	80
5.3.1.4	Electron density representation in plasmasphere	81
5.3.2	Extending ionosphere model using Chapman profile function	83
5.3.2.1	TEC observable and Chapman function	83
5.3.2.2	Solving the unknown parameters	84
5.3.2.3	Global electron density representation using spherical harmonics	85
5.3.3	Ray-tracing technique	86
5.3.4	Linearizing the model	89
5.3.4.1	General linearized model	89
5.3.4.2	Linearized model represented by spherical harmonics coefficients	90
5.3.5	Estimating the unknown parameters	92
5.4	Fourth dimension in modeling electron density	92
5.4.1	Fourier series	93
5.4.2	Extending ionosphere model using Fourier series	93
5.4.3	Linearizing the model	94
III	Results	97
6	Multi-dimensional maps of the ionosphere	99
6.1	Combined 2D Global Ionosphere Maps	99
6.1.1	Acquired data	100
6.1.1.1	GNSS	100
6.1.1.2	Satellite altimetry	100
6.1.1.3	Formosat-3/COSMIC	101
6.1.2	Combination of GNSS, satellite altimetry, and F/C observations	101
6.1.2.1	IGG GNSS-only GIM	102
6.1.2.2	GNSS and satellite altimetry combined GIM	102
6.1.2.3	GNSS, satellite altimetry, and F/C combined GIM	107
6.1.3	Quantification with raw altimetry and F/C data	107
6.1.4	Comparison of the combined GIM with IGS GIM	112

6.1.5	Calibration of GNSS VTEC using satellite altimetry and F/C	114
6.1.5.1	Calculating biases and calibration	114
6.1.5.2	Combining calibrated data for developing GIM	118
6.1.5.3	Quantifying the calibrated GIM with raw data	119
6.2	Global maps of electron density	121
6.2.1	Simulating GNSS data	122
6.2.1.1	True position of GNSS satellites	124
6.2.1.2	Simulated values from IGS VTEC maps	124
6.2.2	Calculating a priori values	126
6.2.3	Performing outliers test	127
6.2.4	Least-squares estimation of the unknown parameters	129
6.2.4.1	Global mean constraint	129
6.2.4.2	Surface function constraint	132
6.2.5	Assimilating the estimated parameters	134
6.2.6	Assessment of the estimated parameters	134
6.2.6.1	Evaluating the accuracy of developed maps	134
6.2.6.2	Comparison with the IRI model	136
6.2.6.3	Comparison with the F/C peak parameters	138
7	Final remarks	145
7.1	Summary	146
7.2	Discussion	147
7.3	Conclusions	149
7.4	Outlook	150
IV	Appendices	155
A	Single-frequency Single Point Positioning	157
	List of Figures	163
	List of Tables	167
	Bibliography	169
	Acknowledgments	183
	Author's declaration	185
	Curriculum Vitae	187
	Examiners	188

Acronyms

AAC	Associate Analysis Centers
AC	Analysis Centers
ADS	Altimeter Database System
AFRL	Air Force Research Laboratory
AFWA	Air Force Weather Agency
AKR	Auroral Kilometric Radiation
ARPL	Aeronomy and Radiopropagation Laboratory
BC	Before Christ
BPM	Base Point Model
C/A code	Coarse/Acquisition code
CCIR	Comité Consultatif International des Radiocommunications
CDDIS	Crustal Dynamics Data Information System
CHAMP	CHAllenging Mini-Satellite Payload
CME	Coronal Mass Ejection
CNES	French space agency
CODE	Center for Orbit Determination in Europe
COSPAR	Committee on Space Research
DCB	Differential Code Biases
DGFI	Deutsches Geodtisches Forschungsinstitut
DGR model	Di Giovanni and Radicella model
DLR	German Aerospace Center
DMSP	Defense Meteorological Satellite Program
DoD	Department of Defense
DOF	degree of freedom
DORIS	Doppler Orbitography and Radio positioning Integrated by Satellite
doy	day of year
EDP	Electron Density Profile
EGNOS	European Geostationary Navigation Overlay Service
EGU	European Geosciences Union
ESA	European Space Agency
ESOC	European Space Operations Center

Eumetsat	Exploitation of Meteorological Satellites
EUV	Extreme Ultra Violet
F/C	Formosat-3/Cosmic
FM	Frequency Modulation
FWF	Austrian Science Funds
gAGE	Research Group of Astronomy and Geomatics
GAIM	Global Assimilative Ionospheric Model
GFZ	Deutsches GeoForschungsZentrum
GFZ	Deutsches GeoForschungsZentrum
GGOS	Global Geodetic Observing System
GIM	Global Ionosphere Map
GLONASS	GLObal NAvigation Satellite System
GMT	Generic Mapping Tools software
GNSS	Global Navigation Satellite Systems
GPStk	GPS Toolkit software
GPS	Global Positioning System
GRACE	Gravity Recovery and Climate Experiment
GRGS	Groupe de Recherche en Géodésie Spatiale
GRMS	Global RMS
IAAC	IGS Associate Analysis Centers
IAG	International Association of Geodesy
IAU	International Astronomical Union
IGG	Institute of Geodesy and Geophysics of Vienna University of Technology
IGN	Institut Géographique National
IGOS	Integrated Global Observing Strategy
IGRF	International Geomagnetic Reference Field
IGS	International GNSS Service
IONEX	IONospheric EXchange format
IPP	Ionospheric Pierce Point
IRI	International Reference Ionosphere
ITU-R	International Telecommunication Union, Radiocommunication Sector
IVS	International VLBI Service
JPL	Jet Propulsion Laboratory
LEO	Low Earth Orbiting
LSTID	Large-scale TID
MCS	Master Control Station
MCVCE	Fast Monte-Carlo implementation of the iterative maximum likelihood component estimation
MIDAS	Multi-Instrument Data Analysis System
MSLM	modified single-layer mapping function

MSTID	Medium-scale TID
MS	Monitor Stations
MURI	Multidisciplinary University Research Initiatives
NASA	National Aeronautics and Space Administration
NOAA	National Oceanic and Atmospheric Administration
NSSDC	National Space Science Data Center
NTCM-EU	European region NTCM
NTCM-GL	Global NTCM
NTCM-NP	North Polar region NTCM
NTCM-SP	South Polar region NTCM
NTCM	Neustrelitz TEC Model
OSTM	Ocean Surface Topography Mission
P code	Precise code
PIM	Parameterized Ionospheric Model
PPP	Precise Point Positioning
PRN	Pseudo Random Noise
RMS	Root Mean Square
RO	Radio Occultation
SITEC	Sudden Increase of TEC
SLM	Single Layer Model
SOPAC	Scripps Orbit and Permanent Array Center
SPP	Single Point Positioning
SSB	Sea State Bias
SSTID	Small-scale TID
SSULI	Special Sensor Ultraviolet Limb Imager
STEC	Slant TEC
TBB	Tri Band Beacon
TDIM	Time-Dependent Ionospheric Model
TECU	Total Electron Content Unit
TEC	Total Electron Content
TID	Traveling ionospheric disturbances
TIP model	Topside Ionosphere and Plasmasphere model
TIP sensor	Tiny Ionospheric Photometer sensor
UCAR	University Corporation for Atmospheric Research
UPC	Technical University of Catalonia
URSI	International Union of Radio Science
UV	Ultraviolet
VCE	Variance Component Estimation
VLBI	Very Long Baseline Interferometry
VTEC	Vertical TEC

WG	Working Group
-----------	---------------

Chapter 1

Introduction and motivation

In the last decades, the new technological systems which transmit signals through the Earth's atmosphere, have been rapidly evolved, serving both military and civilian purposes, such as in telecommunication, navigation, and surveillance systems. Among these systems, the current space geodetic techniques, such as Global Navigation Satellite Systems (GNSS), Low Earth Orbiting (LEO) satellites, Very Long Baseline Interferometry (VLBI), and others (see Fig. 1.1) have found several applications in a broad range of commercial and scientific fields. The increase in using space geodetic techniques, surges the demand for obtaining the most accurate and reliable results. This can be achieved by either technical improvement of the observing instruments, or by minimizing the effect of the error sources. This minimization can be accounted for by combining the results derived from different space geodetic techniques. For this purpose, a special project called the Global Geodetic Observing System (GGOS) was established by the International Association of Geodesy (IAG) in July 2003 (IAG, 2012). This international cooperation has led to the establishment of the IAG Services, which provide valuable observations and products not only to the scientific community but also for a wide range of non-scientific applications. The main vision of GGOS as stated in GGOS (2012) is: "GGOS integrates different geodetic techniques, different models, different approaches in order to ensure a long-term monitoring of the geodetic observables in agreement with the Integrated Global Observing Strategy (IGOS)."

Following this global objective in geodetic science, this study effectively contributes to the GGOS aims by integrating observations from different space geodetic techniques for multi-dimensional modeling of the upper part of the Earth's atmosphere, the ionosphere.

The ionosphere is an upper part of the Earth's atmosphere which is extended from approximately 60 *km* to 1,000 *km* or higher altitudes. Solar radiation produces free electrons and ions in this region. The density of these free electrons and ions are high enough to affect the propagation of electromagnetic radio frequency waves (Hargreaves, 1995). Ionosphere is dispersive with respect to the electromagnetic signals. This means that the electromagnetic signals traveling through the ionosphere are in the first approximation, affected proportional to the inverse of the square of their frequencies. This effect is known as the ionospheric re-

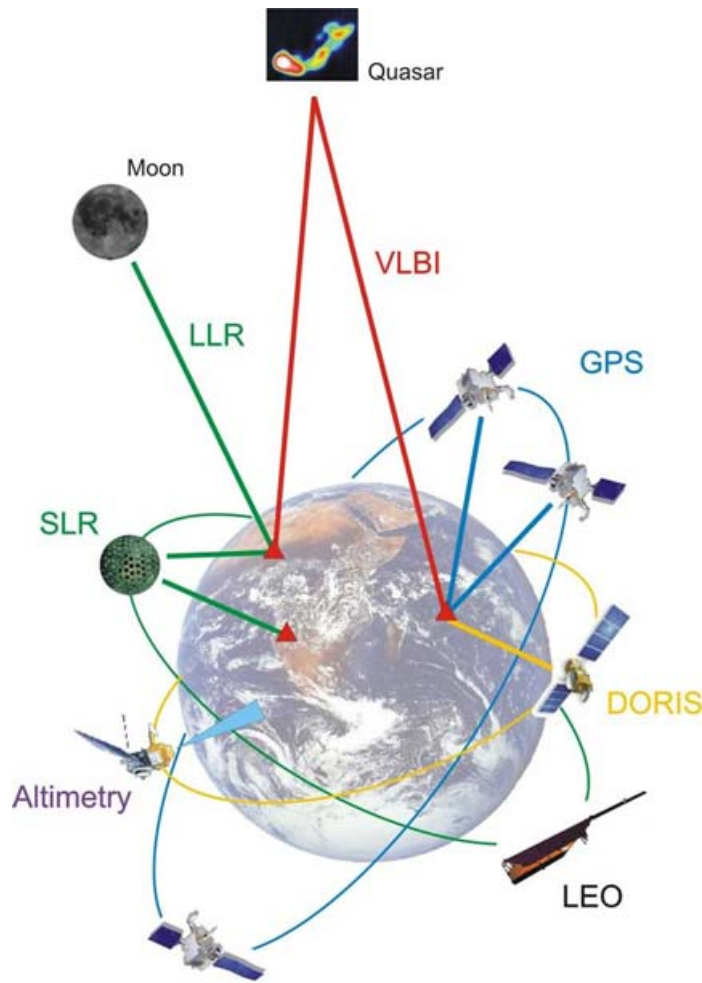


Figure 1.1: Infrastructure contributing to GGOS (figure courtesy of IAG (2012))

fraction, and should be considered in determination of the propagation velocity of the signals traveling through this medium. This phenomenon is the reason why the measurements of most of the space geodetic techniques are carried out in two different frequencies. Applying this phenomenon, by using measurements in two different frequencies, the effect of the ionosphere can -in the first approximation- be eliminated. This approximation is accurate enough for many of the commercial or scientific applications which want to get rid of the ionospheric effects.

But on the other hand, this effect allows gaining information about the parameters of the ionosphere in terms of Total Electron Content (TEC) or the electron density, compromising the ionospheric models. If the ionospheric model would be known for a special location and time, the ionospheric refraction can be computed for that specified location and time, therefore, the effect of ionosphere could be accounted for. For many applications in the navigation and positioning field, where the single frequency measurements are used, an accurate and reliable ionospheric model is essential. Furthermore, the empirical ionospheric models are

permanently updated by integration of real observations. The involvement of precise empirical results improves the ionospheric models towards a higher temporal and spatial resolution and increases their accuracy. Empirical ionospheric models are widely used in radio science and for climate and plasma studies as well as for aviation and marine navigation. In general, a better understanding of the ionosphere, which is the main goal of this study, is fundamental for all studies of the upper atmosphere, and for the solar-terrestrial environment.

To derive the information about the ionospheric parameters, following space geodetic techniques were implemented within this study:

- Global Navigation Satellite Systems (GNSS), including the Global Positioning System (GPS), and the GLObal NAVigation Satellite System (GLONASS),
- satellite altimetry mission, including Jason-1, and Jason-2, and
- LEO satellites, including Formosat-3/COSMIC (F/C).

The different principles of these observation techniques provide specific features of the ionospheric parameters derived by each of them. Combining these different techniques for modeling the ionospheric parameters makes use of the advantage of each of these individual technique, and compensates the disadvantages of each technique by certain extent.

In this study, ionospheric parameters have been modeled in different dimensions. To model the ionosphere in 2D, TEC should be modeled in two dimensions, i.e. in longitude and latitude. However, due to the fact that 2D models of TEC provide information about the integral of the whole electron content along the vertical or slant ray-path, when information about the ionosphere at different altitudes is needed, these maps are not useful; e.g. when electron density profile is required, or when satellite to satellite observation is being performed. Besides the geodetic applications, 3D modeling approach can include geophysical parameters like maximum electron density, and its corresponding height. High resolution modeling of these parameters, allow an improved geophysical interpretation. For these cases, a 3D modeling of the ionospheric parameters becomes necessary. To model the ionosphere in 3D, one has the possibility of modeling either the TEC or the electron density. We concentrated on modeling electron density in 3D, i.e. in longitude, latitude, and height. Finally to model ionosphere in 4D, electron density should be modeled in longitude, latitude, height, and time. This is accomplished by taking the temporal variations of electron density into account explicitly.

In conclusion, due to several developments and modifications of conceptual approaches, this study can be considered as a pioneer in the field of modeling the upper atmosphere, using space geodetic techniques.

To have a better perspective of the structure of this thesis, a brief overview of the dissertation is presented here. This thesis is presented in three parts, including seven chapters in total. After this chapter, the first part includes:

Part I - Basic Concepts

Chapter 2: Basics of the ionosphere

This chapter overviews some basics of the ionosphere, including ionization and recombination, and layer formation. Subsequently the spatial and temporal variations within the ionosphere are briefly explained. Then the effects of the ionosphere on microwave signals are discussed, starting with the explanation on the group and phase velocities, and the ionospheric refractive index is derived using the Appleton-Hartree formula. Finally the first and higher-order ionospheric delay is presented.

Chapter 3: Ionosphere and space geodetic observation techniques

In this chapter the space geodetic techniques, which provide information about the ionosphere are discussed. First the GNSS is briefly presented. The fundamental observation of GNSS is reviewed, following the smoothed-code pseudorange. Then the linear combinations which are used in the ionospheric studies, i.e. the ionospheric-free linear combination and the geometric-free linear combination are explained. Then the Satellite altimetry mission and its corresponding ionospheric-related measurements are over viewed. The LEO missions, such as Formosat-3/Cosmic (F/C), Champ, and Grace are discussed afterwards. Brief description on VLBI and ionosphere is presented, and finally, DORIS mission is briefly outlined.

Part II - Modeling Theory

Chapter 4: Ionosphere models

Within this chapter, some of the ionospheric models are reviewed. The ionospheric models are categorized into physical, empirical, and mathematical models. The Global Assimilative Ionospheric Model (GAIM), and the Parameterized Ionospheric Model (PIM) are discussed from the physical models. As for the empirical models, Klobuchar, International Reference Ionosphere (IRI) model, NeQuick, Multi-Instrument Data Analysis System (MIDAS), and Neustrelitz TEC Model (NTCM) are over viewed. Finally, for the mathematical models, one sample for the global modeling, i.e. modeling vertical TEC (VTEC) using spherical harmonics base-function, and one sample for regional ionosphere modeling, i.e. modeling VTEC applying B-spline base-functions are presented. A brief overview of VTEC interpolation, IONEX format, and International GNSS Service (IGS) ionosphere working group is also presented in this chapter.

Chapter 5: New ionosphere reconstructing approaches

This chapter contains the main theoretical literature, applied for the investigations within this thesis. In the first part, least-squares estimation is presented, continued with an explanation on the constrained estimation procedure. A brief overview of possible base-functions which can be used for modeling the ionospheric parameters is mentioned, and the accuracy

of the estimated parameters is shortly outlined. In the second part of this chapter, 2D modeling of VTEC is presented. The combination approach and the weighting scheme is followed in this part. Third part of this chapter, deals with 3D modeling of the electron density. Different models used for representing electron density are first discussed, then the ionospheric observable is extended applying the selected model. Within this chapter, a brief description on the ray-tracing technique, which is implemented in this thesis is provided. Then the linearized model is calculated and the estimation procedure of the unknown parameters is briefly discussed. Finally, in the last part of this chapter, 4D modeling of the electron density is discussed and the formulae are presented.

Part III - Results

Chapter 6: Multi-dimensional maps of the ionosphere

The key part of the study is presented in this chapter. As already discussed in the previous chapter, first 2D model of VTEC is developed combining GNSS, satellite altimetry, and F/C. The developed maps are quantified using raw satellite altimetry and F/C data. The maps are then compared with other VTEC maps and models. Finally, the procedure for calibrating GNSS VTEC using satellite altimetry and F/C data is discussed. In the next part, electron density is modeled in 3D, i.e. in longitude, latitude, and height. For this, GNSS data are considered only. To accomplish this task, electron density is expressed by the F2 maximum electron density and its corresponding height. To model the parameters of the electron density globally, two sets of spherical harmonic expansions are implemented; therefore, the coefficients of these expansions are our new unknowns. To estimate these unknowns, first the GNSS input data are simulated using true GNSS positions, but simulated values from the IGS VTEC maps. The a priori values are calculated using the IRI model and the ray-tracing technique. The least-squares adjustment of the unknown parameters is presented after a brief outline on the outliers test, and an explanation on the constraints used for estimating the unknown parameters. After obtaining the unknown coefficients of the spherical harmonics expansions, the F2 maximum electron density and its corresponding height is obtained. The results are provided in a global grid-wise map with a spatial resolution of 2.5° in latitude, and 5° in longitude, and temporal resolution of $2h$. The estimated F2-peak values are compared with the IRI model values, as well as the F2-peak parameters obtained from the F/C data.

Chapter 7: Final remarks

This chapter reviews the summary of the procedures applied in this thesis. A brief discussion on developed procedures and the obtained results of the thesis is presented. The final outcome, and its pros and cons are represented as conclusions. Finally the thesis is concluded with some remarks on the further work and some ideas for detailed investigations.

Appendix Applications of the global VTEC models

In the appendix, the GNSS single-frequency single point positioning is introduced as a sample application of the 2D global VTEC models.

Part I

Basic Concepts

Chapter 2

Basics of the ionosphere

Ionosphere is an upper part of the Earth's atmosphere, which is extended from about 60 *km* to 2,000 *km*, with the main concentration of the particles between 300 to 400 *km* (Hargreaves, 1995; Rishbeth & Garriott, 1969). Solar Extreme Ultra Violet (*EUV*) radiation at wave lengths $< 130\text{ nm}$ significantly ionizes the neutral gas. In addition to photo-ionization by electromagnetic radiation, also energetic particles from the solar wind and cosmic rays contribute to the ionization but to a much lesser extent (Hunsucker & Hargreaves, 2002). The electron production in the ionosphere is a direct consequence of the interaction of the solar radiation with atoms and molecules in the Earth's upper atmosphere. These free electrons and ions affect the propagation of electromagnetic waves. This effect is called ionosphere refraction and has to be considered when determining the propagation velocity of signals of all space geodetic techniques operating in microwave band.

2.1 Ionization and recombination

Within the ionosphere, solar radiation hits the atmosphere with a power density of 1,370 *Watts per meter*². This value is known as the solar constant. The intense level of solar radiation is spread over a wide spectrum, ranging from radio frequency through infrared (*IR*) radiation and visible light to X-ray. Due to the fact that the photons of energy at ultraviolet (*UV*) or shorter wavelengths are capable of separating an electron from a neutral gas atom or molecule during a collision, they are considered to be ionizing. During a strike, the incoming solar radiation hits a gas atom (or molecule); the atom absorbs part of this radiation and produces a free electron and a positively charged ion.

Ionization

There are different sources for ionization within the ionosphere:

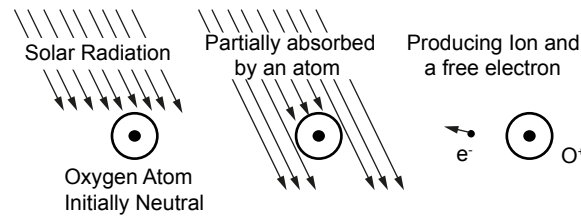


Figure 2.1: Ionization of an Oxygen molecule due to solar radiation

- Extreme UV and X-ray radiation
- High-energy particles
- Cosmic rays

Extreme UV and X-ray radiation: At the highest altitudes of the Earth's atmosphere, solar radiation is very strong but not so many atoms exist to interact with, thus the ionization is limited. As the altitude decreases, more gas atoms would be present, therefore the ionization process increases. In this process, a neutral atom X absorbs energy hf , to produce a positive atom X^+ and a free electron e^-



High-energy particles: Could reach up to several thousands of electron volts (eV) in the auroral zone due to magnetosphere activities.

Cosmic rays: The Ultra-high energy particles with cosmic origin can penetrate deep into the atmosphere and cause ionization within the lower ionosphere.

Recombination

Meanwhile an opposing process begins to take place. In this process a free electron moves close enough to a positive ion and gets captured by it. This process is called recombination. The recombination process accelerates at lower altitudes. This is due to the fact the gas density increases at lower altitudes and the gas molecules and ions get closer to each other. The balance between the ionization and recombination process determines the degree of ionization present at any time.

If ionization was not swept away by recombination, the atmosphere would have become fully ionized. But this is not the case. In reality, the production and loss of ionization reaches

an equilibrium; therefore recombination exists. In recombination process, negative electrons e^- , and positive ions X^+ , combine to produce neutral particles. There are two basic types of recombination.

Radiative recombination: In this procedure an electron combines with an atomic ion and produces a neutral atom and a photon $h\nu$:



Dissociative recombination: Within this procedure an electron combines with a molecular ion XY^+ and produces two neutral atoms X and Y :



As the altitude decreases, the number of gas atoms and molecules increase, so there should be more opportunity for energy absorption. But the energy from the solar UV radiation is already absorbed within higher altitudes, therefore the intensity of radiation is smaller in lower altitudes. There are points where lower radiation and greater gas density balances. In these points recombination rates balance out the ionization rate. This leads to formation of ionization peaks and consequently different layers, known as the Chapman layers.

2.2 Chapman layer profile

It is known that the density of the atmosphere decreases exponentially with altitude (neglecting, for the moment, variations caused by the temporal structure or the diffusive separation of species). It is also known that monochromatic radiation is attenuated exponentially by an absorbing medium (Aghanajafi, 2000). With these two facts, it can be conceived how solar radiation produces ionized layers. At the outer fringes of the atmosphere, the density is low and radiation is absorbed only slightly; but deeper in the atmosphere, the density increases and so does the absorption of radiation. Both the density of the atmosphere and the absorption of radiation increase exponentially with depth; and in particular altitude region, this double exponential absorption process will produce a very rapid attenuation of a particular wavelength radiation, below this region, virtually none of that particular radiation will penetrate. If the absorption is caused by ionization processes, an ionized layer will result. This phenomenon is represented schematically by Fig. 2.2 (Whitten & Poppoff, 1971).

This layer formation theory was put in good quantitative form by Sydney Chapman in 1931. The Chapman law describes the direct relation of the density of free electrons and ions to height and daily solar motion. The production rate of ion pairs is given by the Chapman function under the following simplifying assumptions (Todorova, 2008):

- only the solar radiation is taken into account, i.e. the impact of the cosmic rays, which

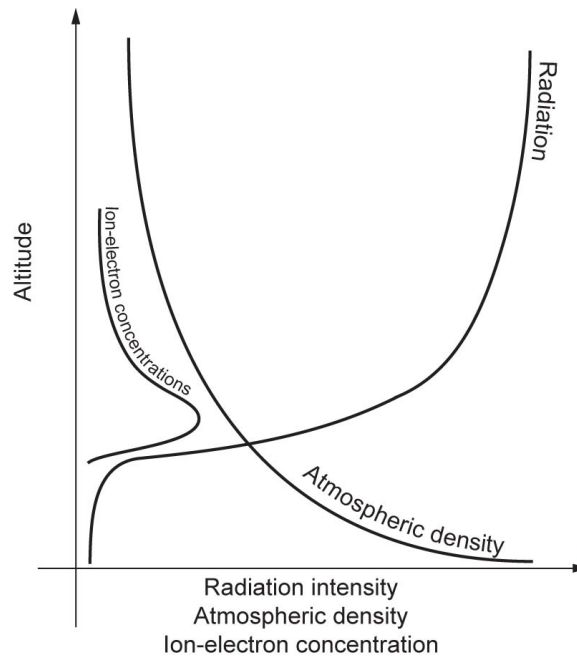


Figure 2.2: Schematic representation of layer formation

are the second main (but less strong) cause of ionization, is neglected;

- the atmosphere consists of a one-component isothermal gas distributed in horizontally stratified shells with constant scale height;
- the solar radiation is monochromatic and absorbed proportionally to the concentration of gas particles.

In spite of the simplifying assumptions under which the Chapman theory is derived, it is able to explain the main characteristics of the ionosphere and provides a reliable reference for the basics in the ionosphere modeling (Kelly, 1989). As shown by the altitude profiles, the maximum electron density is concentrated in a relatively thin layer, typically located at a height between 300 and 500 *km* above the Earth's surface. Based on that result, the Single Layer Model (*SLM*) (see Sect. 2.4.3) has been introduced. In this model it is assumed that all free electrons are concentrated in an infinitesimally thin layer at a fixed height. Usually, this height slightly exceeds the altitude of maximum electron density in order to balance the effect of the more extended topside ionosphere. For more details on Chapman function please refer to Sect. 5.3.1).

2.3 Variations in the ionosphere

Ionosphere is a complicated medium. It varies with different number of parameters, which cause variations in spatial and temporal structure of electron density and so in the ionospheric

layers. The main parameters driving the ionosphere are the solar activity and the behavior of the geomagnetic field, so when studying the electron density it will be beneficial to introduce two additional coordinate systems besides the geographical coordinate system, which take the characteristics of the medium into account:

- **Sun-fixed coordinate system**

To keep the change in the Sun position minimal, the coordinate system should co-rotate with it, so the temporal variation of the electron content is slow and can be averaged for a short period, e.g. one to two hours. The origin of this Sun-fixed coordinate system is set in the center of mass of the Earth, the terrestrial rotation axis is chosen for Z-axis and the X-axis is defined by the mean solar meridian; the Y-axis completes the coordinate system to a right-handed one. In that way the geographical longitude and latitude (λ_g, φ_g) can be transformed into sun-fixed longitude and latitude (λ_s, φ_s) as follows:

$$\lambda_s = s = \lambda_g + UT - \pi = \lambda_g + (UT - 12)^{hours}, \quad (2.4)$$

$$\varphi_s = \varphi_g, \quad (2.5)$$

where φ_s and λ_s are in degrees and UT is the Universal Time in hours. To unify the units in Eq. 2.4, $(UT - 12)$ should be multiplied by $15^\circ/hours$. After the transformation the latitude remains unchanged Eq. 2.5 and the sun-fixed longitude Eq. 2.4 matches the hour angle of the Sun.

- **Geomagnetic coordinate system**

This system is defined by its Z-axis parallel to the axis of magnetic dipole, and its Y-axis perpendicular to the geographic poles. So if \overrightarrow{DP} would be the dipole position and \overrightarrow{SP} the south pole, we have $\overrightarrow{Y} = \overrightarrow{DP} \times \overrightarrow{SP}$. Finally the X-axis of the system completes an orthogonal right-handed set. The relation between the geomagnetic coordinates (λ_m, φ_m) and the geographic coordinates (λ_g, φ_g) follows:

$$\sin \varphi_m = \sin \varphi_g \sin \varphi_0 + \cos \varphi_g \cos \varphi_0 \cos(\lambda_g - \lambda_0) \quad (2.6)$$

$$\sin \lambda_m = \frac{\cos \varphi_g \sin(\lambda_g - \lambda_0)}{\cos \varphi_m} \quad (2.7)$$

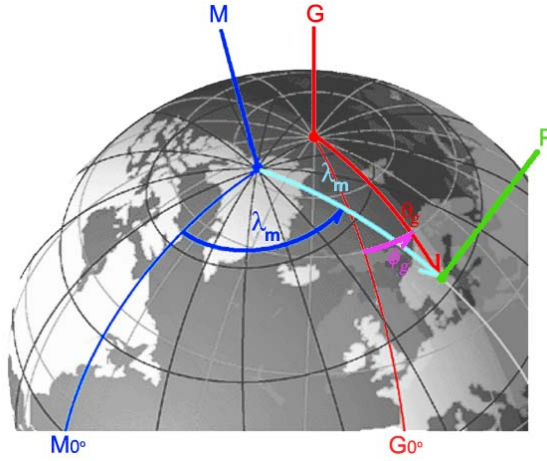


Figure 2.3: Relation between the geographic and geomagnetic system, where G is the geographic pole, M is the geomagnetic pole, P an arbitrary point, θ_g the geographic co-latitude ($= 90 - \varphi_g$), θ_m is the geomagnetic co-latitude ($= 90 - \varphi_m$), and geographic and geomagnetic longitudes are expressed by λ_g and λ_m (figure courtesy of World Data Center for Geomagnetism (IGRF, 2011))

where φ_0 and λ_0 are the geographical coordinates of the geomagnetic north pole. According to the International Geomagnetic Reference Field (IGRF), the coordinates of the north magnetic pole for the year 2010 are $\varphi_0 = 80.0^\circ$ (N) and $\lambda_0 = 72.2^\circ$ (W) (IGRF, 2011). According to Schaer (1999) the geomagnetic north pole is moving about $+0.03^\circ$ in south-north direction and -0.07° in west-east direction per year.

2.3.1 Spatial variations

2.3.1.1 Height dependent

Ionosphere is subdivided into different height-dependent layers, based on the solar radiation wavelength which is most absorbed in that layer or the level of radiation which is required to photo dissociate the molecules within these individual regions. The main layers are known as D, E, F1 and F2.

D Layer This layer is the part from approximately 60-90 *km*, which absorbs the most energetic part of solar radiation. This layer reflects long wavelength radio waves transmitted from Earth's surface back to the Earth. This phenomenon makes long distance radio communication possible. The D region is the most complex part of the ionosphere from the chemical point of view. Several different sources cause the ion production within this layer. The most important are: Lyman- α (Rhoads *et al.*, 2000) that ionizes the *NO* molecule, ultraviolet radiation that ionizes *O₂* and *N₂*, hard X rays that depend strongly on the solar activity and are not significant at sunspot minima, and galactic cosmic rays that

affect mainly the lower parts of the D region. The D region shows sudden changes in the electron concentration near sunrise and sunset and remains almost constant during the day. During the nighttime at mid latitudes this layer vanishes.

E Layer This region is the part from about 85-140 *km*, although the production peak is at 110-115 *km*. Since at this height different molecular gases are present, molecular ions are produced directly and the loss rate is dominated by dissociative recombination. As this is not height dependant, the resulting electron concentration in this region closely follows the production profile. Among the solar radiation, this layer absorbs soft X-rays. The E region reflects standard AM radio waves, which are transmitted from the Earth, back to its surface. The variations are regular and are mainly controlled by the Sun and may be described by a Chapman law (see Sect. 2.2). The E layer does not vanish at night, but a weakly ionized layer remains with an electron density of approximately $2 \times 10^9 \text{ electrons/m}^3$.

Sporadic E Layer In addition to the regular E layer of the ionosphere, there exists other irregular layers known as the sporadic E layers *Es*. Depending on the mechanism of formation, there are different Sporadic E layers. In the equatorial zone, the E layer may be interpreted in terms of the two-stream ion wave instability in the plasma Feltens *et al.* (2009). In the polar ionosphere, the same mechanism may sometimes apply as well as ionization due to penetration of charged particles. In other cases, turbulence may also play role in the formation of the Sporadic E layer. Auroral sporadic E is produced by energetic electrons from the magnetosphere. Furthermore, in the auroral zone, nighttime ionization is produced by particles from the magnetosphere Mayer & Jakowski (2009).

Sporadic E can occur over a range of heights from about 90 to 120 *km* or even more. In some cases the *Es* is a relatively thick layer with a well-defined maximum of electron density whereas in other cases it is extremely thin. In some cases the *Es* layer is opaque and blankets the upper layers; in other cases the upper layers can be seen through the *Es*, which suggests that the radio waves are penetrating through the gaps.

F Layer In the F layer the peak production height is at 150-160 *km*. But the electron concentration peak is well above this height at around 250-300 *km*. Among the solar radiation the F layer absorbs EUV radiation. The F region reflects radio waves with shorter lengths transmitted from earth's surface. Visible light, radar, television and FM wavelengths are all too short to be reflected by the ionosphere and they penetrate through this medium. So these wavelengths are suitable for satellite communications. Through the F layer, by increase in height, the loss rate gradually becomes dominated by the ion-atom exchange rate and starts to decrease. In fact the loss rate drops down faster than the rate of production, resulting an actual increase in electron concentration. As the plasma diffusion takes over, the electron concentration becomes distributed similar to the neutral gas concentration, and a maximum is reached. The height where the loss rate transits from dissociative to ion-atom exchange can vary. If this height is above the peak production, a reduction in the actual

Layer		D	E	F1	F2
Height domain [km]		60 - 90	85 - 140	140 - 200	200 - 1,000
Electron density [elec/m ³]	Day	$10^8 - 10^{10}$	10^{11}	5×10^{11}	10^{12}
	Night	-	$2 \cdot 10^9$	10^9	3×10^{11}

Table 2.1: Characteristics of the main ionospheric layers

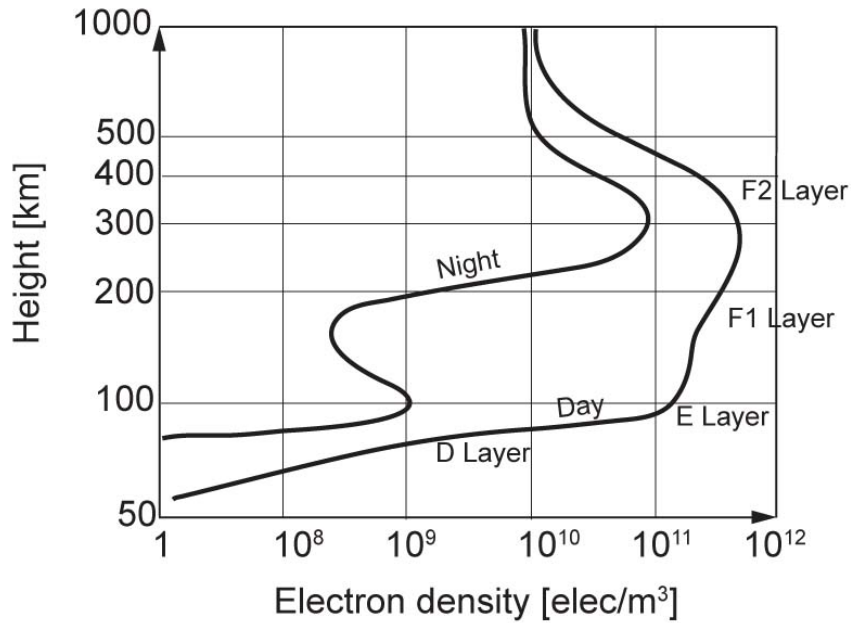


Figure 2.4: Chapman electron density profile and the ionospheric layers D, E, and F for both night and day conditions at mid-latitudes

electron concentration happens. This results a secondary peak in the electron concentration profile at the peak of production called the F1 peak. Therefore the F layer is subdivided into two layers: The F1 layer extending from about 140-200 km and the F2 layer from 200-1000 km. Table 2.1 designates the four principal layers of the ionosphere.

Plasmasphere From altitudes about 1,000 km the density of O^+ ion starts to fade and the H^+ ion turns into the dominate particle. This height is known as the transition height. This layer of the upper atmosphere is called the plasmasphere. Plasmasphere is bounded on the upper side by the plasmopause at which the plasma density drops by one or two orders of magnitude. Due to the fact that neutral densities are very low in this region, the plasma profiles are determined by transport of electrons and ions.

The position of the transition height (at which the concentration of O^+ and H^+ are equal)

varies from around 800 *km* on a winter night at low solar activity to a few around 4,000 *km* during a summer day, high solar activity (Feltens *et al.*, 2009). Since there is almost no plasma production in the plasmasphere, the ionized particles diffuse up from the ionosphere to plasmasphere. The plasmasphere takes ionized particles from the ionosphere by day, acting like a reservoir and stores them in a loss-free environment. At nighttime this procedure gets inversed and the plasmasphere returns the ions back to the ionosphere. Thus the nighttime F layer is maintained in ionosphere

2.3.1.2 Latitude dependent

Due to the Earth's magnetic field the behavior of the ionosphere can be divided into three latitudinal regions: low latitude (equatorial), mid latitude and high latitude (see Fig. 2.5). The boundaries between the regions are not constant, but vary according to local time, geomagnetic condition and solar activity.

Low latitude region This region contains the highest values of the Total Electron Content (TEC) (see Sect. 2.4.3), and the peak electron density. The scintillation effect (see Sect. 2.3.2) has its greatest amplitude at these latitudes. The distribution of the peak electron density at the F2 layer depicts a minimum at the geomagnetic equator with two maximum peaks on both sides of the equator, at the magnetic latitudes of 15° - 20° north and south. This phenomenon is called equatorial (or Appelton) anomaly and this region is also called the equatorial region. Investigations by several authors (e.g. Hoque & Jakowski (2012)) show that the peak over the geomagnetic equator extends during daytime, but becomes weaker during nighttime. Various processes significantly disturb these areas, which display a strong diurnal dependence.

Mid latitude region This region is the least variable region of the ionosphere. It shows the most regular and predictable variations of TEC. There are several ionospheric models that estimate the mean ionosphere in this region with a high degree of accuracy. Nevertheless, the daily variations of TEC in this region reveals a residual mean square (r.m.s.) variations of 20 – 30% from the average value. Within this regions there are zones of low electron densities lying between 50° - 70° geomagnetic latitude called the mid latitude troughs (Muldrew, 1965). The electron density inside the trough is drastically reduced by as much as a factor of 2 at 1,000 *km* altitude and as much as an order of magnitude at the F2 peak (Timleck & Nelms, 1969).

High latitude region In the high latitude region photo-ionization is the main source of ionization. Another important driver in this region is the high energy particles. Geomagnetic field lines guide energetic protons and electrons from the magnetosphere down to the Earth's atmosphere. Accelerating particles lose their energy after colliding with the neutral

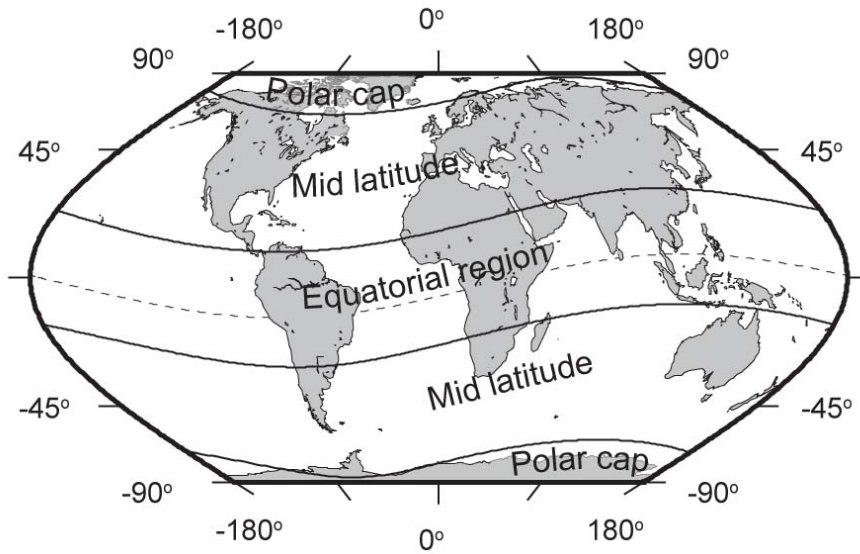


Figure 2.5: Latitude dependent regions of the ionosphere

particles and ionize them at the same altitude where solar UV radiation is absorbed by the atmosphere. Precipitating particles also lose their energy before collisions with the neutral particles through the particle-wave interaction, which finally generates intense electromagnetic waves named Auroral Kilometric Radiation (AKR), whose frequency is 100-500 *kHz*. Additionally, some of the atmospheric elements are excited to higher energy levels. This leads to emission of visible lights, called the auroral lights. This activity occurs mainly within the auroral oval. The maximum is near $67^\circ N$ at midnight, increasing to about $77^\circ N$ at noon. They tend to occur in bursts, each lasting about 30-60 *min*, which are separated by intervals of several hours.

2.3.2 Temporal variations

Variations within the solar radiation and the solar zenith angle causes temporal variations of the ionosphere. These variations could be classified into regular and irregular variations. The ionosphere exhibits daily, seasonal and longer variations controlled by the solar activity. Over the course of the day, season, and sunspot cycle the ionosphere parameters might change by several orders of magnitude. However, during irregular variations, the change can happen within a few minutes up to several days.

2.3.2.1 Regular variations

Solar cycle variations The long-period temporal variations in the ionosphere depend on the solar activity. A basic indicator for the level of solar activity is the sunspot number. Due to their relatively low temperature, the sunspots are visible on the solar surface

as darker regions and are usually located between 5° and 30° solar latitude (Hobiger, 2005). A widely used quantity is the Wolf sunspot number R :

$$R = k(f + 10g) \quad (2.8)$$

where:

- f total number of the observed single spots,
- g number of sunspot groups,
- k constant, depending on the instrumental sensitivity.

Sunspots are first noticed around 325 BC and have been recorded for several centuries. The spectral analysis of sunspot number time series shows a very prominent period of about 11.1 years. However the typical cycle is not symmetric, the time from minimum to maximum is about 4.3 years and the time from maximum to minimum is 6.6 years on average. The latest solar minimum was recorded in the period 2008-2009 (Fox, 2012). The next solar maximum is expected to occur in 2013. The solar activity level is also measured by the $F10.7\text{ cm}$ solar radio flux which is a proxy for the solar EUV radiation.

Seasonal variations In general, the maximum electron density and the TEC of the nighttime F region are higher in summer than in winter. However, in mid latitudes, the peak density of noon profiles is considerably greater in winter than in summer; this is called winter anomaly. This anomaly is more evident in mid latitudes than in low and high latitudes (Feltens *et al.*, 2009). The winter anomaly occurs in the daytime only and is thought to be due to a large summer electron loss rate caused by an increase in the molecular-to-atomic composition of the neutral atmosphere (Davies, 1990). The night time F2 layer tends to be at higher altitudes in summer than in winter, the tendency being accentuated in lower latitudes. The night time F2 layer tends to be thicker when higher. In the summer months, in middle latitudes, the F layer bifurcates into the F1 and F2 layers. Under these conditions the F2 peak density is fairly small and is located at a relatively high altitude. The F1 layer is not so much a distinct layer but rather a minor inflection in the profile at about 180 to 220 *km*. However, in the summer or around noon time, it is more liable to see the F1 layer as an individual layer comparing to winter time or in the sunrise and sunset.

Diurnal variations The most apparent effect is seen within the ionosphere as the Earth rotates around its axis. The ionization increases in the sunlit hemisphere, reaching a peak shortly after local noon time, and decreases on the shadowed side. In general, the electron densities are greater at all heights by day than by night and large diurnal changes occur

Classification	LSTID	MSTID	SSTID
Horizontal wavelentgh [km]	> 1000	> 100	> 10
Period [min]	30-180	10-60	> 1
Phase velocity [ms^{-1}]	300-1,000	100-300	-

Table 2.2: Traveling ionospheric disturbances

particularly in the lower ionosphere. While the D layer causes the weakening of propagated radio waves through the ionosphere during the day, it almost disappears during the night. The E layer appears promptly at sunrise and essentially disappears at sunset, except for the residual ionization at night.

2.3.2.2 Irregular variations

Ionospheric storms Ionospheric storms are large scale disturbances of the ionospheric structure and dynamics caused by a Coronal Mass Ejection (CME) from the sun. The storm is usually initiated by a huge solar flare followed by several coronal mass ejections on the subsequent days. The strong enhancements of the solar wind energy generate large perturbations in the high-latitude ionosphere and thermosphere resulting in significant variability of the plasma density, which commonly propagate towards lower latitudes (e.g. Förster & Jakowski (2000), and Ho *et al.* (1996)). The ionospheric storm can increase the TEC by more than 10 Total Electron Content Unit (*TECU*) (see sect. 2.4.3) (Feltens *et al.*, 2009).

Traveling ionospheric disturbances Traveling ionospheric disturbances (TID) are wave shape plasma density fluctuations propagating through the ionosphere at different range of velocities and frequencies. TID are observable in most of the ionospheric measurements (e.g. Faraday rotation, VLBI, GPS, and etc.). TID can change the value of the TEC in the region of their occurrence in the range of several percent (Schaer, 1999). Three types of TID are defined: large- (LSTID), medium- (MSTID) and small-scale (SSTID). LSTID present a period of 30-180 *min* and move at about 300 m/s. LSTID are related to geomagnetic activities and Joule effect in high latitudes, producing thermospheric waves towards lower latitudes. MSTID move slower (50-300 m/s) and have shorter periods (ranging from ten minutes to one hour). The origin of MSTID are related to meteorological phenomena like neutral winds or solar terminators which produce atmospheric gravity waves revealing TID at different ionospheric heights. Table 2.2 lists the main classifications of TID. According to Hobiger (2005) TID occur mostly in mid latitudes and are more evident close to solar maximum (Hernández-Pajares *et al.*, 2006).

Scintillations The term scintillation is used to describe the irregular variations of the

amplitude or of the phase of a radio signal received after passing through, or being reflected by the ionosphere. The strong scintillation typically can last for periods of up to several hours in the evening, broken up with varying intervals of time with no scintillation. The most severe scintillation effects are observed at and near the equatorial regions (Goodman & Aarons, 1990). However, the times of strong scintillation effects are generally limited to approximately one hour after local sunset to local midnight except some exceptions. The occurrence of strong scintillation is closely related to the sunspot number. During the years of maximum solar activity strong scintillation effects on GPS in the equatorial and low-latitude region are observed. In the months from September through March, chances are high for significant scintillation in the American, African, and Indian longitude regions. However, in the Pacific region, scintillation effects maximize during April through August months. In the auroral and polar cap latitudes, any significant magnetic storm activity can produce scintillation effects. Although the high-latitudes scintillations are not as strong as those measured in the near-equatorial belt, they can last for many hours, even days, and are not limited to the local late evening hours as the near equatorial scintillation effects (Feltens *et al.*, 2009).

Solar flare effects Solar radiation bursts known as solar flares may cause a rapid and severe increase of ionization in the ionosphere. Sudden Increase of TEC (SITEC) are caused by enhanced photo-ionization due to solar radiation bursts at wavelengths less than 130 nm. SITEC can effect TEC values in the range from less than 1 TECU up to 20 TECU or even more (Jakowski & Lazo, 1977). These TEC jumps are within few minutes and may seriously limit the accuracy and reliability of GNSS applications.

2.4 Ionospheric effects on microwave signals

In the following sections of this chapter, we mainly follow the overview paper Alizadeh *et al.* (2013).

2.4.1 Group and phase velocity

The characteristic of an electromagnetic wave propagating in space is defined by its frequency f and wavelength λ . In a dispersive medium, the propagation velocity of an electromagnetic wave is dependent on its frequency. In such a medium the propagation velocities of a sinusoidal wave and a wave group are different. The propagation velocity of a sinusoidal wave with a uniform wavelength is called the phase velocity ν_{ph} , while the propagation velocity of the wave group is referred to as group velocity ν_{gr} . Within the vacuum the phase and group velocities are the same, but in the real conditions, this is not the case. Following Wells (1974) the velocity of phase is

$$\nu_{ph} = \lambda f . \quad (2.9)$$

In general, the carrier waves propagate with the phase velocity. For the group velocity we have (Hofmann-Wellenhof *et al.*, 1993)

$$\nu_{gr} = -\left(\frac{df}{d\lambda}\right)\lambda^2 . \quad (2.10)$$

According to Bauer (2003) for Global Navigation Satellite Systems (GNSS), code measurements propagate with the group velocity.

By forming the differential of Eq. 2.9 we get

$$d\nu_{ph} = f d\lambda + \lambda df . \quad (2.11)$$

This equation can be re-arranged to

$$\frac{df}{d\lambda} = \frac{1}{\lambda} \frac{d\nu_{ph}}{d\lambda} - \frac{f}{\lambda} . \quad (2.12)$$

Substituting Eq. 2.12 into Eq. 2.10 yields the relation between group and phase velocities

$$\nu_{gr} = \nu_{ph} - \lambda \frac{d\nu_{ph}}{d\lambda} . \quad (2.13)$$

In a non-dispersive media phase and group velocities are the same and are equal or lower than the speed of light $c = 299,792,458 \text{ m s}^{-1}$ in vacuum.

As we know the wave propagation velocity in a medium depends on the refractive index n of that medium

$$\nu = \frac{c}{n} . \quad (2.14)$$

Implementing this equation to the phase and group velocities, the formulae for the phase and group refractive indices n_{ph} and n_{gr} read

$$n_{ph} = \frac{c}{\nu_{ph}} , \quad (2.15)$$

$$n_{gr} = \frac{c}{\nu_{gr}} . \quad (2.16)$$

Differentiating Eq. 2.15 with respect to λ yields

$$\frac{d\nu_{ph}}{d\lambda} = -\frac{c}{n_{ph}^2} \frac{dn_{ph}}{d\lambda} . \quad (2.17)$$

Substituting Eq. 2.17, Eq. 2.16, and Eq. 2.15 into Eq. 2.13 we get

$$\frac{c}{n_{gr}} = \frac{c}{n_{gr}} + \lambda \frac{c}{n_{ph}^2} \frac{dn_{ph}}{d\lambda} , \quad (2.18)$$

or

$$\frac{1}{n_{gr}} = \frac{1}{n_{ph}} \left(1 + \lambda \frac{1}{n_{ph}} \frac{dn_{ph}}{d\lambda} \right) . \quad (2.19)$$

Using the approximation $(1 + \varepsilon)^{-1} \doteq 1 - \varepsilon$, valid for small quantities of ε , Eq. 2.19 is rewritten as

$$n_{gr} = n_{ph} \left(1 - \lambda \frac{1}{n_{ph}} \frac{dn_{ph}}{d\lambda} \right) . \quad (2.20)$$

Thus the group refractive index follows

$$n_{gr} = n_{ph} - \lambda \frac{dn_{ph}}{d\lambda} , \quad (2.21)$$

Equation 2.21 is the modified Rayleigh equation (Hofmann-Wellenhof *et al.*, 1993). Another form is obtained by differentiating the relation $c = \lambda f$ with respect to λ and f , that is

$$\frac{d\lambda}{\lambda} = -\frac{df}{f} , \quad (2.22)$$

and by substituting the results into Eq. 2.21, the group refractive index yields

$$n_{gr} = n_{ph} + f \frac{dn_{ph}}{df} . \quad (2.23)$$

2.4.2 Ionosphere refractive index

Ionosphere is a dispersive medium with respect to microwave signals. This means that the propagation of microwave signals through the ionosphere depends on the frequency of the signals. To quantify these effects, the refractive index of the ionosphere must be specified. For a general derivation of the refractive index n in the ionosphere, we refer to Budden (1985). If the collision effects of the particles are ignored, the formula for the phase ionospheric refractive index can be presented as

$$n_{ph}^2 = 1 - \frac{X}{1 - \frac{\frac{1}{2}Y^2 \sin^2 \theta}{1-X} \pm \frac{1}{1-X} \left(\frac{1}{4}Y^4 \sin^4 \theta + Y^2 \cos^2 \theta (1-X)^2 \right)^{1/2}}, \quad (2.24)$$

where

$$X = \frac{\omega_0^2}{\omega^2}, \quad Y = \frac{\omega_H}{\omega},$$

$$\omega_0 = 2\pi f_0 = \sqrt{\frac{N_e e^2}{\varepsilon_0 m_e}}, \quad \omega_H = 2\pi f_H = \frac{B_0 |e|}{m_e},$$

n	complex refractive index	ν	electron collision frequency
ω	$= 2\pi f$ (radial frequency)	f	wave frequency
ω_0	electron plasma frequency	ω_H	electron gyro frequency
ε_0	permittivity of free space	B_0	magnitude of the magnetic field vector \mathbf{B}_0
θ	angle between the ambient magnetic field vector and the wave vector	e	electron charge
N_e	electron density	m_e	electron mass

Equation 2.24 is called the Appleton-Hertree formula for the ionospheric refractive index of phase. To evaluate the ionospheric effects more easily, various approximations of Eq. 2.24 were proposed. According to Tucker & Fanin (1968) and Hartmann & Leitinger (1984) the traditional way of deriving approximate expressions of the refractive index is by assuming that the magnetic field is associated with the propagation direction, with $\sin \theta \approx 0$. Without taking any assumptions about the propagation direction, Brunner & Gu (1991) preferred to use the order of magnitude of the various terms in Eq. 2.24 in deriving a suitable approximate expression for the ionospheric refractive index and their result is identical to the quasi-longitudinal refractive index expression derived by Budden (1985).

$$n_{ph}^{ion} = 1 - \frac{X}{2} \pm \frac{XY}{2} \cos \theta - \frac{X^2}{8}. \quad (2.25)$$

Following Brunner & Gu (1991), it is convenient to define the constants C_X and C_Y as

$$C_X \equiv \frac{e^2}{4\pi^2\epsilon_0 m_e} = 80.62 , \quad (2.26)$$

$$C_Y \equiv \frac{e}{2\pi m_e} , \quad (2.27)$$

so that Eq. 2.25 can be expressed in orders of $\frac{1}{f^n}$

$$n_{ph}^{ion} = 1 - \frac{C_X}{2} N_e f^{-2} \pm \frac{C_X C_Y}{2} N_e B_0 \cos \theta f^{-3} - \frac{C_X^2}{8} N_e^2 f^{-4} , \quad (2.28)$$

Equation 2.28 includes the first-order term and higher order terms of the ionospheric propagation effects of microwaves frequencies.

First order refractive index

The first two terms in Eq. 2.28 are denoted as the first and second order refractive index. Since the third- and fourth-order terms are each one order of magnitude smaller than the second-order term, they are in first approximation, usually neglected (Alizadeh *et al.*, 2011). Thus, equation Eq. 2.28 can be reduced to

$$n^{ion} = 1 - \frac{C_X}{2} N_e f^{-2} . \quad (2.29)$$

Evaluating the constant factor in Eq. 2.29, we obtain:

$$C_2 = \frac{C_X}{2} = \frac{e^2}{8\pi^2\epsilon_0 m_e} \approx 40.31 \quad [\text{m}^3/\text{s}^2] . \quad (2.30)$$

By substituting Eq. 2.30 into Eq. 2.29 the first-order refractive index is obtained. Equation 2.29 is used for the phase measurements, so it is denoted as phase refractive index n_{ph}^{ion} :

$$n_{ph}^{ion} = 1 - C_2 \frac{N_e}{f^2} = 1 - 40.31 \frac{N_e}{f^2} . \quad (2.31)$$

To obtain the group refractive index, Eq. 2.31 is differentiated:

$$\frac{dn_{ph}}{df} = \frac{2C_2}{f^3} N_e , \quad (2.32)$$

substituting Eq. 2.31 and Eq. 2.32 into Eq. 2.23 yields:

$$n_{gr}^{ion} = 1 - \frac{C_2}{f^2} N_e + f \frac{2C_2}{f^3} N_e df , \quad (2.33)$$

or

$$n_{gr}^{ion} = 1 + C_2 \frac{N_e}{f^2} = 1 + 40.31 \frac{N_e}{f^2} . \quad (2.34)$$

It can be seen from Eq. 2.31 and Eq. 2.34 that the group and phase refractive indices have the same diversity from one but with an opposite signs. As $n_{gr} > n_{ph}$ it is simply concluded that $v_{gr} < v_{ph}$. As a consequence of the different velocities, when a signal travels through the ionosphere, the carrier phase is advanced and the modulated code is delayed. In the case of GNSS, code measurements which propagate with the group velocity are delayed and the phase measurements that propagate with phase velocity are advanced. Therefore, compared to the geometric distance between a satellite and a receiver, the code pseudo-ranges are measured too long and phase pseudo-ranges are measured too short. The amount of this difference is in both cases the same (Hofmann-Wellenhof *et al.*, 1993).

High order refractive index

The first order refractive index only accounts for the electron density within the ionosphere, while the effect of the Earth's magnetic field and its interactions with the ionosphere are considered in the higher order terms; i.e. the third and fourth terms of Eq. 2.28. For precise satellite positioning, these terms have to be considered as they will introduce an ionospheric delay error of up to a few centimeters (Bassiri & Hajj, 1993; Brunner & Gu, 1991).

2.4.3 Ionospheric delay

According to Fermat's principle (Born & Wolf, 1964), the measured range s is defined below by assuming the speed of light is equal to its value in vacuum

$$s = \int_s n ds , \quad (2.35)$$

where the integration is performed along the path s of the signal. The geometric distance s_0

between the satellite and the receiver may be obtained analogously by setting $n = 1$:

$$s_0 = \int_s ds_0 . \quad (2.36)$$

The delay (or advance) experienced by signals traveling through the ionosphere is the difference between measured and geometric range. This is called the ionosphere delay or ionospheric refraction:

$$\Delta\rho^{ion} = \int_s n ds - \int_s ds_0 . \quad (2.37)$$

By substituting Eq. 2.28 into Eq. 2.37, the ionospheric total delay for the phase observations is expressed as

$$\Delta\rho_{ph}^{ion} = -\frac{C_X}{2f^2} \int_s N_e ds \pm \frac{C_X C_Y}{2f^3} \int_s N_e B_0 \cos \theta ds - \frac{C_X^2}{8f^4} \int_s N_e^2 ds + \kappa , \quad (2.38)$$

where $\kappa = \int_s ds - \int_s ds_0$ represents the curvature effect. The first three terms of Eq. 2.38 denote the first order and higher order ionospheric delays. Assuming that the integrations are evaluated along the geometric path s_0 for simplification, the curvature effect is neglected; thus ds turns to ds_0 and the equation results in

$$\Delta\rho_{ph}^{ion} = -\frac{C_X}{2f^2} \int_s N_e ds_0 \pm \frac{C_X C_Y}{2f^3} \int_s N_e B_0 \cos \theta ds_0 - \frac{C_X^2}{8f^4} \int_s N_e^2 ds_0 . \quad (2.39)$$

First order delay

In the first-order approximation, the ionospheric delay for phase measurements is derived by neglecting the second and third terms of Eq. 2.39) and making use of Eq. 2.30:

$$\Delta\rho_{ph}^{ion1} = -\frac{C_2}{f^2} \int_s N_e ds_0 , \quad (2.40)$$

by substituting C_2 from Eq. 2.30 we get the phase delay

$$\Delta\rho_{ph}^{ion1} = -\frac{40.31}{f^2} \int_s N_e ds_0 . \quad (2.41)$$

The group delay is similarly obtained using Eq. 2.34

$$\Delta\rho_{gr}^{ion1} = \frac{40.31}{f^2} \int_s N_e ds_0 . \quad (2.42)$$

Second order delay

According to Eq. 2.39, the second order ionospheric phase delay is

$$\Delta\rho_{ph}^{ion2} = \frac{C_X C_Y}{2f^3} \int_s N_e B_0 \cos \theta ds_0 . \quad (2.43)$$

Examining the constants C_X and C_Y from Eq. 2.26 and 2.27, Eq. 2.43 can be written as

$$\Delta\rho_{ph}^{ion2} = -\frac{7527 c}{2f^3} \int_s N_e B_0 \cos \theta ds_0 , \quad (2.44)$$

where c is the speed of light. To solve Eq. 2.44, information of the magnetic field B_0 and the angle θ along the ray path have to be known. Since this is difficult to accomplish, Brunner & Gu (1991) assumed that $B_0 \cos \theta$ does not vary greatly along the ray path, so that one may take the average $\overline{B_0 \cos \theta}$ in front of the integration:

$$\Delta\rho_{ph}^{ion2} = -\frac{7,527 c}{2f^3} \overline{B_0 \cos \theta} \int_s N_e ds_0 . \quad (2.45)$$

An alternative way was proposed by Bassiri & Hajj (1993) who assumed the Earth's magnetic field as a co-centric tilted magnetic dipole and approximated the ionospheric layer as a thin shell at the height of 400 km. Thus, the magnetic field vector \mathbf{B}_0 can be written as:

$$\mathbf{B}_0 = B_g \left(\frac{R_E}{R_E + H} \right) [\sin \theta_m \cdot \mathbf{Y}_m - 2 \cos \theta_m \cdot \mathbf{Z}_m] , \quad (2.46)$$

B_g represents the magnetic field near the equator at surface height ($B_g \approx 3.12 \times 10^{-5}$ Tesla). R_E is the Earth's radius ($R_E \approx 6,370$ km). H denotes the height of the ionospheric thin shell above the Earth's surface ($H = 400$ km). \mathbf{Y}_m and \mathbf{Z}_m are the Y and Z unit vectors in the geomagnetic coordinate system, and θ_m is the angle between the ambient magnetic field vector and wave vector in the geomagnetic coordinate system (see Sect.2.3). The scalar product of the magnitude field vector \mathbf{B}_0 and the signal propagation unit vector \mathbf{k} is:

$$\mathbf{B}_0 \cdot \mathbf{k} = B_0 |\mathbf{k}| \cos \theta = B_0 \cos \theta . \quad (2.47)$$

Combining Eq. 2.44, Eq. 2.46, and Eq. 2.47, an expression similar to Eq. 2.45 can be derived

$$\Delta \rho_{ph}^{ion2} = -\frac{7,527}{2f^3} c \mathbf{B}_0 \cdot \mathbf{k} \int_s N_e ds_0 . \quad (2.48)$$

Equation 2.48 is sufficient to approximate the effect of the second order term to better than 90% on the average (Fritsche, 2005).

Third order delay

According to Eq. 2.39 and evaluating the constant C_X , the third order ionospheric phase delay is expressed as

$$\Delta \rho_{ph}^{ion3} = -\frac{812.4}{f^4} \int_s N_e^2 ds_0 . \quad (2.49)$$

Brunner & Gu (1991) applied the shape parameter η in such a way that the integral in Eq. 2.49 can be approximated by

$$\int_s N_e^2 ds_0 = N_{max} \eta \int_s N_e ds_0 . \quad (2.50)$$

The shape parameter η may be assumed with 0.66 as an appropriate value to account for different electron density distributions. N_{max} represents the peak electron density along the ray path. Substituting Eq. 2.50 into Eq. 2.49, the third order ionospheric phase delay can be written as:

$$\Delta \rho_{ph}^{ion3} = -\frac{812.4}{f^4} N_{max} \eta \int_s N_e ds_0 . \quad (2.51)$$

Integrated electron density

As already shown, the first, second and third order ionospheric delays require the distribution of the electron density N_e along the ray path. If one is interested in signal propagation in the ionosphere, however, the integral of the electron density along the ray path becomes relevant (e.g. Schaer (1999)). This quantity is defined as the Total Electron Content (TEC) and represents the total amount of free electrons in a cylinder with a cross section of 1 m^2 and a height equal to the slant signal path. TEC is measured in Total Electron Content Unit (*TECU*), with 1 *TECU* equivalent to 10^{16} electrons per m^2 (*elec/m*²). For an arbitrary ray

path the slant TEC (STEC) can be obtained from

$$STEC = \int_s N_e(s) ds , \quad (2.52)$$

where N_e is the electron density along the signal path s .

Using Eq. 2.52 the relation between the TEC in *TECU* and ionospheric delay in meters can be obtained. Taking Eq. 2.41 into account for the carrier phase measurements we get

$$\Delta\rho_{ph}^{ion} = -\frac{40.31}{f^2} STEC \quad [m] , \quad (2.53)$$

in the case of group delay measurements, the result is the same, but with opposite sign

$$\Delta\rho_{gr}^{ion} = \frac{40.31}{f^2} STEC \quad [m] . \quad (2.54)$$

Finally, using the constant derived from Eq. 2.30 the factor ϑ can be defined as the ionospheric path delay in meters per one *TECU*, related to a certain frequency f in *Hz*

$$\vartheta = \frac{40.31 \times 10^{16}}{f^2} \quad [m/TECU] . \quad (2.55)$$

Table 2.3 shows some relations between the various GNSS parameters and the TEC extracted from Klobuchar (1996)

Single layer model and mapping function

For absolute TEC mapping using ground-based GNSS data, TEC along the vertical should be taken into account. Since GPS basically provides measurements of STEC, an elevation dependent mapping function $F(z)$ is required which describes the ratio between the STEC and the vertical TEC (VTEC):

$$F(z) = \frac{STEC}{VTEC} . \quad (2.56)$$

To get an approximation, a single-layer model (SLM) is usually adopted for the ionosphere. In SLM it is assumed that all free electrons are concentrated in an infinitesimally thin layer above the Earth's surface (Schaer, 1999). The height H of that shell is usually set between

Table 2.3: Relation between various GNSS first-order measured parameters and TEC of Earth's ionosphere extracted from Klobuchar (1996)

$L_2 - L_1$, differential group delay caused by the ionosphere	
1 ns of differential code delay	$2.852 \times 10^{16} \text{ el}/m^2$ 1.546 ns of delay at L_1 0.464 m of range error at L_1
1 ns of delay, measured at L_1	$1.8476 \times 10^{16} \text{ el}/m^2$ 0.300 m of range error at L_1
1 m of range error	measured at $L_1 = 6.15 \times 10^{16} \text{ el}/m^2$ measured at $L_2 = 3.73 \times 10^{16} \text{ el}/m^2$
1 TEC Units [$1 \times 10^{16} \text{ el}/m^2$]	0.351 ns of differential delay 0.524 ns of delay at L_1 0.163 m of range delay at L_1 0.853 cycles of phase advance at L_1

350 km and 500 km, which is slightly above the height where the highest electron density is expected (approximately above the height of the F2 layer peak). Figure 2.6 depicts the basic geometry of the SLM in the sun-fixed coordinate system. The signal transmitted from the satellite to the receiver crosses the ionospheric shell in the so-called Ionospheric Pierce Point (IPP). The zenith angle at the IPP is z' and the signal arrives at the ground station with zenith angle z . From Fig. 2.6 the relation between z' and z could be derived:

$$\sin z' = \frac{R_E}{R_E + H} \sin z . \quad (2.57)$$

In Eq. 2.57 R_E is the mean Earth radius and H is the height of the single layer in km.

Applying the Chapman function (see Sect. 5.3.1) and the TEC definition Eq. 2.52 into Eq. 2.56 leads to the so-called SLM mapping function

$$F(z') = \frac{1}{\cos z'} = \frac{1}{\sqrt{1 - \sin^2 z'}} , \quad (2.58)$$

where z' is obtained from Eq. 2.57.

A modified single-layer mapping function (MSLM) is adopted by Dach *et al.* (2007):

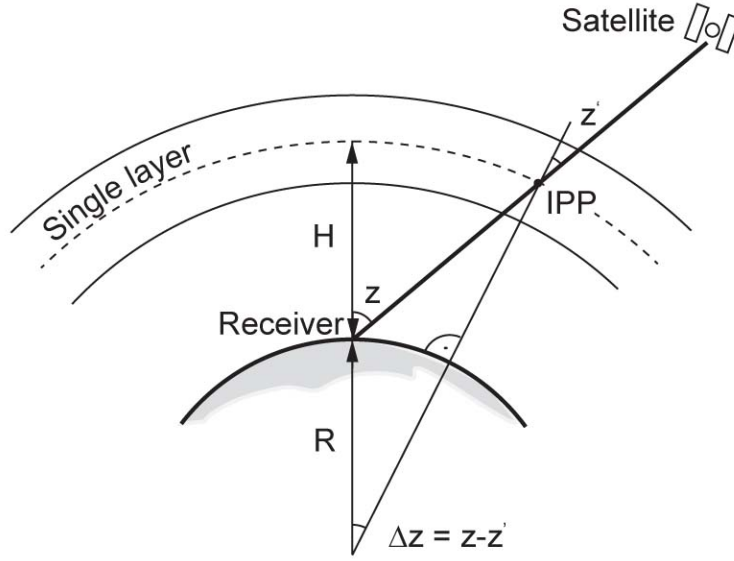


Figure 2.6: Single-layer model for the ionosphere

$$F(z) \cong \frac{1}{\sqrt{1 - \left(\frac{R_E}{R_E + H} \sin(\alpha z) \right)^2}}, \quad (2.59)$$

where $\alpha = 0.9782$ and $H = 506.7 \text{ km}$. It should be clarified that the only difference between MSLM and SLM is the heuristic factor α . The MSLM approximates the Jet Propulsion Laboratory (JPL) extended slab model mapping function. Based on results showing that a single layer height of 550 km tends to be the best choice overall, the extended slab model provides an approximation which closely matches a single layer model with the same shell height of 550 km (Sparks *et al.*, 2000).

Chapter 3

Ionosphere and space geodetic observation techniques

The most important parameter of the ionosphere that affects the signals from space geodetic techniques is the electron density distribution within the ionosphere. As already described in Sect. 2.4.3 the integrated number of electrons, commonly called Total Electron Content (TEC), is connected to the phase delay Eq. 2.53 and to group delay Eq. 2.54. There are different ways to deal with ionosphere and TEC depending on the specific technique being used; some methods are discussed in the following.

3.1 GNSS

3.1.1 General concepts

The Global Navigation Satellite Systems (GNSS) include of the U.S.A. Global Positioning System (GPS), the Russian Globalnaya Navigatsionnaya Sputnikovaya Sistema (GLONASS), the upcoming European Galileo and the Chinese COMPASS system. The fundamental of satellite navigation is the simultaneous observation of at least four satellites with known coordinates. The measurements are carried out through correlation of the received satellite signal with an identical signal generated in the ground receiver. The difference between the received and the generated signal is directly proportional to the travel time of a signal from satellite to the receiver. As the satellite and receiver have different clocks, in addition to the three unknown coordinates of the receiver, an additional unknown appears in the observation equation (see Sect. 3.1.2.1). Therefore, only the simultaneous observation to at least four satellites enables the equation to be solved for all positioning parameters, i.e. for longitude, latitude, height, and clock correction.

As there are many literatures describing GNSS principles, in the following section, we briefly overview the GPS concepts associated to our study. For more details on GPS please refer to e.g. Hofmann-Wellenhof *et al.* (1993). Details on GLONASS could be found in e.g. H.

(1999).

GPS

Global Position System (GPS) is a Satellite based navigation system developed by the U.S.A. Department of Defense (DoD) in 1973, to satisfy the requirements for the military forces to accurately determine their position, velocity and time in a common reference system anywhere on or near Earth on a continuous basis, at any meteorological conditions (Wooden, 1984). GPS primary goals were military ones, but later, in 1983, it became available for civilian users with limited access. The system was fully operational in July 1995, with a constellation of 24 operating satellites. GPS consists of three different segments, namely

- Space segment with active Satellites,
- Control segment steering the whole system, and
- User segment including different receiver types.

Space segment The space segment consists of 24 operational satellites, launched in six orbits of about 20,200 *km* altitude above the Earth surface with inclination of 55° with respect to the Earth's equator. The orbital period is 11*h* and 58*min*. The constellation of satellites is in such a way that at least four of them are simultaneously visible above 15° from the horizon at anytime and anyplace of the Earth. Caesium or rubidium atomic clocks on board each satellite oscillate fundamental frequency of 10.23 *MHz* with long-term stability of 10^{-13} to 10^{-14} over one day. Two carrier frequencies in the L-band are coherently derived by multiplying the fundamental frequency by two different integers, providing L1 (1575.42 *MHz*) and L2 (1227.60 *MHz*). Each Satellite transmits both frequencies. These are the navigation signals (codes), and the navigation and system data (message). The codes modulated on the carrier frequencies are Pseudo Random Noise (PRN) sequences. L1 contains both, the Precise code (P-code) and the less precise Coarse/Acquisition code (C/A-code). L2 signal contains only the P-code. Navigation message is also modulated on both L1 and L2 carriers. The message contains information about GPS time, clock behavior, system status, satellite health and some other necessary information. The GPS satellites are identified by plane/slot and PRN numbers from 1 to 32, and usually denoted as "G" and the PRN number, i.e. (G1, G2, \dots , G32).

Control segment The main operational tasks of the control segment are tracking satellites for the orbit and clock determination, prediction modeling, time synchronization, and uploading data message to the satellites. This segment consists of a Master Control Station (MCS) near Colorado Springs, U.S.A., several Monitor Stations (MS) located around the world and ground stations for uploading data into the satellites. The monitor stations receive all satellite signals, from which they determine the pseudoranges to all visible satellites,

and transmit the range data along with the meteorological data via a data link to the master control station. From these data, master control station pre-computes satellite ephemerides and the behavior of the satellite clocks and formulates the navigation data. The message data are then transmitted to ground antennas and up linked to the satellites in view. Because of the global distribution of upload antennas at least three contacts per day can be realized between the control segment and each satellite. Given the daily upload, the satellite broadcasts its position and clock corrections continued in 4h interval. Although predictions beyond the next days upload overwrites them with results derived from more current data. If the contact of a satellite with the control segment is lost, the satellite data can still be used for positioning up to a certain time limit. This limit depends on the type of the satellite. The limit for the satellites of Block II is 14 days, for satellites of Block IIA is 180 days , and more than 180 days for satellites of Block IIR.

User segment Aforesaid, GPS was primarily developed for military use, but today, civilians can also use the system with some restrictions. Appropriate receivers are required to use the GPS signals for navigation, positioning, or other purposes. The GPS receivers vary depending on the purpose of their use, but in general, they are classified as one or double-frequency receivers, and according to their ability to receive code pseudorange and/or carrier phase. Within the user segment, there are several information services. The most important of these services is the International GNSS Service (IGS) (Dow *et al.*, 2009), established in 1993 by the International Association of Geodesy (IAG). IGS is a voluntary federation of more than 200 worldwide agencies that pool resources and permanent station data to generate precise GPS and GLONASS products. As of November 2007, the IGS global tracking network was increased to 341 active tracking stations. The data obtained at these stations are processed at the IGS Analysis Center (AC), and provided to the users. These products include:

- GPS satellite ephemerides and satellite and station clocks,
- geocentric coordinates and velocities of the IGS tracking stations,
- final, rapid, and ultra-rapid earth rotation parameters: length-of-day, polar motion and polar motion rates, and
- atmospheric parameters, including ionospheric TEC grid.

The IGS data and products are obtained freely to the users via the servers of the IGS data centers (IGS, 2012). The GNSS observation data is stored in daily station specific files in the Receiver INdependent EXchange (RINEX) format.

Differential Code Biases

The Differential Code Biases (DCB) or the so-called hardware delay biases are frequency

dependent time delays of the satellite and receiver, expressed in *nano-sec*. The receiver DCB are usually known, but in case of satellite DCB, as the measurements of these biases before and after launch are significantly different, it becomes necessary to calculate DCB values for both satellite and receiver. Since the satellite and receiver DCB are frequency-dependent, they can be estimated as a by-product, along with the ionospheric parameters (see Sect. 3.1.3.2). The estimated DCB contain information about the stability of instrumental biases and also the quality of the estimated ionospheric parameters (Schaer, 1999).

3.1.2 Observables

In this section, the fundamental GNSS observation equations along with a second level observable which is commonly used in ionospheric studies are briefly discussed.

3.1.2.1 Fundamental observation equation

Referring to Teunissen & Kleusberg (1998), the code pseudorange P_i transmitted from the satellite S and received at the receiver R is given by

$$P_i = \rho + c(\delta t_R - \delta t^S) + \Delta\rho^{trop} + \Delta\rho_i^{ion} + c(b_R + b^S)_i + \varepsilon_i, \quad (3.1)$$

where

P_i	slant range between satellite and receiver, observed at the i frequency
ρ	geometric distance between receiver and satellite
$\delta t_R, \delta t^S$	receiver and satellite clock offsets to the GPS time
$\Delta\rho^{trop}$	delay of the signal due to the troposphere
$\Delta\rho_i^{ion}$	frequency-dependent delay of the signal due to the ionosphere
b_R, b^S	frequency-dependent hardware delays of the satellite and receiver (DCB) (in <i>ns</i>)
ε_i	random error, at the i frequency.

In the equation above, subscript ' i ' indicates the frequency-number of the transmitted signal and the term ρ includes the periodic relativistic effect and the gravitational field refraction (Rothacher *et al.*, 1996).

For carrier phase, the phase-pseudorange L_i , expressed in units of length, is given by

$$L_i = \rho + c(\delta t_R - \delta t^S) + \Delta\rho^{trop} - \Delta\rho_i^{ion} + \lambda_i B_i + \varepsilon_i \quad (3.2)$$

where λ_i is the wavelengths at i frequency-band, and the term λB at each frequency denotes a constant bias expressed in cycles, which contains the initial carrier phase ambiguity N , the effect due to calibration, including the phase windup δN , and the phase hardware biases of satellite and receiver. According to Schaer (1999) one cannot separate N from the hardware biases and therefore has to be substitute with λB term.

The phase observations are two to three orders of magnitude more accurate than the code observations. However, the ambiguity term which affects the phase observation only, makes usage of this accurate observable rather critical (Schaer, 1999).

3.1.2.2 Pseudo-range smoothing

Based on the fundamental code and phase pseudorange observables, a new observable can be created, which makes use of the advantages of each of the fundamental observables. As already mentioned, the code pseudorange has the problem of being noisy and less accurate compared to the phase pseudorange. The phase pseudorange in turn, has the problem of resolving the ambiguity term. The phase-smoothed code pseudorange that is built from the dual-frequency code measurements smoothed by the phase pseudorange, has a significantly reduced noise level with respect to code pseudorange, and its ambiguity is approximately determined by leveling the phase measurements to code (Todorova, 2008). The smoothed code observable \tilde{P} at the two frequencies, at a certain epoch t is written as

$$\begin{aligned}\tilde{P}_1(t) &= \bar{P}_1 + \Delta L_1(t) + 2 \frac{f_{L_1}^2}{f_{L_1}^2 - f_{L_2}^2} (\Delta L_1(t) - \Delta L_2(t)) , \\ \tilde{P}_2(t) &= \bar{P}_2 + \Delta L_2(t) + 2 \frac{f_{L_1}^2}{f_{L_1}^2 - f_{L_2}^2} (\Delta L_1(t) - \Delta L_2(t)) ,\end{aligned}\tag{3.3}$$

with

$$\begin{aligned}\Delta L_1(t) &= L_1(t) - \bar{L}_1 , \\ \Delta L_2(t) &= L_2(t) - \bar{L}_2 ,\end{aligned}\tag{3.4}$$

where

$L_1(t), L_2(t)$	phase measurements at epoch t ,
\bar{L}_1, \bar{L}_2	mean phase measurements over a time period in which no cycle-slips occurred during the satellite pass,
\bar{P}_1, \bar{P}_2	mean code measurements over the same 'cycle-slip free' time interval.

Referring to Schaer (1999), the noise of the smoothed code pseudorange is reduced by a factor of \sqrt{n} with respect to the noise of un-smoothed code measurements. n denotes the number of epochs taken into account.

3.1.3 Ionosphere-related combination of observables

3.1.3.1 Ionosphere-free linear combination

Considering Eq. 2.53 and 2.54, designating the ionosphere is restricted to determination of the TEC. However, TEC is a very complex quantity, depending on many parameters such as sunspot activity, seasonal and diurnal variations, line of signal propagation, and the

position of the observation site. Therefore it's usually hard to find an appropriate model for it. Thus the most efficient method is to eliminate its effect by using signals of different frequencies. This is the main reason why many of space geodetic techniques transmit signals in at least two different frequencies. Forming linear combinations with different frequencies allows eliminating the effect of the ionosphere by large extent.

Eliminating first-order ionospheric effect

Recalling the fundamental observation equation for the GNSS code pseudorange Eq. 3.1, for each frequency we can write

$$\begin{aligned} P_1 &= \rho + c(\delta t_R - \delta t^S) + \Delta\rho^{trop} + \Delta\rho_1^{ion} + c(b_R + b^S)_1 + \varepsilon_1 , \\ P_2 &= \rho + c(\delta t_R - \delta t^S) + \Delta\rho^{trop} + \Delta\rho_2^{ion} + c(b_R + b^S)_2 + \varepsilon_2 , \end{aligned} \quad (3.5)$$

The code ranges are obtained from measurements of the signals P_1 and P_2 modulated at the two carriers with the frequencies denoted by 1 and 2 and the ionospheric term $\Delta\rho^{ion}$ is equivalent to the group delay in Eq. 2.54.

A linear combination is now performed by

$$P_{1,2} = n_1 P_1 + n_2 P_2 , \quad (3.6)$$

where n_1 and n_2 are factors to be determined, in such a way that the ionospheric refraction cancels out. Substituting Eq. 3.5 into Eq. 3.6 leads to the postulate

$$n_1 \Delta\rho_1^{ion} + n_2 \Delta\rho_2^{ion} = 0 . \quad (3.7)$$

Assuming n_1 and n_2 as

$$n_1 = +\frac{f_{L_1}^2}{f_{L_1}^2 - f_{L_2}^2} , \quad n_2 = -\frac{f_{L_2}^2}{f_{L_1}^2 - f_{L_2}^2} . \quad (3.8)$$

Substituting these values for n_1 and n_2 , Eq. 3.7 is fulfilled due to Eq. 2.54 and the linear combination Eq. 3.6 becomes:

$$P_{1,2} = \frac{f_{L_1}^2}{f_{L_1}^2 - f_{L_2}^2} P_1 - \frac{f_{L_2}^2}{f_{L_1}^2 - f_{L_2}^2} P_2 = P_3 . \quad (3.9)$$

The P_3 ionospheric-free linear combination for code ranges. This linear combination can be

written in a more convenient expression:

$$P_3 = \frac{1}{1 - \gamma} (P_1 - \gamma P_2) , \quad (3.10)$$

where

$$\gamma = \frac{f_{L_2}^2}{f_{L_1}^2} . \quad (3.11)$$

A similar ionospheric-free linear combination for carrier phase may be derived using the fundamental equation for phase pseudorange Eq. 3.2. The carrier phase models can be written as:

$$\begin{aligned} L_1 &= \rho + c(\delta t_R - \delta t^S) + \Delta\rho^{trop} - \Delta\rho_1^{ion} + \lambda_1 B_1 + \varepsilon_1 , \\ L_2 &= \rho + c(\delta t_R - \delta t^S) + \Delta\rho^{trop} - \Delta\rho_2^{ion} + \lambda_2 B_2 + \varepsilon_2 , \end{aligned} \quad (3.12)$$

Now a linear combination is performed analogously to Eq. 3.6

$$L_{1,2} = n_1 L_1 + n_2 L_2 , \quad (3.13)$$

with similar coefficients as in Eq. 3.8, the linear combination would follow:

$$L_{1,2} = \frac{f_{L_1}^2}{f_{L_1}^2 - f_{L_2}^2} L_1 - \frac{f_{L_2}^2}{f_{L_1}^2 - f_{L_2}^2} L_2 = L_3 . \quad (3.14)$$

The L_3 ionospheric-free linear combination for phase ranges and can also be expressed as

$$L_3 = \frac{1}{1 - \gamma} (L_1 - \gamma L_2) . \quad (3.15)$$

Eliminating higher-order ionospheric effects

The elimination of the ionospheric refraction is the huge advantage of the two ionospheric - free linear combinations Eq. 3.10 and Eq. 3.15. Although the term "ionospheric - free" is not completely correct as in this combination the higher-order terms as well as the curvature effects which are less than 0.1 % of the total value in L-band, are neglected (Wijaya, 2010).

Based on the geometrical optic approximation Brunner & Gu (1991) proposed an im-

proved model for the ionospheric-free linear combination that considers the significant higher-order terms, the curvature effect of the ray paths, and the effect of the magnetic field. The improved model is written as:

$$L_3 = \frac{1}{1 - \Gamma} (L_1 - \Gamma L_2) - [\kappa_1 - \kappa_2] , \quad (3.16)$$

where

$$\Gamma = \frac{\Gamma_1}{\Gamma_2} , \quad (3.17)$$

$$\kappa_2 = \frac{\Gamma}{1 - \Gamma} \nu , \quad (3.18)$$

with

$$\Gamma_1 = \frac{C_X}{2f_{L_1}^2} \left(1 \pm \frac{C_Y}{f_{L_1}^2} \overline{N_e B_0 \cos \theta} - \frac{C_X}{4f_{L_1}^2} N_{max} \eta \right) , \quad (3.19)$$

$$\Gamma_2 = \frac{C_X}{2f_{L_2}^2} \left(1 \pm \frac{C_Y}{f_{L_2}^2} \overline{N_e B_0 \cos \theta} - \frac{C_X}{4f_{L_2}^2} N_{max} \eta \right) . \quad (3.20)$$

A comparison of Eq. 3.15 with Eq. 3.16 shows that the improved model replaces γ by the more complete Γ and includes two curvature correction terms κ_1 and κ_2 .

3.1.3.2 Geometry-free linear combination

GNSS allows determination of the station specific ionosphere parameters in terms of STEC values, using carrier phase, code or the smoothed code measurements. To extract information about the ionosphere from the GNSS observations, a linear combination is formed, which eliminates the geometric term. This linear combination is called geometry-free linear combination L_4 or the ionospheric observable.

Ionospheric observable

To form the ionospheric observable or the geometry-free linear combination, simultaneous observations at two carriers L_1 and L_2 are subtracted. In this way along with the geometric term, all frequency-independent effects such as clock offsets and tropospheric delay are eliminated. This leads to an observable, which contains only the ionospheric refraction and the differential inter-frequency hardware delays. The geometry-free linear combination has the form:

$$L_4 = k_{1,4}L_1 + k_{2,4}L_2 = L_1 - L_2 , \quad (3.21)$$

with $k_{1,4} = 1$ and $k_{2,4} = -1$.

Applying the above combination to the observation equations Eq. 3.5 and Eq. 3.12 leads to the geometry-free linear combination for the code and phase measurements, respectively

$$P_4 = +\xi_4 I + c (\Delta b^S - \Delta b_R) , \quad (3.22)$$

$$L_4 = -\xi_4 I + B_4 , \quad (3.23)$$

where:

$\xi_4 = 1 - f_{L_1}^2 / f_{L_2}^2 \approx -0.647$	factor for relating the ionospheric refraction on L_4 to L_1 ,
$B_4 = \lambda_{L_1} B(f_{L_1}) - \lambda_{L_2} B(f_{L_2})$	ambiguity parameter with undefined wavelength, thus defined in length units,
$\Delta b^S = b^{S,1} - b^{S,2}$	differential inter-frequency hardware delay of the satellite S in time units,
$\Delta b_R = b_{R,1} - b_{R,2}$	differential inter-frequency hardware delay of the receiver R in time units.

The geometry-free linear combination can also be applied to the smoothed code measurements Eq. 3.3, resulting

$$\tilde{P}_4 = \xi_4 I + c (\Delta b^S - \Delta b_R) , \quad (3.24)$$

The ionospheric refraction I in Eq. 3.22, Eq. 3.23, and Eq. 3.24 can be related to the VTEC as a function of the geomagnetic latitude and the sun-fixed longitude in the following way:

$$I = \xi_E STEC(\beta, s) = \xi_E F(z) VTEC(\beta, s) , \quad (3.25)$$

with:

β	geomagnetic latitude,
s	sun-fixed longitude,
$\xi_E = \frac{C_x}{2} f_1^{-2}$	$\approx 0.162 \text{ m/TECU}$.

By substituting Eq. 3.25 in equations Eq. 3.22, Eq. 3.23, or Eq. 3.24, the ionospheric observable for code, phase or the smoothed code measurements could be obtained

$$P_4 \approx +\xi_4 \xi_E F(z) VTEC(\beta, s) + c (\Delta b^S - \Delta b_R) , \quad (3.26)$$

$$L_4 \approx -\xi_4 \xi_E F(z) VTEC(\beta, s) + B_4 . \quad (3.27)$$

$$\tilde{P}_4 \approx \xi_4 \xi_E F(z) VTEC(\beta, s) + c (\Delta b^S - \Delta b_R) , \quad (3.28)$$

In Eq. 3.26 - 3.28, the equation sign '=' has been replaced by the approximate equation sign ' \approx ' because of including the simplified single layer assumption. Depending on the study and whether we want to estimate VTEC on a local, regional or global basis, $VTEC(\beta, s)$ will be represented by a series expansion with an appropriate base-function. As an example Taylor series expansion can be used for local representation of TEC (Schaer, 1999); B-splines are very suitable for studying TEC in regional applications (Schmidt *et al.*, 2008), and for global representation of TEC, spherical harmonics expansion is most commonly used (Alizadeh *et al.*, 2011). Details will follow in the next chapter.

3.2 Satellite altimetry

3.2.1 General concepts

Satellite altimetry is a particular way of ranging in which the vertical distance between a satellite and the surface of the Earth is measured (Seeber, 1993). The range between the satellite and the Earth's surface is derived from the traveling time of the radar impulse transmitted by the radar-altimeter and reflected from the ground. Therefore the method is best applicable over the oceans, due to the good reflective properties of the water. The signals are transmitted permanently in the high frequency domain (about 14 GHz) and the received echo from the sea surface is used for deriving the round-trip time between the satellite and the sea. The satellite-to-ocean range is obtained by multiplication of the traveling time of the electromagnetic waves with the speed of light and averaging the estimates over a second (Todorova, 2008).

Satellite altimetry missions The first satellite-borne altimeter missions were the US SKYLAB, consisting of three satellites launched in 1973-1974, GEOS-3 launched in 1975, followed by SEASAT in 1978 and GEOSAT in 1985. As part of several international oceanographic and meteorological programmes a number of satellite altimetry missions were launched in the nineties: ERS-1 (1991-1996), Topex/Poseidon (1992) and ERS-2 (1995). The Jason-1 mission, which was the follow-on to Topex/Poseidon, was launched in 2001 at the same orbit. On the contrary to the ERS-1 and ERS-2 missions, Topex/Poseidon and Jason-1 carried two-frequency altimeters, which gave the opportunity to measure the electron density along the ray path. The latest satellite altimetry mission Jason-2, which is also known as the Ocean Surface Topography Mission (OSTM) was launched in June 2008.

The Topex/Poseidon mission was a joint project between NASA and the French space agency (CNES) with the objective of observing and understanding the ocean circulation (AVISO, 2012). The satellite was equipped with two radar altimeters and precise orbit determination systems, including the DORIS system (see Sect. 3.5). The follow-on mission Jason-1 was the first satellite of a series designed to ensure continuous observation of the oceans for several decades. It had received its main features like orbit, instruments, measurement accuracy, and others from its predecessor Topex/Poseidon. The orbit altitude of the two missions was 1,336 *km* with an inclination of 66°, known as the repeat orbit, causing the satellite pass over the same ground position every ten days. Jason-1 was followed by Jason-2 as a cooperative mission of CNES, European Organization for the Exploitation of Meteorological Satellites (Eumetsat), NASA, and the National Oceanic and Atmospheric Administration (NOAA). It continued monitoring global ocean circulation, discovering the relation between the oceans and the atmosphere, improving the global climate predictions, and monitoring events such as El Nino conditions and ocean eddies (ILRS, 2011). Jason-2 carries nearly the same payload as Jason-1 including the next generation of Poseidon altimeter, the Poseidon-3. The Poseidon-3 altimeter is a two-frequency solid-state sensor, measuring range with accurate ionospheric corrections. Poseidon-3 has the same general characteristics of Poseidon-2, which was onboard Jason-1, but with a lower instrumental noise. The accuracy is expected to be about 1 *cm* on the altimeter and also on the orbit measurements (Dumont *et al.*, 2009). Figure 3.1 depicts schematic view of Jason-2 satellite. For more details about the Jason-2 mission we refer to CNES (2011).

3.2.2 TEC from dual-frequency altimetry measurements

Although the initial aim of the space-borne altimeters is the accurate measurement of the sea surface height, the two separate operational frequencies give the opportunity to obtain information about TEC along the ray path as well. The primary sensor of both Topex/Poseidon and Jason-1 as well as Jason-2 is the NASA Radar Altimeter, operating at 13.6 *GHz* (Ku-band) and 5.3 *GHz* (C-band), simultaneously (Fu *et al.*, 1994). Similar

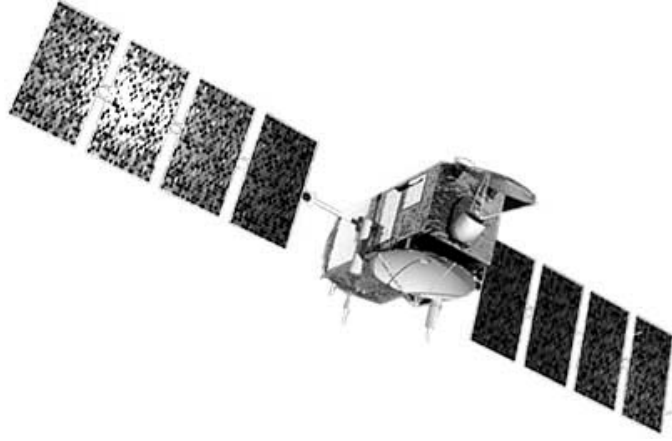


Figure 3.1: Jason-2 satellite, figure courtesy of AVISO (AVISO, 2012)

to GNSS, the ionospheric effect on the altimetry measurements is proportional to the TEC along the ray path and inversely proportional to the square of the altimeter frequency. At the Ku-band, the sensitivity of the range delay to the TEC is $2.2 \text{ mm}/\text{TECU}$. Thus, the range at this signal can be over-estimated by 2 to 40 cm due to the ionosphere (Brunini *et al.*, 2005). According to Imel (1994), the precision of the Ku-band range delay correction in one-second data averages is about 5 TECU or 1.1 cm . In fact, the precision of the satellite altimetry derived TEC is a more complex issue, since it is also affected by non-ionospheric systematic effects. A systematic error which might bias the TEC estimates due to its frequency dependence is the so-called Sea State Bias (SSB) (Chelton *et al.*, 2001).

The ionospheric range delay dR derived from the altimeter measurements at the two frequencies is directly provided in mm , and has to be transformed into TECU . It has to be noted, that in the case of satellite altimetry derived TEC no mapping function is needed, since the measurements are carried out normal to the sea surface and thus, the ray path is assumed vertical. Consequently, the transformation formula is:

$$VTEC_{alt} = -dR \cdot 10^{-3} \frac{f_{Ku}^2}{40.31 \cdot 10^{16}} \quad [\text{TECU}] , \quad (3.29)$$

with f_{Ku} being the Ku-band carrier frequency in Hz .

Theoretically, the TEC values obtained by satellite altimetry are expected to be lower than the ones coming from GNSS, since unlike GNSS the altimetry satellites do not sample the topside ionosphere due to their lower orbit altitude. However, several studies have demonstrated that Topex/Poseidon and Jason-1 systematically overestimate the VTEC by about 3-4 TECU compared to the values delivered by GNSS; e.g. Brunini *et al.* (2005), and

Todorova (2008).

3.3 LEO satellites

3.3.1 General concepts

Low Earth Orbit (LEO) satellites operate at orbital altitudes between 400 and ~ 3500 km. Among their different scientific objectives, the global sounding of the vertical layers of the neutral atmosphere and the ionosphere is of great importance. These missions carry dual-frequency GPS receivers onboard, which makes them capable of remote sensing the atmosphere using the Radio Occultation (RO) technique. The RO technique is based on detecting the change in a radio signal passing through the neutral atmosphere and the ionosphere. As a radio signal travels through the atmosphere, it bends depending on the gradient of refractivity normal to the path. Using the RO measurements onboard a LEO satellite the vertical refractivity profile from the LEO satellite orbit height down to the Earth's surface can be computed. Since the index of refractivity depends mainly on the number of free electrons within the ionosphere, the refractivity profile can be inverted to obtain the vertical Electron Density Profile (EDP) (Jakowski *et al.*, 2002b).

Here we will not go into details about the RO technique and the inversion procedure. For more details about the RO technique refer to e.g. Ware *et al.* (1996), Rocken *et al.* (1997), and Jakowski *et al.* (2004). Details about the inversion procedure could be found in e.g. Schreiner *et al.* (1999), Hernández-Pajares *et al.* (2000), and Garcia-Fernandez *et al.* (2005). In the following some of the LEO missions capable of ionosphere monitoring are briefly described:

3.3.2 Formosat-3/COSMIC

The Formosat-3/COSMIC - Formosa Satellite Mission-Constellation Observing System for Meteorology, Ionosphere and Climate (F/C) is a joint project between Taiwan and the USA for weather, climate, space weather, and geodetic research. The F/C mission was successfully launched in April 2006. The mission consists of six micro satellites, each carrying an advanced GPS RO receiver, a Tiny Ionospheric Photometer sensor (TIP) and a Tri Band Beacon (TBB) (Rocken *et al.*, 2000). The satellites were gradually raised from their launched orbit to reach their final orbit altitude of 800 km. F/C mission is currently providing between 1000-2500 daily RO profiles in the neutral atmosphere, 1,000 and 2,500 daily electron density profiles and total electron content arcs, and TIP radiance products (UCAR, 2011). Figure 3.2 shows a schematic view of a F/C space craft.

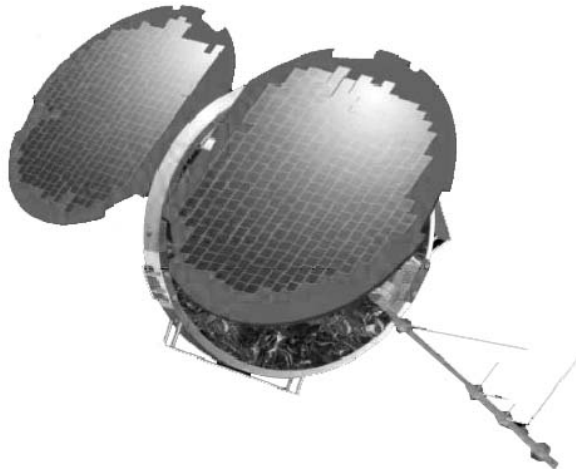


Figure 3.2: F/C space craft, figure courtesy of UCAR (UCAR, 2011)

3.3.3 CHAMP

The German CHALLENGING Mini-Satellite Payload (CHAMP) was mainly used for geophysical research and application. The satellite was successfully launched by a Russian COSMOS rocket in July 2000. Although the mission was scheduled for five years, providing a sufficient observation time to resolve long-term temporal variations in the magnetic field, the gravity field and within the atmosphere, the mission lasted more than ten years and the satellite re-entered the Earth's atmosphere on September 2010. The advanced "Black Jack" GPS receiver developed by the JPL could measure GPS carrier phases in the limb sounding mode, starting at CHAMP orbit tangential heights down to the Earth's surface (Jakowski *et al.*, 2002c). The RO measurements performed on board CHAMP were used to retrieve vertical temperature profiles of the global troposphere/stratosphere system (Wickert *et al.*, 2001). The first ionospheric RO measurements were carried out in April 2001 yielding reasonable electron density profiles (Jakowski *et al.*, 2002b).

3.3.4 GRACE

The Gravity Recovery and Climate Experiment (GRACE) was a NASA and German Aerospace Center (DLR) science mission satellite system, established to measure primarily variations in the Earth's gravity field. The system consists of two satellites in a near-polar orbit at about 500 km altitude in the same orbital plane 220 km apart. The twin satellites were launched in March 2002 with an expected life of five years; however the satellites are still operating by the end of 2012. The dual-frequency Blackjack GPS receivers were used for precise orbit determination and atmospheric occultation on each of the satellites, providing capability of global monitoring of the vertical electron density distribution (Wickert *et al.*, 2005).

3.4 VLBI

3.4.1 General concepts

According to Hobiger (2005) Very Long Baseline Interferometry (VLBI) consists of two antennas separated by any distance, pointing at the same radio source and collecting the signal in the same frequency bands. These sources emit radio waves which are propagating through the universe like an expanding sphere. When these wavefronts reach the Earth's surface, they arrive as a plane wave perpendicular to the antenna's pointing direction. The emitted signal consists of a continuous sequence of waves. First the reference antenna is reached and after a certain time delay the wave front strikes the second (remote) antenna. This time-of-arrival difference is called time delay and is the main measurement type for geodetic and geophysical applications. Figure 3.3 depicts the VLBI concept schematically (IVS, 2012).

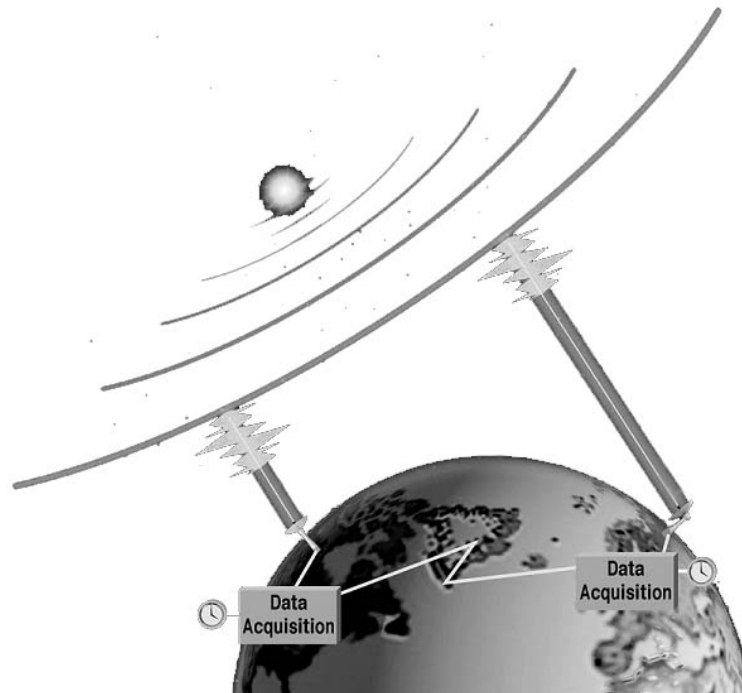


Figure 3.3: VLBI concept, figure courtesy of IVS (IVS, 2012)

3.4.2 TEC from VLBI data

Although VLBI is a differential space geodetic technique it is possible to derive absolute ionosphere parameters, i.e. VTEC for each station. As shown by Hobiger *et al.* (2006)

VTEC values can be determined similar as troposphere parameters by taking advantage of the fact that the slant ionosphere delays are elevation dependent and can be described by an empirical mapping function (Eq. 2.58). Thus VTEC values can be estimated for each station and constant instrumental delays can be separated from these parameters within the adjustment process. As one of the drawbacks, the estimation of ionosphere parameters from VLBI needs a mathematical relation between VTEC above the site and the VTEC of each observation as described in Hobiger (2005) or Hobiger *et al.* (2006). Moreover, as VLBI provides only a single scan per epoch and station, it is important that mapping function errors are reduced to a minimum to obtain unbiased VTEC estimates. Dettmering *et al.* (2010) carried out a thorough investigation of systematic differences between VTEC obtained by different space-geodetic techniques including VLBI by applying the estimation strategy proposed by Hobiger *et al.* (2006). Thereby it is concluded that VLBI derived ionosphere parameters are comparable to other space geodetic techniques, like GPS, DORIS, Jason and F/C concerning the accuracy of the estimation. Moreover, the mean biases found in that study are similar to those given in Hobiger *et al.* (2006) being in the range of a few *TECU*.

3.5 DORIS

The Doppler Orbitography and Radio positioning Integrated by Satellite (DORIS) was developed by the French CNES, Institut Géographique National (IGN) and Groupe de Recherche en Géodésie Spatiale (GRGS) to meet scientific and operational user requirements in very precise orbit determination. Although the DORIS system was primarily designed for the precise orbit computation required for observing the oceans by altimetry missions, the unique network of ground stations and its highly accurate positioning capability have also played a great role for geodesy and geophysical applications. This includes measuring continental drift, fitting the local geodetic network, monitoring the geophysical deformations, determining the rotation and the gravity parameters of the Earth, and contributing to the realization of an international terrestrial reference system. Due to the fact that DORIS system uses two different frequencies for its measurement, it is capable of monitoring the ionosphere as well.

The basic principle of the DORIS system is based on the accurate measurement on board the spacecraft of the Doppler shift of radio frequency signals emitted by ground beacons. Measurements are made on two frequencies: $\sim 2\text{ GHz}$ and 400 MHz . About 56 ground beacon stations transmit dual frequency signals from locations distributed all over the world. The satellites carrying the DORIS receivers include Jason, Topex, Envisat, SPOT 2, SPOT 4, and SPOT 5. These satellites are at the range of $800\text{--}1,336\text{ km}$ altitude. The ionospheric products deduced from the Doppler measurements are recorded at each count interval of about 10s, and are used to derive the ionospheric TEC. The ionospheric corrections are available at the CDDIS website (CDDIS, 2011). For more details on DORIS mission refer to Fleury *et al.* (1991) or Yin & Mitchell (2011).

Part II

Modeling Theory

Chapter 4

Ionosphere Models

The dispersion of the ionosphere pertaining to the microwave signals allows gaining information about this medium and thus modeling its parameters in terms of TEC or electron density along individual ray paths. There are different approaches for modeling these parameters. According to Alizadeh *et al.* (2011) some models are based on physical properties, e.g. the Global Assimilative Ionospheric Model (GAIM) (Schunk *et al.* (2004)); others are empirical models, e.g. the International Reference Ionosphere (IRI) (Bilitza & Reinisch (2007), Bilitza *et al.* (2011)) or the NeQuick (Hochegger *et al.* (2000), Radicella & Leitinger (2001)), and finally the mathematical models which are based on purely mathematical/statistical approaches. The corresponding model parameters could be calculated from space geodetic techniques or ionosonde data. Among these approaches are the TEC maps developed within the Analysis Centers (AC) of the International GNSS Service (IGS), which compute TEC maps. Therefrom, Global Ionosphere Maps (GIM) are developed as an official product of the IGS Ionosphere Working Group by performing a weighted mean of the various AC TEC maps ((Feltens, 2003), Hernández-Pajares *et al.* (2009)). In the following chapter some of these models are briefly discussed.

4.1 Physical models

Physical models are based on physical and/or chemistry principles. They are capable of reproducing certain sets of non-auroral observations by solving set of first principle equations of the ionospheric parameters, such as energy, continuity, or momentum equations for the electrons or ions (Schunk (1988), Anderson (1993)). Due to their complexity, these models are restricted to large amount of computational time and also extensive preparation of required inputs.

4.1.1 GAIM

In 1999 the Multidisciplinary University Research Initiatives (MURI) sponsored by the U.S. Department of Defense developed the Global Assimilative Ionospheric Model (GAIM).

The GAIM model is a time-dependent, three-dimensional global assimilation model of the ionosphere and neutral atmosphere (JPL, 2011). GAIM uses a physical model for the ionosphere/plasmasphere and for assimilating real-time measurements, it uses the Kalman filter approach. Within GAIM the ion and electron volume densities are solved numerically using the hydrodynamic equations for individual ions. The model is physical-based or first-principles based and includes state of the art optimization techniques providing the capability of assimilating different ionospheric measurements. GAIM reconstructs 3-dimensional electron density distribution from the height of 90 *km* up to the geosynchronous altitude (35,000 *km*) in a continuous basis (Scherliess *et al.*, 2004).

The optimization techniques which is incorporated into GAIM include the Kalman Filter and four dimensional variational approaches. Currently different data types are being examined with GAIM, these data types include line of sight TEC measurements made from ground-based GPS receiver networks and space-borne GPS receivers, ionosondes, and satellite UV limb scans. To validate the model, different independent data sources were used. These sources are namely VTEC measurements from satellite ocean altimeter radar (such as those onboard Topex and Jason-1), ionosonde and incoherent scatter radars (JPL, 2011). An updated version of the GAIM model became operational at the Air Force Weather Agency (AFWA) on February, 2008. The new version of GAIM assimilates ultraviolet (UV) observations from Defense Meteorological Satellite Program (DMSP) sensors, including the Special Sensor Ultraviolet Limb Imager (SSULI), which has been developed by the U.S. Naval Research Laboratory (NRL) Space Science Division (NRL, 2008).

4.1.2 PIM

The Parameterized Ionospheric Model (PIM) developed at the Air Force Research Laboratory (AFRL) is a parametric model based on combination of the parameterized output of several theoretical ionospheric models and an empirical plasmaspheric model. According to Daniell *et al.* (1993) PIM uses the F2 layer critical frequency (foF2) (Rush *et al.*, 1984) coefficients from either CCIR (Comité Consultatif International des Radiocommunications) model or from TDIM (Time-Dependent Ionospheric Model) for normalizing the electron density profile.

As a parametric model, PIM simplifies the theoretical models by expressing them in terms of geographical locations and solar-terrestrial parameters using a limited number of coefficients. PIM consists of a FORTRAN source code and a database of coefficients for an orthogonal function expansion. For a specified geophysical condition and a spatial location, PIM produces TEC and also electron density profiles between 90 and 2,500 *km* altitude, corresponding to the critical frequency and the height of the ionospheric E and F2 layers (Daniell *et al.*, 1995).

4.2 Empirical models

Empirical models obtain systematic ionospheric variations from the measured data. Therefore they mainly describe the average conditions for the non-auroral regions and for the non-disturbed conditions. These models are realistic in providing information about the parameters of the ionosphere in areas sufficiently covered by the observations. But in regions or time periods not well covered by the measurements, the accuracy and reliability of such models reduces. However an advantage of the empirical models is that they do not depend on evolving theoretical understanding of the ionosphere, but instead evolve in time as the arrival of new measurements allows improvements of these models.

4.2.1 Klobuchar

In the mid-80s, a simple algorithm was developed for the GPS single-frequency users to correct about 50% of the ionospheric range error. This correction method was established because the GPS satellite message had space for only eight coefficients to describe the world-wide behavior of the Earth's ionosphere. Furthermore, these coefficients could not be updated more often than once per day, and generally not even that often. Finally, simple equations had to be used to implement the algorithm to avoid causing excessive computational stress on the GPS users. The algorithm was developed by Klobuchar (1986) and led to the model that approximated the entire ionospheric vertical refraction by modeling the vertical time delay for the code pseudo-ranges.

The Klobuchar model does not directly compute the TEC. Instead, it models time delay due to ionospheric effects. Equation 4.1 shows time delay in *nanoseconds*. Multiplying this expression by the speed of light will result the vertical ionospheric range delay. The obtained range delay, after applying the SLM function, can be used to correct the ionospheric error in the measurements. Although the model is an approximation, it is nevertheless of importance because it uses the ionospheric coefficients broadcast within the fourth sub frame of the navigation message (Hofmann-Wellenhof *et al.*, 1993). The time delay derived from the Klobuchar model follows from

$$\Delta T_{\nu}^{ion} = A_1 + A_2 \cos \left(\frac{2\pi(t - A_3)}{A_4} \right), \quad (4.1)$$

with

$$A_1 = 5 \cdot 10^{-9} \text{ s} = 5 \text{ ns} ,$$

$$A_2 = \alpha_1 + \alpha_2 \varphi_{IP}^m + \alpha_3 \varphi_{IP}^{m^2} + \alpha_4 \varphi_{IP}^{m^3} ,$$

$$A_3 = 14^h \text{ local time} ,$$

$$A_4 = \beta_1 + \beta_2 \varphi_{IP}^m + \beta_3 \varphi_{IP}^{m^2} + \beta_4 \varphi_{IP}^{m^3} .$$

The values A_1 and A_3 are constant values, the coefficients α_i , β_i , $i = 1, \dots, 4$ are uploaded daily from the control segment to the satellites and broadcast to the users through the broadcast ephemeris. t is the local time of the IPP, and is derived from:

$$t = \frac{\lambda_{IP}}{15} + t_{UT} , \quad (4.2)$$

where λ_{IP} is the longitude of IPP in degrees (positive to East) and t_{UT} is the observation epoch in Universal Time. Finally φ_{IP}^m in Eq. 4.1 is the geomagnetic latitude of IPP and is calculated by (Lilov, 1972):

$$\cos \varphi_{IP}^m = \sin \varphi_{IP} \sin \varphi_P + \cos \varphi_{IP} \cos \varphi_P \cos(\lambda_{IP} - \lambda_P) . \quad (4.3)$$

At present (as of 2012) the coordinates of geomagnetic pole are:

$$\varphi_P = 80.0^\circ N , \quad \lambda_P = 72.2^\circ W . \quad (4.4)$$

For more details refer to (Boehm *et al.*, 2013).

4.2.2 IRI

The International Reference Ionosphere (IRI) is the result of an international cooperation sponsored by the Committee on Space Research (COSPAR) and the International Union of Radio Science (URSI). Since first initiated in 1969, IRI is an internationally recognized standard for the specification of plasma parameters in Earth's ionosphere. It describes monthly averages of electron density, electron temperature, ion temperature, ion composition, and several additional parameters in the altitude range from 60 to 1,500 *km*. IRI has been steadily improved with newer data and better modeling techniques leading to the release of a number of several key editions of the model. The latest version of the IRI model, IRI-2012 (Bilitza *et al.*, 2011), will include significant improvements not only for the representations of electron density, but also for the description of electron temperature and ion composition. These improvements are the result of modeling efforts, since the last major release, IRI-2007 (Bilitza & Reinisch, 2007). IRI is an empirical model based on most of the available data sources for the ionospheric plasma. The data sources of IRI include the worldwide network of ionosondes, which is monitoring the ionospheric electron densities at and below the F-peak since more than fifty years, the powerful incoherent scatter radars which measure plasma temperatures, velocities, and densities throughout the ionosphere, at eight selected locations, the topside sounder satellites which provide a global distribution of

electron density from the satellite altitude down to the F-peak, in situ satellite measurements of ionospheric parameters along the satellite orbit, and finally rocket observations of the lower ionosphere. Since IRI is an empirical model it has the advantage of being independent from the advances achieved in the theoretical understanding of the processes that shape the ionospheric plasma. But a drawback is that such a model is strongly dependent on the underlying database. Therefore regions and time periods not well covered by the data base will result a lower reliability of the model in that area (Bilitza *et al.*, 2011).

The vertical electron density profile within IRI is divided into six sub-regions: the topside, the F2 bottom-side, the F1 layer, the intermediate region, the E region valley, the bottom-side E and D region. The boundaries are defined by characteristic points such as F2, F1, and E peaks. The strong geomagnetic control of the F region processes is taken into account for the analysis of the global electron density behavior (Feltens *et al.*, 2010).

IRI has a wide range of applications. Among these applications, IRI has played an important role in geodetic techniques as well. In several studies IRI has been used as a background ionosphere to validate the reliability and accuracy of an approach for obtaining ionospheric parameters from geodetic measurements (e.g. Hernández-Pajares *et al.* (2002)). Another field which IRI has helped geodetic techniques is with interpolating in areas with no or few available GPS measurements (e.g. Orús *et al.* (2002)).

4.2.3 NeQuick

The NeQuick ionospheric model developed by the Aeronomy and Radiopropagation Laboratory (ARPL) of the Abdus Salam International Centre for the Theoretical Physics in Trieste (Italy) and the Institute for Geophysics, Astrophysics and Meteorology of the University of Graz (Austria) allows calculation of TEC and electron density profile for any arbitrary path (Nava, 2006). The NeQuick model is based on the so-called DGR model introduced by Di Giovanni & Radicella (1990). The original DGR model uses a sum of Epstein layers to analytically construct the electron density distribution within the ionosphere. The general expression for the electron density in an Epstein layer following Radicella & Nava (2010) is:

$$N_{Epstein}(h, hm, Nm, B) = \frac{4Nm}{(1 + \exp(\frac{h-hm}{B}))^2} \exp\left(\frac{h-hm}{B}\right), \quad (4.5)$$

where h is the height, hm is the layer peak height, Nm is the layer peak electron density and B is the layer's thickness parameter.

Based on the anchor points related to the ionospheric characteristics which are routinely scaled from ionogram data, the analytical functions are constructed. The basic equations that describe the latest NeQuick model (NeQuick 2) are given by Nava *et al.* (2008):

$$N_{bot}(h) = N_E(h) + N_{F1}(h) + N_{F2}(h) , \quad (4.6)$$

where:

$$\begin{aligned} N_E(h) &= \frac{4(NmE - N_{F1}(hmE) - N_{F2}(hmE))}{\left(1 + \exp\left(\frac{h-hmE}{B_E}\xi(h)\right)\right)^2} \exp\left(\frac{h-hmE}{B_E}\xi(h)\right) , \\ N_{F1}(h) &= \frac{4(NmF1 - N_E(hmF1) - N_{F2}(hmF1))}{\left(1 + \exp\left(\frac{h-hmF1}{B_1}\xi(h)\right)\right)^2} \exp\left(\frac{h-hmF1}{B_1}\xi(h)\right) , \\ N_{F2}(h) &= \frac{4NmF2}{\left(1 + \exp\left(\frac{h-hmF2}{B_2}\right)\right)^2} \exp\left(\frac{h-hmF2}{B_2}\right) . \end{aligned} \quad (4.7)$$

With

$$\xi(h) = \exp\left(\frac{10}{1 + 1|h - hmF2|}\right) . \quad (4.8)$$

$\xi(h)$ is a function assuring a fadeout of the E and F1 layers in the proximity of the F2 layer peak to avoid the second maxima around $hmF2$. The Nm values are obtained from the E and F2 layer critical frequencies $f0E$ and $f0F2$, obtained from the ionograms. The peak height of the F2 layer $hmF2$ is computed from $M(3000)F2$ and the ratio $f0F2/f0E$. $M(3000)F2$ is the ratio of the maximum usable frequency at a distance of 3000 km to the $f0F2$. The F1 peak height $hmF1$ is modeled in terms of $NmF1$. The geomagnetic dip of the location and the E peak height hmE is fixed at 120 km. The thickness parameter $B2$ of the F2 layer is calculated using the empirical determination of the base point of the F2 layer defined by Mosert de Gonzalez & Radicella (1990) and the thickness parameters corresponding to the F1 and E regions are adjusted numerically (Radicella & Leitinger, 2001).

The NeQuick model gives electron density as a function of geographic latitude and longitude, height, solar activity (specified by the sunspot number or by the 10.7 cm solar radio flux), season (month) and time (Universal or local) (Radicella, 2009).

The Fortran source code of the NeQuick model is available at Radiocommunication Sector website (ITU, 2011). The basic inputs of the code are: position, time and solar flux (or sunspot number) and the output is the electron concentration at any given location in space and time. In addition the NeQuick package includes specific routines to evaluate the electron density along any ray-path and the corresponding TEC by numerical integration (Nava, 2006). The first version of the model has been used by the European Space Agency (ESA), European Geostationary Navigation Overlay Service (EGNOS) project for assessment analysis and has been adopted for single-frequency positioning applications in the framework of the European Galileo project. It has also been adopted by the International Telecommunication Union,

Radiocommunication Sector (ITU-R) as a suitable method for TEC modeling (ITU, 2007).

4.2.4 MIDAS

The Multi-Instrument Data Analysis System (MIDAS) was designed and developed at the University of Bath in 2001. The analysis algorithm makes use of GPS dual-frequency observations to produce four-dimensional images of electron concentration over large geographical regions or even over the globe (Mitchell & Cannon, 2002). Different types of measurements that can be put into the MIDAS are the satellite to ground measurements, satellite to satellite observations, measurements from sea-reflecting radars, electron-concentration profiles from inverted ionograms, and in-situ measurements of ionized concentration from LEO satellites. The MIDAS algorithm reconstructs the free electron density as a piecewise constant 3D distribution, starting from collections of slant TEC data along ray paths crossing the region of interest (Mitchell & Spencer, 2003). The essential ingredient of the MIDAS inversion is the use of Empirical Orthogonal Functions (Sirovich & Everson, 1992), along which the solution of the inverse problem is assumed to be linearly decomposable (Materassi, 2003). MIDAS produces four-dimensional electron density maps which can be used to correct the phase distortions and polarization changes by Faraday rotation in the ionosphere. MIDAS also has a ray tracer which allows accurate determination of the refracting ray paths and hence the apparent sky location of a radio source.

4.2.5 NTCM

Neustrelitz TEC Model (NTCM) is an empirical model approach developed at the German Aerospace Center (DLR), which estimates TEC in global and regional basis. NTCM is a climatological model meaning that it provides the average behavior under quiet geomagnetic conditions. Depending on the area of the coverage, the model is described in different representations.

Regional modeling According to Jakowski *et al.* (2011) regional NTCM model is developed in three different areas:

- European region (NTCM-EU)
- Northern polar region (NTCM-NP)
- Southern polar region (NTCM-SP)

For each of these regions an empirical TEC model is developed and combined with the measured data within that region. The basis version of NTCM approximates TEC as a function of geographic location (λ, φ), time (h, d), and solar activity ($F10.7$). The model approach is based on a polynomial consisting of 60 linear terms (Jakowski, 1996)

$$TEC_{60}^{vert} = \sum_{i=1}^5 \sum_{j=1}^3 \sum_{k=1}^2 \sum_{l=1}^2 c_{ijkl} H_i(h) Y_j(d) L_k(\varphi, \lambda, h, d) S_l(F10.7) , \quad (4.9)$$

where c_{ijkl} denotes the model coefficients, $H_i(h)$ denotes the diurnal and semidiurnal variation, $Y_j(d)$ the annual and semi-annual variation, $L_k(\varphi, \lambda, h, d)$ the dependence on the latitude and the solar zenith angle and $S_l(F10.7)$ the dependence on the solar activity. The model coefficients are determined by a least-squares fitting procedure.

Global modeling For Global TEC model (NTCM-GL) the basic NTCM approach used for regional modeling is followed. Therefore, dependencies on local time, season, geomagnetic field and solar activities are treated in a similar manner.

Within the global approach the terms describing the crest regions should be also taken into account. The terms describing the above mentioned dependencies are combined in a multiplicative way as used in Eq. 4.9, but the coefficients of the new global model are determined by an iterative non-linear least squares technique (Jakowski *et al.*, 2011).

4.3 Mathematical models

4.3.1 Global TEC representation using spherical harmonics

As mentioned in Sect. 3.1.3.2, to develop a global ionosphere model, the VTEC has to be represented as a function of longitude, latitude and time, or according to the definition of the adopted coordinate system given in Sect. 2.3, as a function of the geomagnetic latitude β and sun-fixed longitude s . This can be accomplished by applying e.g. a spherical harmonics expansion (Schaer, 1999):

$$VTEC(\beta, s) = \sum_{n=0}^{n_{max}} \sum_{m=0}^n \tilde{P}_{nm}(\sin \beta) (a_{nm} \cos(ms) + b_{nm} \sin(ms)) , \quad (4.10)$$

where:

$VTEC(\beta, s)$	VTEC in <i>TECU</i> ,
$\tilde{P}_{nm} = N_{nm} P_{nm}$	normalized Legendre function of degree n and order m ,
N_{nm}	normalizing function,
P_{nm}	classical Legendre function,
a_{nm} and b_{nm}	the spherical harmonics coefficients.

The normalizing function is given by:

$$N_{nm} = \sqrt{\frac{(n-m)!(2n+1)(2-\delta_{0m})}{(n+m)!}}. \quad (4.11)$$

where δ_{0m} denotes the Kronecker delta. The total number of coefficients of spherical harmonics expansion Eq. 4.10 is given by:

$$u = (n_{max} + 1)^2, \quad (4.12)$$

and the spatial resolution of a truncated spherical harmonics expansion is given by:

$$\Delta\beta = \frac{2\pi}{n_{max}}, \quad \Delta s = \frac{2\pi}{m_{max}}, \quad (4.13)$$

where

$\Delta\beta$	the resolution in latitude, and
Δs	the resolution in sun-fixed longitude and local time, respectively,
n_{max}, m_{max}	maximum degree and order of the spherical harmonics expansion.

It is shown that the mean $VTEC$ of the global VTEC distribution expressed by Eq. 4.10 is generally represented by the zero-degree spherical harmonics coefficient \tilde{a}_{00} (Schaer, 1999):

$$\overline{VTEC} = \frac{1}{4\pi} \int_0^{2\pi} \int_{-\frac{\pi}{2}}^{+\frac{\pi}{2}} VTEC(\beta, s) \cos \beta d\beta ds = N_{00} \tilde{a}_{00} = \tilde{a}_{00}. \quad (4.14)$$

4.3.1.1 Parametrization of VTEC

To estimate a global VTEC model, GNSS observations from a set of globally distributed GNSS stations are collected by the Analysis Centers (AC). The computation is carried out on a daily basis, using observations with sampling rate of 30 seconds and elevation cut-off angle 10° . For all of the observations the ionospheric observable is calculated using code pseudorange Eq. 3.26, phase pseudorange Eq. 3.27, or the smoothed code pseudorange Eq. 3.28. This observable forms the observation equation. The observation equations are then solved for every two hour epoch and the unknowns which are the coefficients of the spherical harmonics expansion (a_{nm} and b_{nm} in Eq. 4.10) are estimated for every two hours (one hour or 15 minutes solution is also possible) by a least-squares adjustment procedure.

The estimated unknown coefficients are then entered to calculate grid-wise VTEC values over the globe using Eq. 4.10. The VTEC is represented as a function of geocentric longitude and latitude (λ, φ), and time (t) in UT, in the form of a raster grid. The spatial resolution of this grid is usually $\Delta\lambda = 5^\circ$ in longitude and $\Delta\varphi = 2.5^\circ$ in latitude, and the time resolution

of the maps are $\Delta t = 2h$; although higher time resolution of $1h$ or $15min$ is also possible. Assuming a time resolution of $2h$, one will obtain thirteen two-hourly global maps for one complete day. These maps are usually called Global Ionosphere Maps (GIM), and are provided in the IONospheric EXchange (IONEX) format, described in Schaer *et al.* (1998).

4.3.1.2 VTEC interpolation

To obtain VTEC in any arbitrary position in globe, an interpolation could be performed. The interpolation of VTEC for a given epoch T_i with $i = 1, 2, \dots, n$, was proposed by Schaer *et al.* (1998), which is interpolating between consecutive rotated TEC maps. This can be formulated as follow:

$$VTEC(\beta, \lambda, t) = \frac{T_{i+1} - t}{T_{i+1} - T_i} VTEC_i(\beta, \lambda'_i) + \frac{t - T_i}{T_{i+1} - T_i} VTEC_{i+1}(\beta, \lambda'_{i+1}), \quad (4.15)$$

with

$$T_i \leq t < T_{i+1} \quad \text{and} \quad \lambda'_i = \lambda + (t - T_i).$$

The TEC maps are rotated by $t - T_i$ around the Z-axis to compensate the strong correlation between the ionosphere and the Sun's position. For the grid interpolation, a bi-variate interpolation method can be applied, which uses a simple four-point interpolation formula:

$$\begin{aligned} VTEC(\lambda_0 + p\Delta\lambda, \beta_0 + q\Delta\beta) = & (1-p)(1-q)VTEC_{0,0} \\ & + p(1-q)VTEC_{1,0} + (1-p)qVTEC_{0,1} + pqVTEC_{1,1}, \end{aligned} \quad (4.16)$$

where $0 \leq p < 1$ and $0 \leq q < 1$. $\Delta\lambda$ and $\Delta\beta$ denote the grid widths in longitude and latitude. Figure 4.1 depicts the interpolation concept.

4.3.1.3 Ionosphere Working Group at IGS

In 1998 a special Ionosphere Working Group of the International GNSS service (IGS) was initiated for routinely developing ionospheric products, as described by Schaer *et al.* (1998) and Hernández-Pajares (2004). The main products provided on a regular basis by the IGS Ionosphere WG are the GIM, representing the VTEC over the entire Earth as a two-dimensional raster in latitude and longitude in two-hourly snapshots, as well as the corresponding Root Mean Square (RMS) maps. Figure 4.2 depicts a sample of VTEC map developed by IGS for 9 July 2006.

Additionally, daily and monthly values of the satellite and receiver DCB are provided as well. It is worth to mention that at the recent IGS-Workshop in Newcastle, UK (28 June - 2 July 2010), it was decided to reduce the time resolution of IGS TEC maps from $2h$ to $1h$,

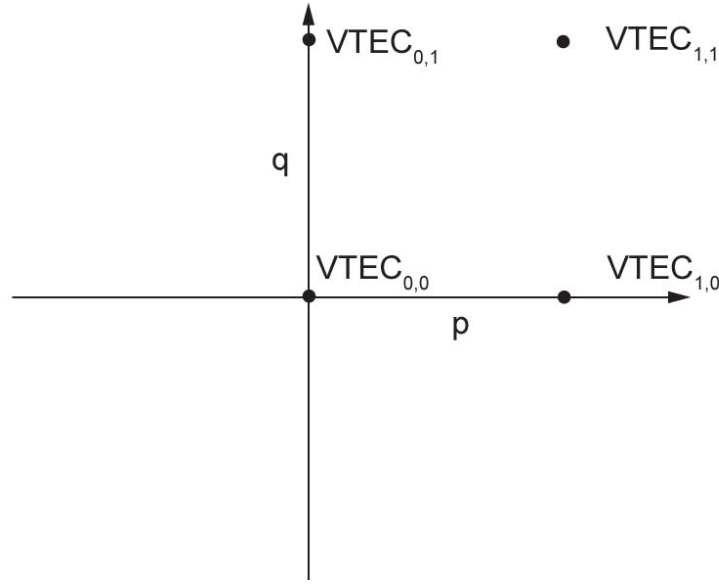


Figure 4.1: Bi-variate interpolation using the nearest four TEC values

and finally to 15min in the future.

The routine generation of ionosphere VTEC maps is currently done at four IGS Associate Analysis Centers (IAAC) for ionosphere products. These IAAC are namely:

- Center for Orbit Determination in Europe (CODE), University of Berne, Switzerland,
- European Space Operations Center of ESA (ESA/ESOC), Darmstadt, Germany,
- Jet Propulsion Laboratory (JPL), Pasadena, USA,
- Technical University of Catalonia (gAGE/UPC), Barcelona, Spain.

These centers provide results computed with different approaches, which are transmitted to the IGS Ionosphere Product Coordinator, who calculates a weighted combined product. Presently the weights are defined by the IAAC global TEC maps evaluation carried out at the Geodynamics Research Laboratory of the University of the Warmia and Mazury (GRL/UWM) in Olsztyn, Poland (Krakowski *et al.*, 2010). IGS releases a final ionosphere map in IONEX format with resolution of 5° in longitude and 2.5° in latitude with a latency of 10 days and a rapid solution with a latency of 1 day. The IGS GIM and the corresponding RMS maps are available through the IGS server in IONEX format (CDDIS-IONEX, 2011).

4.3.2 Regional TEC representation using B-splines

According to Schmidt *et al.* (2008) a multi-dimensional approach based on Euclidean quadratic B-spline wavelets can be used for representation of the ionospheric parameters characterized by an effective numerical algorithm. Due to the fact that these base functions

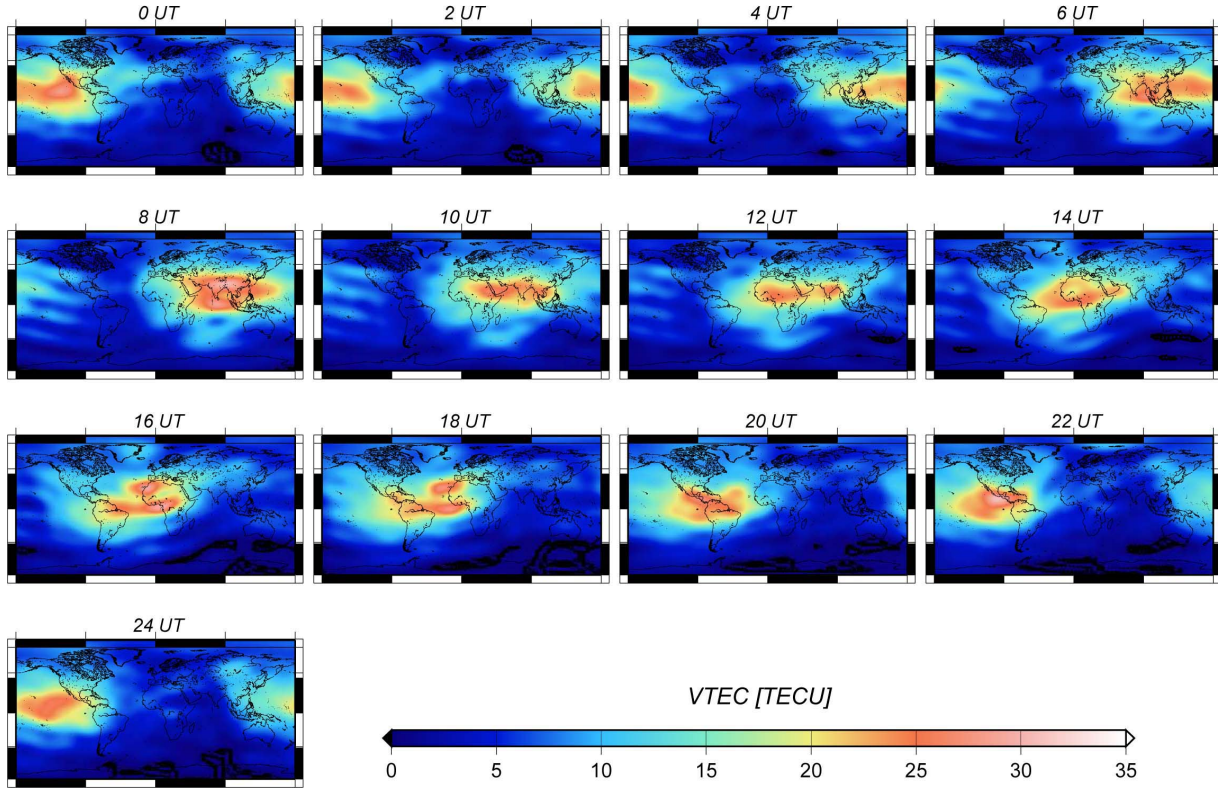


Figure 4.2: VTEC GIM developed by IGS for 9 July 2006

are compactly supported, they provide a great advantage when used for regional modeling of the ionosphere or when the observations are unevenly distributed over the globe. In this approach the parameters of the ionosphere, e.g. VTEC is separated into a reference part and a correction part

$$VTEC(\varphi, \lambda, t) = VTEC_{ref}(\varphi, \lambda, t) + \Delta VTEC(\varphi, \lambda, t) . \quad (4.17)$$

Following Dettmering *et al.* (2011b) $\Delta VTEC$ can be expressed by means of spline series expansion

$$\Delta VTEC(\varphi, \lambda, t) = \sum_{k_1=0}^{k_1-1} \sum_{k_2=0}^{k_2-1} \sum_{k_3=0}^{k_3-1} d_{k_1, k_2, k_3} \Phi_{k_1}^{J_1}(\varphi) \Phi_{k_2}^{J_2}(\lambda) \Phi_{k_3}^{J_3}(t) , \quad (4.18)$$

where each of the $\Phi_k^J(x)$ denote a 1-D scaling function of level $J \in \{J_1, J_2, J_3\}$, shift $k \in \{k_1, k_2, k_3\}$ and variable $x \in \{\varphi, \lambda, t\}$. The scaling functions each consist of $k = 2^J + 2$ single B-spline functions distributed on the unit interval.

In Eq. 4.18 d_{k_1, k_2, k_3} are the unknown coefficients of the expansion and should be estimated

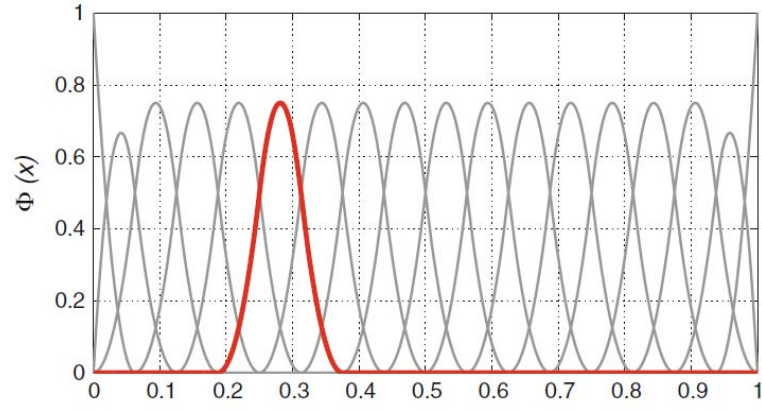


Figure 4.3: 1-D quadratic endpoint-interpolating B-spline functions of level e.g. $J = 4$ (figure curtesy of Dettmering *et al.* (2011b))

through a least-squares adjustment procedure. More details can be found in Schmidt (2007).

As mentioned before, B-Spline is compactly supported, i.e. its values are different from zero only in a finite range within the unit interval $[0, 1]$. This concept is depicted in Fig. 4.3.

Chapter 5

New ionosphere reconstructing approaches

5.1 Basics of data analysis and estimation

5.1.1 Least-Squares adjustment

Due to the fact that the unknown parameters should be estimated through least-squares adjustment procedure, here we provide a brief overview of this parameter estimation technique. Based on the chosen mathematical model, described in Sect. 4.3, the observation equation is formulated as $f(x, l) = 0$, where \mathbf{x} indicates the unknown parameter vector in parameter space \mathfrak{X} , and l the observation vector in observation space \mathfrak{L} . Following Koch (1999) the explicit observation equation is written as

$$l_i + r_i = f_i(x) = f_i(x_0) + \left. \frac{\partial f_i}{\partial x} \right|_{x=x_0} \delta x, \quad (5.1)$$

with

r_i	residuals,
l_i	actual observations,
$\delta x = x - x_0$	vector of corrections,
$\delta l = l - l_0$	vector of reduced observations, and
x_0	vector of approximate values of the model parameters,
l_0	vector of a priori values of the observations.

The partial differential term is known as the design matrix and is defined as

$$A = \left. \frac{\partial f}{\partial x} \right|_{x=x_0} . \quad (5.2)$$

The A matrix is referred to as the first design matrix and is regarded as a Jacobian Matrix. Substituting the design matrix A from Eq. 5.2 into Eq. 5.1, the linearized observation equation would simply read

$$\delta l + r = A\delta x , \quad (5.3)$$

where $\delta l = [\delta l_i]$ and $r = [r_i]$, are vectors of the actual observations and residuals respectively.

Stochastic model

To solve the least-squares problem the stochastic model for the observation must be defined. The stochastic model describes the statistics of the measurements. This is in the form of the weight matrix P , or its inverse the cofactor matrix Q_l of the observations

$$P = Q_l^{-1} = \sigma_0^2 C_l^{-1} , \quad (5.4)$$

where

- P is the observations weight matrix,
- C_l is the covariance matrix of the observations, and
- σ_0 a priori standard deviation.

If the observations are uncorrelated, the weight matrix is a diagonal matrix. In such a case, P is given by

$$P = \text{diag} \left(\frac{\sigma_0^2}{\sigma_l^2} \right) . \quad (5.5)$$

σ_l^2 in Eq. 5.5 is the a priori variance of the corresponding observation. If the observations are uncorrelated with equal accuracy, the weight matrix P becomes the identity matrix I .

Solving the least-squares problem

Equation 5.3 is solved through minimizing the scalar target function $r^T P r$. The minimization of this function with respect to x leads to the normal equations

$$(A^T P A) \delta x = (A^T P \delta l) . \quad (5.6)$$

The normal equation matrix N and the right-hand side matrix u are now defined as

$$N = A^T P A , \quad u = A^T P \delta l . \quad (5.7)$$

With these notations, the least-squares solution of the estimated correction will be

$$\delta \hat{x} = N^{-1} u . \quad (5.8)$$

The "hat" sign ($\hat{}$) in the above equation and the equations followed, indicates the least-squares estimation. Using the estimated correction Eq. 5.8, and the a priori vector of the unknown parameters x_0 , the estimated vector of unknown parameter is calculated

$$\hat{x} = x_0 + \delta \hat{x} . \quad (5.9)$$

The least-squares estimate of residuals \hat{r} is derived by applying $\delta \hat{x}$ from Eq. 5.8 to Eq. 5.3

$$\hat{r} = A \delta \hat{x} - \delta l , \quad (5.10)$$

and therefrom the least-squares estimate of the observations is computed

$$\hat{l} = f(\hat{x}) + \hat{r} , \quad (5.11)$$

The estimated variance factor or the so called a posteriori variance factor is

$$\hat{\sigma} = \left(\frac{r^T P r}{d} \right)^{\frac{1}{2}} \quad \text{if} \quad d > 0 , \quad (5.12)$$

where $d = n - u$ is the degree of freedom (DOF). n is the number of observations and u the number of unknown parameters. Finally the covariance matrix of the adjusted model is given by

$$C_{\hat{x}} = \hat{\sigma}^2 N^{-1} . \quad (5.13)$$

$C_{\hat{x}}$ is an important parameter as the uncertainties of the observation vector l , given in terms of the covariance matrix C_l , as well as the uncertainties of the estimation model, traced into estimated parameter \hat{x} are characterized by $C_{\hat{x}}$. For more details on least-squares adjustment procedure please refer to Koch (1999).

5.1.2 Constrained Least-Squares

Replicating the linearized observation equation Eq. 5.3, the reduced observation vector δl can be expressed in terms of the correction vector δx and the residual vector r by

$$\delta l + r = A\delta x , \quad (5.14)$$

assuming the design matrix A is given.

Suppose the original observations in Eq. 5.14 are partitioned into sub-systems δl and w

$$\begin{bmatrix} \delta l \\ \text{---} \\ w \end{bmatrix} + \begin{bmatrix} r \\ \text{---} \\ 0 \end{bmatrix} = \begin{bmatrix} A_1 \\ \text{---} \\ A_2 \end{bmatrix} \delta x . \quad (5.15)$$

where

- δl an $m_1 \times 1$ vector of measured reduced observations,
- A_1 an $m_1 \times n$ design matrix corresponding to δl ,
- r an $m_1 \times 1$ vector of residuals,
- w an $m_2 \times 1$ given vector of constraints, and
- A_2 an $m_2 \times n$ coefficient matrix corresponding to w .

The equation system Eq. 5.15 can be re-written as

$$\delta l + r = A_1\delta x , \quad (5.16)$$

$$w = A_2\delta x . \quad (5.17)$$

Eq. 5.17 is a constraint and equation system Eq. 5.15 is a constrained minimizing problem (Crassidis & Junkins, 2004). In this problem we aim at finding an estimated $\delta \tilde{x}$, which minimizes $r^T P r$ and also satisfies the constraint Eq. 5.17.

Using the method of Lagrange multipliers explained by e.g Koch (1999), the explicit solution of the constrained least-squares estimation yields

$$\delta \tilde{x} = \delta \hat{x} + K (w - A_2\delta \hat{x}) \quad (5.18)$$

where

$$K = (A_1^T P A_1)^{-1} A_2^T \left[A_2 (A_1^T P A_1)^{-1} A_2^T \right]^{-1}, \quad (5.19)$$

and

$$\delta \hat{x} = (A_1^T P A_1)^{-1} A_1^T P \delta l. \quad (5.20)$$

It can be noticed that $\delta \hat{x}$ represented by Eq. 5.20 is the least-squares estimate of the unknown correction parameter δx when no constraint is applied. So the final estimate of the unknown parameter $\delta \tilde{x}$ is obtained from the original estimate $\hat{\delta x}$ plus the additive correction term, implied from the constraint residual (second term in Eq. 5.19).

In a special case where only one constraint is implied, i.e. $m_2 = 1$, then the matrix K in Eq. 5.19 simplifies to a scalar.

5.1.3 Assigning appropriate base-function

To estimate the proportion of the ionosphere, parameters of the ionosphere, i.e. TEC or the electron density should be modeled. Concentrating only on mathematical models explained in Sect. 4.3, there are several ways to model the ionospheric parameters. Depending on the chosen parameter of the ionosphere, its required dimension, and the area of the coverage, appropriate base functions should be chosen. Table 5.1 summarizes some of the mathematical approaches and base functions for different modeling techniques. Of course applying other procedures and base functions is also possible.

As our study aims mainly at global modeling of the ionospheric parameters, we focus on spherical harmonics base function, and as the title of the dissertation describes, our goal is to model the ionospheric parameters in different dimensions. So we start with two-dimensional modeling of $VTEC(\lambda, \varphi)$. Then we investigate three-dimensional model of the ionospheric parameter. For that we concentrate on modeling electron density $N_e(\lambda, \varphi, h)$ in longitude, latitude, and height. Our final goal is to investigate modeling electron density on fourth dimension, which is including the time dependency.

5.1.4 Accuracy of the estimated parameters

It was mentioned in Sect. 5.1.1 that the accuracy of the estimated parameters is obtained from the covariance matrix \hat{C}_x derived from Eq. 5.13. As we use spherical harmonics expansion (e.g. Eq. 4.10) to estimate the unknown parameters, \hat{C}_x contains the accuracy of the spherical harmonics expansion (i.e. a_{nm} and b_{nm} in Eq. 4.10). To obtain the accuracy of the estimated parameter (i.e. \hat{VTEC} in Eq. 4.10), we have to apply the variance-covariance propagation law to the spherical harmonics expansion.

Modeling dimension	Parameter	Coverage	Base function	
2D	$VTEC(\lambda, \varphi)$	global	Spherical Harmonics (SH)	
		regional	2D B-splines	
3D	$VTEC(\lambda, \varphi, t)$	global	2D SH + Fourier function for time	
			trigonometric B-splines	
		regional	3D B-splines	
	$N_e(\lambda, \varphi, h)$	global	2D SH + function for height:	EOF function
				Chapman function
				Epstein function
4D	$N_e(\lambda, \varphi, h)$	global	2D SH + function for height + Fourier function for time	
		regional	4D B-splines	

Table 5.1: Samples base function/mathematical approaches for multi-dimensional modeling of the ionosphere

Considering the estimated \hat{VTEC} value as an example and replicating Eq. 4.10, we have

$$\hat{VTEC}(\beta, s) = \sum_{n=0}^{n_{max}} \sum_{m=0}^n \tilde{P}_{nm}(\sin \beta) \left(\hat{a}_{nm} \cos(ms) + \hat{b}_{nm} \sin(ms) \right) . \quad (5.21)$$

Expressing Eq. 5.21 in the matrix form, we can write

$$\hat{VTEC}(\beta, s) = Fx \quad (5.22)$$

with

$$x^T = \begin{bmatrix} \vdots \\ \hat{a}_{nm} \\ \hat{b}_{nm} \\ \vdots \end{bmatrix} , \quad (5.23)$$

and

$$F = \begin{bmatrix} \vdots \\ \tilde{P}_{nm}(\sin \beta) \cos(ms) \\ \tilde{P}_{nm}(\sin \beta) \sin(ms) \\ \vdots \end{bmatrix}, \quad (5.24)$$

where x is a $1 \times (n+1)^2$ vector of unknown parameters, n is the number of degree of spherical harmonics expansion, and F is a $(n+1)^2 \times 1$ vector of partial derivatives, constructed from

$$\frac{\partial V\hat{T}EC}{\partial \hat{a}_{nm}} = \tilde{P}_{nm}(\sin \beta) \cos(ms), \quad (5.25)$$

and

$$\frac{\partial V\hat{T}EC}{\partial \hat{b}_{nm}} = \tilde{P}_{nm}(\sin \beta) \sin(ms). \quad (5.26)$$

Now applying the variance-covariance propagation law to Eq. 5.22, we get

$$C_{V\hat{T}EC} = F^T \hat{C}_x F, \quad (5.27)$$

The square root of $C_{V\hat{T}EC}$ is known as the standard deviation of $V\hat{T}EC$, or the so-called RMS of $V\hat{T}EC$

$$RMS_{V\hat{T}EC} = \sqrt{F^T \hat{C}_x F}. \quad (5.28)$$

The $RMS_{V\hat{T}EC}$ value at each point indicates the accuracy of the estimated $V\hat{T}EC$ at that point. RMS values for other estimated parameters, represented by spherical harmonics expansion, i.e. the maximum electron density N_m , or the height of maximum electron density h_m (see Sect. 5.3.2.3) is obtained in a similar procedure. The RMS values are usually expressed in a global grid-wise maps known as the RMS maps, and are presented along with the global maps of the estimated values.

5.2 Two-dimensional modeling of VTEC

5.2.1 Combined global maps

In the last decade space geodetic techniques have turned into a promising tool for monitoring and modeling the ionosphere. Among these techniques, GNSS observations are widely used for measuring ionospheric parameters in terms of TEC or the electron density N_e . Afore-said in Sect. 3.1.3.2, the classical input data for development of GIM of the VTEC is obtained from the dual-frequency GNSS ground-based observations. Nevertheless due to the fact that GNSS ground stations are in-homogeneously distributed around the world with poor coverage over the oceans (namely southern Pacific and southern Atlantic), and also parts of Africa (see Fig. 5.1), the precision of VTEC maps are rather low in these areas. From long term analysis, it is believed that the IGS VTEC maps have an accuracy of few *TECU* in areas well covered with GNSS receivers; conversely, in areas with poor coverage, the accuracy can be degraded by a factor of up to five (Feltens *et al.*, 2010). On the other hand, dual-frequency satellite altimetry missions, such as Jason-1&2 (see Sect. 3.2.1) provide direct VTEC values exactly over the oceans, and furthermore the six Formosat-3/COSMIC (F/C) Spacecraft (see Sect. 3.3.2) provide about 2,500 globally distributed occultation measurements per day. This data can be used for obtaining VTEC values as well. Combining these data with the ground-based GNSS data, improves the accuracy and reliability of the VTEC maps by closing the observation gaps that arise when using ground-based data only.

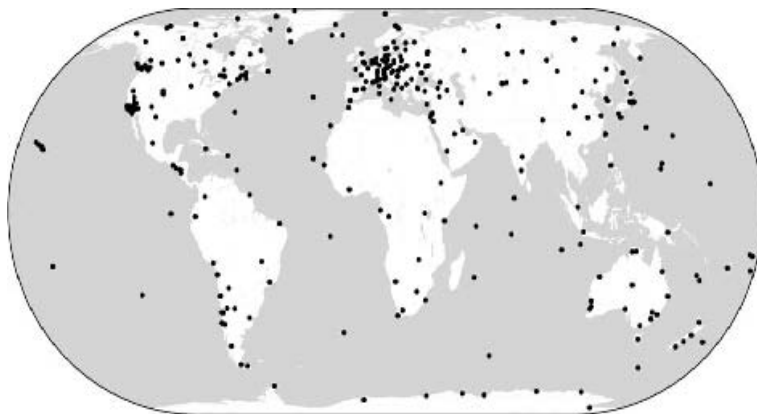


Figure 5.1: IGS global ground stations, figure curtsey of IGS (Dow *et al.*, 2009)

5.2.2 Inter-technique combination

For the combination, a least-squares adjustment is applied on each set of observation techniques and then the normal equations are combined. This procedure is a common technique for solving combination problems in geodesy such as the International Terrestrial Reference Frame (ITRF) solution (Altamimi *et al.*, 2007). This procedure is accomplished by stacking

the relevant normal equation matrices obtained from each type of observations

$$\begin{aligned}
 N_{COMB} &= \sigma_{GNSS}^2 N_{GNSS} + \sigma_{ALT}^2 N_{ALT} + \sigma_{F/C}^2 N_{F/C} \\
 &= \sigma_{GNSS}^2 \left(A_{GNSS}^T P_{GNSS} A_{GNSS} \right) \\
 &\quad + \sigma_{ALT}^2 \left(A_{ALT}^T P_{ALT} A_{ALT} \right) \\
 &\quad + \sigma_{F/C}^2 \left(A_{F/C}^T P_{F/C} A_{F/C} \right),
 \end{aligned} \tag{5.29}$$

where N is the normal equation matrix, A is the design matrix, P is the weight matrix, and σ^2 is the variance component of each of the observations. Figure 5.2 depicts the inter-technique combination scheme.

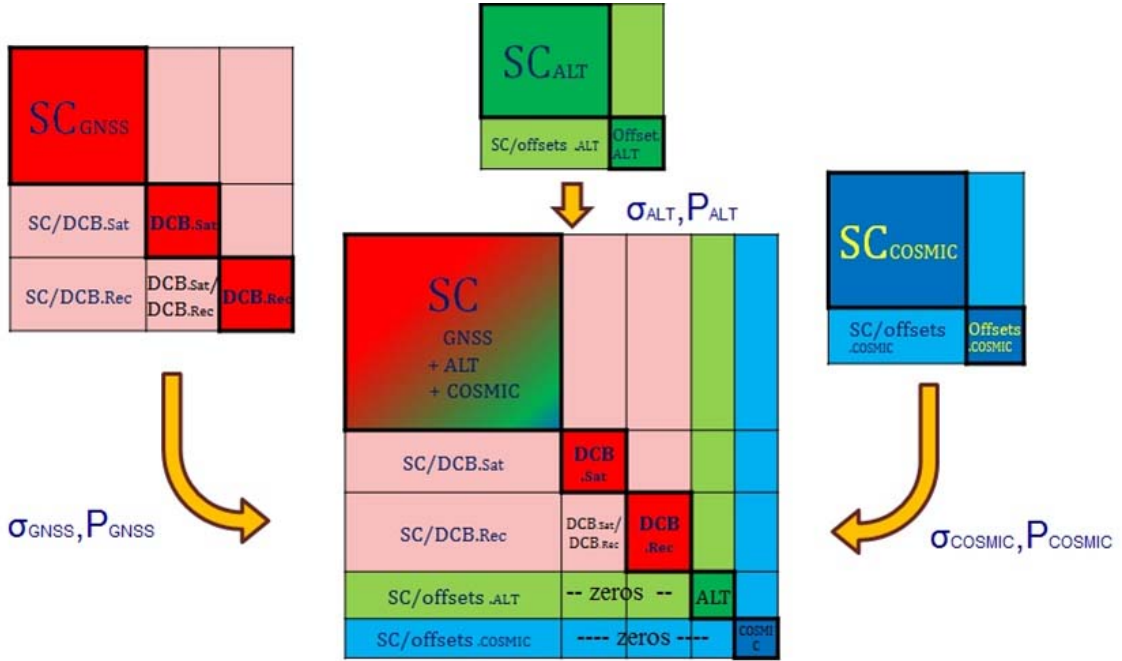


Figure 5.2: Inter-technique combination scheme (SCs are the spherical harmonic coefficients) (Alizadeh *et al.*, 2011)

5.2.3 Relative weighting of different techniques

For relative weighting of different techniques several strategies are possible. Due to the much higher number of GNSS measurements compared to satellite altimetry and F/C, the satellite altimetry and F/C data should be up-weighted, to increase their impact on the combined GIM (over weighting). On the other hand, if we take into account the higher noise

of the altimetry measurements compared to the carrier-phase smoothed code observations from GNSS (see Sect. 3.1.2.2), a lower weight should be applied on all altimetry derived observations (down weighting). In fact the relative weighting acts like a scaling factor for the contribution of the different techniques in the combination. This depends on the different spatial and temporal distribution of the observations and on their specific systematic errors. The relative weighting can be accomplished through several procedures, namely:

- Physical aspect
- Mathematical aspect
- Empirical

Physical weighting Due to in-homogenous distribution of IGS GNSS stations in the northern and southern hemisphere, to balance the model, the observations of the GNSS stations in the southern hemisphere could be up-weighted comparing to ones in the northern hemisphere. Concerning the altimetry data, a dynamical weighting procedure could be applied. In this procedure, the altimetry data are related to the latitude and time of which they were observed. Such an epoch-wise weighting applied to both GNSS and altimetry data will enhance the spatial agreement between the VTEC derived from both techniques and improves the result of the combination (Todorova, 2008).

Mathematical weighting In mathematical weighting, first, all the observations techniques are assumed to have the same accuracy levels in the stochastic model. Therefore the weight matrix is set to identity. Due to the fact that this is an unrealistic assumption, a variance component estimation technique (VCE) should be implemented which accounts for different accuracy levels of different observation techniques (Dettmering *et al.*, 2011a). In this procedure, instead of estimating a single a posteriori variance factor σ_0^2 for the whole observations, a variance factor for each technique is estimated σ_i^2 , $i = \{1, \dots, p\}$, where p is the number of the observation techniques.

Usually no correlations are assumed between the different techniques, therefore the weight matrix turns into a block diagonal matrix

$$P_L = \begin{bmatrix} \frac{1}{\sigma_1^2} P_1 & 0 & \cdots & 0 \\ 0 & \frac{1}{\sigma_2^2} P_2 & & 0 \\ \vdots & & \ddots & \vdots \\ 0 & 0 & \cdots & \frac{1}{\sigma_p^2} P_p \end{bmatrix} \quad (5.30)$$

Estimating variance factors can be accomplished through stochastic estimation technique, invented by Girard (1989), Hutchinson (1990), and Koch (1999); or as an effective computation the fast Monte-Carlo implementation of the iterative maximum likelihood component estimation (MCVCE) developed by Koch & Kusche (2002) could be used.

Empirical weighting In empirical weighting the altimetry and F/C measurements are down-weighted and over-weighted with respect to the GNSS observations in different turns. The results of VTEC maps, and also RMS maps are compared with each other and also with the IGS VTEC and RMS maps. The criteria for selecting the final weights are the mean values for the RMS maps in the whole day. This means that the mean RMS of all two-hourly maps in a whole day are calculated from each of the weighting schemes, and the weighting which provides the least mean RMS is finally selected as the best adopted weight. As the correlations between different observation techniques are unknown, no correlations are considered between the different techniques, therefore, diagonal weight matrices are applied in this procedure (Alizadeh *et al.*, 2011).

5.3 Three-dimensional modeling of the electron density

To model ionosphere in 3D we have the possibility to model VTEC in three dimensions i.e. in longitude, latitude, and time; or to model electron density in three dimensions i.e. in longitude, latitude, and height (see Sect. 5.1.3). In this study we investigate the latter one. To develop a 3D global model for electron density a spherical harmonics expansion is used for longitude and latitude variations. For height dependency several procedures can be applied. One procedure is to apply Empirical Orthogonal Functions (EOF) introduced by Fremouw *et al.* (1992) and further improved by Howe *et al.* (1998). Rawer (1988) as well as Radicella & Leitinger (2001) applied Epstein functions to present the height dependencies. And finally Chapman profile function can be used to express the hight variations of the electron density. In the following section, the Chapman profile function approach is briefly described.

5.3.1 Chapman profile function

To describe the vertical structure of the electron density in the ionosphere, Chapman profile function can be derived. Taking the hydrostatic equilibrium assumption of the upper atmosphere into account, the barometric equation, which relates the pressure gradient to the mass density reads (Alizadeh, 2002)

$$\frac{dP}{dh} = -\rho g, \quad (5.31)$$

where

P is the pressure,
 h is the height,
 ρ is the density, and
 g is the gravitational constant.

The density ρ can, in turn, be expressed in terms of the particle masses m and number density n of the various components as

$$\rho = \sum_i m_i n_i . \quad (5.32)$$

Due to the long mean free path of the particles at high altitudes, one can treat the gases as ideal, therefore

$$P = nkT , \quad (5.33)$$

with k being the Boltzman constant, and T the temperature. In such a case the variations of pressure are related to the variations in height by

$$\frac{dP}{P} = -\frac{dh}{H} . \quad (5.34)$$

H in Eq. 5.34 is the scale height and is defined as

$$H = \frac{kT}{mg} . \quad (5.35)$$

The scale height is not constant, but for a short range of altitude, one can approximate it as a linear function of altitude. More details on scale height will follow in the next sections.

5.3.1.1 Simple Chapman profile function

After defining the scale height, we now introduce the ion production rate under simplifying assumptions described in Section 2.2. Following Schaer (1999), the ion production rate is given by the Chapman function

$$q(h, \chi) = q_0 e^{(1 - z - \sec \chi e^{-z})} \quad \text{and} \quad z = \frac{h - h_0}{H} , \quad (5.36)$$

where:

- $q(h, \chi)$ ion production rate,
- q_0 maximum ion production rate at $\chi = 0$, i.e. the Sun at zenith,
- h_0 reference height of maximum ion production at $\chi = 0$,
- H scale height, and
- χ Sun zenith angle, and
- e base of natural exponential function.

The maximum ion production rate is defined as:

$$q_0 = \frac{\phi(\infty)\eta}{H e} , \quad (5.37)$$

where:

- $\phi(\infty)$ solar flux density outside the atmosphere (in photons/area),
- η number of ion pairs produced per proton.

To obtain the altitude of maximum ion production rate h_{max} , the Chapman function Eq. 5.36 is differentiated. This yields

$$h_{max} = h_0 + H z_{max} \quad \text{with} \quad z_{max} = \ln \sec \chi . \quad (5.38)$$

The maximum of the ion production is obtained from:

$$q_{max} = q_0 \cos \chi . \quad (5.39)$$

As we know, within the ionosphere, ions and electrons recombine proportional to the electron density. Neglecting the electron transportation processes, the following equation holds

$$\frac{dN_e}{dt} = q - aN_e^{\frac{1}{\alpha}} , \quad (5.40)$$

where a is the mean recombination coefficient for molecular ions and α is a constant depending on the ionospheric altitude. Using Eq. 5.36 and Eq. 5.40 in the photochemical equilibrium condition, where $dN_e/dt = 0$ holds, the electron density is derived by

$$N_e(h, \chi) = N_0 e^{\alpha(1 - z - \sec \chi e^{-z})} \quad \text{with} \quad N_0 = \left(\frac{q_0}{a} \right)^\alpha, \quad (5.41)$$

where N_0 is the maximum electron density at $\chi = 0$. This distribution is called the simple Chapman profile function or just the simple Chapman function (Rishbeth & Garriott, 1969).

According to Ratcliffe (1972) the maximum electron density N_m and its corresponding height h_m vary with the Sun zenith angle χ , i.e. with the day time. At noon, (where $\chi = 0$) N_m reaches its maximum and h_m its minimum. During the time of sunset and sunrise h_m has its maximum and N_m its minimum. The relation between the electron density maximum N_m and its corresponding value at $\chi = 0$, i.e. N_0 is simply derived by

$$N_m = N_0 \cos \chi. \quad (5.42)$$

Replacing N_0 in Eq. 5.41 with the more general quantity N_m from Eq. 5.42 leads to

$$N_e(h) = N_m e^{\alpha(1 - z - e^{-z})}. \quad (5.43)$$

Figure 5.3 shows the electron density profile using Eq. 5.41 for different solar zenith angles. Though at lower latitudes there is a large amount of ionizable molecules, the ion production rate decreases due to the ionization of the high atmospheric layers and the reduction of photons. The potential of the increased quantity of photons at higher latitudes however, is limited by the low molecules density. Therefore, the altitude of maximum ion production is found at heights of about 200 to 700 *km*.

5.3.1.2 Multi-layer Chapman profile function

It was briefly discussed in the previous section that recombination of ions and electrons is proportional to the inverse power of electron density (i.e. $1/\alpha$ in Eq. 5.40). Several authors have shown that α depends on the ionospheric height. Chiu (1975) proposed an empirical model that assumed a linear dependency between the loss rate and the electron density. This results α equal to unity. So the ion production rate would be

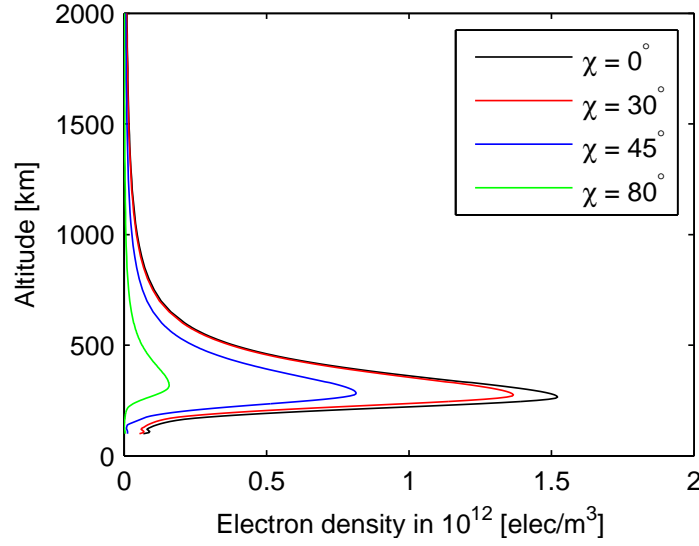


Figure 5.3: Electron density profile for different solar zenith angles

$$q = aN_e + \frac{dN_e}{dt} , \quad (5.44)$$

and in equilibrium conditions

$$q = aN_e . \quad (5.45)$$

The Base Point Model (BPM), proposed by Ezquer *et al.* (1996) assumed two different behaviors for the bottom-side and topside ionosphere. Similar to Chiu (1975) model, the BPM assumed a linear relation between loss rate and electron density within the bottom-side ionosphere. But in the topside, the loss rate is presumed proportional to the square of the electron density

$$q = aN_e^2 . \quad (5.46)$$

Following this proposal, Chapman profile function will also be different for the bottom-side and topside ionosphere. So for the bottom-side ionosphere, (i.e. for the E, F1, and bottom-side F2 layer) we have

$$N_e^{bottom}(h) = Nm \ e^{\alpha(1 - z - e^{-z})} , \quad (5.47)$$

with $\alpha = 1$. This is known as the α -Chapman function. For the topside ionosphere, using Eq. 5.46, the Chapman profile function would be

$$N_e^{top}(h) = Nm \ e^{\beta(1 - z - e^{-z})} , \quad (5.48)$$

with $\beta = 1/2$. This function is known as the β -Chapman function.

5.3.1.3 Electron density representation in topside ionosphere

Topside ionosphere is usually referred to as the part of the ionosphere extended from the F2 peak density height (i.e. from hmF2), until the plasmasphere, which starts approximately from ~ 1000 km altitude (see Sect. 2.3.1.1). According to Bilitza (2009) a major challenge for modeling electron density $N_e(h)$ in topside ionosphere is finding an appropriate representation of the profiles. Several authors have proposed different representations. Bent *et al.* (1972) and Llewellyn & Bent (1973) proposed exponential functions. Rawer (1988), Radicella & Leitinger (2001), and Depuev & Pulinets (2004) proposed using Epstein functions for electron density representation in the topside ionosphere. Reinisch & Huang (2004) applied a Chapman function with constant scale height. It was then figured out that this function is suitable for modeling electron density up to a limit height of ~ 700 km. Above this height, the function should be modified. So Kutiev *et al.* (2006) proposed a combination of two Chapman functions with constant scale heights, for O+ and H+ ions. Finally Reinisch *et al.* (2007) proposed the Vary-Chap function, which is a modified general Chapman function with a continuously varying scale height.

In the Vary-Chap function the scale height is represented by a modified hyperbolic tangent function (Reinisch *et al.*, 2007). Electron density in this representation is given by

$$N_e(h) = Nm \left(\frac{H_m}{H(h)} \right)^{1/2} e^{\frac{1}{2}(1 - Y - e^{-Y})} , \quad (5.49)$$

with

$$Y = \int_{h_m}^h \frac{dh}{H(h)} , \quad (5.50)$$

$H_m = H(h_m)$ is the scale height at h_m . As it can be seen in Eq. 5.49 and 5.50, electron density $N_e(h)$ is depending on $H(h)$. The varying scale height $H(h)$ can now be solved as a function of $N_e(h)$ (Huang & Reinisch, 2001)

$$H(h) = H_m \left(\frac{N_e(h)}{N_m} \right)^{-2} X(h) (1 - \ln X(h)) , \quad (5.51)$$

where

$$X(h) = 1 + \frac{1}{H_m} \int_{h_m}^h \left(\frac{N_e(h)}{N_m} \right)^2 dh . \quad (5.52)$$

This approach uses the H_m values derived from bottom-side profiles for constructing the topside normalized scale height function $\frac{H(h)}{H_m}$ (Bilitza *et al.*, 2011).

Nsumei *et al.* (2012) further modified the Vary-Chap function by applying a shape function which has a value of one at $h = h_m$

$$N_e(h) = N_m S(h)^{-1/2} e^{\frac{1}{2}(1 - Y - e^{-Y})} , \quad (5.53)$$

with

$$Y = \frac{1}{h_m} \int_{h_m}^h \frac{dh}{S(h)} . \quad (5.54)$$

The shape function $S(h)$ can be solved

$$S(h) = \left(\frac{N_e(h)}{N_m} \right)^{-2} X(h) (1 - \ln X(h)) , \quad (5.55)$$

with similar $X(h)$ function as in Eq. 5.52.

According to Nsumei *et al.* (2012) the new Vary-Chap function describes the electron density profile at the topside ionosphere as a function of local time, latitude, and season for any foF2/hmF2 layer peak specification.

5.3.1.4 Electron density representation in plasmasphere

Plasmasphere is the upper part of Earth's atmosphere starting from ~ 1000 km altitude (see Sect. 2.3.1.1). Due to the very low density of neutral molecules in the plasmasphere, the main ionized particles within the atmosphere are found in the ionosphere. Nevertheless, because of the transport of ions and electrons within this region, plasmasphere also contains some amount of free electrons and ions and therefore should be considered when modeling the ionospheric parameters.

To represent electron density in plasmasphere, several models have been developed. Based on

IMAGE/RPI measurements, Huang *et al.* (2004) developed a preliminary empirical model, which specified the electron density profile for a given location and time in the altitude range from $\sim 2,500$ km to $5,000$ km. The model had a smooth transition connection of the topside ionosphere and plasmasphere

Jakowski *et al.* (2002a) proposed a model for topside ionosphere and plasmasphere (TIP) to improve the operational retrieval of vertical electron density profile from CHAMP mission (see Sect. 3.3.3). The electron density $N_e(h)$ represented by TIP is described by

$$N_e(h) = NmF2 e^{0.5(1 - z - e^{-z})} + N_{P0} e^{(-h/H_P)} . \quad (5.56)$$

with

$$z = \frac{h - hmF2}{H_{TS}} , \quad (5.57)$$

where

h	height,
$NmF2, hmF2$	peak electron density and height,
H_{TS}	topside scale height,
N_{P0}, H_P	plasmasphere basis density and scale height.

The five unknown parameters in Eq. 5.56, i.e. $NmF2$, $hmF2$, H_{TS} , N_{P0} , and H_P are adjusted through an iterative process. The iteration results a smooth transition from the electron densities derived from TIP to the first values computed from the CHAMP radio occultation data. According to Jakowski *et al.* (2002a) this procedure directly provides the scale height at the upper boundary of the retrieved electron density profile. Figure 5.4 depicts the TIP model over Sofia vertical sounding station for 9 September 2000 at 08:10 UT. The model is feeded by the ionosonde data and checked by independent GPS derived vertical TEC estimates over Sofia (Jakowski *et al.*, 2002a).

This composite global scale model, is based on F2 layer peak model coefficients from CCIR (e.g. Bradely (1990), CCIR (1967)) and URSI (e.g. Fox & McNamara (1988), Rush *et al.* (1989)). These estimated parameters are then used to reconstruct the vertical electron density profile above the height of the CHAMP satellite. The plasmasphere model part includes two vertical scale heights. One for the $O+$ ion dominated ionosphere above the CHAMP orbit height and the second for the $H+$ ion in the plasmasphere. According to Jakowski *et al.* (2002a), the preliminary validation of the developed model with the ionosonde data, reveals an RMS error of 1.0 MHz and 45.2 km for f0F2 and hmF2, respectively.

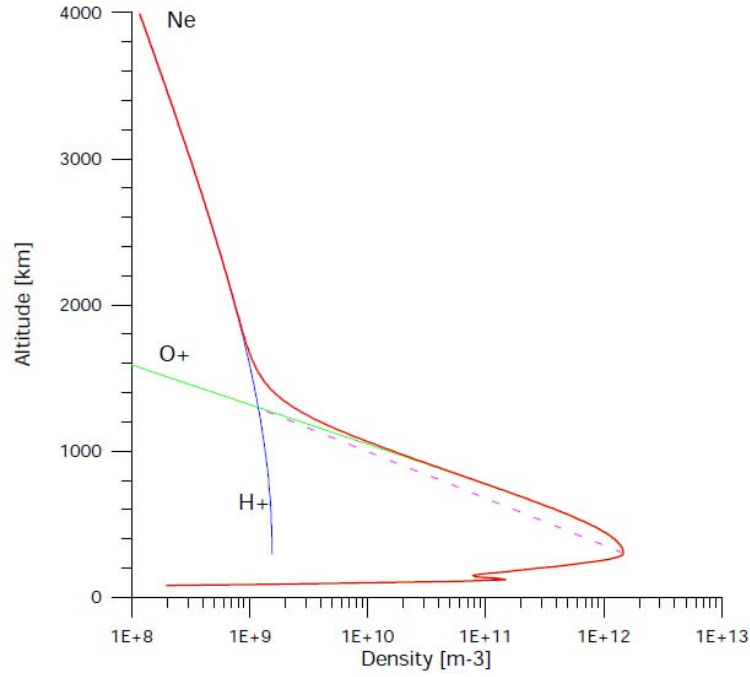


Figure 5.4: Example for an improved TIP model over Sofia vertical sounding station. 9 September 2000 - 08:10 UT (figure curtsey of Jakowski *et al.* (2002a))

5.3.2 Extending ionosphere model using Chapman profile function

5.3.2.1 TEC observable and Chapman function

Considering the smoothed code measurements (see Sect. 3.1.2.2), Eq. 3.24 relates the TEC observable \tilde{P}_4 to the STEC

$$\tilde{P}_4 = \tilde{P}_1 - \tilde{P}_2 = \xi STEC(\beta, s) + c(\Delta b^S - \Delta b_R) + \varepsilon. \quad (5.58)$$

It was declared in Sect. 2.4.3, STEC is the integral of electron density along the ray-path from receiver R to satellite S

$$STEC = \int_R^S N_e(s) ds. \quad (5.59)$$

Applying Eq. 5.59 into Eq. 5.58, gives the relation between TEC observable \tilde{P}_4 and the electron density

$$\tilde{P}_4 = \xi \int_R^S N_e(h) ds + c(\Delta b^S - \Delta b_R) + \varepsilon. \quad (5.60)$$

Note that $N_e(s)$ in Eq. 5.59 is substituted by $N_e(h)$ in Eq. 5.60, as we mainly focus on height variations within the electron density. The variations in the horizontal component (i.e. in longitude and latitude) are implicitly indicated in the further formulae.

Now taking into account the simplest form of Chapman profile function (described in Sect. 5.3.1.1), and substituting $N_e(h)$ from Eq. 5.43 into Eq. 5.60 yields

$$\tilde{P}_4 = \xi \int_R^S N_m \cdot e^{\alpha(1-z-e^{-z})} ds + c(\Delta b^S - \Delta b_R) + \varepsilon . \quad (5.61)$$

Equation 5.61 relates the smoothed GNSS TEC observable \tilde{P}_4 to the maximum electron density N_m , and its corresponding height h_m , changing along the ray-path. In this equation, the parameters of the Chapman profile function (N_m and h_m) and the receiver and satellite DCB (Δb_R and Δb^S) are the unknown parameters.

5.3.2.2 Solving the unknown parameters

To solve the unknown parameters of Eq. 5.61, Feltens (1998) tried to perform the integration along the ray-path analytically. In the first step, he assumed the ionosphere as a single layer model, and mapped the integration increment ds to vertical dh , using the counter part to the SLM mapping function $1/\cos(z)$ (see Sect. 2.4.3), where z is the satellite zenith angle at the receiver point.

Following Cappellari *et al.* (1976) he then performed the analytical integration over the simple form of the Chapman profile function (see Sect. 5.43), and obtained the relation between the TEC observable and the integral over the Chapman profile. In the next step, he took the real form of ionosphere into account by assuming this medium as a spherical stratified layer. Therefore he performed his calculations in different integration steps. This led to a very sophisticated procedure, including several approximations, that in turn, made the solution inaccurate.

In this study we investigated a new approach for solving the integral in Eq. 5.61. In this approach, ray-tracing technique (see Sect. 5.3.3) is applied to calculate the parameters of the integral along the ray-path. Applying this technique, ionosphere is subdivided into several layers, and therefore the integral along the track, from the receiver R to the satellite S , turns into a simple summation along the step points of the ray-path

$$\tilde{P}_4 = \xi \sum_{i=1}^k N_{mi} e^{\alpha(1-z_i-e^{-z_i})} ds_i + c(\Delta b^S - \Delta b_R) + \varepsilon , \quad (5.62)$$

with

$$z_i = \frac{h_i - h_{mi}}{H_i} , \quad (5.63)$$

where

N_{mi} maximum electron density at each step point,

h_{mi} height of maximum electron density at each step point,

H_i scale height at each step point,

h_i geocentric height of each step point, and

ds_i differential increment of slant range at each step point.

In Eq. 5.62 the summation is performed in k step points along the ray-path, from receiver to the satellite. Figure 5.5 depicts the concept of applying this technique.

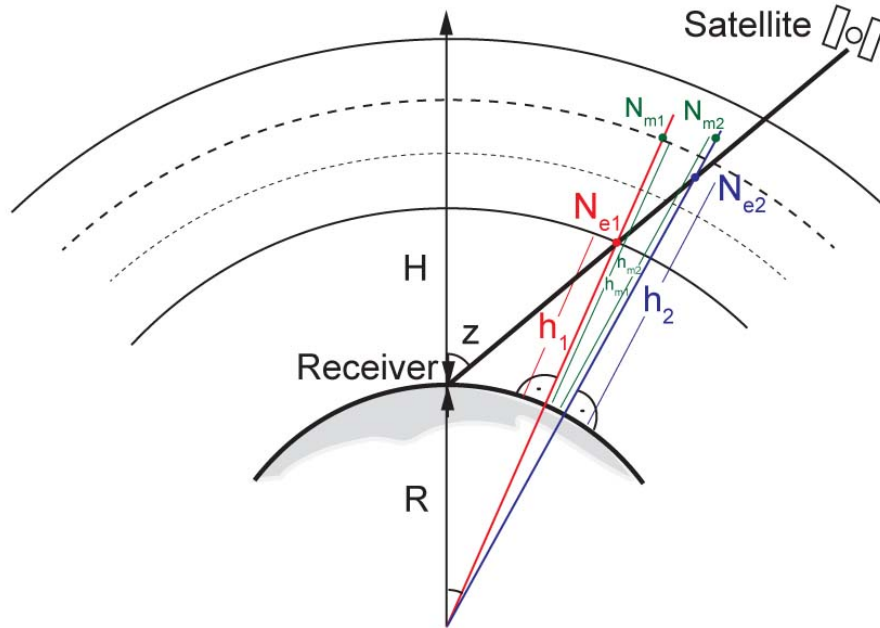


Figure 5.5: Concept of applying ray-tracing technique to the Chapman profile function

5.3.2.3 Global electron density representation using spherical harmonics

According to Eq. 5.62 for each step point along the ray-path, one individual N_{mi} and h_{mi} should be calculated. This is also shown schematically in Fig. 5.5. Therefore for each ray-path i.e. for each observation, we will have two sets of unknown parameters, which obtain k number of unknowns each. Thus for each observation equation, we will have $2k$ unknown parameters. This in fact, turns our model into an under-determined situation, and the problem becomes unsolvable.

However, these different N_{mi} (or h_{mi}) are not completely individual unknowns, but in principle, they are related to each other. Similar to Sect. 4.3.1, the different N_{mi} and h_{mi} values could be represented by series expansions with appropriately defined base-function. In this

study, as we aim to model electron density globally, we use spherical harmonics base functions for representing the unknown parameters as

$$N_{mi} = \sum_{n=0}^{n_{max}} \sum_{m=0}^n \tilde{P}_{nm}(\sin \beta_i) (a_{nm} \cos(ms_i) + b_{nm} \sin(ms_i)) , \quad (5.64)$$

$$h_{mi} = \sum_{n=0}^{n_{max}} \sum_{m=0}^n \tilde{P}_{nm}(\sin \beta_i) (a'_{nm} \cos(ms_i) + b'_{nm} \sin(ms_i)) , \quad (5.65)$$

where

- a_{nm}, b_{nm} unknown coefficients of first spherical harmonics expansion,
- a'_{nm}, b'_{nm} unknown coefficients of second spherical harmonics expansion,
- β_i geomagnetic latitude of each step point,
- s_i sun-fixed longitude of each step point, and
- \tilde{P}_{nm} normalized Legendre function of degree n and order m .

Applying these representations, the unknown parameters would reduce from $2k$ to the number of spherical harmonics coefficients, and the model gets solvable.

5.3.3 Ray-tracing technique

Ray-tracing estimates the propagation of an electromagnetic wave through a medium. In contrary to the mapping function method, ray-tracing estimates the delays for any arbitrary slant direction.

Ray-tracing technique was first proposed by Bean & Thayer (1959) for a spherically stratified atmosphere. But due to large number of calculations and lack of powerful computers, several simplification assumptions were introduced in solving the problem. Nowadays, with evolving technologies and presence of super fast computers, many fields of science in which the propagation of an electromagnetic wave through a medium has to be traced, ray-tracing technique can be used.

In this technique, the propagation path of an electromagnetic wave in a 3D Cartesian coordinate system is derived by the Eikonal equation (Born & Wolf, 1999)

$$\sum_{i=1}^3 \left(\frac{\partial S}{\partial x_i} \right)^2 = n^2(x, y, z) , \quad (5.66)$$

where

S	the signal path through the medium,
$x_i = \{x, y, z\}$	Cartesian coordinate, and
n	refractive index of the medium depending on (x,y,z).

According to Born & Wolf (1999) in a general case, the Eikonal equation can be written in a vector notation

$$|\nabla S|^2 = n^2(\vec{r}) , \quad (5.67)$$

where ∇S is the components of ray direction, S is the optical path length, and \vec{r} is the position vector.

The Eikonal equation is used to establish a ray-tracing system to determine the ray-path and the optical path. This equation can generally be written in Hamiltonian canonical formalism (Cervney (2005), Nafisi *et al.* (2012))

$$H(\vec{r}, \nabla S) = \frac{1}{\alpha} \{ (\nabla S \cdot \nabla S)^{\alpha/2} - n(\vec{r})^\alpha \} = 0 , \quad (5.68)$$

$$\frac{d\vec{r}_i}{du} = \frac{\partial H}{\partial \nabla S_i} , \quad (5.69)$$

$$\frac{d\nabla S_i}{du} = -\frac{\partial H}{\partial \vec{r}_i} , \quad (5.70)$$

$$\frac{dS}{du} = \nabla S_i \frac{\partial H}{\partial \nabla S_i} . \quad (5.71)$$

The scalar value α defines the parameter of our interest. For instance $\alpha = 1$ indicates the path length S along the ray-path. $H(\vec{r}_i, \nabla S_i)$ is called the Hamiltonian function or simply the Hamiltonian.

In a 3D space, the Hamiltonian system consists of seven equations. Six are derived from Eq. 5.69 and Eq. 5.70, and should be solved simultaneously to result the trajectory of a 3D curve $r_i = r_i(u)$. The last equation can be solved independently and yields the optical

path length. Using a spherical coordinate system with radial distance r , co-latitude θ , and longitude λ , the Hamiltonian can be rewritten as

$$H(r, \theta, \lambda, S_r, S_\theta, S_\lambda) = \left(S_r^2 + \frac{1}{r^2} S_\theta^2 + \frac{1}{r^2 \sin^2 \theta} S_\lambda^2 \right)^{\frac{1}{2}} - n(r, \theta, \lambda, t) = 0, \quad (5.72)$$

where $S_r = \partial S / \partial r$, $S_\theta = \partial S / \partial \theta$, and $S_\lambda = \partial S / \partial \lambda$ are the vector components of the ray direction. Merging the equations above, the ray-tracing system, consisting of six coupled partial differential equations are obtained

$$\begin{aligned} \frac{dr}{ds} &= \frac{1}{B} S_r & \frac{dS_r}{ds} &= \frac{\partial n(r, \theta, \lambda, t)}{\partial r} + \frac{1}{Br} \left(\frac{S_\theta^2}{r^2} + \frac{S_\lambda^2}{r^2 \sin^2 \theta} \right) \\ \frac{d\theta}{ds} &= \frac{1}{B} \frac{S_\theta}{r^2} & \frac{dS_\theta}{ds} &= \frac{\partial n(r, \theta, \lambda, t)}{\partial \theta} + \frac{1}{B} \frac{S_\lambda^2}{r^2 \sin^3 \theta} \\ \frac{d\lambda}{ds} &= \frac{1}{B} \frac{S_\lambda}{r^2 \sin^2 \theta} & \frac{dS_\lambda}{ds} &= \frac{\partial n(r, \theta, \lambda, t)}{\partial \lambda} \end{aligned} \quad (5.73)$$

where

$$B = \left(S_r^2 + \frac{1}{r^2} S_\theta^2 + \frac{1}{r^2 \sin^2 \theta} S_\lambda^2 \right)^{\frac{1}{2}} = n(r, \theta, \lambda, t). \quad (5.74)$$

As already stated, the equation system Eq. 5.73 should be solved simultaneously using a numerical integration method. For this, the Runge-Kutta method can be used which is an important implicit and explicit method for the approximation of solution of ordinary differential equations (Hairer *et al.*, 1993). Eq. 5.74 can be solved independently to provide the optical length. The final outputs are the positions of the trajectory of the ray and its path length Nafisi *et al.* (2012)

$$S = \int n(r, \theta, \lambda, t) ds. \quad (5.75)$$

Within our study, ray-tracing technique is applied to the GNSS signals, propagating through the upper atmosphere. Assuming the geocentric Cartesian coordinates of the receiver and the satellites position as the known parameters, ray-tracing is applied to each of the observations between IGS ground stations and the observed GNSS satellites at each observation epoch. The ray-tracing equation systems Eq. 5.73 and Eq. 5.74 are solved for every single ray-path and the parameters of the trajectory and their corresponding path length are calculated.

Finally the required parameters of the Chapman profile function Eq. 5.62 are calculated. These parameters include the geocentric coordinates of the intersection points of signal path

and the stratified layers of the ionosphere, slope distance between the two closest intersection points ds_i , geocentric height of each intersection point h_i , and satellite zenith angle at each intersection point. Furthermore the solar azimuth and zenith angle at each intersection point is also calculated and can be used when applying the non-general form of Chapman function Eq. 5.41.

5.3.4 Linearizing the model

5.3.4.1 General linearized model

Aforesaid in Sect. 5.1.1, to perform least-squares adjustment, the observation equations have to be linearized. In the following section, the linearization is performed over the simple chapman profile function Eq. 5.43. Considering Eq. 5.62, which denotes the relation between the smoothed TEC observable and the simplest form of Chapman profile function after applying the ray-tracing technique, the primary unknown parameters in this equation are the maximum electron density for each step point along the ray-path N_{mi} , its corresponding height h_{mi} , satellite hardware delay Δb^S , and receiver hardware delay Δb_R . To linearize the model, the partial derivatives of the observation equation Eq. 5.62 with respect to the unknown parameters have to be calculated. Except for h_{mi} , Eq. 5.62 is linear with respect to all the other unknown parameters.

For satellite and receiver hardware biases we have

$$\frac{\partial \tilde{P}_4}{\partial \Delta b^S} = -\frac{\partial \tilde{P}_4}{\partial \Delta b_R} = c, \quad (5.76)$$

Forming the partial derivative of the model Eq. 5.62 with respect to N_{mi} we get

$$\frac{\partial \tilde{P}_4}{\partial N_{mi}} = \sum_{i=1}^k e^{\alpha} (1 - z_i - e^{-z_i}) ds_i. \quad (5.77)$$

For h_{mi} the procedure is not that straightforward. Taking Eq. 5.62 and Eq. 5.63 into account, the partial derivative of the model with respect to h_{mi} is calculated in two steps, i.e.

$$\frac{\partial \tilde{P}_4}{\partial h_{mi}} = \frac{\partial \tilde{P}_4}{\partial z_i} \cdot \frac{\partial z_i}{\partial h_{mi}}. \quad (5.78)$$

In the first step we have

$$\frac{\partial \tilde{P}_4}{\partial z_i} = \sum_{i=1}^k \alpha N_{mi} e^{\alpha} (1 - z_i - e^{-z_i}) (e^{-z_i} - 1) ds_i. \quad (5.79)$$

Before performing the second step, we briefly discuss the scale height H_i in Eq. 5.63 here. It was declared in Sect. 5.3.1.3 and 5.3.1.4 scale height is a complicated parameter and is usually assumed as one of the unknown parameters of the ionosphere. Therefore it is estimated separately from N_{mi} and h_{mi} . But in the simple Chapman function Eq. 5.63, one can either assume it constant, or a better assumption proposed by Feltens (1998) assumed scale height as a function of the maximum electron density height h_{mi}

$$H_i = \frac{h_{mi} - 50}{3} , \quad (5.80)$$

where h_{mi} is in km .

Following this assumption, we now perform the second step for every single step point i

$$\frac{\partial z_i}{\partial h_{mi}} = -3 \frac{h_i - 50}{(h_{mi} - 50)^2} . \quad (5.81)$$

Substituting Eq. 5.79 and Eq. 5.81 into Eq. 5.78 we obtain

$$\frac{\partial \tilde{P}_4}{\partial h_{mi}} = \sum_{i=1}^k \left[\alpha N_{mi} e^{\alpha(1 - z_i - e^{-z_i})} (e^{-z_i} - 1) ds_i \left(-3 \frac{h_i - 50}{(h_{mi} - 50)^2} \right) \right] . \quad (5.82)$$

Equations 5.77 and 5.82 form the final linearized observation equation which will be used for further calculations.

5.3.4.2 Linearized model represented by spherical harmonics coefficients

As already specified in Sect. 5.3.2.3, we aim at representing N_{mi} and h_{mi} globally, by the applying spherical harmonics expansions Eq. 5.64 and Eq. 5.65. Therefore the final unknowns along with the satellite and receiver hardware delays, would be the coefficients of the spherical harmonics expansion, i.e. a_{nm} , b_{nm} , a'_{nm} , and b'_{nm} .

Now to derive the linearized observation equation, we have to form the partial derivatives of our observable \tilde{P}_4 with respect to the new unknowns as follow

$$\frac{\partial \tilde{P}_4}{\partial a_{nm}} = \frac{\partial \tilde{P}_4}{\partial N_{mi}} \cdot \frac{\partial N_{mi}}{\partial a_{nm}} , \quad (5.83)$$

$$\frac{\partial \tilde{P}_4}{\partial b_{nm}} = \frac{\partial \tilde{P}_4}{\partial N_{mi}} \cdot \frac{\partial N_{mi}}{\partial b_{nm}} , \quad (5.84)$$

$$\frac{\partial \tilde{P}_4}{\partial a'_{nm}} = \frac{\partial \tilde{P}_4}{\partial h_{mi}} \cdot \frac{\partial h_{mi}}{\partial a'_{nm}} , \quad (5.85)$$

$$\frac{\partial \tilde{P}_4}{\partial b'_{nm}} = \frac{\partial \tilde{P}_4}{\partial h_{mi}} \cdot \frac{\partial h_{mi}}{\partial b'_{nm}} . \quad (5.86)$$

Differentiating N_{mi} in Eq. 5.64 and h_{mi} in Eq. 5.65 with respect to the unknowns yields

$$\frac{\partial N_{mi}}{\partial a_{nm}} = \tilde{P}_{nm}(\sin \beta_i) \cos(ms_i) , \quad (5.87)$$

$$\frac{\partial N_{mi}}{\partial b_{nm}} = \tilde{P}_{nm}(\sin \beta_i) \sin(ms_i) , \quad (5.88)$$

$$\frac{\partial N_{mi}}{\partial a'_{nm}} = \tilde{P}_{nm}(\sin \beta_i) \cos(ms_i) , \quad (5.89)$$

$$\frac{\partial N_{mi}}{\partial b'_{nm}} = \tilde{P}_{nm}(\sin \beta_i) \sin(ms_i) . \quad (5.90)$$

By substituting values computed in Eq. 5.77 and Eq. 5.82, and the partial derivatives in Equations 5.87 - 5.90 into Equations 5.83 - 5.86 we get the final partial derivatives

$$\frac{\partial \tilde{P}_4}{\partial a_{nm}} = \sum_{i=1}^k \left[e^{\alpha(1 - z_i - e^{-z_i})} ds_i \tilde{P}_{nm}(\sin \beta_i) \cos(ms_i) \right] , \quad (5.91)$$

$$\frac{\partial \tilde{P}_4}{\partial b_{nm}} = \sum_{i=1}^k \left[e^{\alpha(1 - z_i - e^{-z_i})} ds_i \tilde{P}_{nm}(\sin \beta_i) \sin(ms_i) \right] , \quad (5.92)$$

$$\frac{\partial \tilde{P}_4}{\partial a'_{nm}} = \sum_{i=1}^k \left[\alpha N_{mi} e^{\alpha(1 - z_i - e^{-z_i})} (e^{-z_i} - 1) ds_i \left(-3 \frac{h_i - 50}{(h_{mi} - 50)^2} \right) \tilde{P}_{nm}(\sin \beta_i) \cos(ms_i) \right] , \quad (5.93)$$

$$\frac{\partial \tilde{P}_4}{\partial b'_{nm}} = \sum_{i=1}^k \left[\alpha N_{mi} e^{\alpha(1 - z_i - e^{-z_i})} (e^{-z_i} - 1) ds_i \left(-3 \frac{h_i - 50}{(h_{mi} - 50)^2} \right) \tilde{P}_{nm}(\sin \beta_i) \sin(ms_i) \right], \quad (5.94)$$

These equations are used to reconstruct the design matrix Eq. 5.2 and to finally form the linearized observation equation system.

5.3.5 Estimating the unknown parameters

To perform the estimation on the observation equation level, the linearized model Eq. 5.91 - 5.94 is used to form the design matrix A in Eq. 5.2. As we have two sets of unknown parameters, i.e. one set of spherical harmonics coefficients for N_m and one set for h_m , we accomplish the estimation procedure in two different steps. In the first step h_m is assumed known and consequently constant and N_m is estimated. In the second step the estimated values of N_m are used for estimating the h_m values. To accomplish this procedure, we preliminarily neglect the correlation between the unknown parameters N_m and h_m , and later on investigate this correlation. So in the first step, Eq. 5.91 and 5.92 are used to construct the design matrix and the least-squares adjustment is performed following Sect. 5.1.1. Since the observation equation Eq. 5.62 is linear with respect to N_m , there is no need for iteration. The unknown parameters for N_m , i.e. a_{nm} and b_{nm} are obtained after performing the least-squares adjustment. Using the estimated coefficients, the estimated N_m value is calculated and will be assumed as the known parameter for the next step of the estimation procedure. In the next step we concentrate on estimating the spherical harmonics coefficients a'_{nm} and b'_{nm} related to h_m . The estimation of h_m related parameters is done in an iterative procedure, as the observation equation Eq. 5.62 is non-linear with respect to h_m . Applying the equations explained in Sect. 5.1.1, the unknown parameters are estimated using Eq. 5.9. After each iteration, the estimated spherical harmonics coefficients are used to calculate the h_m values using Eq. 5.65 and together with the estimated N_m value are used to calculate the estimated residuals \hat{r} using Eq. 5.10 and \hat{l} using Eq. 5.11, which will be used for the next iteration. The variance factor is calculated after each iteration and if it reaches the tolerance range, the iteration is stopped and the latest estimated coefficients are used for calculating the final h_m values.

5.4 Fourth dimension in modeling electron density

To model ionospheric parameters in four dimensions, electron density should be modeled in longitude, latitude, height and time. In previous section, electron density parameters (maximum electron density N_m and its corresponding height h_m) were modeled in three dimensions, i.e. in longitude, latitude, and height. In this section we focus on the fourth

dimension by taking the temporal variations of the ionospheric parameters into account.

5.4.1 Fourier series

The theory of Fourier series was first developed by Joseph Fourier studying on the heat conduction in the early 19th century (Fourier, 1955). The principle of the series applied to the periodic functions occurring in a wave motion. However, the generalization of the Fourier series is usually applied to the time-frequency analysis. Considering a function f with a period 2π , the Fourier series of the function is given by (Walker, 1988)

$$f(x) = a_0 + \sum_{n=1}^{\infty} \{a_n \cos nx + b_n \sin nx\} , \quad (5.95)$$

with Fourier coefficients a_0 , a_n , and b_n defined as

$$\begin{aligned} a_0 &= \frac{1}{2\pi} \int_{-\pi}^{\pi} f(x) dx , \\ a_n &= \frac{1}{\pi} \int_{-\pi}^{\pi} f(x) \cos nx dx , \\ b_n &= \frac{1}{\pi} \int_{-\pi}^{\pi} f(x) \sin nx dx . \end{aligned} \quad (5.96)$$

5.4.2 Extending ionosphere model using Fourier series

To take the temporal dependency of the ionospheric parameters explicitly into account, the maximum electron density and its corresponding height can be expressed by Fourier series expansion. As in previous section, these unknown parameters were expressed by means of spherical harmonics expansion, and our unknown parameters were modified to the coefficients of spherical harmonics, in this section we represent these coefficients by means of Fourier series. So for each of the coefficients a_{nm} , b_{nm} , a'_{nm} , and b'_{nm} (see Sect. 5.3.2.3) we will apply a time-dependent Fourier series expansion

$$a_{nm}(t) = \sum_{p=0}^P \left[A1_{nmp} \cos(2\pi p \frac{t}{T_0}) + B1_{nmp} \sin(2\pi p \frac{t}{T_0}) \right] , \quad (5.97)$$

$$b_{nm}(t) = \sum_{p=0}^P \left[A2_{nmp} \cos(2\pi p \frac{t}{T_0}) + B2_{nmp} \sin(2\pi p \frac{t}{T_0}) \right] , \quad (5.98)$$

$$a'_{nm}(t) = \sum_{p=0}^P \left[A3_{nmp} \cos(2\pi p \frac{t}{T_0}) + B3_{nmp} \sin(2\pi p \frac{t}{T_0}) \right], \quad (5.99)$$

$$b'_{nm}(t) = \sum_{p=0}^P \left[A4_{nmp} \cos(2\pi p \frac{t}{T_0}) + B4_{nmp} \sin(2\pi p \frac{t}{T_0}) \right]. \quad (5.100)$$

where

p degree of Fourier series,

t desired time epoch,

T_0 the whole time interval of interest (here 24^{hours}).

The coefficients $A1_{nmp}$, $B1_{nmp}$, $A2_{nmp}$, $B2_{nmp}$, $A3_{nmp}$, $B3_{nmp}$, $A4_{nmp}$, and $B4_{nmp}$ are the unknown coefficients of the Fourier series expansion, and have to be estimated.

5.4.3 Linearizing the model

Similar to previous sections, linearizing the observation equation \tilde{P}_4 requires setting up the partial derivatives of the model with respect to the unknown parameters. Since now the unknown parameters are the coefficients of Fourier series expansion, we have to calculate the partial derivatives with respect to these parameters. We apply the chain rule to simplify the calculations

$$\frac{\partial \tilde{P}_4}{\partial A1_{nmp}} = \frac{\partial \tilde{P}_4}{\partial N_{mi}} \cdot \frac{\partial N_{mi}}{\partial a_{nm}} \cdot \frac{\partial a_{nm}}{\partial A1_{nmp}}, \quad (5.101)$$

$$\frac{\partial \tilde{P}_4}{\partial B1_{nmp}} = \frac{\partial \tilde{P}_4}{\partial N_{mi}} \cdot \frac{\partial N_{mi}}{\partial a_{nm}} \cdot \frac{\partial a_{nm}}{\partial B1_{nmp}}, \quad (5.102)$$

$$\frac{\partial \tilde{P}_4}{\partial A2_{nmp}} = \frac{\partial \tilde{P}_4}{\partial N_{mi}} \cdot \frac{\partial N_{mi}}{\partial b_{nm}} \cdot \frac{\partial b_{nm}}{\partial A2_{nmp}}, \quad (5.103)$$

$$\frac{\partial \tilde{P}_4}{\partial B2_{nmp}} = \frac{\partial \tilde{P}_4}{\partial N_{mi}} \cdot \frac{\partial N_{mi}}{\partial b_{nm}} \cdot \frac{\partial b_{nm}}{\partial B2_{nmp}}, \quad (5.104)$$

$$\frac{\partial \tilde{P}_4}{\partial A3_{nmp}} = \frac{\partial \tilde{P}_4}{\partial h_{mi}} \cdot \frac{\partial h_{mi}}{\partial a'_{nm}} \cdot \frac{\partial a'_{nm}}{\partial A3_{nmp}}, \quad (5.105)$$

$$\frac{\partial \tilde{P}_4}{\partial B3_{nmp}} = \frac{\partial \tilde{P}_4}{\partial h_{mi}} \cdot \frac{\partial h_{mi}}{\partial a'_{nm}} \cdot \frac{\partial a'_{nm}}{\partial B3_{nmp}}, \quad (5.106)$$

$$\frac{\partial \tilde{P}_4}{\partial A4_{nmp}} = \frac{\partial \tilde{P}_4}{\partial h_{mi}} \cdot \frac{\partial h_{mi}}{\partial b'_{nm}} \cdot \frac{\partial b'_{nm}}{\partial A4_{nmp}}, \quad (5.107)$$

$$\frac{\partial \tilde{P}_4}{\partial B4_{nmp}} = \frac{\partial \tilde{P}_4}{\partial h_{mi}} \cdot \frac{\partial h_{mi}}{\partial b'_{nm}} \cdot \frac{\partial b'_{nm}}{\partial B4_{nmp}}. \quad (5.108)$$

Using Equations 5.97 - 5.100 the partial derivatives will be

$$\frac{\partial a_{nm}}{\partial A1_{nmp}} = \frac{\partial b_{nm}}{\partial A2_{nmp}} = \frac{\partial a'_{nm}}{\partial A3_{nmp}} = \frac{b'_{nm}}{\partial A4_{nmp}} = \cos(2\pi p \frac{t}{T_0}), \quad (5.109)$$

and

$$\frac{\partial a_{nm}}{\partial B1_{nmp}} = \frac{\partial b_{nm}}{\partial B2_{nmp}} = \frac{\partial a'_{nm}}{\partial B3_{nmp}} = \frac{b'_{nm}}{\partial B4_{nmp}} = \sin(2\pi p \frac{t}{T_0}), \quad (5.110)$$

By substituting Eq. 5.109 and Eq. 5.110 in Equations 5.101 - 5.108 and then in Equations 5.91 - 5.94 we get the final partial derivatives

$$\frac{\partial \tilde{P}_4}{\partial A1_{nmp}} = \sum_{i=1}^k \left[e^{\alpha(1 - z_i - e^{-z_i})} ds_i \tilde{P}_{nm}(\sin \beta_i) \cos(ms_i) \cos(2\pi p \frac{t}{T_0}) \right], \quad (5.111)$$

$$\frac{\partial \tilde{P}_4}{\partial B1_{nmp}} = \sum_{i=1}^k \left[e^{\alpha(1 - z_i - e^{-z_i})} ds_i \tilde{P}_{nm}(\sin \beta_i) \cos(ms_i) \sin(2\pi p \frac{t}{T_0}) \right], \quad (5.112)$$

$$\frac{\partial \tilde{P}_4}{\partial A2_{nmp}} = \sum_{i=1}^k \left[e^{\alpha(1 - z_i - e^{-z_i})} ds_i \tilde{P}_{nm}(\sin \beta_i) \sin(ms_i) \cos(2\pi p \frac{t}{T_0}) \right], \quad (5.113)$$

$$\frac{\partial \tilde{P}_4}{\partial B_{2nmp}} = \sum_{i=1}^k \left[e^{\alpha(1-z_i-e^{-z_i})} ds_i \tilde{P}_{nm}(\sin \beta_i) \sin(ms_i) \sin(2\pi p \frac{t}{T_0}) \right] , \quad (5.114)$$

$$\begin{aligned} \frac{\partial \tilde{P}_4}{\partial A_{3nmp}} = \sum_{i=1}^k \left[\alpha N_{mi} e^{\alpha(1-z_i-e^{-z_i})} (e^{-z_i}-1) ds_i \left(-3 \frac{h_i-50}{(h_{mi}-50)^2} \right) \right. \\ \left. \tilde{P}_{nm}(\sin \beta_i) \cos(ms_i) \cos(2\pi p \frac{t}{T_0}) \right] , \end{aligned} \quad (5.115)$$

$$\begin{aligned} \frac{\partial \tilde{P}_4}{\partial B_{3nmp}} = \sum_{i=1}^k \left[\alpha N_{mi} e^{\alpha(1-z_i-e^{-z_i})} (e^{-z_i}-1) ds_i \left(-3 \frac{h_i-50}{(h_{mi}-50)^2} \right) \right. \\ \left. \tilde{P}_{nm}(\sin \beta_i) \cos(ms_i) \sin(2\pi p \frac{t}{T_0}) \right] , \end{aligned} \quad (5.116)$$

$$\begin{aligned} \frac{\partial \tilde{P}_4}{\partial A_{4nmp}} = \sum_{i=1}^k \left[\alpha N_{mi} e^{\alpha(1-z_i-e^{-z_i})} (e^{-z_i}-1) ds_i \left(-3 \frac{h_i-50}{(h_{mi}-50)^2} \right) \right. \\ \left. \tilde{P}_{nm}(\sin \beta_i) \sin(ms_i) \cos(2\pi p \frac{t}{T_0}) \right] , \end{aligned} \quad (5.117)$$

$$\begin{aligned} \frac{\partial \tilde{P}_4}{\partial A_{4nmp}} = \sum_{i=1}^k \left[\alpha N_{mi} e^{\alpha(1-z_i-e^{-z_i})} (e^{-z_i}-1) ds_i \left(-3 \frac{h_i-50}{(h_{mi}-50)^2} \right) \right. \\ \left. \tilde{P}_{nm}(\sin \beta_i) \sin(ms_i) \sin(2\pi p \frac{t}{T_0}) \right] . \end{aligned} \quad (5.118)$$

Part III

Results

Chapter 6

Multi-dimensional maps of the ionosphere

6.1 Combined 2D Global Ionosphere Maps

An autonomous Matlab-based software was developed for this study and further integrated for computing twelve GIM per day with the same spatial and temporal resolution as IGS GIM, i.e. spatial resolution of 2.5° in latitude and 5° in longitude, and temporal resolution of $2h$. To achieve this spatial resolution, VTEC is represented by spherical harmonic expansion of degree and order 15 (see Sect. 4.3.1). This leads to estimation of 256 coefficients for every single two-hourly map. As already discussed in Sect. 4.3.1.3, IGS produces thirteen two-hourly maps par day with the reference epoch starting at 0 UT each day and ending at 0 UT next day. The IGS GIM corresponds to the results of the middle day of a 3-day combination analysis (Schaer, 1999). This solution requires processing observations over three consecutive days and solving for 37 times 256, or 9,472 VTEC parameters. Since our investigation is just experimental, to reduce the computational time, we shifted the reference epoch from IGS reference epochs, i.e. $\{0, 2, 4, \dots, 24\}$ to $\{1, 3, 5, \dots, 23\}$. Therefore, we could process the observations of only one day and to solve 12 times 256, or 3,072 VTEC parameters, to obtain the GIM for that day. In our solution, in addition to spherical harmonic coefficients, the daily values of the GNSS satellite and receiver DCB are also computed as a by-product. For this, a zero mean condition is imposed to the estimates of satellite bias, for defining the DCB datum. For more details please refer to Todorova (2008). Furthermore, the corresponding RMS maps are developed as well. The final outputs are provided in the IONEX format (Schaer *et al.*, 1998), in which the estimated VTEC values are presented globally in a grid in the Earth-fixed geomagnetic frame.

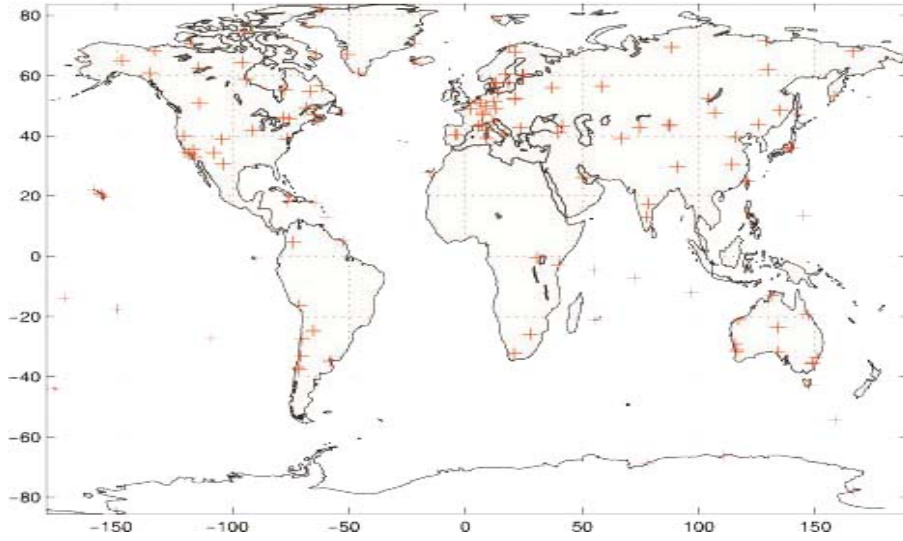


Figure 6.1: IGS GNSS stations used for computing GIM at day 190, 2006

6.1.1 Acquired data

6.1.1.1 GNSS

Ground-based GNSS observations from about 160 IGS stations with the sampling rate of 30sec and cut-off angle 10° were used for computation of GIM for each day. The daily RINEX observation files for the selected stations were downloaded from the SOPAC public ftp server (SOPAC, 2011) or the CDDIS ftp site (CDDIS, 2011). The GPS observations were preprocessed with the GPS ToolKit open source software (Tolman *et al.*, 2004). The preprocessing included setting-up the geometry-free linear combination from every pair of double-frequency code and phase observation. The GPS and GLONASS daily broadcast ephemeris files were downloaded from CDDIS website (CDDIS, 2011). The GNSS-derived STEC values were extracted, following routines developed by Todorova (2008), from the geometry-free linear combination applied on the carrier-phase smoothed code observations Eq. 3.28. The STEC was normalized using MSLM mapping function (see Sect. 2.58). The ionospheric pierce point is computed adopting a spherical layer with height $H = 450 \text{ km}$. Figure 6.1 depicts GNSS stations used for developing the twelve two-hourly GIM in a sample day, e.g. 9 July 2006.

6.1.1.2 Satellite altimetry

The VTEC values from satellite altimetry Jason-1 and Jason-2 were obtained from the ionospheric range delay provided by the Altimeter Database System (ADS) operated by the 'Deutsches GeoForschungsZentrum' (GFZ) in Potsdam, Germany (Central, 2012). This range delay is directly obtained from the altimeter measurements in two frequencies and is transformed to VTEC using Eq. 3.29.

Figure 6.2 illustrates the footprints of altimeter satellite, Jason-1 on 9 July 2006, in twelve two-hourly time intervals.

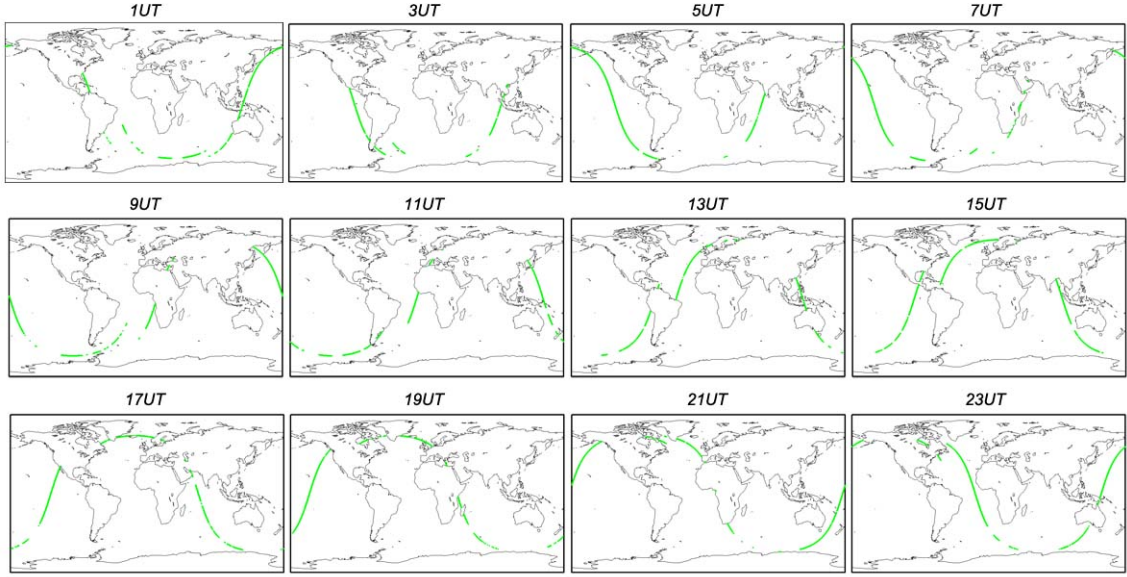


Figure 6.2: Footprints of satellite altimetry mission, Jason-1 on day 190, 2006

6.1.1.3 Formosat-3/COSMIC

For this study, VTEC values of F/C were provided by the ionospheric sounding lab of the National Central University, Taiwan (Tsai, 2012). The VTEC values were calculated from electron density profiles derived from the radio occultation measurements through applying the improved Abel transform. In this procedure, ionosphere is not assumed locally spherical asymmetric. Although the effect of large-scale horizontal gradients and of an inhomogeneous electron density distribution was taken into account. Subsequently, the VTEC below satellites were directly measured and the VTEC above the height of the satellites were calculated using extrapolation technique; for more details see Tsai & Tsai (2004) or Schmidt *et al.* (2008). Figure 6.3 depicts the footprints of F/C occultation measurements in twelve two-hourly time intervals for the whole day of 9 July 2006.

6.1.2 Combination of GNSS, satellite altimetry, and F/C observations

The following section is mainly following the procedure in the article published by Alizadeh *et al.* (2011) at the Journal of Geodesy special issue "Geodetic Contribution to Ionospheric Research" (Schmidt, 2011).

The modeling techniques using GNSS-only, GNSS and satellite altimetry, and finally GNSS, satellite altimetry, and F/C data developed within this study are referred to as IGG (Institute

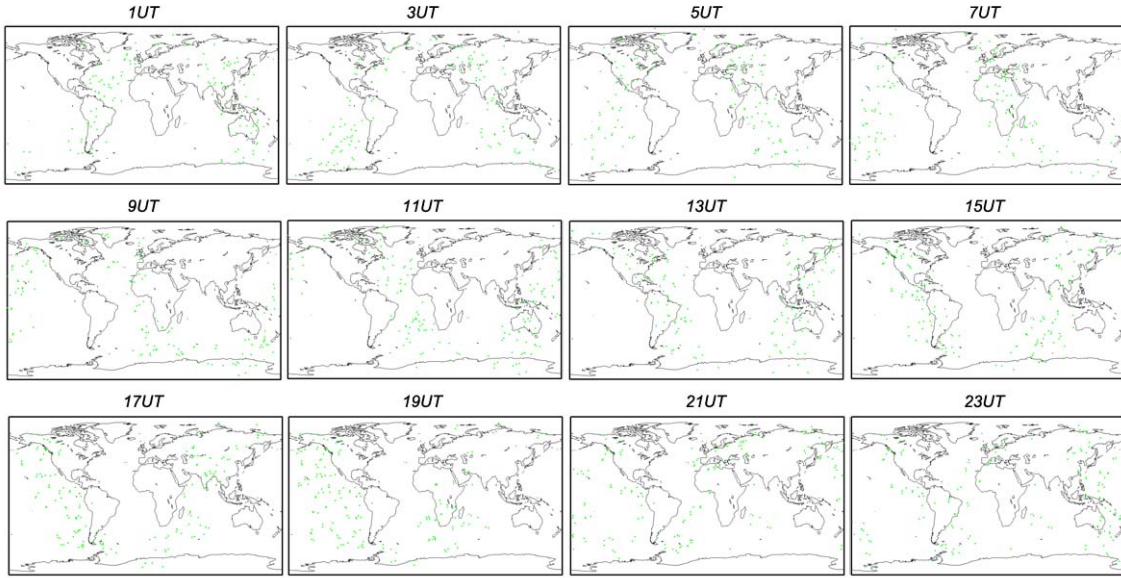


Figure 6.3: Footprints of F/C occultation measurements on day 190, 2006

of Geodesy and Geophysics of Vienna University of Technology) GNSS-only or IGG combined models.

6.1.2.1 IGG GNSS-only GIM

Considering as an example, the results for 9 July 2006 (day 190) are presented here. As shown in Fig. 6.1 observations of ~ 160 stations were included in the calculation of these maps. Figure 6.4 depicts twelve two-hourly maps of the IGG GNSS-only solution for the whole day 190 of 2006. Figure 6.5 shows the corresponding RMS map (see Sect. 5.1.4) in 12 two-hourly reference epochs, applying the IGG GNSS-only solution for the same day.

Figure 6.22 shows a snap shot of the GNSS-only VTEC map and its corresponding RMS map at 1 UT of day 190, 2006. Taking Fig. 6.22 into account, the precision of the maps are clearly lower in areas less covered by the GNSS observations. This is mainly over the oceans and in the southern polar region. The global mean bias between the VTEC maps estimated here and the GIM provided by IGS (see Sect. 4.3.1.3) is 0.5 TECU with a standard deviation of $\pm 0.7 \text{ TECU}$, proving a good agreement between IGG GIM and the IGS GIM.

6.1.2.2 GNSS and satellite altimetry combined GIM

In the first step, GIM from GNSS data is integrated with observations from satellite altimetry mission, Jason-1. As described in Sect. 5.2.2 the combination procedure is performed at the normal equation level, i.e. the normal equations of GNSS observations, and satellite altimetry data are constructed, then stacked together to form the combined normal equation. In this procedure, a daily constant systematic bias between GNSS and satellite altimetry

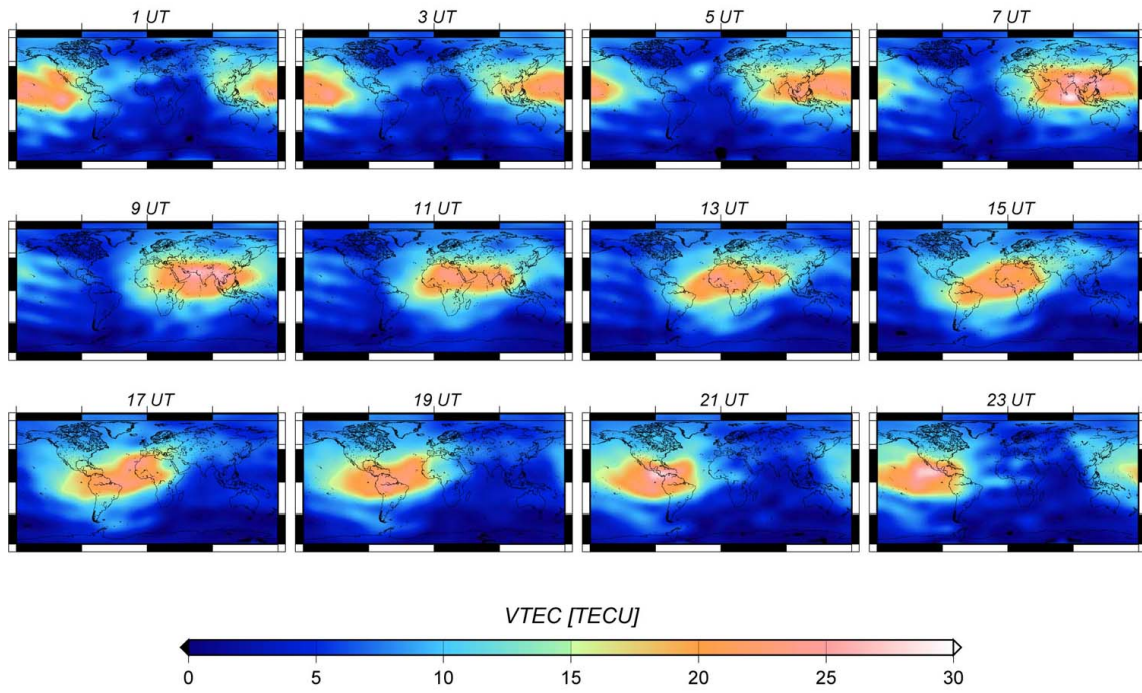


Figure 6.4: GNSS-only VTEC map for the whole day 190, 2006

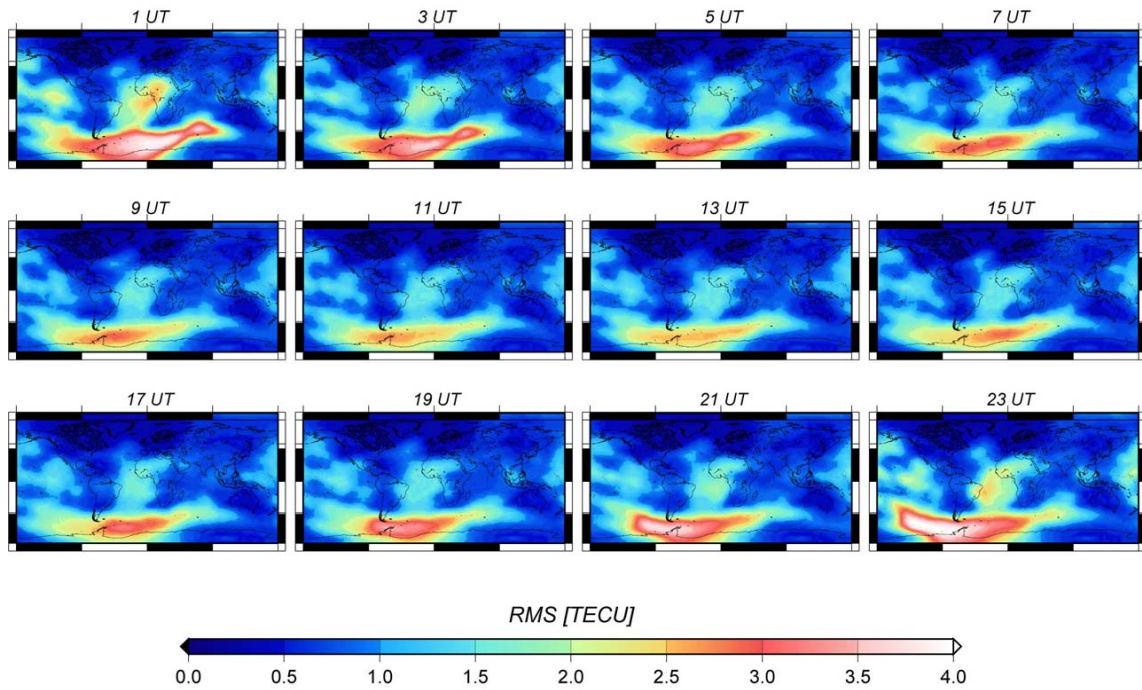


Figure 6.5: GNSS-only RMS map for the whole day 190, 2006

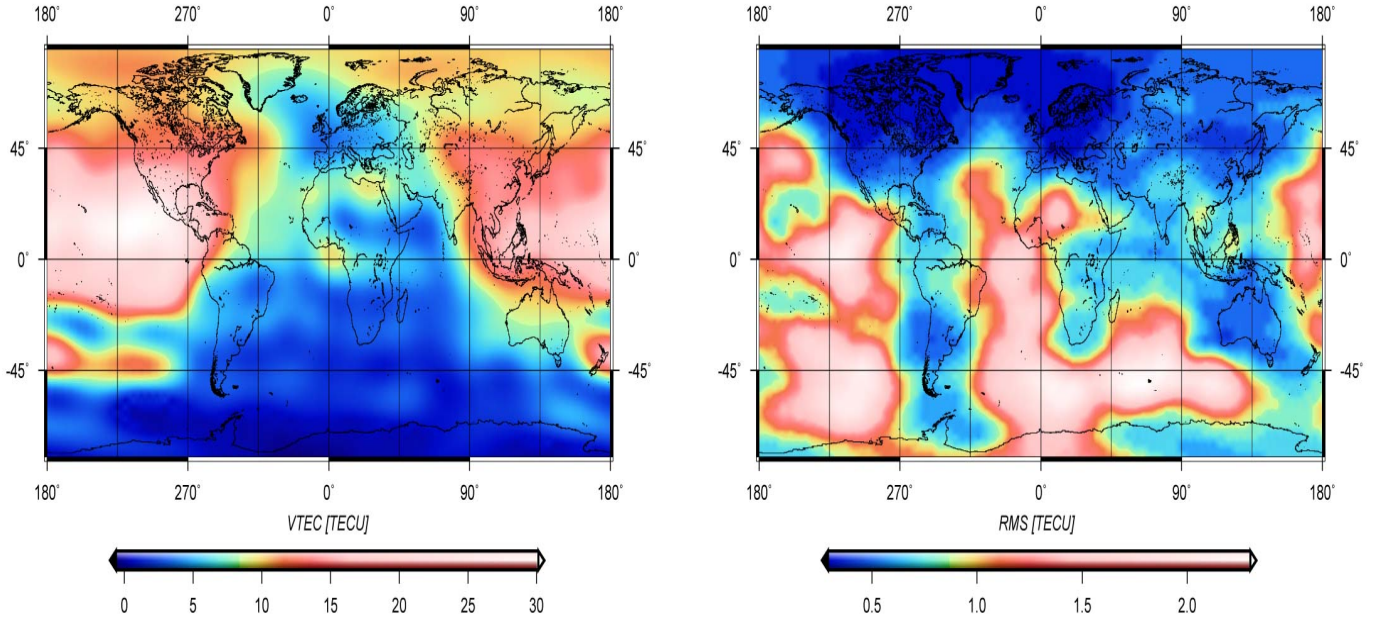


Figure 6.6: **a** VTEC map and **b** RMS map of GNSS-only solution, day 190, 2006 - 1 UT

mission is inserted as an additional unknown in the observation equation and is estimated along with the other unknown parameters. Figure 6.7 depicts the VTEC differences between the GNSS and satellite altimetry combined solution and the GNSS-only solution in twelve two-hourly maps for the whole day 190, 2006. Figure 6.8 depicts the corresponding RMS map.

Taking a closer look at a snapshot of the combined maps, we consider e.g. the map for 1 UT. Figure 6.9a shows the footprints of Jason-1 through the whole day 190, 2006; and Fig. 6.9b depicts the two-hourly snapshot of the footprints around 1 UT. Figure 6.10 shows the VTEC and RMS differences between GNSS and satellite altimetry combined map and the GNSS-only map at 1 UT of day 190, 2006. Taking Fig. 6.9b and Fig. 6.10 into account, it can be inferred that combining altimetry data with GNSS GIM, influences the maps approximately over the regions where satellite altimetry provides information. As it can be seen from Fig. 6.10a there is an increase of the VTEC values, up to 0.30 *TECU* in the low southern latitudes particularly over the oceans. Concerning the accuracy of the maps, the difference between the combined and the GNSS solution Fig. 6.10b shows a general decrease of the RMS in the combined model of up to 0.14 *TECU*. This coincides with the footprints of Jason-1 in 1 UT map.

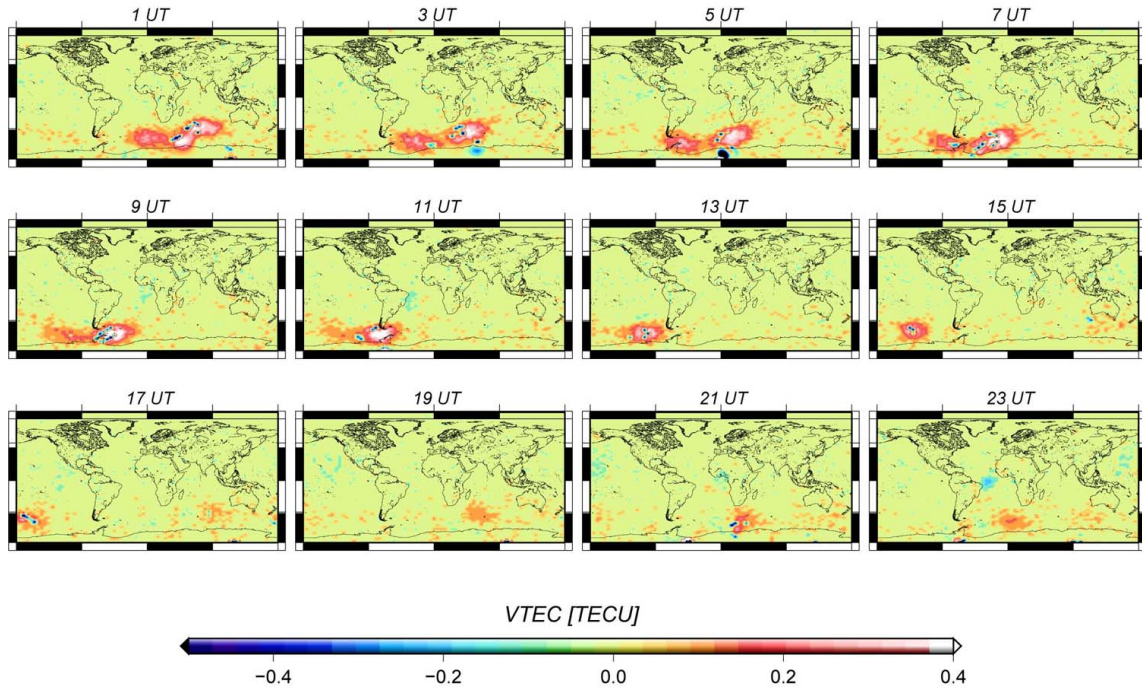


Figure 6.7: GNSS and satellite altimetry combined minus GNSS-only VTEC map for the whole day 190, 2006

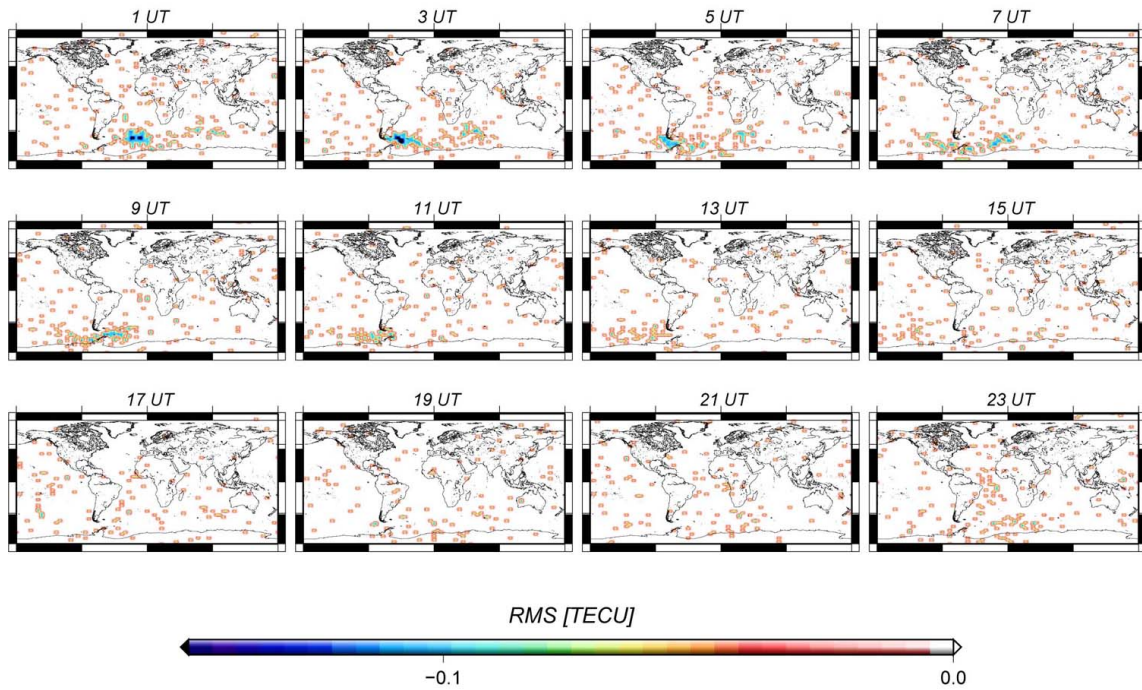


Figure 6.8: GNSS and satellite altimetry combined minus GNSS-only RMS map for the whole day 190, 2006

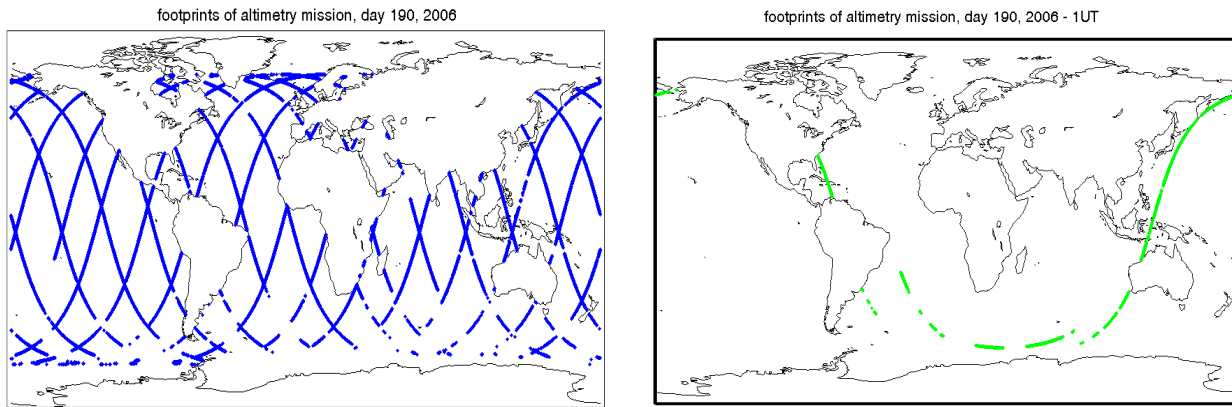


Figure 6.9: Footprints of satellite altimetry mission, Jason-1 **a** for the whole day and **b** for 2h around 1 UT of day 190, 2006

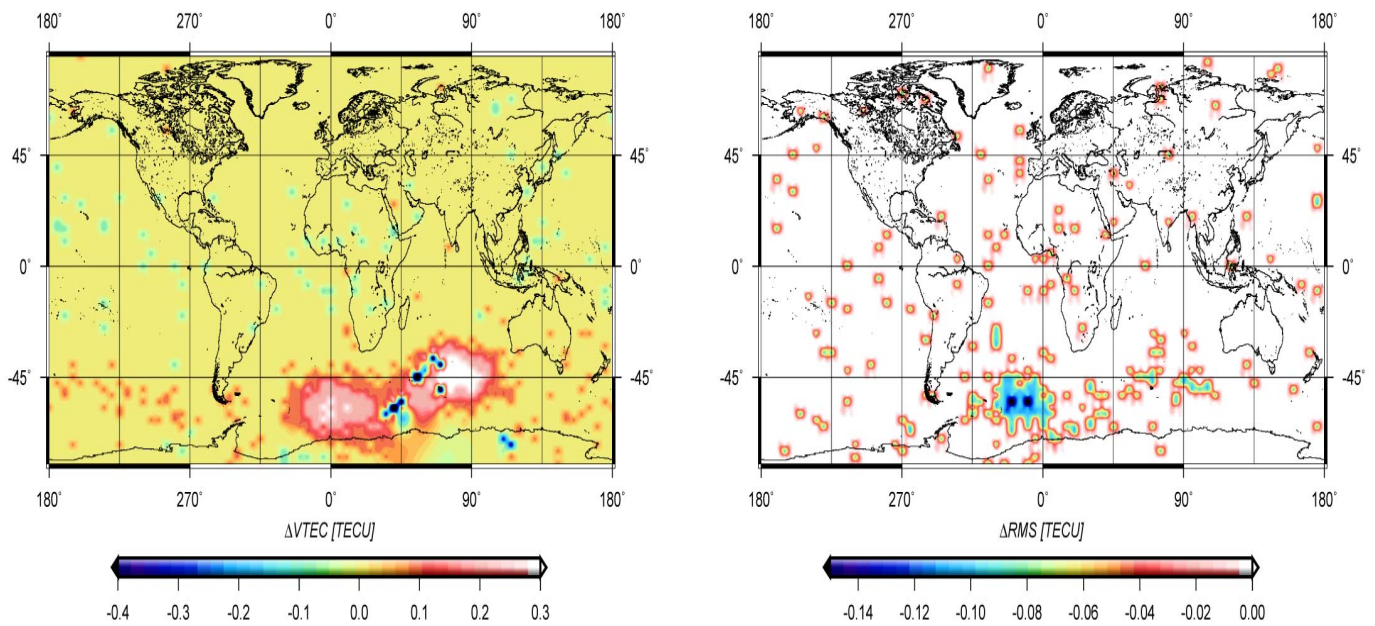


Figure 6.10: **a** VTEC map and **b** RMS map of GNSS and satellite altimetry combined minus GNSS-only solution, day 190, 2006 - 1 UT

6.1.2.3 GNSS, satellite altimetry, and F/C combined GIM

In the next step of integration, ionosphere information from F/C satellites is included in the combination. As F/C satellites provide globally well-distributed information of the ionosphere in a whole day (see Fig. 6.13b), combining this information with the GNSS and satellite altimetry GIM has the potential to improve the models by some extent. This combination is again performed at the normal equation level, as illustrated in Sect. 5.2.2. For this study the empirical weighting scheme was applied, and finally the best adopted weight was a diagonal matrix with the diagonal element of $P_{alt} = 1/4$, and $P_{F/C} = 4$, which corresponds to an a priori variance $\sigma_0^{alt} = 2 \text{ TECU}$, and $\sigma_0^{F/C} = 0.5 \text{ TECU}$. Figure 6.11 shows the VTEC differences between the GNSS, satellite altimetry, and F/C combined solution and the GNSS and satellite altimetry combined solution in twelve two-hourly intervals for the whole day 190, 2006. Figure 6.12 depicts the corresponding RMS map. Figure 6.13a shows footprints of all F/C occultation measurements through the whole day 190, of 2006. Figure 6.13b depicts the snapshot of the footprints at 1 UT of the same day. In the procedure of this combination, it is essential to assess the TEC bias between GNSS, satellite altimetry, and F/C. Thus, similar to previous step, a daily constant systematic bias between GNSS and F/C is also inserted as an additional unknown in the observation equation system and is estimated along with other unknown parameters. In fact other procedures are also possible, e.g. to include a daily constant bias or a frequency dependent bias for each of the six satellites of the F/C mission with respect to GNSS.

Figure 6.14 depicts a snap shot of VTEC and RMS of GNSS, satellite altimetry, and F/C combined GIM minus GNSS and satellite altimetry combined GIM at 1 UT of day 190, 2006. This will help understanding the effect of combining F/C data to the two previous observation techniques.

As it can be seen in Fig. 6.14a, the VTEC values have slightly increased over the ocean in southern latitudes by the amount of about 1 *TECU*. This is mainly in regions where no or few GNSS observations were available. Concerning the RMS of the combined solution, the GNSS, satellite altimetry and F/C combined maps show a general decrease of 0.1 *TECU* in the whole day, comparing to the GNSS and satellite altimetry combined maps (see Fig. 6.12). Taking a closer look at the RMS map of the snapshot at 1 UT (Fig. 6.14b), the decrease of about 0.08 *TECU* is obvious in the globe. However in the low southern latitudes, over the southern ocean, the RMS decrease reaches 0.5 *TECU*, which coincides with the highest number of F/C observations at this particular epoch. This proves the fact that including F/C measurements into our GIM can significantly improve the accuracy of our modeling techniques, especially when a high number of F/C occultation data are available.

6.1.3 Quantification with raw altimetry and F/C data

To assess the self-consistency of the approach and to evaluate the accuracy of the GIM created within the study, the IGG models are quantified with the VTEC delivered by raw

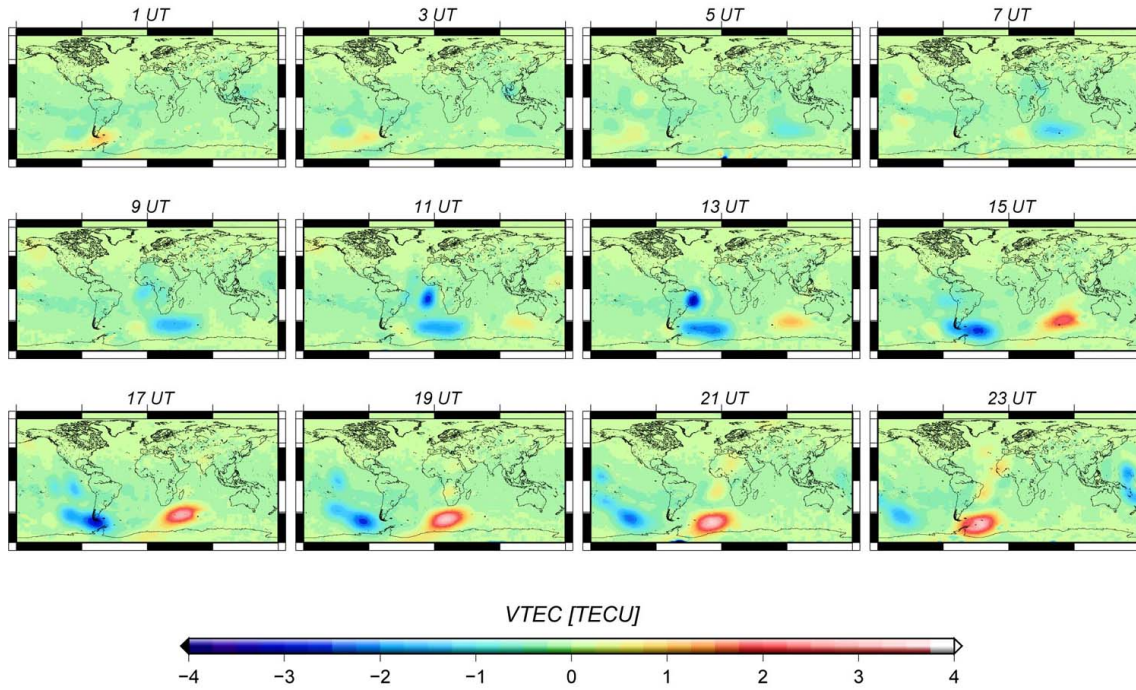


Figure 6.11: GNSS, satellite altimetry, and F/C combined minus GNSS and satellite altimetry combined VTEC map for the whole day 190, 2006

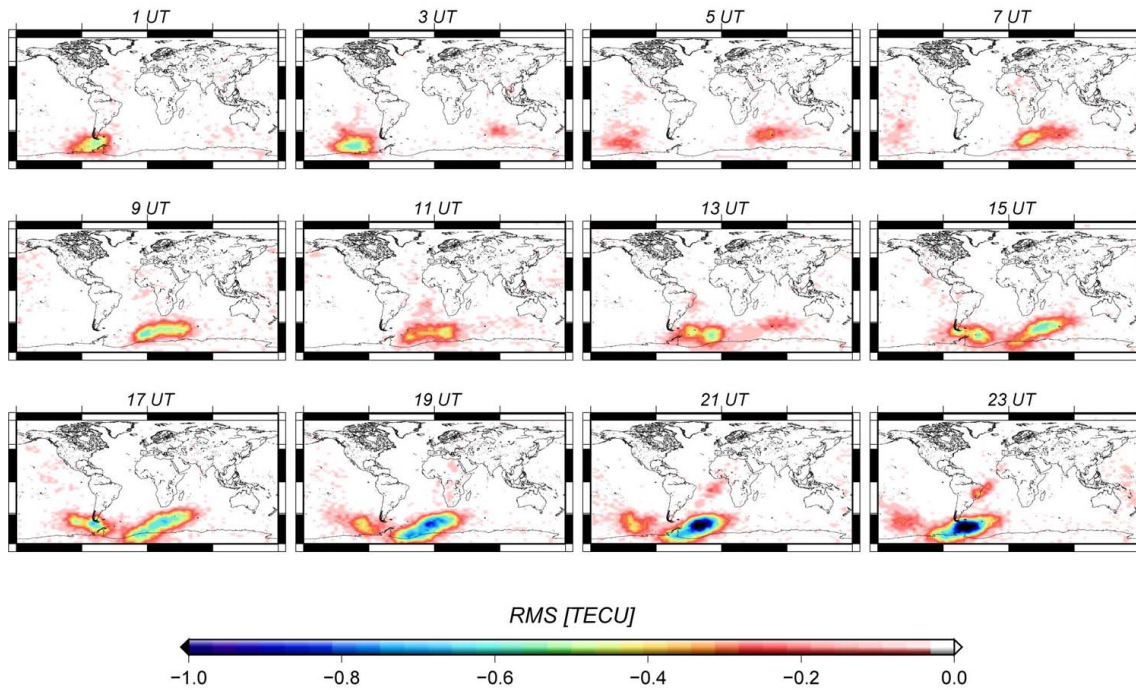


Figure 6.12: GNSS, satellite altimetry, and F/C combined minus GNSS and satellite altimetry combined RMS map for the whole day 190, 2006

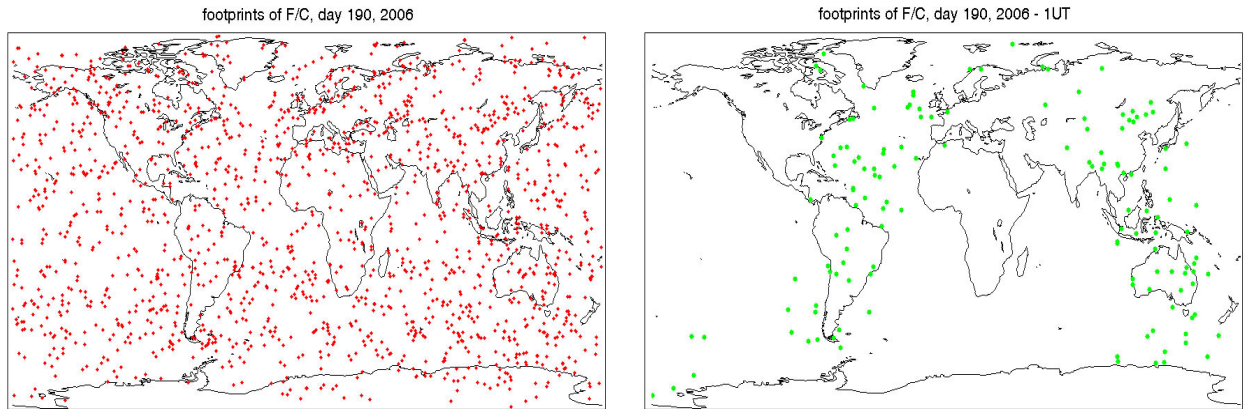


Figure 6.13: Footprints of F/C occultation measurements in two hourly intervals for **a** the whole day 190, 2006 and **b** 2h around 1 UT of the same day

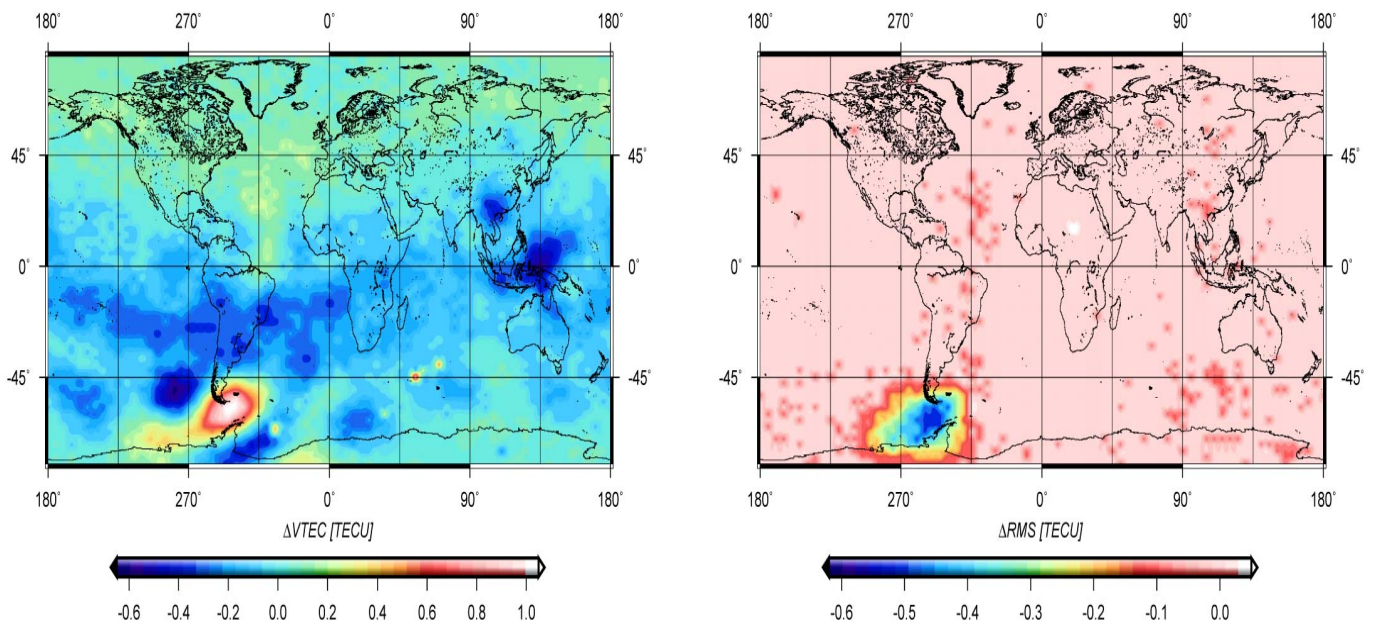


Figure 6.14: **a** VTEC map and **b** RMS map of GNSS, satellite altimetry, and F/C combined GIM minus GNSS and satellite altimetry combined solution, day 190, 2006 - 1 UT

altimetry and F/C data. In this process, 5% of altimetry and F/C observations from each two-hourly maps are left aside from the combination scheme and not included in the modeling process. The number of excluded observations is selected in such a way that the accuracy of the developed model would not reduce by the confidence interval of $(1 - \alpha = 95\%)$. After developing the combined maps, the VTEC values at the footprints of the raw altimetry and F/C observation which were formerly omitted from the combination, are extracted from the combined model. The differences between the VTEC values obtained from the combined model and the raw altimetry and F/C data are used to quantify the combined model. So for the altimetry satellite measurements the difference is formed by

$$\Delta VTEC_{IGG}^{alt}(\varphi_{alt}, \lambda_{alt}, t_{ref}) = VTEC_{IGG}(\varphi_{alt}, \lambda_{alt}, t_{ref}) - VTEC^{alt}(\varphi_{alt}, \lambda_{alt}, t_{alt}) , \quad (6.1)$$

where

$VTEC_{IGG}$	IGG combined VTEC,
$VTEC^{alt}$	raw altimetry VTEC (not included in combination),
$\varphi_{alt}, \lambda_{alt}$	geographic latitude and longitude of the raw altimetry observations,
t_{ref}	reference epoch of each map, i.e. $\{1, 3, 5, \dots, 23 \text{ UT}\}$, and
t^{alt}	time of altimetry observation.

Now the bias $b_V^{alt}(t_{ref})$ for each two-hourly map reference epoch t_{ref} is calculated by averaging the differences at all the raw observation-points

$$b_V^{alt}(t_{ref}) = \frac{1}{n^{alt}} \sum \Delta VTEC_{IGG}^{alt}(\varphi_{alt}, \lambda_{alt}, t_{ref}) . \quad (6.2)$$

n^{alt} in Eq. 6.2 is the number of raw altimetry observations carried out within each 2-hour interval. Similar biases for the F/C observations can be calculated correspondingly. Figure 6.15a presents the biases $b_V^{alt}(t_{ref})$ of altimetry observations through the whole day of 9 July 2006 (day 190). Figure 6.15b depicts the same results for F/C measurements.

As it can be seen from Fig. 6.15a the biases between the raw VTEC values from altimetry and VTEC values estimated by the combined GIM are positive for the whole day with a mean value of 2.84 *TECU*, i.e.

$$\bar{b}_V^{alt} = \frac{1}{12} \sum b_V^{alt}(t_{ref}) = 2.84 \text{ TECU} , \quad (6.3)$$

where 12 is the number of maps in a whole day. The standard deviation of the biases $b_V^{alt}(t_{ref})$ is 0.50 *TECU*. This positive mean bias indicates a systematic over-estimation of

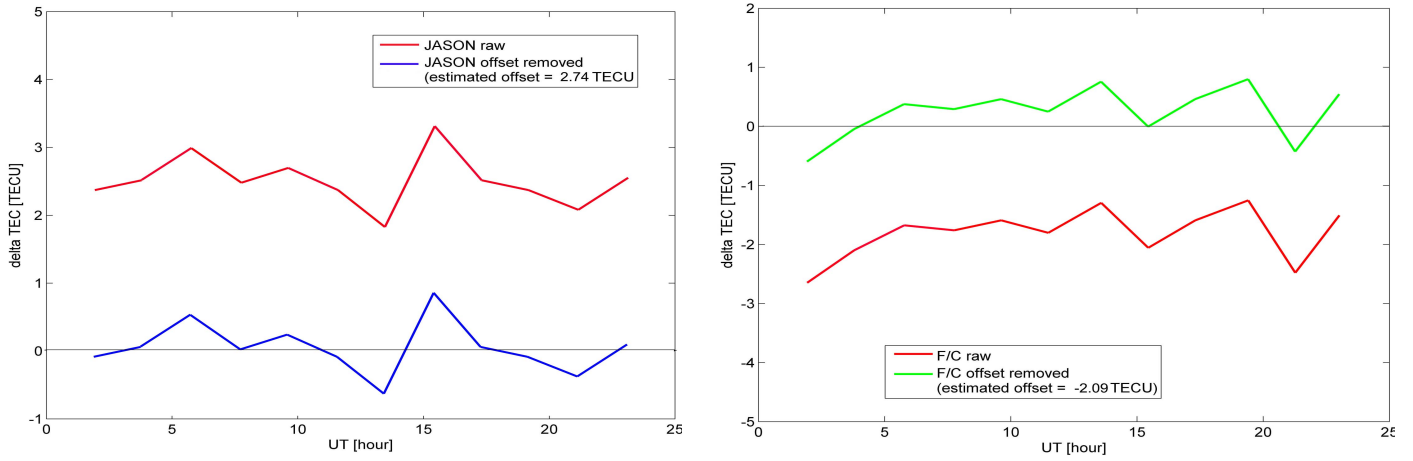


Figure 6.15: Mean VTEC biases before and after removing the estimated offset from IGG combined model minus **a** altimetry and **b** F/C VTEC for day 190, 2006

VTEC delivered by Jason-1 compared to the values delivered by GNSS. This fact has already been shown in several studies, e.g. Brunini *et al.* (2005), Todorova *et al.* (2007), and Todorova (2008).

To account for this bias, as stated in Sect. 6.1.2.2, a daily constant offset for the altimetry measurements is considered within the combination procedure, and is estimated along with the unknown parameters in the least-squares adjustment. In this way, the estimated offset includes both the instrumental bias and the plasmaspheric component (i.e. VTEC above the height of the altimetry mission). In this study, the offset of the altimetry satellite was estimated 2.74 *TECU*. The blue plot in Fig. 6.15a depicts the mean VTEC biases after removing this offset. As it can be seen, the new biases vary between $[-1, 1]$ *TECU*, with the mean value of 0.09 *TECU*, i.e. \bar{b}_V^{alt} after removing the estimated offset. This proves the good agreement of the combined model with the raw altimetry observations. In the case of F/C observations (Fig. 6.15b) the VTEC biases display a more scattered pattern compared to the altimetry biases, with a mean of -2.20 *TECU* and standard deviation of 1.09 *TECU*

$$\bar{b}_V^{F/C} = \frac{1}{12} \sum b_V^{F/C}(t_{ref}) = -2.20 \text{ TECU} . \quad (6.4)$$

The F/C daily constant offset with respect to GNSS, which was estimated with the other unknown parameters in the modeling procedure, is -2.09 *TECU*. Again this offset includes the instrumental bias of F/C with respect to GNSS and also the signature of the plasmaspheric component (i.e. VTEC above the height of the F/C mission). The green plot in Fig. 6.15b depicts the mean VTEC biases of F/C mission after removing the offset. The mean value of the biases $\bar{b}_V^{F/C}$ after removing the estimated offset reduces to -0.08 *TECU*, which again proves the good agreement of the combined model with the raw F/C measurements and might

be further improved when estimating individual biases for each F/C spacecraft.

6.1.4 Comparison of the combined GIM with IGS GIM

For further comparisons, the combined GIM from GNSS, satellite altimetry, and F/C are compared with the GIM from CODE (see Sect. 4.3.1.3), which is one of the IGS Analysis Centers (CODE, 2012). Aforesaid in Sect. 4.3.1.3, IGS provides thirteen two-hourly maps for a complete day, with reference epochs of $\{0, 2, 4, \dots, 24\}$ UT. But the IGG combined GIM is developed in twelve two-hourly maps with reference epochs of $\{1, 3, 5, \dots, 23\}$ UT. To proceed this validation, IGS GIM are interpolated in time to have a common reference epoch as the IGG GIM. Figures 6.16 and 6.17 depict the VTEC and RMS differences of IGG combined GIM minus IGS GIM through the whole day 190, 2006. As it can be seen from Fig. 6.16, the global VTEC differences vary between -6 to 19 TECU in a whole day; although the mean value of VTEC through the whole globe for the complete day is ~ -1.3 TECU. Concerning the accuracy of the maps, the RMS differences between IGG combined GIM and IGS GIM vary between -4 to 6 TECU in a complete day, with a mean value of -0.7 TEC. The area in Fig. 6.17 that are dark, indicate negative RMS differences, and the light area show positive RMS differences. A negative RMS values show that the combined GIM has a lower RMS than IGS GIM, indicating a better accuracy. In contrary, positive RMS show higher RMS values of the combined GIM with respect to the IGS GIM. This indicates a worse accuracy of the combined GIM. As it can be seen in Fig. 6.17 the dark area corresponds mainly to the ocean area, while the land region appear with a light color. This proves the fact that the IGG combined GIM has a better accuracy over the ocean than IGS GIM, while over the land, IGS provides more accurate VTEC values.

To clarify this comparison, we consider a snapshot of 1 UT of the same day. Figure 6.18a shows the VTEC difference between IGG combined solution minus IGS GIM for day 190, 2006 at 1 UT. Figure 6.18b shows the corresponding RMS difference. As it can be seen from Fig. 6.18a the main difference of VTEC at 1 UT between IGG combined GIM and IGS GIM is observed at the equatorial region with a maximum reduction of -4 TECU. At the mid-southern latitude, an increase of more than 8 TECU is evident. Regarding the formal error of the differences between IGG combined GIM and IGS GIM at 1 UT, taking Fig. 6.18b into account, the RMS differences are all in a negative range. This shows that the IGG combined GIM has a lower RMS and a better accuracy through the whole globe. The global mean value of the RMS difference is -1.7 TECU. This reduction reaches a maximum value of -4 TECU over the ocean area at the southern hemisphere. The minimum reduction of -0.5 TECU in RMS is observed over European region. This obviously coincides with the great number of IGS ground stations located in Europe.

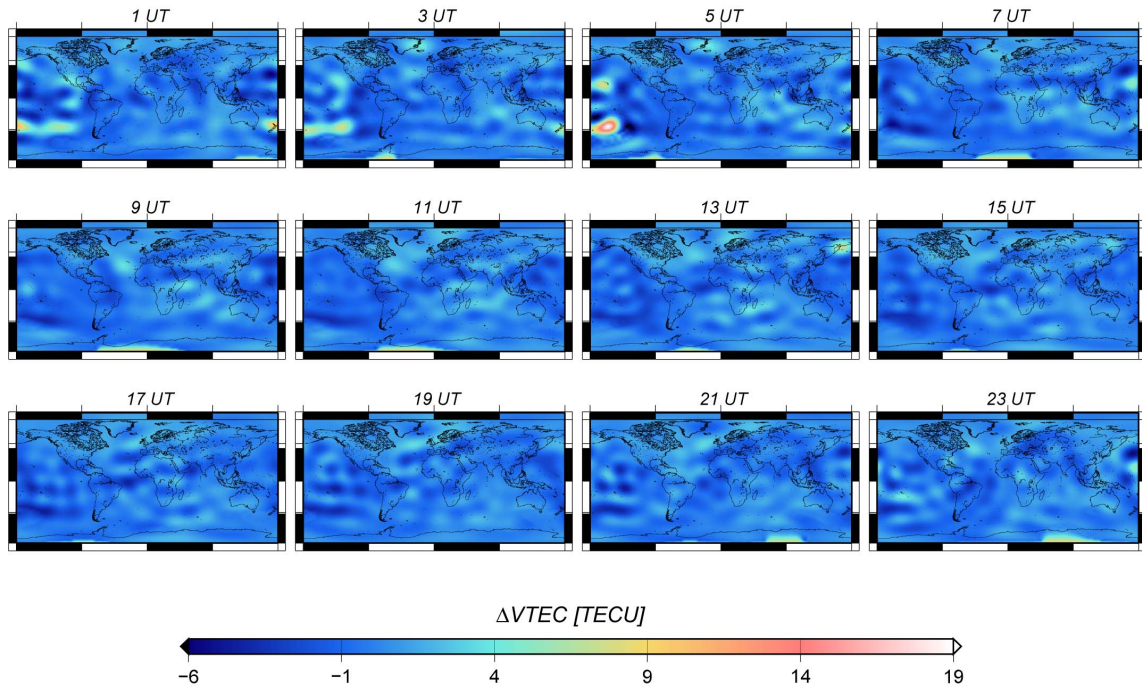


Figure 6.16: VTEC differences between IGG combined minus IGS, for the whole day 190, 2006

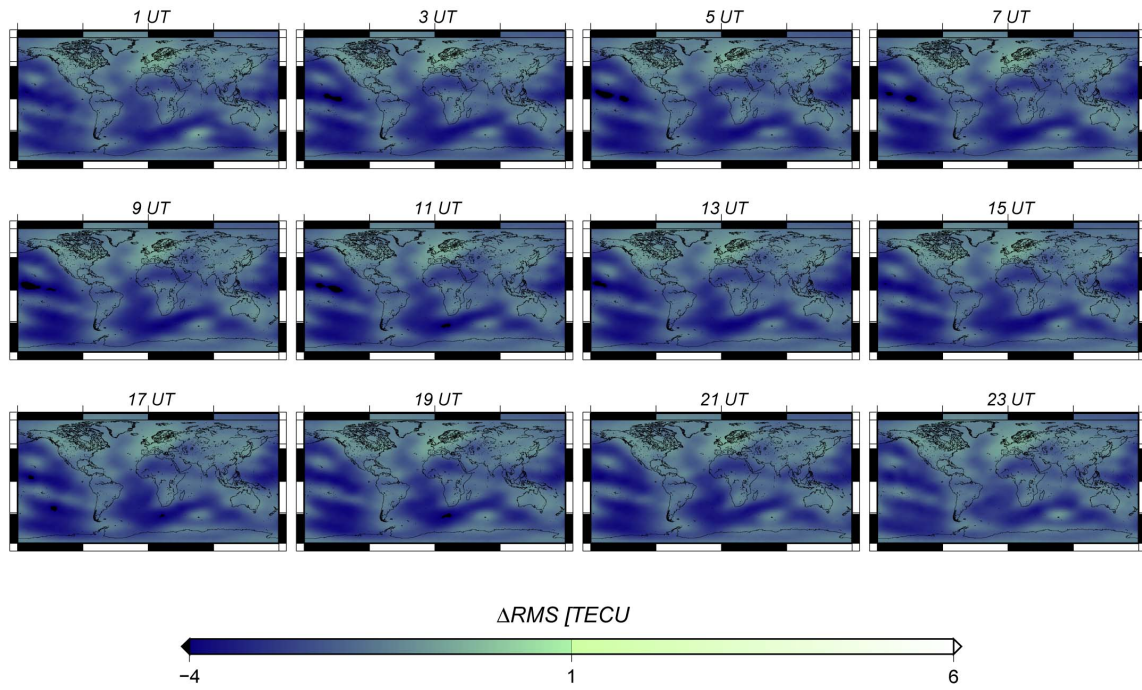


Figure 6.17: RMS differences between IGG combined minus IGS, for the whole day 190, 2006

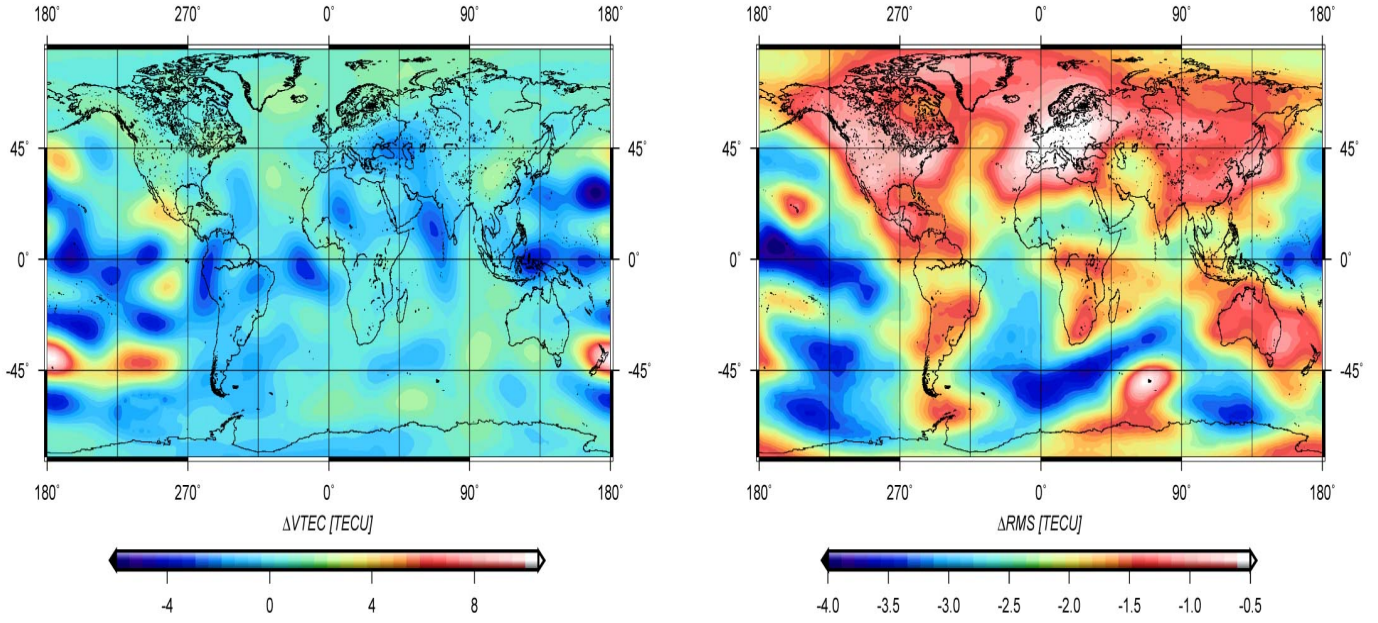


Figure 6.18: **a** VTEC and **b** RMS difference map of GNSS, satellite altimetry, and F/C combined GIM minus IGS GIM for day 190, 2006 - 1 UT

6.1.5 Calibration of GNSS VTEC using satellite altimetry and F/C

For developing combined maps of the ionosphere from different techniques, an essential step is to calibrate the different data sources. Since in our study, we combined GNSS measurements with satellite altimetry and F/C data, in this section we investigate calibrating GNSS VTEC values by satellite altimetry and F/C data. Figure 6.19 illustrates the steps for this procedure schematically.

6.1.5.1 Calculating biases and calibration

To accomplish this task, first the GIM from GNSS-only measurements are developed in a two-hourly basis for the whole day of interest (see Sect. 6.1.2.1). Taking the footprints of satellite altimetry and F/C measurements at each two hour intervals into account (Fig. 6.2 and Fig. 6.3), the VTEC values at those points are extracted from the corresponding GNSS-only GIM.

Now the differences between the extracted VTEC values and the VTEC from satellite altimetry is calculated similar to Eq. 6.1

$$\Delta VTEC_{GIM}^{alt}(\varphi_{alt}, \lambda_{alt}, t_{ref}) = VTEC_{GIM}(\varphi_{alt}, \lambda_{alt}, t_{ref}) - VTEC^{alt}(\varphi_{alt}, \lambda_{alt}, t_{alt}), \quad (6.5)$$

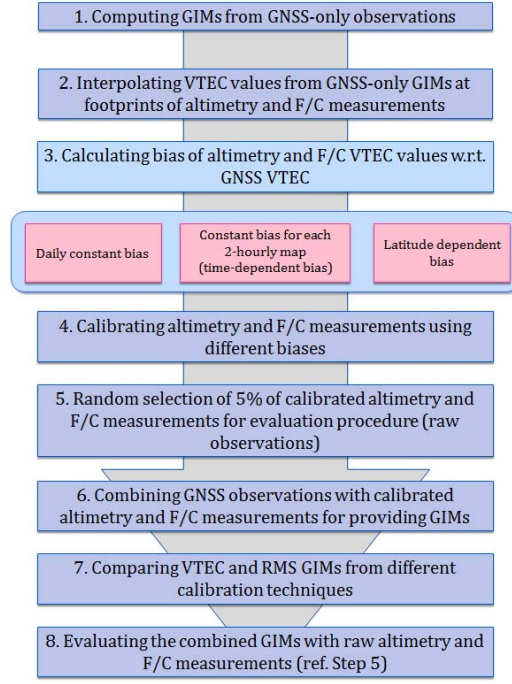


Figure 6.19: Procedure for calibrating GNSS VTEC values by satellite altimetry and F/C data

where

$VTEC_{GIM}$	VTEC extracted from GNSS-only GIM,
$VTEC^{alt}$	VTEC from satellite altimetry data,
$\varphi_{alt}, \lambda_{alt}$	footprint of satellite altimetry,
t_{alt}	time of altimetry measurement, and
t_{ref}	reference epoch of GNSS-only GIM.

The differences between VTEC from GNSS-only GIM and from F/C is computed similarly. These differences are used to calculate the bias between the different observation techniques, and to perform the calibration. The bias is calculated by applying three different strategies, namely

- Daily mean bias
- Time-dependent bias
- Latitude-dependent bias

Daily mean bias In this procedure, the VTEC differences are calculated for all the satellite altimetry measurements through the whole. The bias between GNSS and satellite altimetry VTEC is calculated by making the average of all these differences

$$b_V^{alt} = \frac{\sum \Delta VTEC_{GIM}^{alt}(\varphi_{alt}, \lambda_{alt}, t_{ref})}{N^{alt}}, \quad (6.6)$$

where N^{alt} is the total number of satellite altimetry measurements in a whole day. The bias between GNSS and F/C is calculated in the same way.

Performing the procedure for a sample day of 21 July (doy 202) of 2007, the daily mean bias for the different techniques is given in Table 6.1.

Mean Bias [TECU]

ALT	3.95
F/C	-2.37

Table 6.1: Daily mean bias between GNSS VTEC and satellite altimetry, and F/C measurements for day 202, 2007

Time-dependent bias In this approach, the VTEC differences are calculated between all the satellite altimetry (or F/C) and GNSS VTEC values within each two-hourly map, using Eq. 6.5. The biases are computed by making an average of the differences over each two-hourly time intervals. Writing the equation for satellite altimetry, the bias for each two-hourly map is given by

$$b_V^{alt}(t_{ref}) = \frac{\sum \Delta VTEC_{GIM}^{alt}(\varphi_{alt}, \lambda_{alt}, t_{ref})}{n^{alt}(t_{ref})}, \quad (6.7)$$

where $n^{alt}(t_{ref})$ is the number of altimetry measurements at each two-hourly epoch. The biases for F/C measurements are computed similarly.

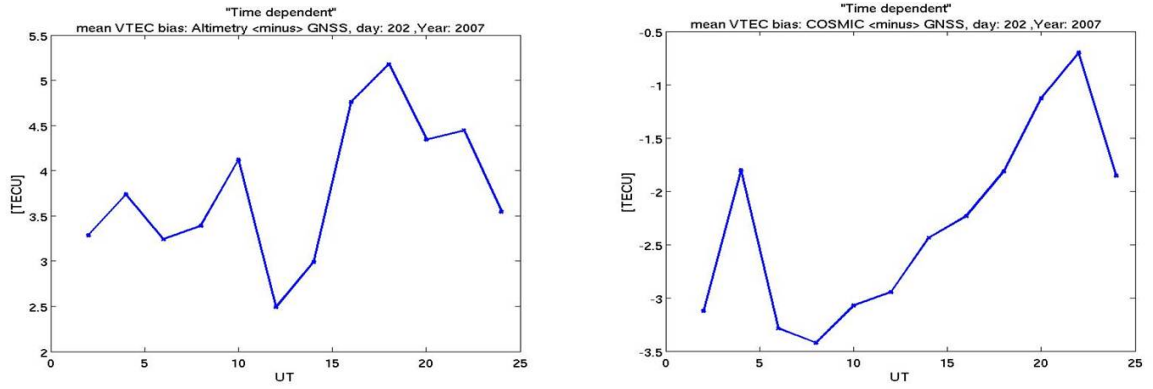
In this procedure, for each two-hourly map we will have one mean bias between GNSS and satellite altimetry VTEC, and one mean bias between GNSS and F/C VTEC. Therefore for the whole day, twelve mean biases for each of the different techniques will be obtained. Table 6.2 presents the time-dependent mean biases between GNSS and satellite altimetry and F/C VTEC values for day 202 of 2007. Figure 6.20a depicts the time-dependent biases between GNSS and satellite altimetry VTEC for day 202, 2007, and Fig. 6.20b shows the same bias between GNSS and F/C measurements for the same day.

Latitude-dependent bias In this procedure, the altimetry and F/C data for the whole day are divided into latitude-dependent segments. For each segment, the differences between

Mean Bias [TECU]

UT	[0,2]	[2,4]	[4,6]	[6,8]	[8,10]	[10,12]	[12,14]	[14,16]	[16,18]	[18,20]	[20,22]	[22,24]
ALT	3.28	3.73	3.24	3.39	4.12	2.49	2.99	4.76	5.17	4.34	4.45	3.46
F/C	-3.12	-1.80	-3.29	-3.42	-3.07	-2.95	-2.43	-2.23	-1.81	-1.13	-0.70	-1.85

Table 6.2: Time-dependent bias between GNSS VTEC and satellite altimetry, and F/C measurements for day 202, 2007


 Figure 6.20: Time-dependent bias between GNSS VTEC and **a** satellite altimetry, and **b** F/C measurements for day 202, 2007

the corresponding VTEC values from GNSS and from satellite altimetry and F/C is calculated separately, and is used for calculating the latitude-dependent biases. For this study, the latitude segment was selected between -80° and 80° with 20° intervals, providing eight different segments. Table 6.3 presents the latitude-dependent biases between GNSS VTEC and satellite altimetry and F/C data for day 202, 2007. Figure 6.21 **a** and **b** depict the latitude-dependent biases between GNSS VTEC and satellite altimetry, and F/C measurements for day 202, 2007.

Mean Bias [TECU]

Latitude	[-80,-60]	[-60,-40]	[-40,-20]	[-20,0]	[0,20]	[20,40]	[40,60]	[60,80]
ALT	10.76	5.76	4.18	2.18	2.75	2.21	3.71	7.36
F/C	-0.59	-1.03	-2.23	-3.94	-4.34	-3.58	-2.27	-1.37

Table 6.3: Latitude-dependent bias between GNSS VTEC and satellite altimetry, and F/C measurements for day 202, 2007

It can be seen in Fig. 6.21**a** that the latitude-bias between GNSS VTEC and satellite altimetry VTEC is larger in high-latitudes, and lower in the equatorial region. This is also

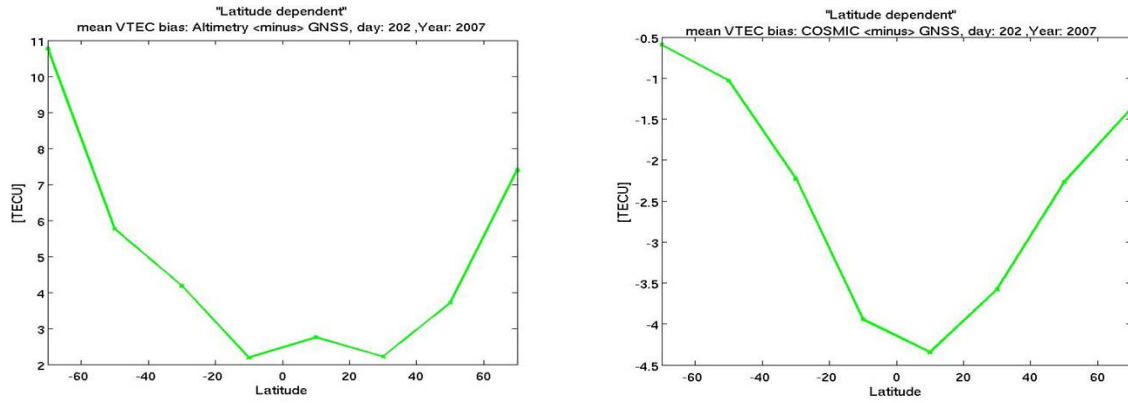


Figure 6.21: Latitude-dependent bias between GNSS VTEC and **a** satellite altimetry, and **b** F/C measurements for day 202, 2007

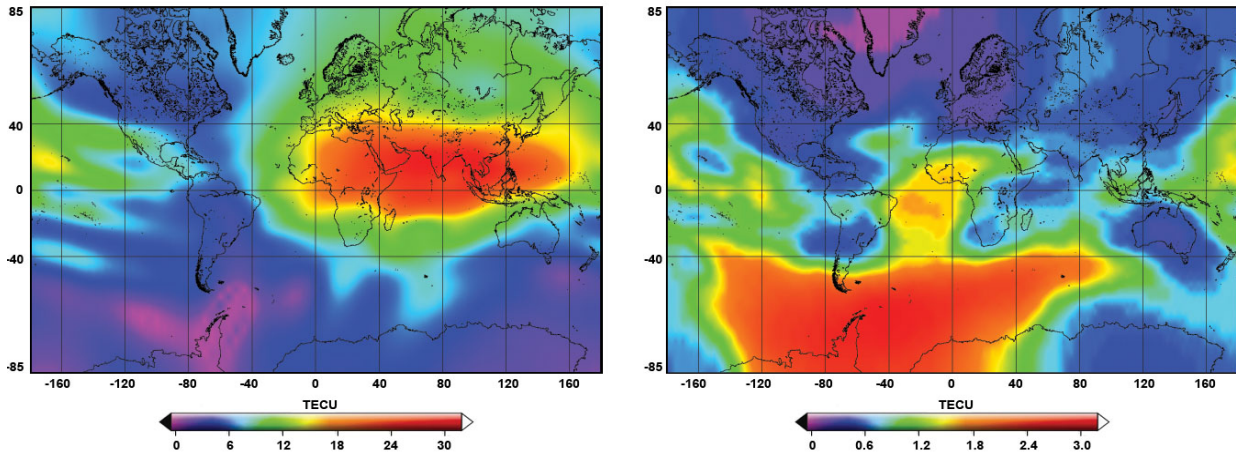


Figure 6.22: **a** VTEC map and **b** RMS map of calibrated GNSS-only solution, day 202, 2007 - 9 UT

evident in Fig. 6.21b which shows similar trend between GNSS VTEC and F/C VTEC. This can be inferred as the pattern which is clearly compatible with the plasmaspheric electron content, since the plasmaspheric contribution is higher in equatorial region than at the poles.

6.1.5.2 Combining calibrated data for developing GIM

The GNSS VTEC values are calibrated with the biases calculated from any of the above mentioned approaches and are used for developing calibrated GIM. The procedure for developing the calibrated maps is similar to the procedure mentioned in Sect. 6.1.2.1; we just use the calibrated data this time. Figure 6.22 illustrates the snapshot of GNSS-only calibrated VTEC and RMS map for day 202 of 2007 at 9 UT.

Now to combine VTEC from satellite altimetry and F/C with GNSS data, first 5% of satellite altimetry and F/C measurements at each two-hourly maps are randomly selected and

set aside. These measurements will later be used for evaluating the developed combined maps (see Sect. 6.1.5.3). The rest of the altimetry and F/C data are included in the combination procedure and the combined GIM is developed as described in Sect. 5.2.1. Figures 6.23 - 6.25 depict snapshots of the difference between the calibrated and non-calibrated VTEC and RMS combined maps from GNSS, satellite altimetry, and F/C measurements for day 202 of 2007 at 9 UT. Figure 6.23 shows the difference of calibrated and non-calibrated VTEC and RMS maps using the mean daily bias calibration approach. Figure 6.24 depicts the VTEC and RMS difference of calibrated minus non-calibrated combined maps using the time-dependent bias calibration approach, and finally Fig. 6.25 shows the same VTEC and RMS map using latitude-dependent bias calibration approach.

To assess the performance of different calibration approaches, the global root mean square (GRMS) of VTEC and RMS difference maps (Figures 6.23 - 6.25) are calculated. The GRMS of the VTEC and RMS map of first approach, i.e. mean daily bias calibration approach for the snapshot 9 UT of day 202 of 2007, is 0.21 *TECU*, and 0.85 *TECU* respectively. The GRMS of VTEC and RMS of time-dependent bias calibration is 0.17 *TECU*, and 0.85 *TECU*; and finally the GRMS of VTEC and RMS of latitude-dependent bias calibration is 0.68 *TECU*, and 0.79 *TECU*. It can be seen that the latitude-dependent GRMS for VTEC differences is the largest (0.68 *TECU*). This indicates that the latitude-dependent calibration approach creates the largest differences to the non-calibrated data comparing to the other calibration approaches. Concerning the GRMS of RMS differences, it can be seen that the latitude-dependent calibration procedure has the least GRMS (0.79 *TECU*). This proves the fact that the latitude-dependent calibration procedures provides the highest accuracy among the different calibration procedures.

6.1.5.3 Quantifying the calibrated GIM with raw data

To quantify the self-consistency of the combined calibrated GIM, the developed maps are quantified with the raw satellite altimetry and F/C data which were not used in the combination procedure (see Sect. 6.1.3). As described before, from each two-hourly maps, 5% of the altimetry and F/C data were set aside and not included in developing the combined maps. These data are referred to as raw altimetry and F/C data. After the combination, the VTEC values are extracted from the combined model at the footprints of the raw data and used to evaluate the developed maps that are obtained from different calibration procedure.

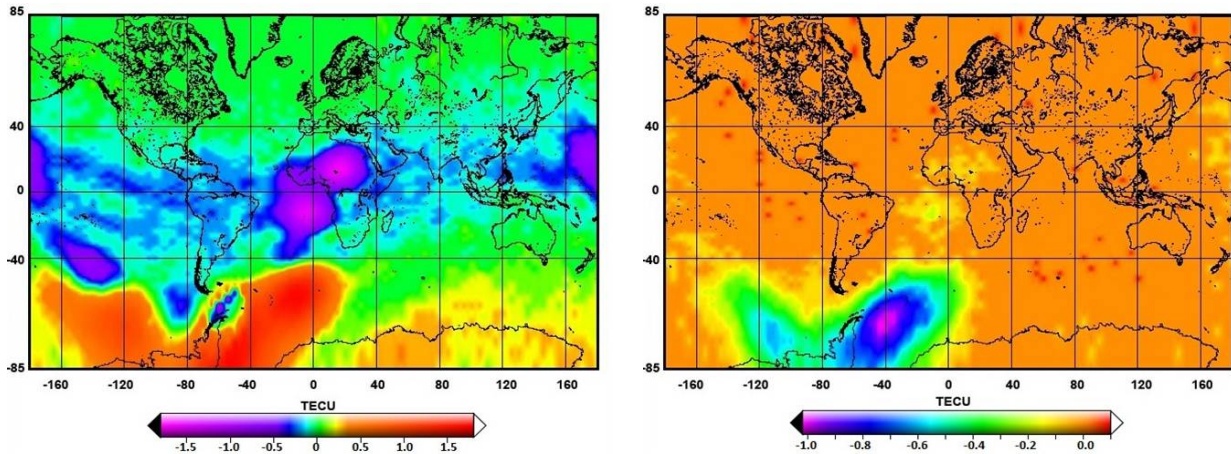


Figure 6.23: Calibrated minus non-calibrated combined **a)** VTEC and **b)** RMS map from GNSS, satellite altimetry and F/C data using mean daily bias for calibration procedure. Snapshot for day 202, 2007 - 9 UT

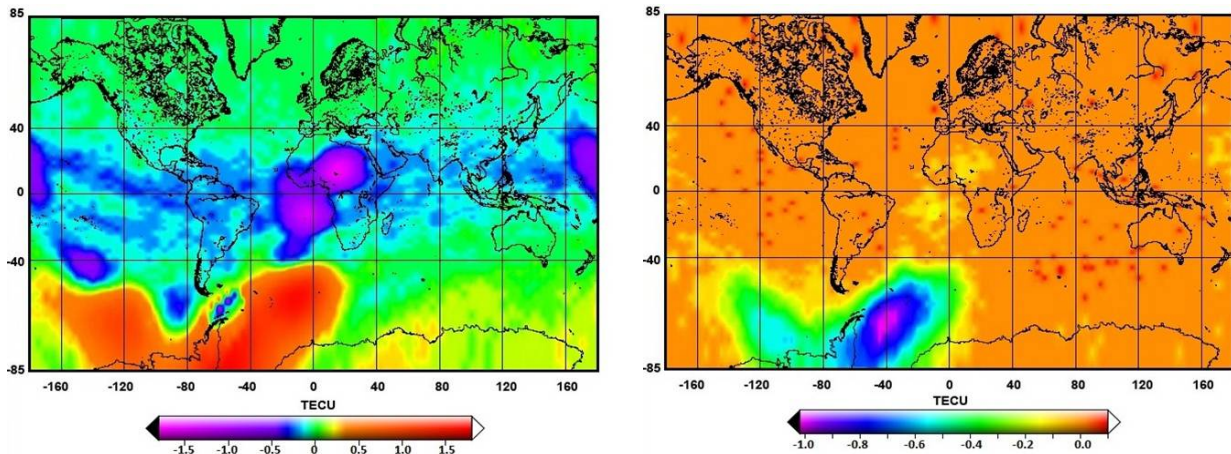


Figure 6.24: Calibrated minus non-calibrated combined **a)** VTEC and **b)** RMS map from GNSS, satellite altimetry and F/C data using time-dependent bias for calibration procedure. Snapshot for day 202, 2007 - 9 UT

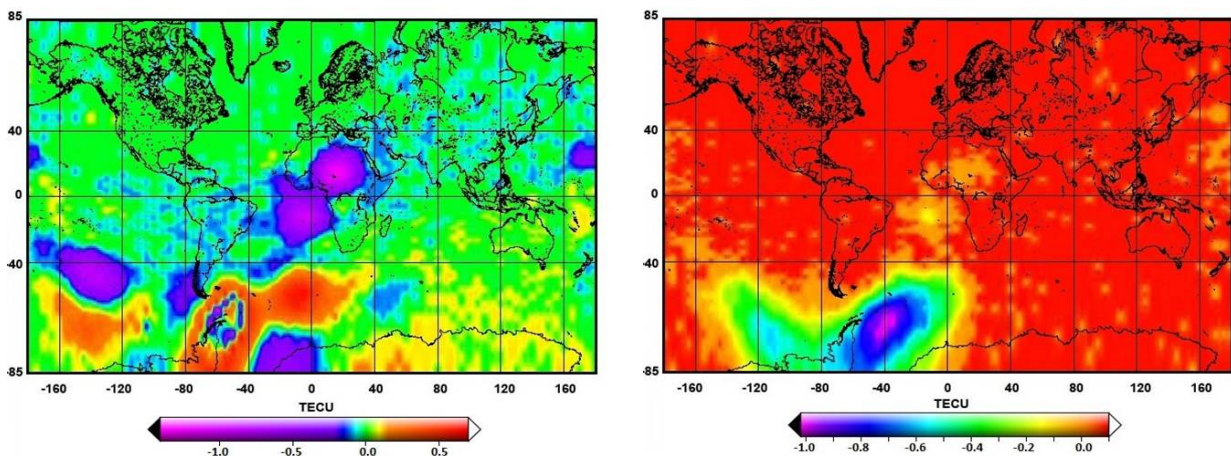


Figure 6.25: Calibrated minus non-calibrated combined **a)** VTEC and **b)** RMS map from GNSS, satellite altimetry and F/C data using latitude-dependent bias for calibration procedure. Snapshot for day 202, 2007 - 9 UT

6.2 Global maps of electron density

Aforesaid in Sect. 5.3, reconstructing ionospheric parameters in three dimensions requires applying appropriate base functions which represent electron density variations in longitude, latitude, and height. For this study, we apply a 2D spherical harmonic expansion for horizontal variabilities. But for the height variability, we use a combination of the multi-layer Chapman profile function Eq. 5.47 and Eq. 5.48 for the bottom-side and topside ionosphere, and the plasmaspheric part of the TIP model Eq. 5.56 for the plasmasphere

$$N_e(h) = N_m e^{\alpha(1-z-e^{-z})} + N_m e^{\beta(1-z-e^{-z})} + N_P e^{(-h/H_P)} . \quad (6.8)$$

with

$$z = \frac{h - h_m}{H} . \quad (6.9)$$

Applying this model, electron density N_e at any point, is obtained by the F2-layer maximum electron density N_m , it's corresponding height h_m , the plasmasphere basis density N_P , and the plasmasphere scale height H_P . Within Eq. 6.8 the bottom-side and topside ionosphere scale height H is assumed to be dependent only on the h_m , and is given by (Feltens, 1998)

$$H = \frac{h_m - 50}{3} , \quad (6.10)$$

where h_m is in km . As a first step for this study, we concentrate only on the ionospheric parameters by assuming the plasmaspheric parameters as known values. Following Jakowski *et al.* (2002a), the value for plasma scale height H_P is fixed at 10,000 km , and the plasmasphere basis density N_P is set equal to the electron density of the highest topside ionosphere, i.e. electron density at the hight of 1,000 km . With this assumption, our unknown parameters will be restricted to N_m and h_m .

As stated in Sect. 5.3.2.3, we use two sets of spherical harmonic expansions to represent the unknown parameters globally. Therefore, the new unknown parameters will be the coefficients of the two sets of spherical harmonic expansion. To achieve a spatial resolution of 2.5° in latitude and 5° in longitude, the degree and order of spherical harmonic expansion is set to 15, and to have a similar temporal resolution as the 2D VTEC maps developed in Sect. 6.1, we split the observations in time span of $2h$. Thus the unknown parameters will be modeled in twelve two-hourly maps for a whole day. Nevertheless, depending on the available observations and the computation time, selecting lower time span is also possible. So applying these conditions we have two time 256 or 512 unknown parameters for each $2h$ map, and for the whole day we will have twelve times 512, or 6,144 unknown parameters. To solve these parameters a Matlab-based software was developed which provides the estimated parameters in 12 two-hourly maps for a complete day solution. For a better understanding

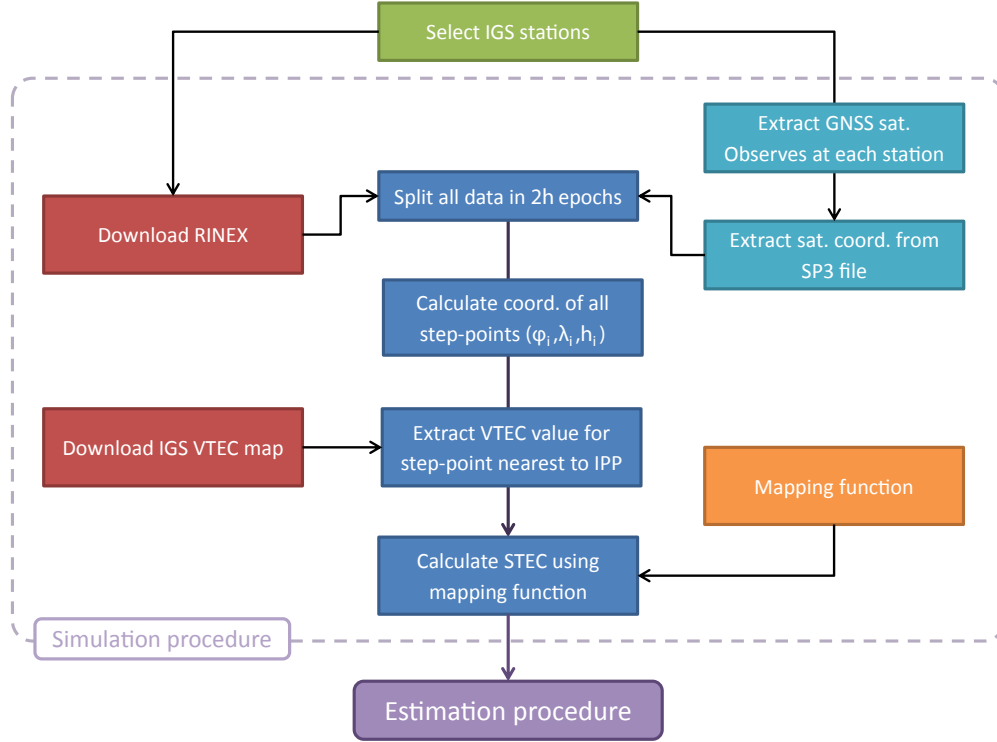


Figure 6.26: Algorithm for simulating input data

of the different steps, Fig. 6.26 illustrates the algorithm for simulating the input data, and Fig. 6.27 shows the algorithm for estimating the unknown parameters.

6.2.1 Simulating GNSS data

Due to the fact that the real observations usually contain uncertainties and random errors, to avoid inconsistencies in the input data and to focus only on the model and the procedure for estimating the unknown parameters, we simulate the GNSS input data.

Recalling Eq. 2.56, STEC is related to VTEC using a mapping function

$$STEC = F(z')VTEC, \quad (6.11)$$

where z' is the satellite zenith angle at IPP. Taking Eq. 5.58 and 5.62 into account and substituting STEC by VTEC from Eq. 6.11 we get

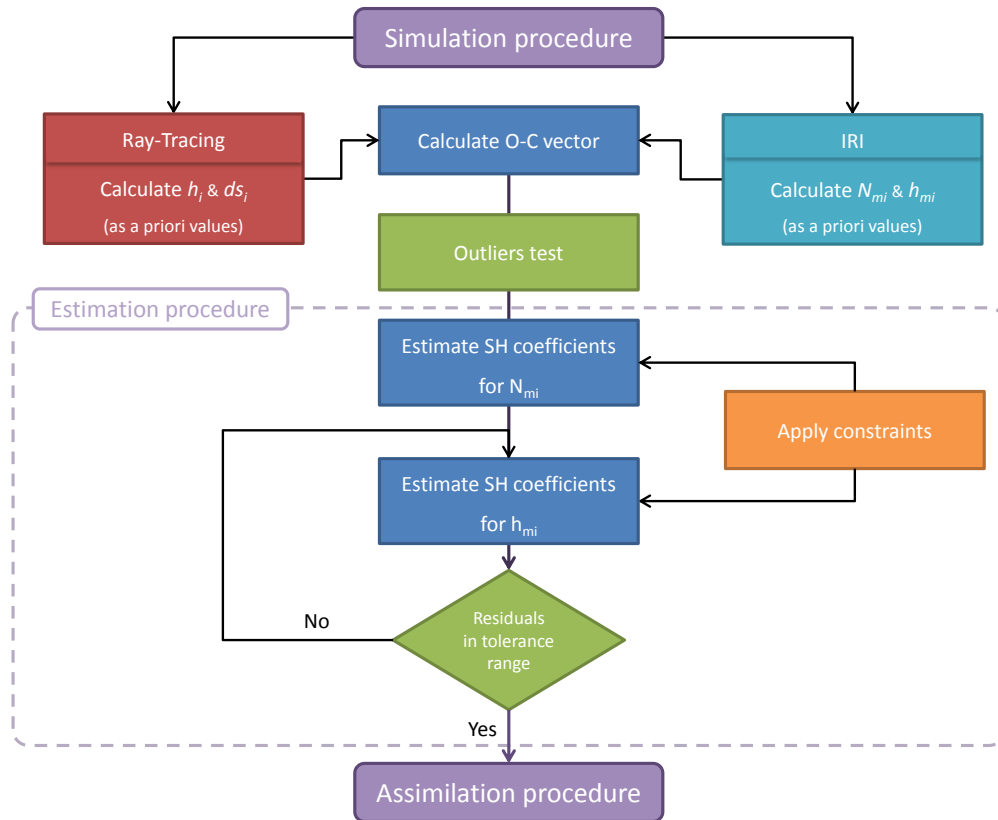


Figure 6.27: Algorithm for Estimating unknown parameters

$$\begin{aligned}\tilde{P}_4 &= \xi F(z') VTEC + c(\Delta b^S - \Delta b_R) + \varepsilon \\ &= \xi \sum_{i=1}^k N_{mi} \cdot e^{\alpha(1 - z_i - e^{-z_i})} ds_i + c(\Delta b^S - \Delta b_R) + \varepsilon ,\end{aligned}\tag{6.12}$$

The terms representing DCB in Eq. 6.12 could be neglected when using simulated VTEC values; so the equation simplifies to

$$F(z') VTEC = \sum_{i=1}^k N_{mi} \cdot e^{\alpha(1 - z_i - e^{-z_i})} ds_i .\tag{6.13}$$

Equation 6.13 is our observation equation for further computations.

6.2.1.1 True position of GNSS satellites

In the first step of simulating input data, GNSS observations from all the selected IGS stations are downloaded from e.g. CDDIS ftp site (CDDIS, 2011) in RINEX format. Splitting the observations into two-hourly time intervals defined previously, the GNSS satellite observed at each IGS stations are determined, and their precise orbital coordinates are extracted from the IGS precise satellite orbits (SOPAC, 2011).

The ray-path between the receiver and satellite is calculated using the coordinates of the stations and the observed satellites at each station. Figure 6.28 depicts the GNSS ray-path observed from approximately 160 IGS stations at day 182, 2010, from 0 to 2 UT.

6.2.1.2 Simulated values from IGS VTEC maps

As the height dependent model selected for this study Eq. 6.8, assumes three different profile functions for bottom-side ionosphere, topside ionosphere, and for the plasmasphere, thus, the step-point heights are selected accordingly.

$$h_{i+1} = h_i + dh_i , \quad i = 1, 2, \dots, k ,\tag{6.14}$$

where

$$dh_i = \begin{cases} 50 \text{ km} & h_i < 250 \text{ km} \\ 100 \text{ km} & 250 \leq h_i < 1,000 \text{ km} \\ 100 \text{ km} & 1,000 \leq h_i \leq 2,000 \text{ km} \end{cases}\tag{6.15}$$

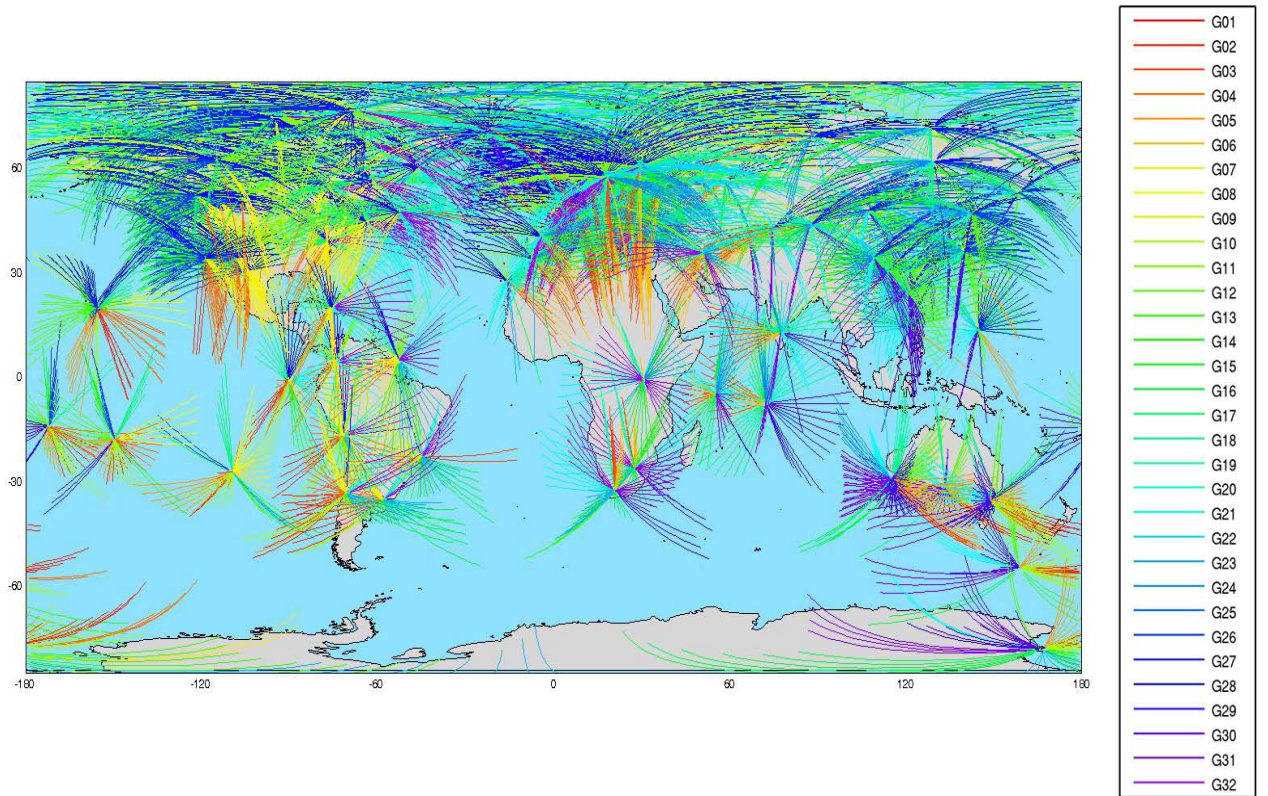


Figure 6.28: Input data with true GNSS ray-path, but simulated values from IGS GIM at day 182, 2010 - $[0,2]$ UT

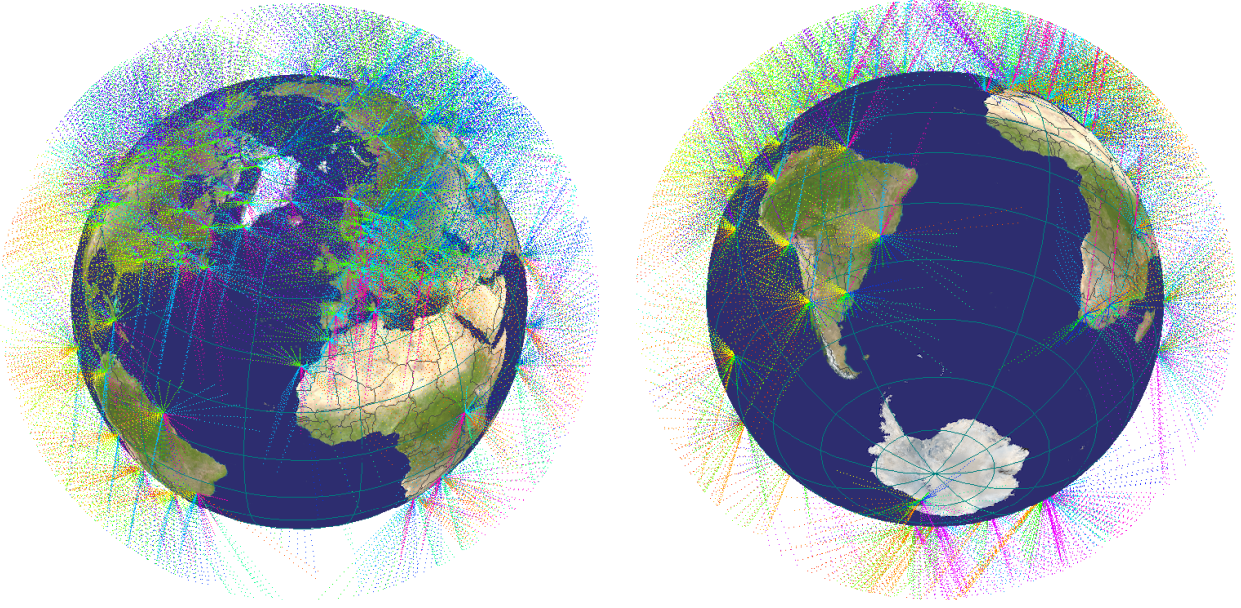


Figure 6.29: Global step-points for simulating input data for stations at **a** Northern, and **b** Southern hemisphere, doy 182, 2010 - [0,2]UT

The height of first layer is set to $h_1 = 50 \text{ km}$, and the plasmaspheric contribution is presumed to be mainly concentrated between $1,000 \text{ km}$ and $2,000 \text{ km}$, therefore the model height is limited to $2,000 \text{ km}$.

After calculating the geocentric heights of the step-points, the coordinates of each step-point is calculated using ray-tracing technique (see Sect. 5.3.3). Therefore, the true positions of all step-points and satellites at each epoch are consequently computed. In the next step, the coordinates of all IPP (with $h = 450 \text{ km}$) are extracted from the step-points of each ray-path, and the VTEC values of these points are calculated from the IGS GIM, using the bi-variate interpolation, explained in Sect. 4.3.1.2. Finally STEC is derived by mapping VTEC to the slant path using Eq. 6.11. The computed STEC serves as the simulated observation for Eq. 6.13.

Figure 6.29 depict the step-points at a sample day of 1st July, 2010 (doy 182) - [0,2]UT for the Northern and Southern hemisphere respectively.

6.2.2 Calculating a priori values

The observation equation Eq. 6.13 contains several parameters which their a priori values should be known prior to the estimation procedure. As mentioned in Sect. 5.3.3, the slope distance between the closest step-points ds_i , and the geocentric height of the step-points h_i are calculated using ray-tracing technique. Within this study, the software package for performing ray-tracing calculations were developed by Dr. Dudy D. Wijaya. The package

is declared from the main function, and after carrying out the calculations, its results are appended to the station-wise information for further computations.

The a priori values for the initial unknown parameters, i.e. N_{mi} and h_{mi} in Eq. 6.13 are calculated using the IRI-2012 model (Bilitza *et al.*, 2011). IRI-2012 is included as a software package, distributed by the National Space Science Data Center (NSSDC), accessible online via IRI website (VITMO Virtual Ionosphere, 2012), or in Fortran source code, downloadable via NSSDC's anonymous ftp site (NSSDC, 2012). In this study, a Matlab function is developed which writes the necessary input data for the IRI code into a text file and then provokes the IRI-2012 Fortran code function. After performing the calculations by the IRI package, the function extracts the calculated N_m and h_m values from IRI output file (i.e. fort.7).

Figure 6.30 represents the a priori values of N_m from IRI-2012 model in a global grid-wise representation for the sample day 182, 2010, between 0 and 2 UT. Figure 6.31 depicts the corresponding height of maximum electron density at the same day.

6.2.3 Performing outliers test

Although our input data is provided through a simulation procedure, due to the necessity of using a priori values provided by ray-tracing technique and the IRI model, there might exist some observations which are considered statistically incompatible with the rest of the series. This in turn makes the performance of outliers test essential.

As mentioned in e.g. Pope (1967) or Vaníček & Krakiwsky (1982), the assessment of individual observations is restricted by the assumption of normality. This means that the residuals of the input data in Eq. 6.13 is assumed to have a normal distribution function with the mean \bar{r} and standard deviation s , i.e.

$$r \sim \mathcal{N}(\xi; \bar{r}, s^2) . \quad (6.16)$$

Since the aim is to find the cut-off points from which the standardized residuals should be rejected, the probability statement would correspondingly be

$$pr\left(\xi_{y, \frac{\alpha}{2}} < y < \xi_{y, 1-\frac{\alpha}{2}}\right) = 1 - \alpha , \quad (6.17)$$

with y indicating the statistic

$$y = \frac{r - \bar{r}}{\sqrt{\frac{n-1}{n}} s} , \quad (6.18)$$

where n is the total number of observations, and α denoting the probability level.

Taking the above probability statement into account, the $1 - \alpha$ confidence interval for the quantity being tested, reads

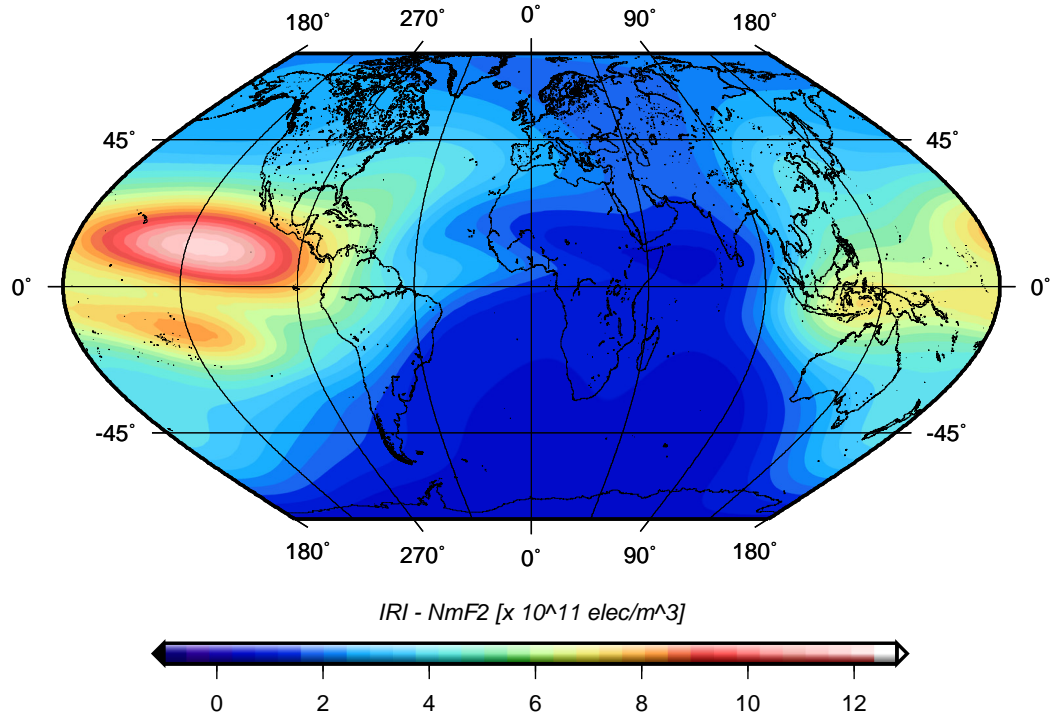


Figure 6.30: Maximum electron density (elec/m^3) from IRI-2012 model for day 182, 2010 - [0,2]UT, used as a priori value for estimating \hat{N}_m

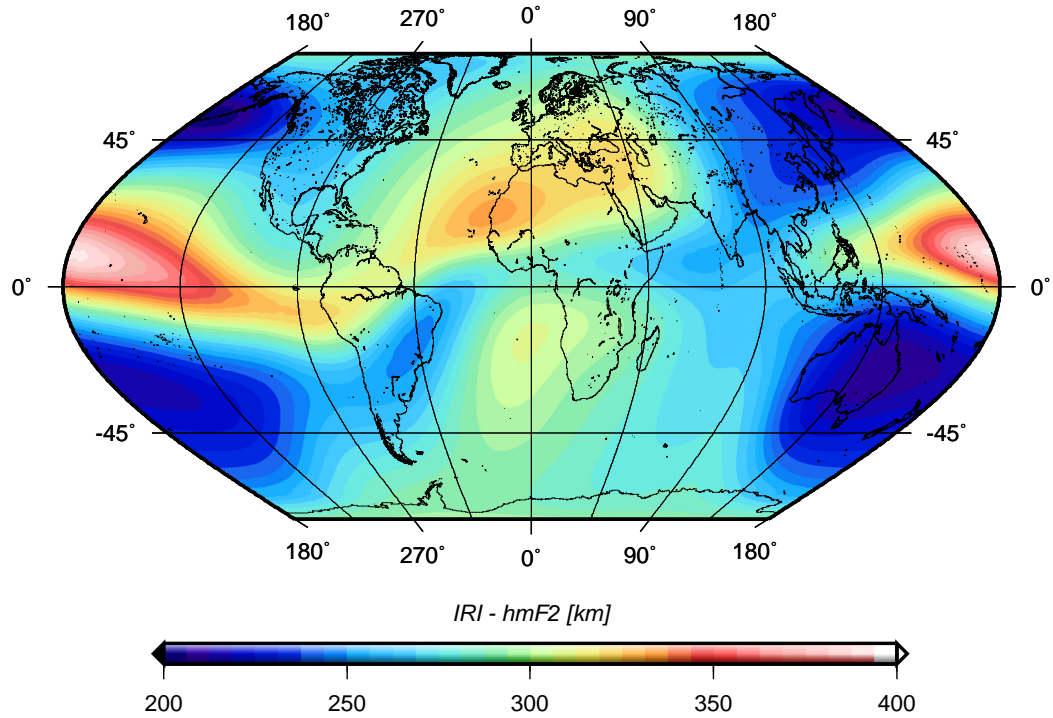


Figure 6.31: Height of maximum electron density (km) from IRI-2012 model for day 182, 2010 - [0,2]UT, used as a priori value for estimating \hat{h}_m

$$\bar{r} - \sqrt{\frac{n-1}{n}} s \xi_{\tau_{n-1}, 1-\frac{\alpha}{2}} < r_i < \bar{r} + \sqrt{\frac{n-1}{n}} s \xi_{\tau_{n-1}, 1-\frac{\alpha}{2}} . \quad (6.19)$$

$\xi_{\tau_{n-1}, 1-\frac{\alpha}{2}}$ indicates the probability density function $\tau(\xi; n-1)$ with $n-1$ degree of freedom (Pope, 1967). For more details on the outliers test, refer to Vaníček & Krakiwsky (1982).

Within our study, the outliers test was performed with the probability level $\alpha = 5\%$, resulting a confidence level of 95%. From the total number of 5,183 input data, 258 were rejected after the outliers test. Figure 6.32 shows the residuals before the test and the confidence intervals. Figure 6.33 depicts the residuals after performing the outliers test.

6.2.4 Least-squares estimation of the unknown parameters

Following Sect. 5.3.5, the least-squares estimation of the unknown parameters, namely the coefficients of two sets of spherical harmonic expansion is applied to the simulated input data Eq. 6.13. As we have two sets of unknown parameters, we accomplish the estimation procedure in two steps. In the first step, we assume h_m as a known parameter by using its a priori values from IRI-2012 model, and estimate the spherical harmonic coefficients related to N_m only. As the observation equation Eq. 6.13 is linear with respect to N_m , there is no need for iteration, and the coefficients are obtained after performing the least-squares adjustment only once. The estimated coefficients are then used to calculate the estimated \hat{N}_m values, which will be assumed as a known parameter for the next step.

In the next step the coefficients related to h_m are estimated. For this, the estimated \hat{N}_m values from previous step are replaced with their a priori values from IRI. The estimation is accomplished in an iterative procedure, as the observation equation Eq. 6.13 is non-linear with respect to h_m . After each iteration, the estimated coefficients are used for calculating the estimated \hat{h}_m values. The estimated residuals \hat{r} (in *TECU*) are also calculated at each iteration using Eq. 5.10. If the absolute value of the estimated residuals was larger than the tolerance range, the estimated observation vector \hat{l} is calculated and the next iteration is performed; if not, then the iteration is stopped and the estimated \hat{h}_m is taken as the final result. Within this study, the tolerance range was empirically set to 2 *TECU*.

6.2.4.1 Global mean constraint

Aforesaid in Sect. 5.1.2, it is often necessary to constrain the unknown parameters by a certain extent. Within this study, several constraints were applied. As the unknown parameters N_m and h_m are presented by spherical harmonic expansion Eq. 5.64 and 5.65, we apply a global mean constraint when estimating N_m and h_m values. Recalling Eq. 4.14, it was shown that the global mean value of the parameter expressed by the spherical harmonic expansion is generally represented by the zero-degree spherical harmonic coefficient. So we

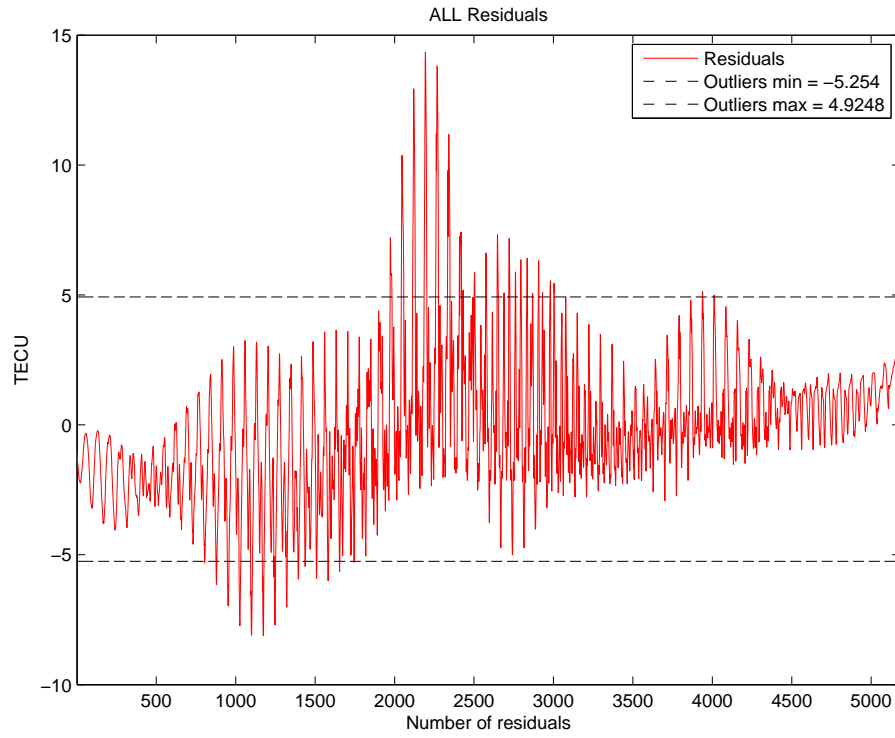


Figure 6.32: Residuals of input data before performing the outliers test and the confidence intervals for day 182, 2010 - $[0,2]$ UT

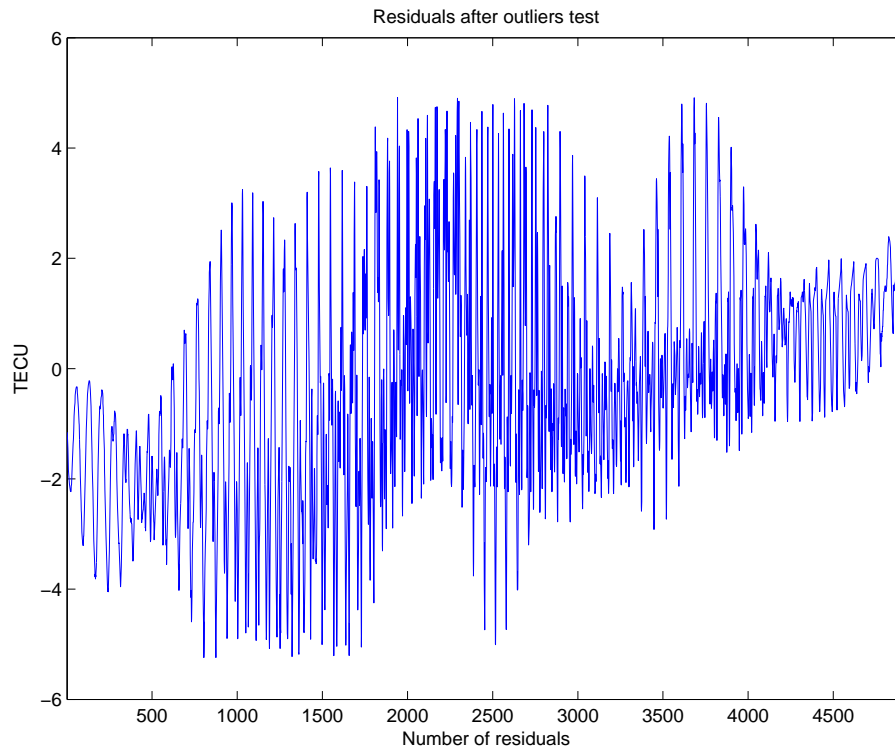


Figure 6.33: Residuals of input data after performing the outliers test for day 182, 2010 - $[0,2]$ UT

can write

$$\bar{N}_m = a_{00} \quad \text{and} \quad \bar{h}_m = a'_{00}, \quad (6.20)$$

where \bar{N}_m and \bar{h}_m are the mean value of the global N_m and h_m distribution. a_{00} is the zero-degree spherical harmonic coefficient for representing N_m and a'_{00} the zero-degree spherical harmonic coefficient for representing h_m . So in this study, using the a priori values from the IRI model, the mean values of N_m and h_m in global distribution is calculated

$$\bar{N}_m^{IRI} = \sum \frac{N_m^{IRI}}{n}, \quad (6.21)$$

$$\bar{h}_m^{IRI} = \sum \frac{h_m^{IRI}}{n}, \quad (6.22)$$

where $\bar{N}_m^{IRI}, \bar{h}_m^{IRI}$ the peak parameters from IRI model at the simulated points, and
 n number of global peak parameters.

We now apply the constraints to our model using Eq. 6.21 and 6.22

$$a_{00} = \bar{N}_m^{IRI}, \quad (6.23)$$

$$a'_{00} = \bar{h}_m^{IRI}. \quad (6.24)$$

So the coefficients matrix A_2 and the constraint vector W_2 in Eq. 5.15 for estimating e.g. N_m would be

$$A_2 = \begin{bmatrix} 1 & 0 & 0 & \cdots & 0 \end{bmatrix}, \quad (6.25)$$

$$W_2 = \begin{bmatrix} \bar{N}_m^{IRI} \end{bmatrix}. \quad (6.26)$$

A_2 in Eq. 6.25 is a (1×256) matrix and W_2 in Eq. 6.26 a scalar. Now setting-up the constrained least-squares system Eq. 5.15, the estimated unknown parameters, which are the spherical harmonic coefficients a_{nm} and b_{nm} are estimated using Eq. 5.18 - 5.20. Similar

procedure is implemented for constrained estimation of h_m parameters.

6.2.4.2 Surface function constraint

To bound the variations of the estimated parameters, a surface function can be applied as a constraint to the observation equation system. The surface function forces the estimated parameters to get values in a predefined range. Since the surface function affects non-linear parameters, we apply this constraint for estimating h_m values only. According to Feltens (1998), h_0 can be expressed as

$$h_0 = \xi(x, y) = h_{0_{min}} + \frac{h_{0_{max}} - h_{0_{min}}}{2} \left(1 + \sin(f(x, y)) \right), \quad (6.27)$$

with

$h_0 = h_m \sec \chi$ height of maximum electron density at noon (i.e. $\chi = 0^\circ$),

χ solar zenith angle, and

$h_{0_{max}}, h_{0_{min}}$ predefined range for h_0 variations.

Feltens (1998) proposed $h_{0_{min}} = 400 \text{ km}$, and $h_{0_{max}} = 450 \text{ km}$. Within this study, we assume a wider range by applying

$$\begin{aligned} h_{0_{min}} &= 200 \text{ km} \\ h_{0_{max}} &= 550 \text{ km} . \end{aligned} \quad (6.28)$$

The inner *sin*-function in Eq. 6.27 is expressed by

$$f(x, y) = c \sin(x + y) + \nu_x \sin^2 x \cos x + \mu_x \sin x \cos^2 x + \nu_y \sin^2 y \cos y + \mu_y \sin y \cos^2 y, \quad (6.29)$$

where

$c = 0.001$ small numerical constant,

$x = \varphi_m$ geomagnetic latitude, and

$y = \tau/2$ local time.

In Eq. 6.29 ν_x , μ_x , ν_y , and μ_y are four coefficients which should be solved prior to applying the constraint. The \sin -function in Eq. 6.29 restricts the output values to a range of $[-1, 1]$, and the inner function $f(x, y)$, removes the effect of 2π period of \sin -function, which could make the convergence unstable.

Solving coefficients of \sin -function

To solve the four coefficients of the \sin -function in Eq. 6.29, we rearrange Eq. 6.27 to express $f(x, y)$ explicitly

$$f(x, y) = \arcsin \left(2 \frac{h_0 - h_{0_{min}}}{h_{0_{max}} - h_{0_{min}}} - 1 \right), \quad (6.30)$$

substituting h_0 by h_m we get

$$f(x, y) = \arcsin \left(2 \frac{h_m \sec \chi - h_{0_{min}}}{h_{0_{max}} - h_{0_{min}}} - 1 \right). \quad (6.31)$$

We select four sample points in globe and calculate their x , y , χ , and h_m values from the IRI model. Assigning Eq. 6.29 and Eq. 6.31 for each of these points, we obtain a linear equation system of four equations, and four unknowns.

$$\left\{ \begin{array}{l} \nu_x \sin^2 x_1 \cos x_1 + \mu_x \sin x_1 \cos^2 x_1 + \nu_y \sin^2 y_1 \cos y_1 + \mu_y \sin y_1 \cos^2 y_1 = \\ \arcsin \left(2 \frac{h_{m_1} \sec \chi_1 - h_{0_{min}}}{h_{0_{max}} - h_{0_{min}}} - 1 \right) - c \sin(x_1 + y_1) \\ \nu_x \sin^2 x_2 \cos x_2 + \mu_x \sin x_2 \cos^2 x_2 + \nu_y \sin^2 y_2 \cos y_2 + \mu_y \sin y_2 \cos^2 y_2 = \\ \arcsin \left(2 \frac{h_{m_2} \sec \chi_2 - h_{0_{min}}}{h_{0_{max}} - h_{0_{min}}} - 1 \right) - c \sin(x_2 + y_2) \\ \nu_x \sin^2 x_3 \cos x_3 + \mu_x \sin x_3 \cos^2 x_3 + \nu_y \sin^2 y_3 \cos y_3 + \mu_y \sin y_3 \cos^2 y_3 = \\ \arcsin \left(2 \frac{h_{m_3} \sec \chi_3 - h_{0_{min}}}{h_{0_{max}} - h_{0_{min}}} - 1 \right) - c \sin(x_3 + y_3) \\ \nu_x \sin^2 x_4 \cos x_4 + \mu_x \sin x_4 \cos^2 x_4 + \nu_y \sin^2 y_4 \cos y_4 + \mu_y \sin y_4 \cos^2 y_4 = \\ \arcsin \left(2 \frac{h_{m_4} \sec \chi_4 - h_{0_{min}}}{h_{0_{max}} - h_{0_{min}}} - 1 \right) - c \sin(x_4 + y_4) \end{array} \right. \quad (6.32)$$

By solving this linear equation system, the four unknown coefficients of Eq. 6.29, i.e. ν_x , μ_x ,

ν_y , and μ_y are obtained.

Applying the constraint to the observation equation system

After solving the four coefficients of the *sin*-function, we now apply the *sin*-surface function Eq. 6.27 to our observation equation system Eq. 5.65

$$\sum_{n=0}^{n_{max}} \sum_{m=0}^n \tilde{P}_{nm}(\sin \beta) (a'_{nm} \cos(ms) + b'_{nm} \sin(ms)) = \left(h_{0min} + \frac{h_{0max} - h_{0min}}{2} \left(1 + \sin(f(x, y)) \right) \right) \cos \chi . \quad (6.33)$$

When applying this equation, care must be taken concerning the correspondence of the notations β and s , and x and y . Following Sect. 5.1.2 the coefficient matrix A_2 and the vector matrix w in Eq. 5.15 are formed for the constrained observation equation system Eq. 6.33, and the unknown parameters, which are the spherical harmonic coefficients a'_{nm} and b'_{nm} for estimating h_m , are calculated using Eq. 5.18 - 5.20.

6.2.5 Assimilating the estimated parameters

After estimating the unknown coefficients of two sets of spherical harmonic expansion, the final unknown parameters (i.e. \hat{N}_m and \hat{h}_m) are calculated using Eq. 5.64 and 5.65. \hat{N}_m and \hat{h}_m are then assimilated in a global grid-wise distribution with a spatial resolution of 2.5° in latitude and 5° in longitude, and temporal resolution of $2h$. Figure 6.36 depicts the global grid-wise values of the estimated \hat{N}_m for the sample day 182 of 2010 at $[0, 2]UT$. Figure 6.35 shows the corresponding \hat{h}_m values.

To illustrate a better understanding of the estimated electron density parameters, the related \hat{N}_m and \hat{h}_m values shown in Fig. 6.36 and 6.35 are depicted in a 3D conjunction plot.

6.2.6 Assessment of the estimated parameters

The estimated \hat{N}_m and \hat{h}_m are assessed through different procedures. First the accuracy of the estimated values from least-squares adjustment is evaluated using their standard deviation values. Then the estimated values are compared with the maximum electron density and corresponding height of maximum electron density derived from the IRI model. Finally the estimated values are compared with the \hat{N}_m and \hat{h}_m derived from the F/C measurements.

6.2.6.1 Evaluating the accuracy of developed maps

Following Sect. 5.1.4, the standard deviation values for \hat{N}_m and \hat{h}_m are calculated using Eq. 5.28. The calculated values are illustrated as global grid-wise maps with the same spatial resolution of 2.5° in latitude and 5° in longitude, and temporal resolution of $2h$. Figure 6.37

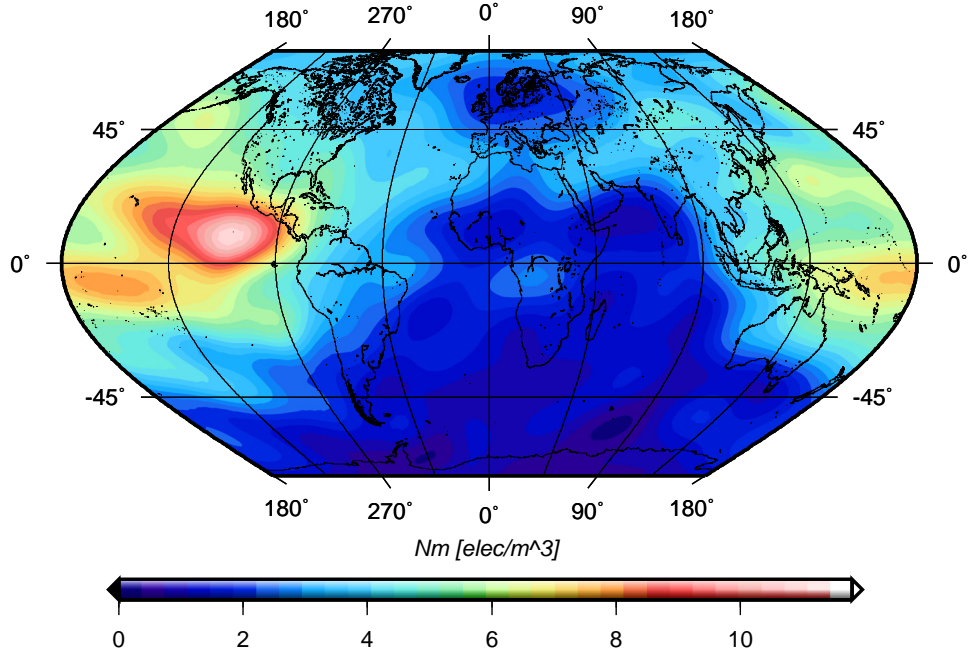


Figure 6.34: Estimated maximum electron density ($\times 10^{11} \text{elec}/\text{m}^3$) for day 182, 2010 - [0,2]UT

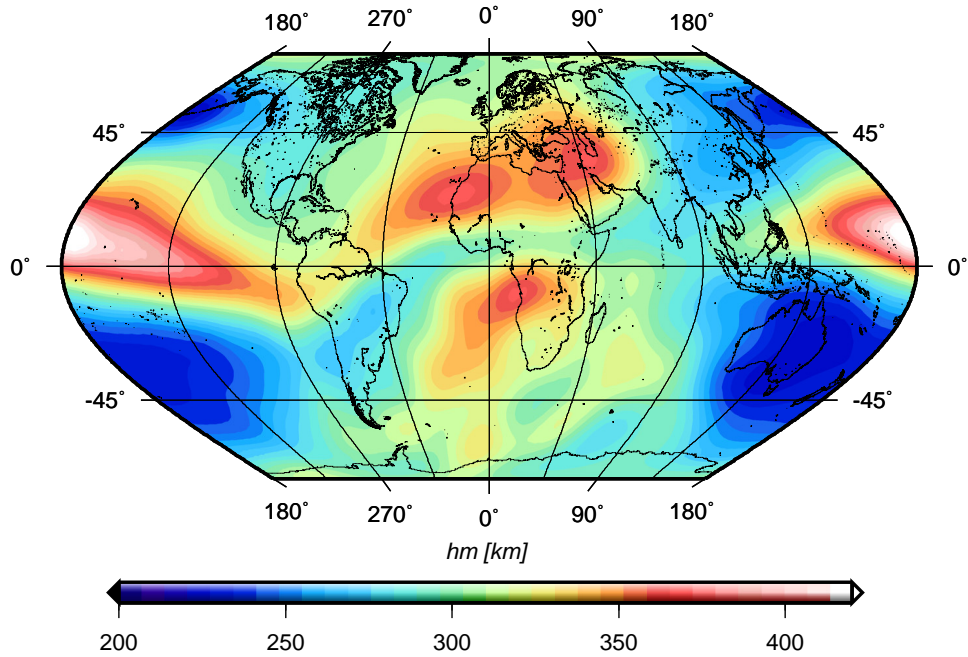


Figure 6.35: Estimated maximum electron density height (km) for day 182, 2010 - [0,2]UT

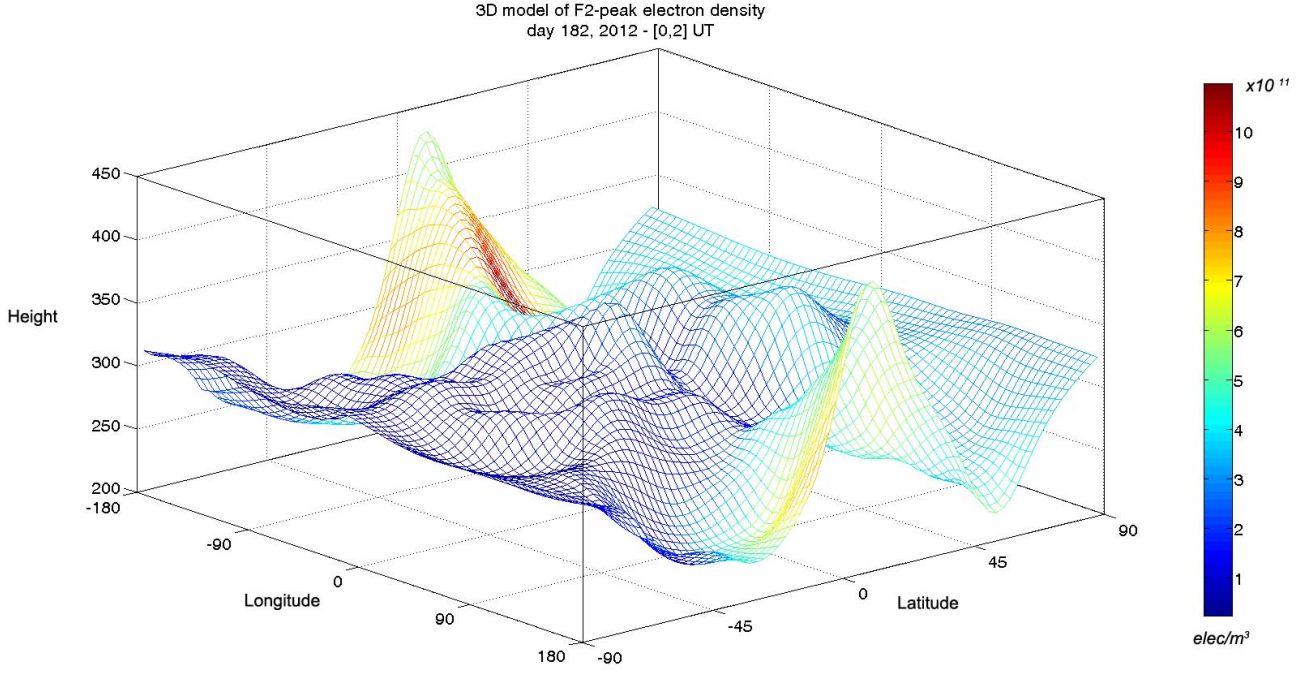


Figure 6.36: 3D model of F2-peak electron density for day 182, 2010 - [0,2]UT; color bar indicates the maximum electron density ($\times 10^{11} \text{ elec/m}^3$) and the Z-axis indicates maximum electron density height in km

depicts the RMS map of \hat{N}_m for day 182 of 2010, at [0,2]UT. Figure 6.38 shows the RMS map of \hat{h}_m for the same day.

Taking Fig. 6.37 into account, the RMS of estimated electron density \hat{N}_m at day 182, 2010, [0,2]UT, varies between $1.019 \times 10^{10} \text{ elec/m}^3$ and $4.093 \times 10^{10} \text{ elec/m}^3$ globally, with a mean of $2.587 \times 10^{10} \text{ elec/m}^3$, and standard deviation of $7.080 \times 10^9 \text{ elec/m}^3$. The highest RMS values, corresponding to the lowest accuracy of estimated \hat{N}_m can be seen at southern mid-latitude region, at the outer skirts of the highest maximum electron density values for this especial time interval, i.e. between 0 and 2UT (see Fig. 6.36).

Considering the height of maximum electron density (Fig. 6.38), the RMS of estimated \hat{h}_m at the same time interval, varies between 0.021 km and 0.327 km in the whole globe, with a mean value of 0.104 km and standard deviation of 0.079 km . Taking Fig. 6.38 into account, the highest RMS values (corresponding to lowest estimation accuracy) are detected at the mid and high southern latitudes. Further discussions would follow after comparing the estimated \hat{N}_m and \hat{h}_m maps with the IRI model.

6.2.6.2 Comparison with the IRI model

In this section, the estimated values \hat{N}_m and \hat{h}_m are compared with the maximum electron density and the height of maximum electron density derived from the IRI model. Since

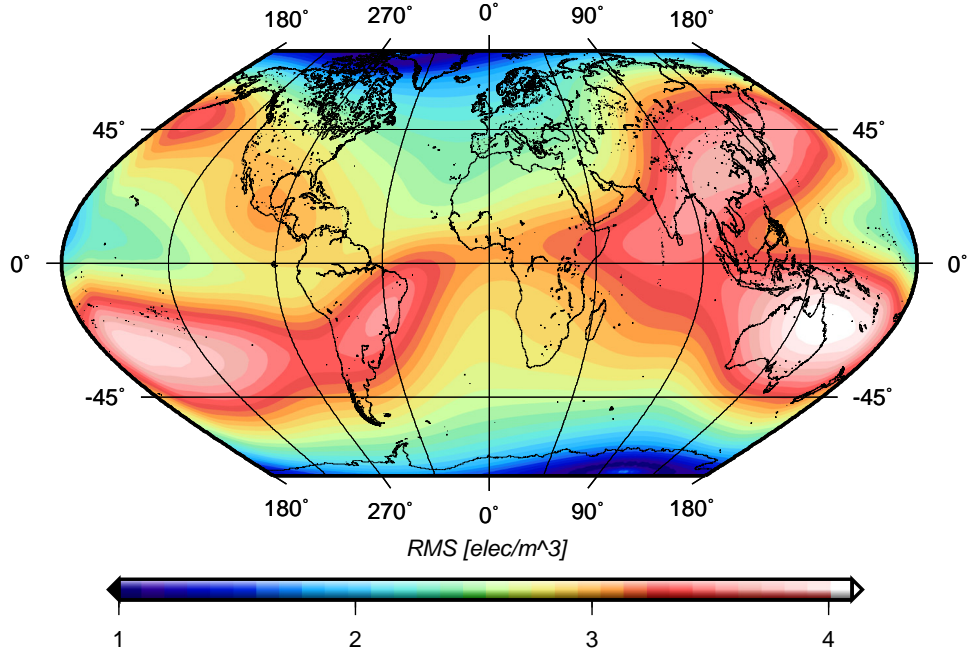


Figure 6.37: RMS map of estimated maximum electron density ($\times 10^{10} \text{elec}/\text{m}^3$) for day 182, 2010 - $[0,2]\text{UT}$

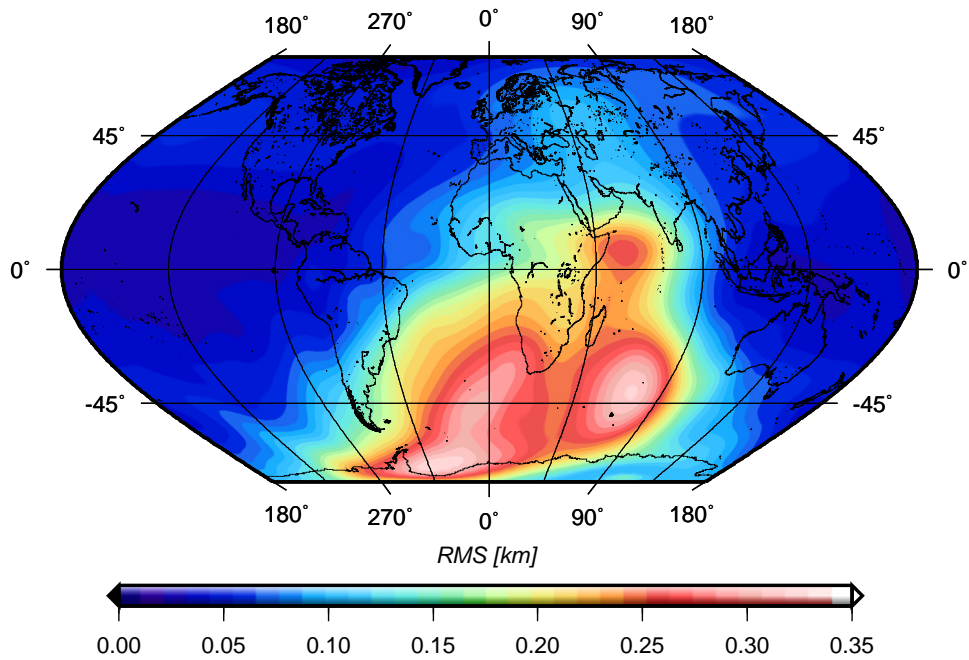


Figure 6.38: RMS map of estimated maximum electron density height (km) for day 182, 2010 - $[0,2]\text{UT}$

the IRI model is used as the a priori values in the estimation procedure, performing this comparison can provide information about the estimation procedure itself. Figure 6.39 depicts the difference map between the estimated maximum electron density \hat{N}_m and the maximum electron density derived from the IRI-2012 model for day 182, 2010 - [0,2] UT. Figure 6.40 depicts the difference of maximum electron density height between our estimation procedure, and the IRI-2012 model.

Figure 6.41a depicts the estimated maximum electron density (in blue curve), and the maximum electron density derived from IRI (red curve). Figure 6.41b illustrates the residuals of estimated minus IRI, which is the difference between the blue and the red curve in Fig. 6.41a. Figure 6.42a and b show the same plots for maximum electron density height.

Taking Fig. 6.41a into account, the mean value of estimated maximum electron density (blue curve) is $3.081 \times 10^{11} \text{ elec}/\text{m}^3$, with standard deviation of $1.948 \times 10^{11} \text{ elec}/\text{m}^3$. The mean value from the IRI model (red curve) is $2.683 \times 10^{11} \text{ elec}/\text{m}^3$, with a standard deviation of $2.137 \times 10^{11} \text{ elec}/\text{m}^3$. Making the difference between the two curves, represents the deviation of the two methods depicted in Fig. 6.41b. As it can be seen from Fig. 6.41b, the mean value of deviations of the estimated minus IRI is positive and equal to $0.3975 \times 10^{11} \text{ elec}/\text{m}^3$. This indicates that our estimation procedure provides higher values for maximum electron density through the whole globe, for the sample day of 182, 2010 - [0,2]UT.

Considering the height of maximum electron density (Fig. 6.42a and b), the mean value of the estimated maximum electron density height (blue curve) in Fig. 6.42a, is 298.5 km , with standard deviation of 33.67 km . The mean value from the IRI model (red curve) is 276.1 km , with a standard deviation of 30.58 km . This indicates that our model-approach provides higher and more scattered results, compared to the values obtained from the IRI model. Taking Fig. 6.42b into account, the deviations of estimated minus IRI maximum electron density height, have a mean value of 22.43 km with a standard deviation of 9.768 km .

This behavior is somehow expectable as the IRI model is monthly averaged forecasting model, therefore it provides smoother results than our modeling approach which uses the now-casting GNSS input data.

6.2.6.3 Comparison with the F/C peak parameters

In previous section, the estimated \hat{N}_m and \hat{h}_m were compared to the N_m and h_m values derived from the IRI model. But as the IRI model is used to derive the a priori values of some of the input parameters, the estimated parameters are further compared to the electron density peak parameters derived from F/C occultation data.

For this study, the F/C F2-peak parameters were provided by Prof. Lung-Chi Tsai from the Ionolab of Taiwan National University (Tsai, 2012). The F/C peak parameters are provided in terms of F2-peak height $h_m\text{F2}$ and F2 critical frequency $f_0\text{F2}$, obtained from the F/C RO measurements. According to Tsai *et al.* (2011), to derive the F2-peak parameters, the electron density profile is obtained individually for the bottom-side ionosphere, i.e. below the

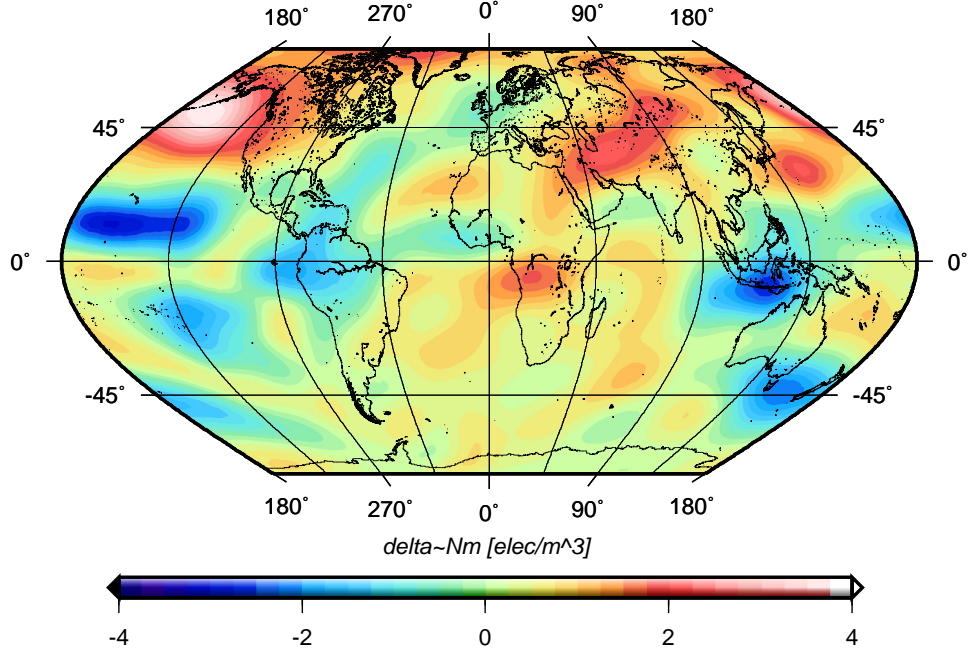


Figure 6.39: Difference between the estimated \hat{N}_m values and N_m derived from the IRI model ($\times 10^{11} \text{ elec/m}^3$) for day 182, 2010 - [0,2]UT

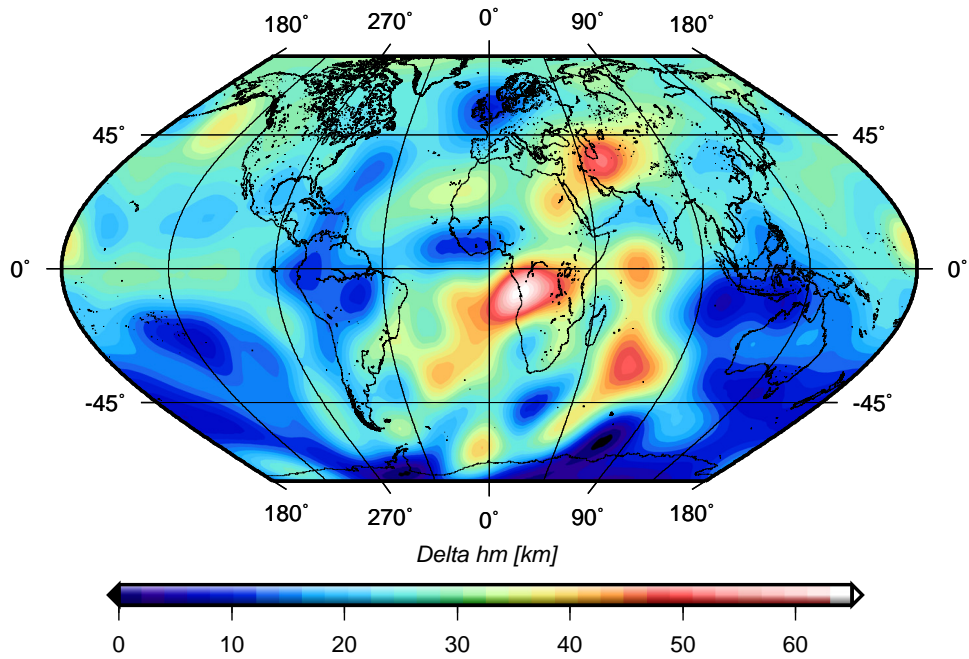


Figure 6.40: Difference between the estimated \hat{h}_m values and h_m derived from the IRI model (km) for day 182, 2010 - [0,2]UT

6.2 Global maps of electron density

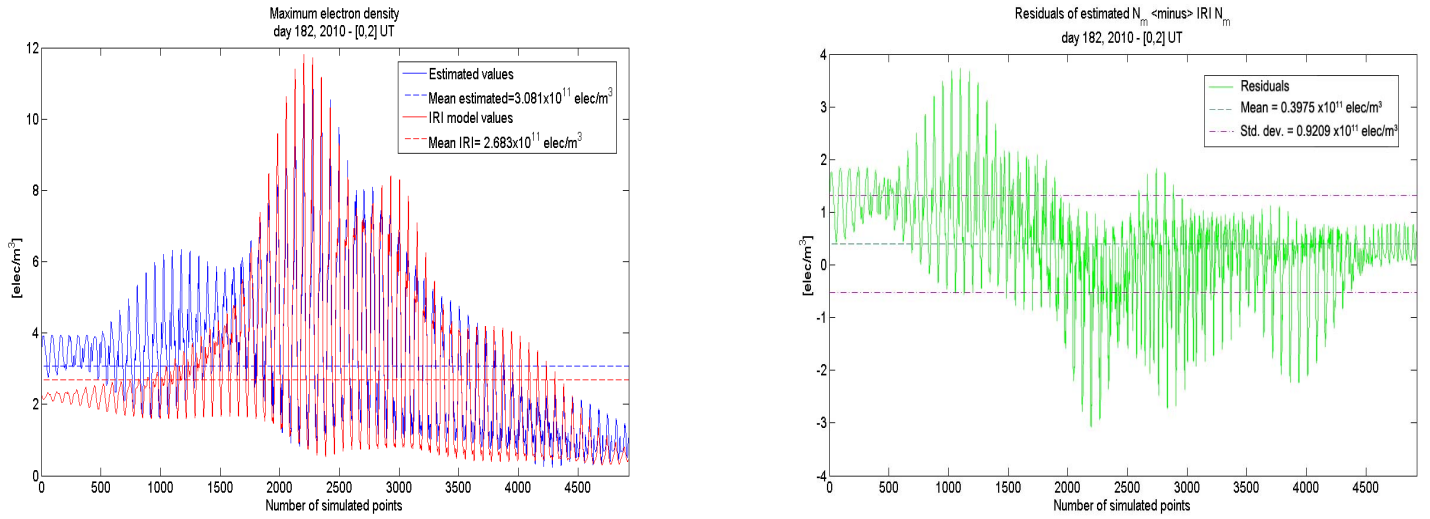


Figure 6.41: **a** Estimated maximum electron density (blue curve) and maximum electron density from the IRI model (red curve), and **b** residual of estimated minus IRI maximum electron density at the simulated input points, day 182, 2010, [0,2] UT

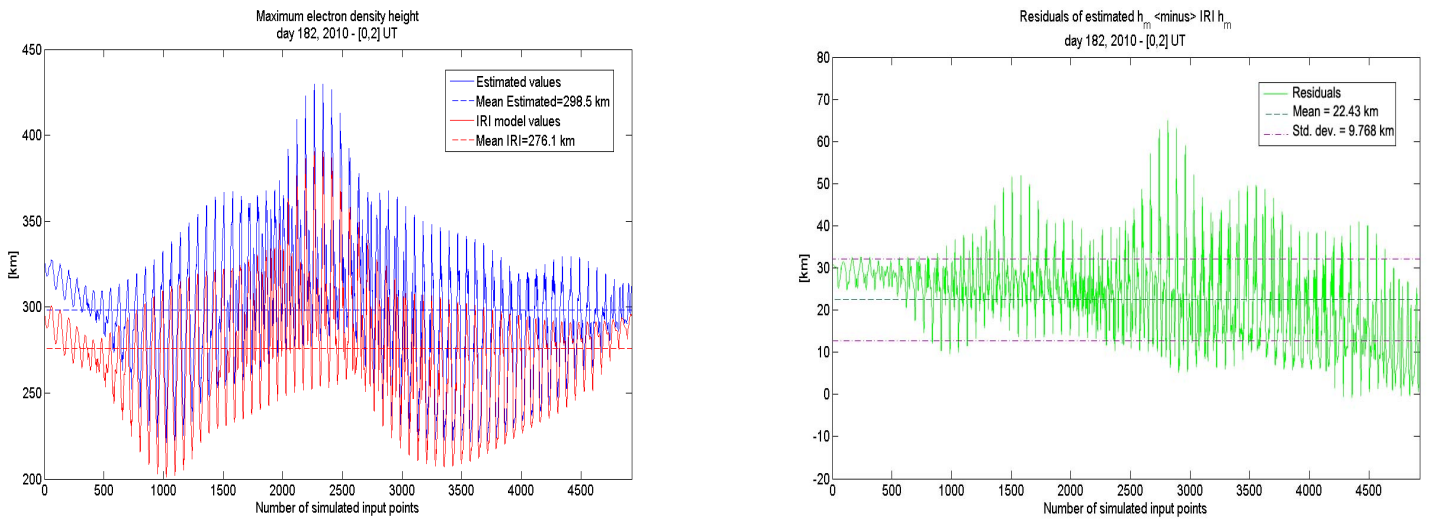


Figure 6.42: **a** Estimated height of maximum electron density (blue curve) and maximum electron density height from the IRI model (red curve), and **b** residual of estimated minus IRI maximum electron density height at the simulated input points, day 182, 2010, [0,2] UT

F/C height, and for the topside ionosphere, i.e. above the F/C height. The profile below the F/C height is computed directly from the measured occultation data. To obtain the topside profile, electron density is extrapolated above the height of the F/C, using an exponential extrapolation.

To compute the maximum electron density from the F/C data, a simple formula is applied to the measured f_0F_2

$$NmF_2 = \frac{1}{80.6} (f_0F_2)^2 . \quad (6.34)$$

Figure 6.43 shows the footprints of F2-peak parameters obtained from F/C radio occultation measurements.

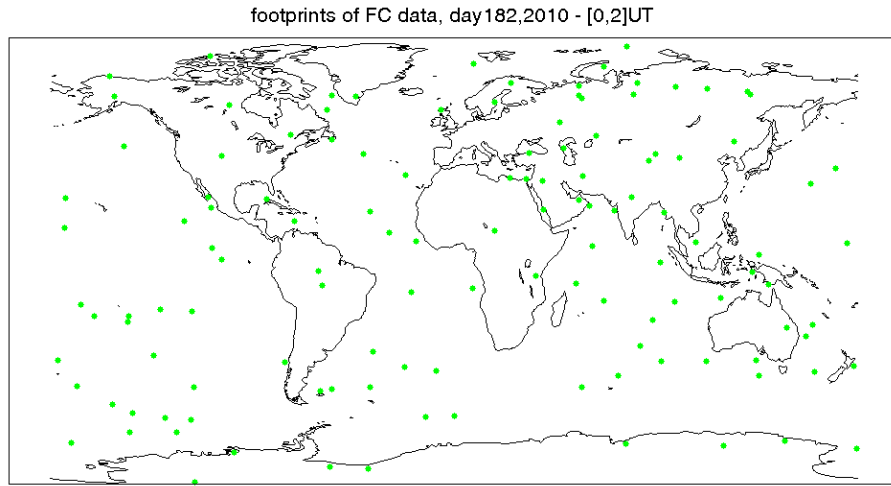


Figure 6.43: Footprints of F2-peak parameters obtained from F/C data, for day 182, 2010 - [0,2]UT

Figure 6.44 and Fig. 6.45 depict the F2-peak electron density and its corresponding height, obtained from the F/C data, for day 182, 2010, -[0,2]UT.

Performing the comparison at the common points, Fig. 6.46 shows the deviations of estimated minus F/C data maximum electron density. Figure 6.47 depicts the corresponding deviations of maximum electron density height.

The mean deviation of estimated maximum electron density minus F/C maximum electron density for day 182, 2010, [0,2]UT is $0.71 \times 10^{11} \text{ elec}/m^3$ with a standard deviation of $1.06 \times 10^{11} \text{ elec}/m^3$. The mean residual of estimated minus F/C of the maximum electron density height for the same day is $\sim 33 \text{ km}$ with a standard deviation of 65.8 km .

To evaluate this difference, the test of significance is performed over the deviation values, i.e. deviations of the estimated peak parameters minus F/C derived peak parameters.

Prior to performing this statistical test, an outlier test (see Sect. 6.2.3) is performed over the F/C raw data and the outliers are omitted. The test of significance is then performed, over the two deviation values. The statistic z for each of the estimated parameter reads

$$z = \frac{\bar{x} - \mu}{s/\sqrt{n}} , \quad (6.35)$$

where

- \bar{x} mean value of the estimated minus F/C eviations,
- μ expected value of the estimated minus F/C deviations (i.e. *zero*),
- s standard deviation of the estimated minus F/C deviations, and
- n number of common data points.

z has a normal probability density function with $\mu = 0$ and standard deviation s

$$z \sim \mathcal{N}(0, s) . \quad (6.36)$$

The statistical test is performed and the null-hypothesis of $H_0 : \mu = 0$ is accepted with a confidence interval of $1 - \alpha = 0.90$, for both N_m and h_m values. This means that difference between estimated NmF2 and hmF2 and the corresponding values derived from F/C is statistically insignificant with a confidence level of %90.

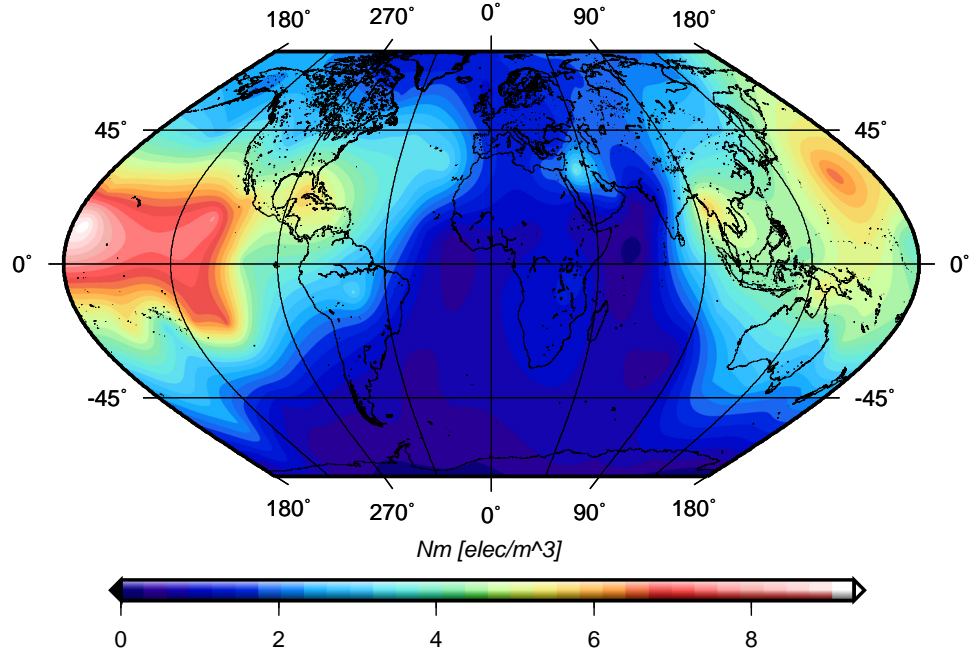


Figure 6.44: F2-peak electron density obtained from F/C data, for day 182, 2010 - [0,2]UT

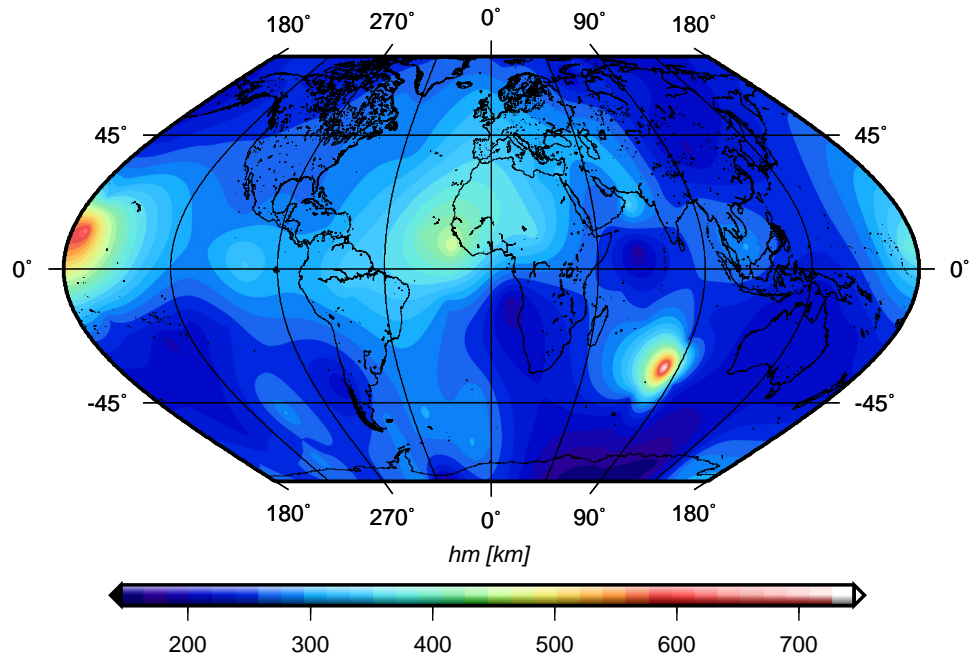


Figure 6.45: F2-peak height obtained from F/C data, for day 182, 2010 - [0,2]UT

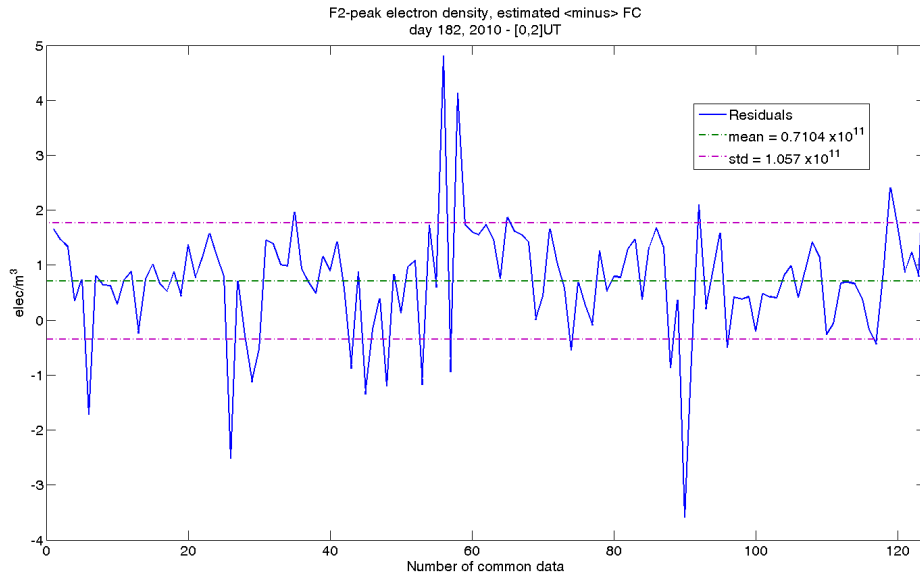


Figure 6.46: F2-peak electron density deviations of estimated minus F/C, for day 182, 2010 - [0,2]UT

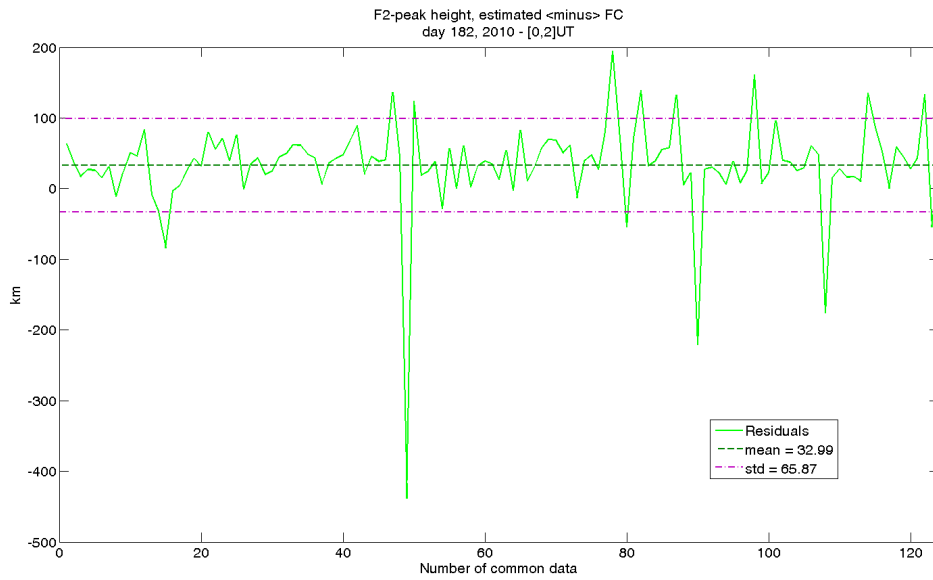


Figure 6.47: F2-peak height deviations of estimated minus F/C, for day 182, 2010 - [0,2]UT

Chapter 7

Final remarks

With rapid development of new scientific and technological systems which transmit signals through the upper atmosphere, accurate modeling of the ionosphere has turned more crucial. Within the IGS, the Ionosphere WG has been providing daily GIM of VTEC since 1998. The IGS GIM is being widely used for different scientific and civilian purposes, therefore increase in the accuracy and reliability of their products is essential. From long term analysis, it is believed that the IGS VTEC maps have an accuracy of few *TECU* in areas well covered with GNSS receivers; conversely, in areas with poor coverage, the accuracy can be degraded by a factor of up to five (Feltens *et al.*, 2010). On the other hand, dual-frequency satellite missions, such as several altimetry missions or the F/C mission, provide valuable information about the ionosphere globally. Combining these data with the ground-based GNSS data, significantly improves the accuracy and reliability of the VTEC maps by closing the observation gaps that arise when using ground-based data only. The developed GIM are considered as 2D maps of VTEC, as they model VTEC in longitude and latitude, and contain the temporal variation implicitly. Due to the fact that 2D models of VTEC provide information about the integral of the whole electron content along the vertical or slant ray-path, when information about the ionosphere at different altitudes is needed, these maps are not useful; e.g. when electron density profile is required, or when satellite to satellite observation is being performed. In this case a 3D modeling of the ionospheric parameters is required. To model ionospheric parameters in 3D, the parameters of electron density, e.g. the F2-peak electron density, and its corresponding F2-peak height could be modeled - assuming the plasmaspheric contribution to be known for the time being. For this, the parameters of the electron density are modeled in longitude, latitude, and height.

All in all, an enhanced knowledge of the processes within the ionosphere is of high importance for all studies of the upper atmosphere and the solar-terrestrial environment, e.g. for radio science, for upper atmosphere climate and plasma studies, and for the marine or arial navigation.

This chapter overviews the summary of the accomplished work within this thesis, followed by a general discussion on the results and findings. The concluding remarks are then briefly overviewed, and finally the dissertation is concluded with some ideas for further development and improvement of the results and for future work.

7.1 Summary

2D modeling of VTEC

To develop the combined 2D GIM, GNSS ionospheric observable which are formed using smoothed-code pseudorange were taken as the primary input data. The GNSS observations of a complete day from about 160 IGS ground stations were downloaded in RINEX format and were split into two-hourly time spans, starting from [0,2] UT to [22,24] UT. For each two-hourly time interval the observation equations were formed by applying spherical harmonic expansion of degree and order 15 to the ionospheric observable. The normal equations for the GNSS input data was then formed. A similar procedure was accomplished for all the other observations techniques, i.e. for observations of satellite altimetry and F/C. The observations of the different techniques were then combined by stacking the normal equations of each of the techniques. The least-squares adjustment was performed using the combined normal equations and the unknown coefficients of the spherical harmonic expansion were estimated along with the satellite and receiver DCB and the daily bias between each of the combined input data with respect to GNSS, i.e. one daily constant bias between GNSS and satellite altimetry and one daily constant bias between GNSS and F/C. The estimated coefficients of the spherical harmonics were then used to calculate the estimated VTEC values through the whole globe. The VTEC values were provided in global grid-wise maps with temporal resolution of 2h and spatial resolution of 2.5° in latitude, and 5° in longitude.

To assess the validity of the combined maps, the developed maps were first quantified with the raw altimetry and F/C data, which were not used in the combination procedure. Comparisons with the IGS GIM and also VTEC profiles from the IRI models was also performed. As a complementary step, a through investigation was performed for calibrating GNSS data, using satellite altimetry and F/C VTEC values. To calibrate the GNSS values, in the first step, GIM from the GNSS-only measurements were computed. Taking the footprints of the satellite altimetry and F/C measurements at each two-hourly intervals into account, the VTEC values at these points were extracted from the GNSS-only GIM. The difference between the extracted VTEC values, and VTEC from satellite altimetry and F/C data was used to calculate the bias between GNSS and satellite altimetry and F/C. The biases were calculated using three different strategies, namely daily mean bias, time-dependent bias, and latitude-dependent bias. Applying each of the calculated biases, the GNSS VTEC values were calibrated with respect to satellite altimetry and F/C VTEC.

3D modeling of electron density

In the next step of this thesis we concentrated on 3D modeling of electron density. To model the electron density, the upper atmosphere was assumed to be a stratified layer with three major subdivisions, i.e. the bottom-side ionosphere, starting from 50 to 200 *km*, the topside ionosphere from 200 to 1,000 *km*, and the plasmasphere from 1,000 to 2,000 *km*. The bottom-side and topside ionosphere were modeled using an appropriate Chapman profile function. To model the plasmaspheric contribution, the plasmaspheric part of the TIP model was implemented. As a first step of this research, we assumed the plasmaspheric contribution to be known by taking the a priori values from the TIP model, so we concentrated only on the ionospheric part. According to the Chapman profile function, electron density at any point is given by the F2 maximum electron density NmF2, and its corresponding height hmF2. So the aim was to model NmF2 and hmF2 in globe. For this two sets of spherical harmonic expansions were applied to the GNSS ionospheric observable, which relate the GNSS input data to the F2-peak parameters. One set of spherical harmonic expansion was used for estimating NmF2, and the other set for estimating hmF2. To perform the estimation, GNSS input data were simulated in such a way that the true position of the satellites were detected and used, but the STEC values were obtained through a simulation procedure, using the IGS VTEC maps. After simulating the input data, the a priori values required for the estimation procedure were calculated using the IRI-2012 model and also by applying the ray-tracing technique. In the course of the estimation, appropriate constraints had to be applied, to avoid unexpected output. For estimating NmF2, a global mean constraint was applied. In this approach, the global mean value of NmF2 from the a priori model, i.e. IRI-2012 was calculated and applied as the constraint. For estimating hmF2, as the observation equation was non-linear with respect to hmF2, a sin-surface function constraint was applied. In this constraint, the final estimated values are limited to a predefined range. For this study, the range was set to the minimum and maximum values of hmF2 derived from the a priori model IRI-2012. After performing the least-squares estimation, the coefficients of two sets of spherical harmonic expansions were estimated. These coefficients were used to calculate the NmF2 and hmF2 values in globe. The calculated values were provided in 2D global grid-wise maps (one map for NmF2, and one map for hmF2), or in a unified 3D global map of NmF2 and hmF2. The final results were compared to the a priori model IRI-2012 to assess the least-squares estimation procedure. Moreover, to validate the developed maps, the results were compared with the F2-peak parameters derived from the F/C data.

7.2 Discussion

2D modeling of VTEC

So far the ionospheric information obtained from satellite altimetry and F/C data were used for cross-validating the GIM developed from the GNSS observations. In the first part of this thesis, we investigated integrating the satellite altimetry and F/C measurements with the

GNSS data to develop combined global maps of the ionosphere. Performing the combination over several days in the solar minimum and maximum conditions, we first concentrated on combining GNSS measurements with the satellite altimetry data only, following the work accomplished by Todorova (2008). The obtained results, show an absolute difference of 1 to 2 *TECU* with respect to the GNSS-only VTEC maps in the whole globe. At the footprints of the satellite altimetry, this difference is positive, indicating a general increase of the VTEC values from the GNSS-only VTEC. This increment corresponds to the systematic VTEC over-estimation of satellite altimetry with respect to GNSS, which is proved by several authors, e.g. Brunini *et al.* (2005), and Todorova *et al.* (2007).

In the next step, F/C measurements were integrated into the combination procedure. Integrating F/C data with the GNSS and satellite altimetry combined maps, compensates the effect of this over-estimation. Taking the GNSS, satellite altimetry, and F/C combined maps into account, a maximum difference of -1.5 to +1 *TECU* could be observed with respect to GNSS and satellite altimetry combined maps. Performing the comparison reveals a general reduction of VTEC by about 0.5 *TECU* in the whole globe after integrating the F/C data. However, in some locations through the globe, the VTEC values are increased after combining the F/C data with GNSS and satellite altimetry combined maps. Taking a closer look at the footprints of satellite altimetry and F/C, reveals that there have been no or a few satellite altimetry observations at the mentioned location, while F/C data were available by great extent.

Concerning the accuracy of the combined maps, the formal error of the developed maps show a general reduction through the whole globe. This reduction is more evident after integrating the F/C data into the combination. This is due to the better global distribution of F/C measurements comparing to the satellite altimetry observations. The reduction of formal errors at the footprints of satellite altimetry or F/C data can reach up to 0.3 *TECU* in the case of GNSS and satellite altimetry combined maps, and up to 0.7 *TECU* in case of combining GNSS, satellite altimetry and F/C data.

3D modeling of electron density

Aforesaid, the 2D models of VTEC provide information about the integral of the whole electron content along the vertical or slant ray-path, when height-dependent information about the parameters of the ionosphere is required, 3D modeling of the ionospheric parameters becomes necessary. In the second part of the thesis, we focused on 3D modeling of electron density. For this, the parameters of electron density, i.e. the F2-peak electron density $NmF2$, and the corresponding F2-peak height $hmF2$ were modeled in longitude, latitude, and height. The procedure was performed for a sample day, 1st July 2010, and the models were assimilated as global grid-wise maps of $NmF2$ and $hmF2$. To evaluate the developed maps, the results were first compared with the IRI-2012 model, and then with the F2-peak parameters derived from F/C data. Comparing the estimated $NmF2$ with the $NmF2$ derived from the IRI model reveals a positive mean bias of $0.398 \times 10^{11} \text{ elec}/m^3$ with standard deviation of $0.920 \times$

$10^{11} \text{ elec}/\text{m}^3$.

7.3 Conclusions

2D modeling of VTEC

Conclusions concerning the first part of this thesis are itemized below:

- This research is considered as a pioneer in the field of 2D modeling of the ionospheric parameters, since it is the first to combine several space geodetic techniques for global integrated modeling of the VTEC. Until now, satellite altimetry and F/C data were only used for comparison and cross/validating the GNSS GIM.
- Combining GNSS VTEC maps with altimetry and F/C data has a great potential to improve the accuracy and reliability of the VTEC GIM, especially when there is a high number of occultation measurements available.
- The oscillations due to the lack of data and limitations of modeling the ionosphere, using spherical harmonic expansion Schmidt *et al.* (2011), is considerably compensated after applying the combination procedure.
- Since in our approach we use spherical harmonic base-function (similar to the IGS), it will not be such a big effort for the IGS to improve their ionospheric products, by implementing this integration technique.
- By rapid evolvement of space geodetic techniques and development of new ones, which are capable of transmitting and/or receiving signals in more than two frequencies, more observations could be integrated into the combination procedure. This will significantly improve the accuracy and reliability of the developed combined maps.
- The combination procedure effectively contributes to the GGOS aims of integrating different geodetic observing techniques for assuring a precise monitoring of the geodetic observables.

3D modeling of electron density

Conclusions concerning the second part of this thesis are itemized below:

- Due to the following facts, this study can be considered a pioneer in multi-dimensional modeling of the electron density

- using ground-based GNSS measurements for 3D and 4D modeling of the ionospheric parameters,
 - implementing a multi-layer ionosphere/plasmasphere model,
 - applying ray-tracing technique to the upper atmosphere,
 - modifying simulation approach,
 - develop and implementing appropriate constraints for estimating the parameters,
 - developing a global integrated 3D map of electron density F2-peak parameters, with a spatial resolution of 2.5° in latitude, and 5° in longitude, and spatial resolution of $2h$.
- The developed 3D model of electron density peak parameters can be used to reconstruct the electron density profiles through the ionosphere. These profiles provide information about the ionosphere at different altitudes. This is in particular useful, when e.g. satellite to satellite observation is being performed.
 - Besides the geodetic applications, 3D modeling approach can include geophysical parameters like maximum electron density, and its corresponding height. High resolution modeling of these parameters, allow an improved geophysical interpretation, which is essential in all studies of the upper atmosphere, space weather, and for the solar-terrestrial environment.

7.4 Outlook

In this section, some ideas for further development and improvement of the results and for future work is outlined.

2D modeling of VTEC

Some steps towards improving the accuracy and reliability of the integrated 2D models of VTEC are:

- Improving relative weighting scheme

To improve the integration results, an appropriate weighting for the different techniques included in the combination procedure should be applied. This could be on both, physical and mathematical aspects. For physical relative weighting, in the case of satellite altimetry data, a latitude dependent weighting can be applied. As for the F/C measurements, a weighting scheme depending on the individual spacecrafts can be applied. For mathematical relative weighting, a fast Monte-Carlo implementation of the iterative maximum likelihood component estimation (MCVCE) can be applied.

- Performing GNSS calibration prior to combination

As a first step of combination procedure, calibration of the different data sources should be performed. This would help removing the systematic bias between the different techniques. Performing combination after removing a latitude dependent bias, provides the best accuracy among other de-biasing techniques.

- Integrating with new evolving techniques

As new space geodetic techniques with globally distributed observations evolve, including their data into the combination procedure can significantly improve the accuracy and reliability of the developed combined maps. Care should be taken for the relative weighting of these techniques.

- Developing maps with the same reference epoch as the IGS GIM

Within this study, to keep the calculation time optimal, the reference epochs of VTEC GIM were shifted with respect to the IGS reference epochs, by one hour. This led to processing observations of only one day, instead of three days, which is performed by IGS, and developing twelve two-hourly maps per day, instead of thirteen two-hourly maps. Shifting back the reference epoch, has the advantage of providing similar maps to the IGS official products, and therefore the comparison to the IGS GIM would become more accurate.

- Increasing temporal resolution of the combined GIM

As IGS Ionosphere WG is planning to increase the temporal resolution of their products from $2h$ to $1h$ and $15min$, it is worth preparing a similar change for developing the combined GIM as well.

- Densifying the global maps using regional models

There are several regional ionosphere models, which implement the same base-functions, i.e. modified spherical harmonic expansion, or other base-functions, e.g. B-spline base-functions. Integrating the combined global maps with these regional models could improve the accuracy and reliability of the developed maps.

3D modeling of electron density

- Applying real GNSS observations

Within this study, to avoid inconsistencies in the input data and to focus only on the model and the procedure for estimating the unknown parameters, we simulated the GNSS input data. Although the GNSS white noise has already entered our procedure through IGS VTEC maps, but using real GNSS data, the real noise is accounted for.

- Integrating data from different space geodetic techniques

Information about the parameters of the electron density from other space geodetic techniques, e.g. F2-peak parameters from F/C, were used for cross-validating the developed maps obtained from GNSS-only data. Integrating information from additional techniques into our modeling approach could improve the accuracy and reliability of the developed maps, by closing the gap within GNSS input data.

- Taking curvature effect into account, using ray-tracing technique

As a first step for this study, curvature effect has not been taken into account, i.e. the ray-path is assumed to be a straight line. Improving the ray-tracing formulations, the curvature effect along the signal path can also be accounted for.

- Accounting for higher-order ionospheric refraction, using ray-tracing technique

The higher-order ionospheric refraction can also be considered in our model, when applying the improved ray-tracing technique.

- Estimating plasmaspheric parameters as individual unknowns

For this study, we assumed the plasmaspheric parameters, i.e. the plasma scale height H_P and the plasmasphere basis density N_P as known parameters, by taking the values from the TIP model. With this assumption, our unknown parameters were restricted to the ionospheric parameters, i.e. N_m and h_m values. In the next step, we can estimate the plasmaspheric parameters, as well as the ionospheric scale height.

- Estimating characteristic parameters of other layers of the ionosphere

Applying appropriate models for other layers of the ionosphere e.g. E-layer, the characteristic of these layers could also be estimated using this modeling approach.

- Applying Vary-Chap function for estimating the transition height

To estimate the ionospheric scale height, the Vary-Chap function proposed by Reinisch *et al.* (2007) could be implemented. Within this function, the transition height is not assumed to be constant, but is varying with height.

- Comparing the developed maps with other models and data

In this study, the developed electron density models were compared with the electron density parameters derived from the IRI-2012 model, and also from the F/C data. The developed maps can also be compared to other models such as the NeQuick or other data such as the electron density profiles derived from the ionosonde.

- Improving the spatial and temporal resolution

For 3D modeling of the electron density parameters, the spatial resolution was assumed 2.5° in latitude, and 5° in longitude, and temporal resolution of $2h$. The reason for selecting such spatial and temporal resolution was to have a similar resolution as the developed 2D maps of VTEC, and to reduce the computational time. The spatial resolution can be improved by selecting higher degree and order spherical harmonics. The temporal resolution can also be improved to $1h$ and also $15min$.

- Developing near real-time models using Kalman-filtering

Applying appropriate Kalman filtering approach, the developed maps could be provided in near-real time.

- 4D modeling of electron density applying Fourier series expansion

Furthermore, by applying the Fourier series expansion, the electron density parameters could be modeled in 4D, i.e. in longitude, latitude, height, and time. Within this thesis, the theoretical concept was presented and the formulae for this approach were developed (see Sect. 5.4).

Part IV

Appendices

Appendix A

Single-frequency Single Point Positioning

In this appendix, GNSS single-frequency Single Point Positioning (SPP), which is a sample application of the developed combined 2D global VTEC model is introduced. The plots and tables presented in the following part are extracted from Alizadeh *et al.* (2010), published at the proceedings of the Geomatics-89 conference in Tehran, Iran.

In the late 90s, JPL pioneered a new technique that did not require calculating differential equations to obtain GPS precise positions; they labeled this procedure, Precise Point Positioning (PPP) (Zumberge *et al.*, 1997). The largest difference between relative processing and PPP was the way of handling the satellite and receiver clock errors. To remove satellite clock errors, PPP uses highly precise satellite clock estimates, instead of between-receiver differencing. These satellite clock estimates are derived from IGS GNSS network (see Sect. 3.1.1). In PPP, receiver clock errors are estimated as part of the least-squares solution for the coordinates, instead of being removed by differentiating between satellites. To accomplish PPP, GNSS dual-frequency group and phase pseudo-ranges are used to compute L3 ionosphere-free linear combination, Eq. 3.10 or Eq. 3.15. As already mentioned in Sect. 3.1.3.1, in this linear combination, the first-order ionospheric effect is eliminated, therefore, in the first approximation, our equation is free of ionosphere. The L3 ionosphere-free linear combination can only be performed when GNSS observations are carried out in two frequencies. Since most of the cheaper GNSS receivers are observing only in single frequency, they cannot apply this technique. Locating these receivers in a non-differential procedure, is known as the SPP. The difference between PPP and SPP in terms of coordinate accuracy is large. SPP produces coordinates accurate at the 1 to 10 *m* level, while PPP can produce coordinates accurate at the millimeter level with 24*h* of observations, which is comparable to relative processing (King *et al.*, 2002).

To improve the accuracy of SPP, the effect of error sources in Eq. 3.1 or 3.2 should be minimized. As ionosphere refraction is one of the major error sources in these equations, its effect should be accounted for. To correct the model for the ionosphere refraction, point positioning was performed by using:

- Single-frequency measurements, applying ionosphere correction from combined GIM,
- Single-frequency measurements, applying ionosphere corrections from CODE GIM, and
- Dual-frequency ionosphere-free linear combination.

In the course of this procedure, Observation of 20 IGS stations world-wide were used in the duration of day 182 to 191 of 2006. The above mentioned approaches were processed with the Bernese GPS Software (ver. 5.0) (Dach *et al.*, 2007), applying final orbits and weekly Earth



Figure 1: Selected IGS stations for performing PPP and SPP

Rotation Parameter solution of CODE, the IAU2000 model for nutation and the absolute antenna phase-center model. The criteria for selecting the IGS stations are focused on the location of the station with respect to the sea-area. Figure 1 shows the world-wide selected stations.

First, using the dual-frequency ionosphere-free linear combination the precise coordinates of the selected stations are calculated in a $24h$ solution. In the second approach, single-frequency measurements are processed in the same $24h$ daily solution, and for the ionosphere correction term, TEC is extracted from the GNSS and satellite altimetry combined GIM, (from now, in this appendix, called the IGG GIM). Similarly in the third approach, the coordinates are calculated by applying ionosphere correction derived from CODE's GIM to single-frequency measurements. Within this study, the L3 ionosphere-free combination serves as a basis for comparing the two different models of the ionosphere. To have a better view for this comparison, the results of position coordinates derived from the different solutions are subtracted from results of the ionosphere-free solution. Figures 2a and b, and 3a and b depict samples of the processed stations. In Fig. 2 and 3 difference between dual-frequency PPP and the single-frequency SPP, applying ionosphere corrections derived from the CODE and IGG GIM are shown. The thick lines depict ionospheric corrections obtained from CODE GIM and the dashed lines depict ionospheric corrections derived from IGG GIM. By subtracting the different SPP solutions from the PPP solution, all other errors will be eliminated, except the ionosphere errors. The process is carried out on a daily basis solution for day 182 to 191 of the year 2006. Figures 2a and b show the results for stations ALGO and CONZ, which are well within the land area. It can be seen that the CODE derived ionosphere corrections with the mean horizontal bias of 0.058 cm at station ALGO, provide slightly better results than IGG derived corrections with 0.067 cm mean horizontal bias at the same station; though position differences of both methods hardly reach 5 mm within 10 days. Figures 3a and b show the results for stations GUAM and KERG which are located in

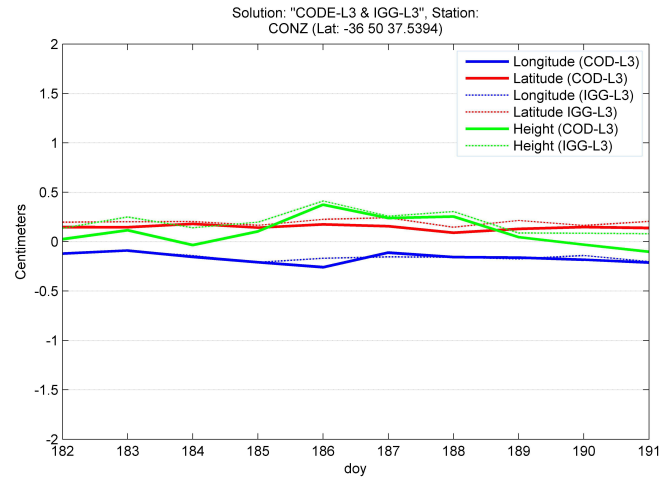
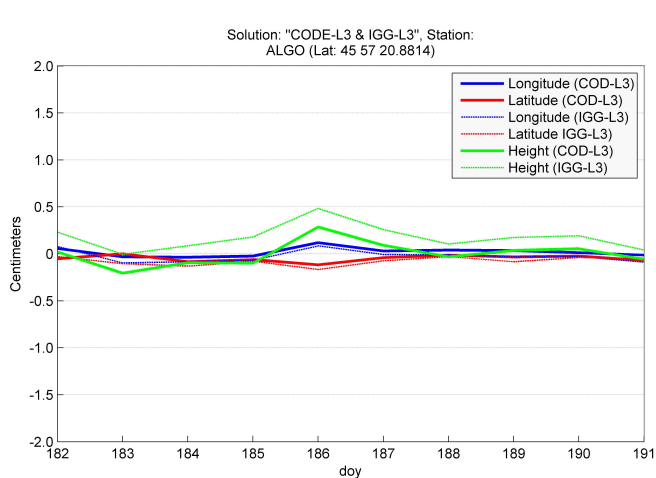


Figure 2: SPP in a daily solution for in-land station **a** ALGO and **b** CONZ, from day 182 to 191, 2006. Thick lines depict SPP using ionospheric corrections derived from CODE GIM minus dual-frequency PPP of the station, and dashed lines show SPP using ionospheric corrections derived from IGG GIM minus dual-frequency PPP of the station

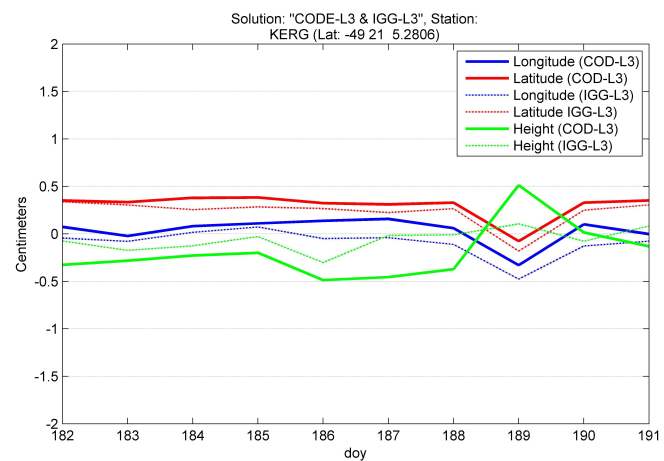
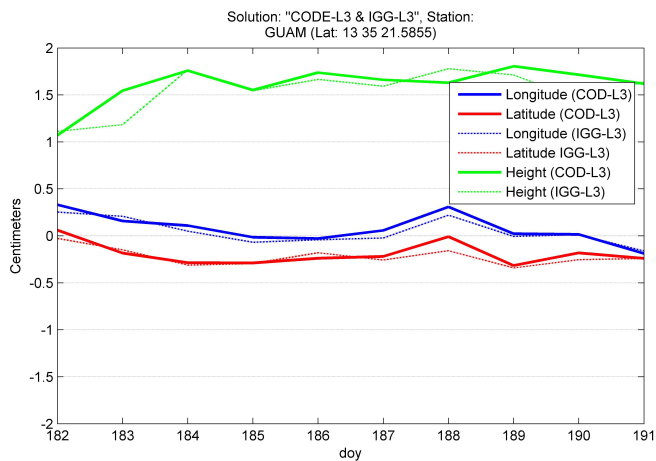


Figure 3: SPP in a daily solution for sea-side station **a** GUAM and **b** KERG, from day 182 to 191, 2006. Thick lines depict SPP using ionospheric corrections derived from CODE GIM minus dual-frequency PPP of the station, and dashed lines show SPP using ionospheric corrections derived from IGG GIM minus dual-frequency PPP of the station

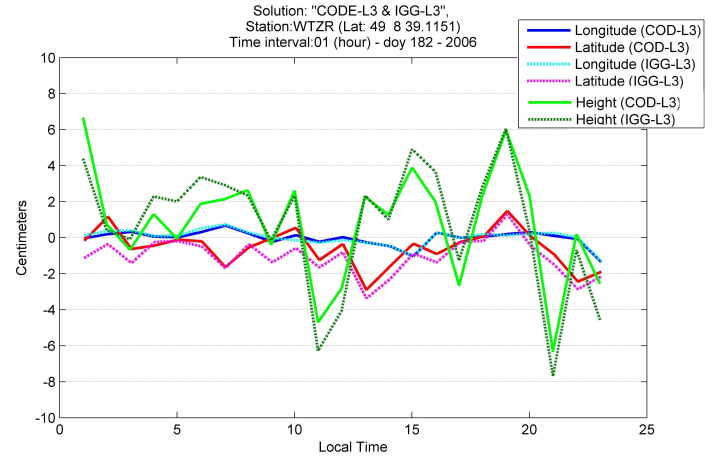
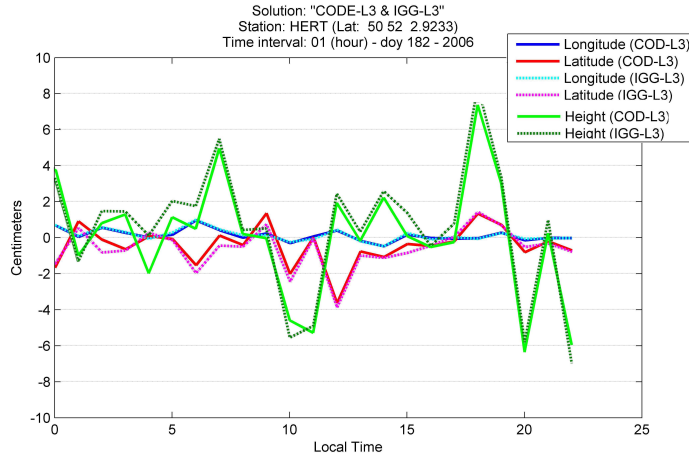


Figure 4: SPP in an hourly solution for in-land station **a** HERT and **b** WTZR, for day 182, 2006. Thick lines depict SPP using ionospheric corrections derived from CODE GIM minus dual-frequency PPP of the station, and dashed lines show SPP using ionospheric corrections derived from IGG GIM minus dual-frequency PPP of the station

the ocean area. Except for the height component at station GUAM, the position differences of both methods at both stations are around 5 *mm*. From these plots, it is apparent that the IGG derived correction method provides better results than the CODE derived correction. For example the mean horizontal bias at station GUAM with the IGG model is 0.165 *cm*, while this amount with ionosphere corrections from CODE is 0.206 *cm*. Table 1 shows the mean bias in longitude, latitude, and height over 10 days and also the RMS of height with respect to the L3 ionosphere-free combination of both methods.

The same solutions are carried out for the selected stations on an hourly basis. Figures 4a and b illustrate the differences between SPP using both correction models and the dual-frequency PPP at day 182 of 2006, for in-land stations HERT and WTZR. Figure 5a and b depict the same plots for the stations BRMU and REUN, which are located in the ocean area. The mean bias in longitude, latitude, and height over 24*h* and also the RMS of height with respect to the L3 ionosphere-free combination of both methods is represented in the Table 2. From the above figures, it can be seen that applying ionospheric corrections for single frequency SPP using the IGG model at the seaside stations provides better results than applying corrections from the CODE model. This is clearly due to the lack of GNSS observations over the ocean area. But for the stations in the land regions, ionospheric corrections derived from the CODE GIM, provide better SPP results compared to the SPP applying corrections from the IGG GIM, although the difference between two correction methods are not significant. From this study, it can be inferred that combining satellite altimetry data with GNSS measurements improves the accuracy of the developed GIM over the area with no or less GNSS observations, i.e. mainly over the oceans.

	IGG				CODE			
	Bias (<i>cm</i>)			RMS (<i>cm</i>)	Bias (<i>cm</i>)			RMS (<i>cm</i>)
	LONG	LAT	H	H	LONG	LAT	H	H
ALGO	-0.03	-0.06	0.27	0.13	0.02	-0.05	0.15	0.13
ALRT	0.03	0.07	0.43	0.11	0.04	0.08	0.30	0.11
BAHR	0.11	-0.34	0.85	0.20	0.11	-0.27	0.75	0.17
BRMU	0.13	-0.39	0.44	0.13	0.09	-0.30	0.39	0.13
CONZ	-0.10	0.20	0.29	0.14	-0.08	0.14	0.21	0.10
DARW	-0.04	0.08	0.35	0.36	-0.03	0.15	1.36	0.39
DGAR	0.26	0.33	0.91	0.41	-0.08	0.14	0.21	0.10
GLPS	-0.02	-0.01	0.13	0.17	-0.06	-0.14	1.04	0.20
GUAM	0.04	-0.16	1.45	0.20	0.08	-0.19	1.61	0.22
HARB	0.01	0.20	0.04	0.12	0.08	-0.19	1.61	0.22
HERT	0.16	-0.26	0.11	0.08	0.04	0.30	-0.20	0.11
HNLC	-0.17	-0.23	0.50	0.20	-0.11	-0.14	0.42	0.29
KERG	-0.09	0.23	-0.06	0.28	0.04	0.30	-0.20	0.11
KOKB	-0.14	-0.27	-0.06	0.26	-0.08	-0.16	0.36	0.32
MDOI	-0.16	-0.47	0.56	0.14	-0.06	-0.34	0.35	0.21
NLIB	-0.10	-0.08	0.11	0.07	-0.11	-0.07	0.03	0.09
REUN	0.05	0.37	0.30	0.17	0.03	0.25	0.10	0.10
SEY1	0.06	0.10	0.64	0.29	0.01	0.15	0.70	0.30
THTI	-0.10	0.11	0.40	0.34	-0.13	0.12	0.52	0.40
WTZR	0.17	-0.25	0.11	0.08	0.07	-0.09	0.03	0.07

Table 1: Mean bias and RMS of different SPP daily solutions with respect to dual-frequency PPP solution, for day 182 to 191, 2006

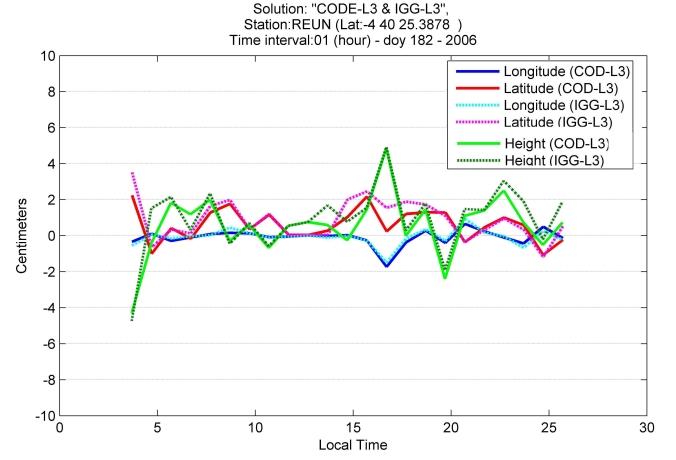
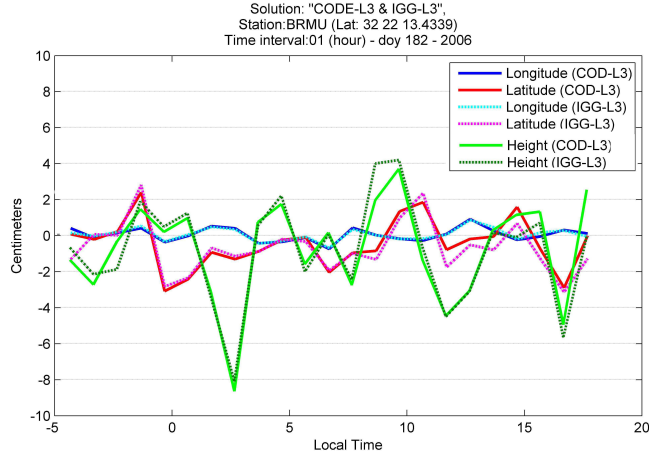


Figure 5: SPP in an hourly solution for see-side station **a** BRMU and **b** REUN, for day 182, 2006. Thick lines depict SPP using ionospheric corrections derived from CODE GIM minus dual-frequency PPP of the station, and dashed lines show SPP using ionospheric corrections derived from IGG GIM minus dual-frequency PPP of the station

	IGG				CODE			
	Bias (<i>cm</i>)			RMS (<i>cm</i>)	Bias (<i>cm</i>)			RMS (<i>cm</i>)
	LONG	LAT	H	H	LONG	LAT	H	H
HERT	1.45	-2.34	4.91	2.74	1.36	-2.12	4.40	2.68
WTZR	0.56	-1.54	3.13	3.52	-0.38	-1.63	2.86	3.28
REUN	-0.50	-0.47	-2.00	1.81	-0.68	0.72	-2.30	1.70
BRMU	0.71	0.61	-0.75	3.46	-0.99	0.87	-0.96	3.03

Table 2: Mean bias and RMS of different SPP hourly solutions with respect to dual-frequency PPP solution, for day 182, 2006.

List of Figures

1.1	Infrastructure contributing to GGOS (figure courtesy of IAG (2012))	2
2.1	Ionization of an Oxygen molecule due to solar radiation	10
2.2	Schematic representation of layer formation	12
2.3	Relation between the geographic and geomagnetic system, where G is the geographic pole, M is the geomagnetic pole, P an arbitrary point, θ_g the geographic co-latitude ($= 90 - \varphi_g$), θ_m is the geomagnetic co-latitude ($= 90 - \varphi_m$), and geographic and geomagnetic longitudes are expressed by λ_g and λ_m (figure courtesy of World Data Center for Geomagnetism (IGRF, 2011))	14
2.4	Chapman electron density profile and the ionospheric layers D, E, and F for both night and day conditions at mid-latitudes	16
2.5	Latitude dependent regions of the ionosphere	18
2.6	Single-layer model for the ionosphere	32
3.1	Jason-2 satellite, figure courtesy of AVISO (AVISO, 2012)	44
3.2	F/C space craft, figure courtesy of UCAR (UCAR, 2011)	46
3.3	VLBI concept, figure courtesy of IVS (IVS, 2012)	47
4.1	Bi-variate interpolation using the nearest four TEC values	61
4.2	VTEC GIM developed by IGS for 9 July 2006	62
4.3	1-D quadratic endpoint-interpolating B-spline functions of level e.g. $J = 4$ (figure courtesy of Dettmering <i>et al.</i> (2011b))	63
5.1	IGS global ground stations, figure courtesy of IGS (Dow <i>et al.</i> , 2009)	72
5.2	Inter-technique combination scheme (Alizadeh <i>et al.</i> , 2011)	73
5.3	Electron density profile for different solar zenith angles	79
5.4	Example for an improved TIP model over Sofia vertical sounding station. 9 September 2000 - 08:10 UT (figure courtesy of Jakowski <i>et al.</i> (2002a))	83
5.5	Concept of applying ray-tracing technique to the Chapman profile function	85
6.1	IGS GNSS stations used for computing GIM at day 190, 2006	100
6.2	Footprints of satellite altimetry mission, Jason-1 on day 190, 2006	101

6.3	Footprints of F/C occultation measurements on day 190, 2006	102
6.4	GNSS-only VTEC map for the whole day 190, 2006	103
6.5	GNSS-only RMS map for the whole day 190, 2006	103
6.6	a VTEC map and b RMS map of GNSS-only solution, day 190, 2006 - 1 UT	104
6.7	GNSS and satellite altimetry combined minus GNSS-only VTEC map for the whole day 190, 2006	105
6.8	GNSS and satellite altimetry combined minus GNSS-only RMS map for the whole day 190, 2006	105
6.9	Footprints of satellite altimetry mission, Jason-1 a for the whole day and b for 2h around 1 UT of day 190, 2006	106
6.10	a VTEC map and b RMS map of GNSS and satellite altimetry combined minus GNSS-only solution, day 190, 2006 - 1 UT	106
6.11	GNSS, satellite altimetry, and F/C combined minus GNSS and satellite altimetry combined VTEC map for the whole day 190, 2006	108
6.12	GNSS, satellite altimetry, and F/C combined minus GNSS and satellite altimetry combined RMS map for the whole day 190, 2006	108
6.13	Footprints of F/C occultation measurements in two hourly intervals for a the whole day 190, 2006 and b 2h around 1 UT of the same day	109
6.14	a VTEC map and b RMS map of GNSS, satellite altimetry, and F/C combined GIM minus GNSS and satellite altimetry combined solution, day 190, 2006 - 1 UT	109
6.15	Mean VTEC biases before and after removing the estimated offset from IGG combined model minus a altimetry and b F/C VTEC for day 190, 2006 . . .	111
6.16	VTEC differences between IGG combined minus IGS, for the whole day 190, 2006	113
6.17	RMS differences between IGG combined minus IGS, for the whole day 190, 2006	113
6.18	a VTEC and b RMS difference map of GNSS, satellite altimetry, and F/C combined GIM minus IGS GIM for day 190, 2006 - 1 UT	114
6.19	Procedure for calibrating GNSS VTEC values by satellite altimetry and F/C data	115
6.20	Time-dependent bias between GNSS VTEC and a satellite altimetry, and b F/C measurements for day 202, 2007	117
6.21	Latitude-dependent bias between GNSS VTEC and a satellite altimetry, and b F/C measurements for day 202, 2007	118
6.22	a VTEC map and b RMS map of calibrated GNSS-only solution, day 202, 2007 - 9 UT	118
6.23	Calibrated minus non-calibrated combined a) VTEC and b) RMS map from GNSS, satellite altimetry and F/C data using mean daily bias for calibration procedure. Snapshot for day 202, 2007 - 9 UT	120

6.24	Calibrated minus non-calibrated combined a) VTEC and b) RMS map from GNSS, satellite altimetry and F/C data using time-dependent bias for calibration procedure. Snapshot for day 202, 2007 - 9 UT	120
6.25	Calibrated minus non-calibrated combined a) VTEC and b) RMS map from GNSS, satellite altimetry and F/C data using latitude-dependent bias for calibration procedure. Snapshot for day 202, 2007 - 9 UT	120
6.26	Algorithm for simulating input data	122
6.27	Algorithm for Estimating unknown parameters	123
6.28	Input data with true GNSS ray-path, but simulated values from IGS GIM at day 182, 2010 - [0,2]UT	125
6.29	Global step-points for simulating input data for stations at a Northern, and b Southern hemisphere, day 182, 2010 - [0,2]UT	126
6.30	Maximum electron density ($elec/m^3$) from IRI-2012 model for day 182, 2010 - [0,2]UT, used as a priori value for estimating \hat{N}_m	128
6.31	Height of maximum electron density (km) from IRI-2012 model for day 182, 2010 - [0,2]UT, used as a priori value for estimating \hat{h}_m	128
6.32	Residuals of input data before performing the outliers test and the confidence intervals for day 182, 2010 - [0,2]UT	130
6.33	Residuals of input data after performing the outliers test for day 182, 2010 - [0,2]UT	130
6.34	Estimated maximum electron density ($\times 10^{11} elec/m^3$) for day 182, 2010 - [0,2]UT	135
6.35	Estimated maximum electron density height (km) for day 182, 2010 - [0,2]UT	135
6.36	3D model of F2-peak electron density for day 182, 2010 - [0,2]UT; color bar indicates the maximum electron density ($\times 10^{11} elec/m^3$) and the Z-axis indicates maximum electron density height in km	136
6.37	RMS map of estimated maximum electron density ($\times 10^{10} elec/m^3$) for day 182, 2010 - [0,2]UT	137
6.38	RMS map of estimated maximum electron density height (km) for day 182, 2010 - [0,2]UT	137
6.39	Difference between the estimated \hat{N}_m values and N_m derived from the IRI model ($\times 10^{11} elec/m^3$) for day 182, 2010 - [0,2]UT	139
6.40	Difference between the estimated \hat{h}_m values and h_m derived from the IRI model (km) for day 182, 2010 - [0,2]UT	139
6.41	a Estimated maximum electron density (blue curve) and maximum electron density from the IRI model (red curve), and b residual of estimated minus IRI maximum electron density at the simulated input points, day 182, 2010, [0,2] UT	140
6.42	a Estimated height of maximum electron density (blue curve) and maximum electron density height from the IRI model (red curve), and b residual of estimated minus IRI maximum electron density height at the simulated input points, day 182, 2010, [0,2] UT	140

6.43	Footprints of F2-peak parameters obtained from F/C data, for day 182, 2010 - [0,2]UT	141
6.44	F2-peak electron density obtained from F/C data, for day 182, 2010 - [0,2]UT	143
6.45	F2-peak height obtained from F/C data, for day 182, 2010 - [0,2]UT	143
6.46	F2-peak electron density deviations of estimated minus F/C, for day 182, 2010 - [0,2]UT	144
6.47	F2-peak height deviations of estimated minus F/C, for day 182, 2010 - [0,2]UT	144
1	Selected IGS stations for performing PPP and SPP	158
2	SPP in a daily solution for in-land station a ALGO and b CONZ, from doy 182 to 191, 2006	159
3	SPP in a daily solution for see-side station a GUAM and b KERG, from doy 182 to 191, 2006	159
4	SPP in an hourly solution for in-land station a HERT and b WTZR, for doy 182, 2006	160
5	SPP in an hourly solution for see-side station a BRMU and b REUN, for doy 182, 2006	162

List of Tables

2.1	Characteristics of the main ionospheric layers	16
2.2	Traveling ionospheric disturbances	20
2.3	Relation between various GNSS first-order measured parameters and TEC of Earth's ionosphere extracted from Klobuchar (1996)	31
5.1	Samples base function/mathematical approaches for multi-dimensional modeling of the ionosphere	70
6.1	Daily mean bias between GNSS VTEC and satellite altimetry, and F/C measurements for day 202, 2007	116
6.2	Time-dependent bias between GNSS VTEC and satellite altimetry, and F/C measurements for day 202, 2007	117
6.3	Latitude-dependent bias between GNSS VTEC and satellite altimetry, and F/C measurements for day 202, 2007	117
1	Mean bias and RMS of different SPP daily solutions with respect to dual-frequency PPP solution, for day 182 to 191, 2006	161
2	Mean bias and RMS of different SPP hourly solutions with respect to dual-frequency PPP solution, for day 182, 2006.	162

Bibliography

- AGHANAJAFI, C. (2000). *Aeronomy*. KNToosi University of Technology Academic Press.
- ALIZADEH, M. (2002). The effect of high temperature plasma on GPS satellite signals. *International Journal of Engineering Science*, 13, 1–17.
- ALIZADEH, M., SCHUH, H., TODOROVA, S. AND WEBER, R. (2010). GPS precise point positioning for assessing GNSS and satellite altimetry combined Global Ionosphere Maps. In *Proceedings of Geomatics Conference 89*, National Cartographic Center (NCC), Tehran, Iran.
- ALIZADEH, M., SCHUH, H., TODOROVA, S. AND SCHMIDT, M. (2011). Global Ionosphere Maps of VTEC from GNSS, satellite altimetry, and Formosat-3/COSMIC data. *J. Geod.*, 85, 975 – 987.
- ALIZADEH, M., WIJAYA, D., HOBIGER, T., WEBER, R. AND SCHUH, H. (2013). Ionospheric effects on microwave signals. In J. Boehm and H. Schuh, eds., *Atmospheric Effects in Space Geodesy*, Springer Verlag, ISBN:978-3-642-36931-5.
- ALTAMIMI, Z., COLLILIEUX, X., LEGRAND, J., GARAYT, B. AND BOUCHER, C. (2007). ITRF2005: A new release of the International Terrestrial Reference Frame based on time series of station positions and Earth orientation parameters. *J. Geophys. Res.*, 112.
- ANDERSON, D. (1993). Global ionospheric modelling. *Modern Radio Science*, 159, edited by H Matsumoto.
- AVISO (2012). The french active archive data center for multi-satellite altimeter missions.
- BASSIRI, S. AND HAJJ, G. (1993). Higher-order ionospheric effects on the global positioning system observables and means of modeling them. *Manuscripta Geodaetica*, 18, 280 – 289.
- BAUER, M. (2003). *Vermessung und Ortung mit Satelliten - GPS und andere satellitengestützte Navigationssysteme*. Wichmann, Karlsruhe, 5th edn.
- BEAN, B. AND THAYER, G. (1959). *CRPL Exponential Reference Atmosphere*, Vol. 4 of *Natl. Bur. of Stand. Monogr.*. U.S. Gov. Print. Off., Washington, D. C.

- BENT, R., LLEWELLYN, S. AND SCHMID, P. (1972). *Description and evaluation of the Bent ionospheric model*, Vol. 1,2, and 3 of *National Information Service*. Springfield, Virginia.
- BILITZA, D. (2009). Evaluation of the IRI-2007 model options for the topside electron density. *Adv. Space Res.*, 44, 701–706.
- BILITZA, D. AND REINISCH, B. (2007). International Reference Ionosphere 2007: Improvements and new parameters. *Adv. Space Res.*, 42, 599 – 609.
- BILITZA, D., MCKINNELL, L., REINISCH, B. AND FULLER-ROWELL, T. (2011). The international reference ionosphere today and in the future. *J. Geod.*, 85, 909 – 920.
- BOEHM, J., SALSTEIN, D., WIJAYA, D. AND ALIZADEH, M. (2013). Geodetic and atmospheric background. In J. Boehm and H. Schuh, eds., *Atmospheric Effects in Space Geodesy*, Springer Verlag, ISBN:978-3-642-36931-5.
- BORN, M. AND WOLF, E. (1964). *Principles of optics: electromagnetic theory of propagation, interference and diffraction of light*. Macmillan, New York, 2nd edn.
- BORN, M. AND WOLF, E. (1999). *Principles of Optics*. Cambridge Univ. Press, New York, 7th edn.
- BRADLEY, P. (1990). Mapping the critical frequency of the F2-layer: part 1-Requirements and developments to around 1980. *Adv. Space Res.*, 10, 47.
- BRUNINI, C., MEZA, A. AND BOSCH, W. (2005). Temporal and spatial variability of the bias between topex- and GPS-derived total electron content. *Journal of Geodesy*, 79, 175–188.
- BRUNNER, F. AND GU, M. (1991). An improved model for the dual frequency ionospheric correction of GPS observations. *Manuscripta geodaeica, Springer-Verlag*, 205–214.
- BUDDEN, K. (1985). *The propagation of radio waves*. Cambridge Univ. Press.
- CAPPELLARI, J., VELEZ, C. AND FUCHS, A. (1976). Mathematical theory of the Goddard trajectory determination system. In *Section 7.6.2, Ionosphere Models*, 7–44 – 7–52, Goddard Space Flight Center, X-582-76-77, Greenbelt, MD, U.S.A.
- CCIR (1967). Atlas of ionospheric characteristics. Tech. rep., Comit Consultatif International des Radiocommunications, International Telecommunications Union, Geneva.
- CDDIS (2011). ftp. Website, <ftp://cddis.gsfc.nasa.gov/>.
- CDDIS-IONEX (2011). IONEX ftp site. Website, <ftp://cddis.gsfc.nasa.gov/pub/gps/products/ionex>.
- CENTRAL, A. (2012). Altimeter database system central, version 4.00. Website, <http://adsc.gfz-potsdam.de/ads/>.

- CERVNEY, V. (2005). *Seismic Ray Theory*. Cambridge Univ. Press, New York.
- CHELTON, D., RIES, J., HAINES, B., FU, L. AND CALLAHAN, P. (2001). *Satellite altimetry and Earth sciences: A handbook of techniques and applications*. Academic Press, London.
- CHIU, Y. (1975). An improved phenomenological model of ionospheric density. *J. Atmos. Terr. Phys.*, 37, 1563–1570.
- CNES (2011). Jason-2 altimetry mission for ocean observation.
- CODE (2012). Center for Orbit Determination in Europe at ftp.unibe.ch. Website, <ftp://ftp.unibe.ch/aiub/CODE>.
- CRASSIDIS, J. AND JUNKINS, J. (2004). *Optimal Estimation of Dynamic Systems*. Chapman and Hall\CRC, Boca Raton, FL.
- DACH, R., HUGENTOBLE, U., FRIDEZ, P. AND MEINDL, M. (2007). *Bernese GPS Software, Version 5.0*. Astronomical Institute, University of Bern.
- DANIELL, R., WHARTENBY, W. AND BROWN, L. (1993). Parameterised real time ionospheric specification model. Prism version 1.2, validation report, Computational Physics, Inc., 385 Elliot St, Newton, MA02164, USA.
- DANIELL, R., BROWN, L., ANDERSON, D., FOX, M., DOHERTY, P., DECKER, D., SOJKA, J. AND SCHUNK, R. (1995). Parameterized ionospheric model: A global ionospheric parameterization based on first principles models. *Radio Sci.*, 30, 1499–1510.
- DAVIES, K. (1990). *Ionospheric radio*, Vol. 31 of IEE Electromagnetic waves series. Peter Peregrinus Ltd, London.
- DEPUEV, V. AND PULINETS, S. (2004). A global empirical model of the ionospheric topside electron density. *Adv. Space Res.*, 34, 2016–2020.
- DETTMERING, D., HEINKELMANN, R. AND SCHMIDT, M. (2010). Systematic differences between vtec obtained by different space-geodetic techniques during CONT08. *Journal of Geodesy*, 1–9, 10.1007/s00190-011-0473-z.
- DETTMERING, D., HEINKELMANN, R. AND SCHMIDT, M. (2011a). differences between VTEC obtained by different space-geodetic techniques during cont08. *Journal of Geodesy*, 85, 443–451.
- DETTMERING, D., SCHMIDT, M., HEINKELMANN, R. AND SEITZ, M. (2011b). Combination of different space-geodetic observations for regional ionosphere modeling. *J. Geod.*, 85, 989 – 998.

- DI GIOVANNI, G. AND RADICELLA, S. (1990). An analytical model of the electron density profile in the ionosphere. *Adv. Space Res.*, 10, 27 – 30.
- DOW, J., NEILAN, R. AND RIZOS, C. (2009). The International GNSS service in a changing landscape of Global Navigation Satellite Systems. *Journal of Geodesy*, 83, 191–198.
- DUMONT, J., ROSMORDUC, V., PICOT, N., DESAI, S., BONEKAMP, H., FIGA, J., LILLIBRIDGE, J. AND SCHARROO, R. (2009). *OSTM/Jason-2 Products Handbook*. CNES and EUMETSAT and JPL and NOAA/NESDIS, issue 1 rev 4 edn.
- EZQUER, R., DE GONZÁLEZ, M. AND HEREDIA, T. (1996). Electron density profile modeling. *Annali Di Geofisica*, XXXIX, 539–542.
- FELTENS, J. (1998). Chapman profile approach for 3D global TEC representation. In *Proceedings of the 1998 IGS The IGS VTEC maps analysis centers workshop*, 285–297, IGS Presentation, ESOC, Darmstadt, Germany.
- FELTENS, J. (2003). The International GPS Service (IGS) ionosphere working group. *Advances in Space Research*, 31, 205–214.
- FELTENS, J., ANGLING, M., JAKOWSKI, N., MAYER, C., HOQUE, M., HERNÁNDEZ-PAJARES, M., GARCÍA-RIGO, A., ORÚS-PÉREZ, R. AND ARAGÓN-ANGEL, A. (2009). Analysis of the state of the art ionosphere modelling and observation techniques. Tech. Rep. OPS-SYS-TN-0017-OPS-GN, Iss. 1/0, ESA/ESOC.
- FELTENS, J., ANGLING, M., JACKSON-BOOTH, N., JAKOWSKI, N., HOQUE, M., MAYER, C., HERNÁNDEZ-PAJARES, M., GARCÍA-RIGO, A., ORÚS-PÉREZ, R., ARAGÓN-ANGEL, A. AND ZORNOZA, M. (2010). GNSS contribution to next generation global ionospheric monitoring. Tech. rep., ESA/ESOC Final Report.
- FLEURY, R., FOUCHER, F. AND LASSUDRIE-DUCHESNE, P. (1991). Global TEC measurements capabilities of the doris system. *Adv. Space Res.*, 11, 1051 – 1054.
- FÖRSTER, M. AND JAKOWSKI, N. (2000). Geomagnetic storm effects on the topside ionosphere and plasmasphere: A compact tutorial and new results. *Surveys in Geophysics*, 21, 47 – 87.
- FOURIER, J. (1955). *The Analytical Theory of Heat*. Dover, New York.
- FOX, K.C. (2012). Science (at) NASA headline news. Website, http://science.nasa.gov/science-news/science-at-nasa/2009/01apr_deepsolarminimum/.
- FOX, M. AND MCNAMARA, L. (1988). Improved world-wide maps of monthly median foF2. *J. Atmos. Terr. Phys.*, 50, 1077.

- FREMOUW, E., SECAN, J. AND HOWE, B. (1992). Application of stochastic inverse theory to ionospheric tomography. *Radio Science*, 27, 721–732.
- FRITSCHÉ, M. (2005). Impact of higher-order ionospheric terms on GPS estimates. *Geophysical Research letters*.
- FU, L., CHRISTENSEN, E., YAMARONE, C., LEFEBVRE, M., MÉNARD, Y., DORRER, M. AND ESCUDIER, P. (1994). Topex/poseidon mission overview. *Journal of Geophysical Research*, 99.
- GARCIA-FERNANDEZ, M., HERNANDEZ-PAJARES, M., JUAN, J. AND SANZ, J. (2005). Performance of the improved abel transform to estimate electron density profiles from GPS occultation data. *GPS Solut*, 9, 105 – 110.
- GGOS (2012). The Global Geodetic Observing System. Website, <http://www.ggos.org/>.
- GIRARD, D. (1989). A fast 'Monte-Carlo cross-validation' procedure for large least squares problems with noisy data. *Numer. Math.*, 56, 1–23.
- GOODMAN, J. AND AARONS, J. (1990). Ionospheric effects on modern electronic systems. *Proc. IEEE*, 78.
- H., H. (1999). *Geodetic applications of the Global Navigation Satellite System (GLONASS) and of GLONASS/GPS combinations*. Ph.D. thesis, Bern University, Switzerland.
- HAIRER, E., NØRSETT, S. AND WANNER, G. (1993). *Solving ordinary differential equations I: Nonstiff problems*. Springer-Verlag, Berlin, New York.
- HARGREAVES, J. (1995). *The Solar-Terrestrial Environment - An Introduction To Geospace - The Science of the Terrestrial Upper Atmosphere, Ionosphere, And Magnetosphere*. Cambridge University Press.
- HARTMANN, G.K. AND LEITINGER, R. (1984). Range errors due to ionospheric and tropospheric effects for signal frequencies above 100 MHz. *Bull. Géod.*, 58, 109–399.
- HERNÁNDEZ-PAJARES, M. (2004). IGS ionosphere WG status report: Performance of IGS ionosphere TEC map. Tech. rep., IGS Workshop, Bern, Switzerland.
- HERNÁNDEZ-PAJARES, M., JUAN, J. AND SANZ, J. (2000). Improving the abel inversion by adding ground GPS data tp leo radio occultation in ionospheric sounding. *Geophysical Research Letters*, 27, 2473 – 2476.
- HERNÁNDEZ-PAJARES, M., JUAN, J., SANZ, J. AND BILITZA, D. (2002). Combining GPS measurements and iri model values for space weather specification. *Adv Space Res*, 29, 949 – 958.

- HERNÁNDEZ-PAJARES, M., JUAN, J. AND SANZ, J. (2006). Medium-scale traveling ionospheric disturbances affecting GPS measurements: Spatial and temporal analysis. *Journal of Geophysical Research*, 111.
- HERNÁNDEZ-PAJARES, M., JUAN, J., SANZ, J., ORÚS-PÉREZ, R., GERCÍA-RIGO, A., FELTENS, J., KOMJATHY, J., SCHAEER, S. AND KRANKOWSKI, A. (2009). The IGS VTEC maps: a reliable source of ionospheric information since 1998. *J. Geod.*
- HO, M., MANNUCCI, A., LINDQUISTER, U., X, P. AND TSURUTANI, T. (1996). Global ionosphere perturbations monitored by the worldwide gps network. *Geophys. Res. Lett.*, 23, 3219 – 3222.
- HOBIGER, T. (2005). *VLBI as tool to probe the ionosphere*. Ph.D. thesis, Inst. of Geodesy and Geophysics, Vienna Univ. of Technology, Austria.
- HOBIGER, T., KONDO, T. AND SCHUH, H. (2006). Very Long Baseline Interferometry as a tool to probe the ionosphere. *Radio Science*, 41, RS1006, doi:10.1029/2005RS003297.
- HOCHEGGER, G., NAVA, B., RADICELLA, S. AND LEITINGER, R. (2000). A family of ionospheric models for different uses. *Phys Chem Earth Part C Sol Terr Planet Sci*, 25, 307–310.
- HOFMANN-WELLENHOF, B., LICHTENEGGER, H. AND COLLINS, J. (1993). *GPS Theory and Practice*. Springer, Wien New York, 2nd edn.
- HOQUE, M. AND JAKOWSKI, N. (2012). A new global model for the ionospheric F2 peak height for radio wave propagation. *Ann. Geophys*, 30, 797–809.
- HOWE, B., RUNCIMAN, K. AND SECAN, J. (1998). Tomography of the ionosphere: Four-dimensional simulations. *Radio Science*, 33, 109.
- HUANG, X. AND REINISCH, B. (2001). Vertical total electron content from ionograms in real time. *Radio Sci.*, 36, 335–342.
- HUANG, X., REINISCH, B., SONG, P., GREEN, J. AND GALLAGHER, D. (2004). Developing an empirical density model of the plasmasphere using IMAGE/RPI observations. *Adv. Space Res.*, 33, 829–832.
- HUNSUCKER, R. AND HARGREAVES, J. (2002). *The high latitude ionosphere and its effects on radio propagation*. Cambridge University Press.
- HUTCHINSON, M. (1990). A stochastic estimator of the trace of the influence matrix for laplacian smoothing splines. *Commun. Statis.*, 19, 433–450.
- IAG (2012). International Association of Geodesy. Website, <http://www.iag-ggos.org/>.
- IGRF, I. (2011). World data center for geomagnetism,kyoto.

- IGS (2012). International GNSS service website. Website, <http://igsceb.jpl.nasa.gov/>.
- ILRS (2011). Jason2 satellite information. Website, http://ilrs.gsfc.nasa.gov/satellite_missions/list_of_satellites/jas2_general.html.
- IMEL, D. (1994). Evaluation of the topex/poseidon dual-frequency ionosphere correction. *Journal of Geophysical Research*, 99, 24895 – 24906.
- ITU (2007). ITU-R recommendation.
- ITU (2011). Radiocommunication sector. Website, <http://www.itu.int/oth/R0A04000018/en>.
- IVS (2012). International VLBI service website. Website, <http://ivscb.gsfc.nasa.gov/>.
- JAKOWSKI, N. (1996). *Modern Ionospheric Science*, chap. TEC monitoring by using satellite positioning systems, 371–390. ProduServ GmbH Verlagsservice, Berlin, EGS, Katlenburg-Lindau.
- JAKOWSKI, N. AND LAZO, B. (1977). Significant events in TEC measurements between 20 march and 5 may, 1976. In *Collected data reports for STIP interval II, 20 March - 5 May 1976*, Vol. 61, 432–435, UAG.
- JAKOWSKI, N., KUTIEV, I., HEISE, S. AND WEHRENPENNIG, A. (2002a). A topside ionosphere-plasmasphere model for operational applications. In *Proceeding of URSI XXVII General Assembly*, 2174–2177.
- JAKOWSKI, N., WEHRENPENNIG, A., HEISE, S., REIGBER, C., LHR, H., GRUNWALDT, L. AND MEEHAN, T. (2002b). GPS radio occultation measurements of the ionosphere from champ early results. *Geophys. Res. Lett.*, 29.
- JAKOWSKI, N., WEHRENPENNIG, A., HEISE, S., REIGBER, C. AND LÜHR, H. (2002c). Status of ionospheric radio occultation champ data analysis and validation of higher level data products. In *1st CHAMP Science Meeting*, GFZ Potsdam, Potsdam - Germany.
- JAKOWSKI, N., LEITINGER, R. AND ANGLING, M. (2004). Radio occultation techniques for probing the ionosphere. *Annals Of Geophysics*, Supplement to Vol. 47, 1049 – 1066.
- JAKOWSKI, N., HOQUE, M. AND MAYER, C. (2011). A new global TEC model for estimating transionospheric radio wave propagation errors. *J. Geod.*, 85, 965–974.
- JPL (2011). JPL - NASA, GAIM introduction. Website, <http://iono.jpl.nasa.gov/gaim/intro.html>.
- KELLY, M. (1989). *The Earths ionosphere: plasma physics and electrodynamics*. Academic Press (San Diego).

- KING, M., EDWARDS, S. AND CLARKE, P. (2002). Precise point positioning: Breaking the monopoly of relative GPS processing. In *Engineering Surveying Showcase*.
- KLOBUCHAR, J. (1986). Design and characteristics of the GPS ionospheric time-delay algorithm for single-frequency users. In *PLANS'86 - Position Location and Navigation Symposium*, 280–286, Las Vegas, Nevada.
- KLOBUCHAR, J.A. (1996). *Ionospheric effects on GPS, in Global Positioning System: theory and Application*, Vol. I. American Institute of Aeronautics and Astronautics, Washington DC., edited by: b. w. parkinson and j. j. spilker edn.
- KOCH, K. (1999). *Parameter Estimation and Hypothesis Testing in Linear Models*. Springer, 2nd edn.
- KOCH, K. AND KUSCHE, J. (2002). Regularization of geopotential determination from satellite data by variance components. *J. Geodesy*, 76, 259–268.
- KRANKOWSKI, A., HERNANDEZ-PAJARES, M., FELTENS, J., KOMJATHY, A., SCHAER, S., GARCIA-RIGO, A. AND WIELGOSZ, P. (2010). Present and future of IGS ionospheric products. Tech. rep., IGS Workshop, Newcastle, England.
- KUTIEV, I., MARINOV, P. AND WATANABE, S. (2006). Model of topside ionosphere scale height based on topside sounder data. *Adv. Space Res.*, 37, 943–950.
- LILOV, L. (1972). On stabilization of steady-state motions of mechanical systems with respect to a part of the variables. *Journal of Applied Mathematics and Mechanics*.
- LLEWELLYN, S. AND BENT, R. (1973). Documentation and description of the Bent ionospheric model. Tech. rep., Hanscom AFB, Massachusetts, USA.
- MATERASSI, M. (2003). Ionospheric tomography, 3d and 4d imaging and data assimilation. In *invited paper*, Atmospheric Remote Sensing using Satellite Navigation Systems Special Symposium of the URSI Joint Working Group FG, ASI Centro di Geodesia Spaziale 'Giuseppe Colombo', Matera, Italy.
- MAYER, C. AND JAKOWSKI, N. (2009). Enhanced E-layer ionization in the auroral zones observed by radio occultation measurements onboard CHAMP and Formosat-3/COSMIC. *Annales Geophysicae*, 27, 1207–1212.
- MITCHELL, C. AND CANNON, P. (2002). Multi-instrumental data analysis system (MIDAS) imaging of the ionosphere. Tech. rep., University of Bath, United States Air Force European Office of Aerospace Research and Development.
- MITCHELL, C. AND SPENCER, P. (2003). A three dimensional time-dependent algorithm for ionospheric imaging using GPS. *Annal. Geophysics*, 46, 687 – 696.

- MOSERT DE GONZALEZ, M. AND RADICELLA, S. (1990). On a characteristic point at the base of the F2 layer in the ionosphere. *Adv. Space Res.*, 10.
- MULDREW, D. (1965). F-layer ionization trough deduced from alouette data. *J. Geophys. Res.*, 70, 2635–2650.
- NAFISI, V., MADZAK, M., BÖHM, J., ARDALAN, A. AND SCHUH, H. (2012). Ray-traced tropospheric delays in VLBI analysis. *Radio Science*, 47.
- NAVA, B. (2006). A near real-time model-assisted ionosphere electron density retrieval method. *Radio Science*.
- NAVA, B., COÏSSON, P. AND RADICELLA, S. (2008). A new version of the NeQuick ionosphere electron density model. *Journal of Atmospheric and Solar-Terrestrial Physics*, 70, 1856 – 1862.
- NRL, U.N.R.L.P.R. (2008). Updated version of GAIM model goes operational. Website, <http://www.nrl.navy.mil/pao/pressRelease.php?Y=2008&R=30-08r>.
- NSSDC, F.S. (2012). IRI 2012 fortran source code. Website, <ftp://nssdcftp.gsfc.nasa.gov/models/>.
- NSUMEI, P., REINISCH, B.W., HUANG, X. AND BILITZA, D. (2012). New vary-chap profile of the topside ionosphere electron density distribution for use with the IRI model and the GIRO real time data. *Radio Sci.*, 47, 1–11.
- ORÚS, R., HERNÁNDEZ-PAJARES, M., JUAN, J., SANZ, J. AND GARCÍA-FERNÁNDEZ, M. (2002). Performance of different TEC models to provide GPS ionospheric corrections. *J Atmos Solar-Terr Phys*, 64, 2055 – 2062.
- POPE, A. (1967). The statistics of residuals and the detection of outliers. Technical Report NOS 65 NGS 1, NOAA, US Department of Commerce, Rockville, USA.
- RADICELLA, S. (2009). The NeQuick model genesis, uses and evolution. *ANNALS OF GEOPHYSICS*, 52, 417 – 422.
- RADICELLA, S. AND LEITINGER, R. (2001). The evolution of the dgr approach to model electron density profiles. *Adv. Space Res.*, 27, 35 – 40.
- RADICELLA, S. AND NAVA, B. (2010). NeQuick model: Origin and evolution. In *Antennas Propagation and EM Theory (ISAPE)*, 422 – 425, IEE Xplore.
- RATCLIFFE, J. (1972). *An introduction to the ionosphere and magnetosphere*. Cambridge University Press.
- RAWER, K. (1988). Synthesis of ionospheric electron density profiles with Epstein functions. *Adv. Space Res.*, 8, 191–198.

- REINISCH, B. AND HUANG, X. (2004). Deducing topside profiles and total electron content from bottomside ionograms. *Adv. Space Res.*, 27, 23–30.
- REINISCH, B., NSUMEI, P., HUANG, X. AND BILITZA, D. (2007). Modeling the F2 topside and plasmasphere for IRI using IMAGE/RPI, and ISIS data. *Adv. Space Res.*, 34, 2026–2031.
- RHOADS, J., MALHOTRA, S., ARJUN, D., HYRON, S. AND BUELL, J. (2000). First results from the large-area lyman alpha survey. *The Astrophysical Journal*, 545, 85–88.
- RISHBETH, H. AND GARRIOTT, O. (1969). *Introduction to Ionospheric Physics*. New York, Academic Press.
- ROCKEN, C., ANTHES, R., M. EXNER AND D. HUNT, S.S., WARE, R., GORBUNOV, M., SCHREINER, W., FENG, D., HERMAN, B., KUO, Y. AND ZOU, X. (1997). Analysis and validation of GPS/MET data in the neutral atmosphere. *J. Geophys. Res.*, 102, 29849 – 29866.
- ROCKEN, C., KUO, Y., SCHREINER, W., HUNT, D. AND SOKOLOVSKIY, S. (2000). Cosmic system description. *Atmospheric and Oceanic Science*, 11, 21 – 52.
- ROTHACHER, M., GURTNER, W. AND HASE, S.S.R.W.W.S. (1996). Azimuth- and elevation-dependent phase center corrections for geodetic GPS antennas estimated from GPS calibration campaigns. In G. Beutler, G. Hein, W. Melbourne and G. Seeber, eds., *GPS Trends in Precise Terrestrial, Airborne, and Spaceborne Applications*, Vol. 115, 333–338.
- RUSH, C., STEWART, F., REASONER, R., ANDERSON, D., PERRY, J. AND POKEMPNER, M. (1984). Maps of f0F2 derived from observations and theoretical data. *Radio Science*, 10, 1083–1097.
- RUSH, C., FOX, M., BILITZA, D., DAVIES, K., MCNAMARA, L., STEWART, F. AND POKEMPNER, M. (1989). Ionospheric mapping: An update of foF2 coefficients. *Telecomm. J.*, 56, 179.
- SCHAER, S. (1999). *Mapping and predicting the Earth’s ionosphere using the Global Positioning System*. Ph.D. thesis, Bern University, Switzerland.
- SCHAER, S., GUNTER, W. AND FELTENS, J. (1998). Ionex: The ionosphere map exchange format version 1. In *In J. M. Dow, J. Kouba, and T. Springer (Eds.)*, 233 – 247, Proceeding of the IGS AC Workshop, Darmstadt, Germany.
- SCHERLISS, L., SCHUNK, R., SOJKA, J. AND THOMPSON, D. (2004). Development of a physics-based reduced state Kalman filter for the ionosphere. *Radio Science*, 39.
- SCHMIDT, M. (2007). Wavelet modelling in support of IRI. *Adv. in Space Res.*, 39, 932–940.

- SCHMIDT, M., ed. (2011). *Geodetic Contribution to Ionospheric Research*, Vol. 85. Springer.
- SCHMIDT, M., KARSLIOGLU, M. AND ZEILHOFER, C., eds. (2008). Regional multidimensional modeling of the ionosphere from satellite data. TUJK Annual Scientific Meeting, Ankara.
- SCHMIDT, M., DETTMERING, D., MÖSSMER, M., WANG, Y. AND ZHANG, J. (2011). Comparison of spherical harmonics and B-spline models for the vertical total electron content. *Radio Science*, 46, RS0D11.
- SCHREINER, W., SOKOLOVSKIY, S., ROCKEN, C. AND HUNT, D. (1999). Analysis and validation of GPS/MET radio occultation data in the ionosphere. *Radio Sci*, 34, 949 – 966.
- SCHUNK, R. (1988). A mathematical model of the middle and high latitude ionosphere. *Pure Appl. Geophys*, 128, 255.
- SCHUNK, R., SCHERLIESS, L., SOJKA, J. AND THOMPSON, D. (2004). Global assimilation of ionospheric measurements (GAIM). *Radio Sci.*, 39.
- SEEBER, G. (1993). *Satellite Geodesy, Foundations, Methods and Application*. Walter de Gruyter, Berlin, New York.
- SIROVICH, L. AND EVERSON, R. (1992). Management and analysis of large scientific datasets. *Int. J. Supercomputer Appl.*, 6, 50 – 68.
- SOPAC (2011). SOPAC ftp site. Website, <ftp://garner.ucsd.edu/pub/rinex/>.
- SPARKS, L., B.A., L., A.J., M., X., P. AND B.D., W. (2000). A new model for retrieving slant TEC corrections for wide area differential GPS. In *2000: Navigating into the New Millennium*, 464–473, Institute of Navigation National Technical Meeting, Anaheim, CA; UNITED STATES.
- TEUNISSEN, P. AND KLEUSBERG, A. (1998). *GPS for Geodesy*. Springer.
- TIMLECK, P. AND NELMS, G. (1969). Electron densities less than 100 electron cm⁻³ in the topside ionosphere. *Proceedings of the IEEE*, 57, 1164 – 1171.
- TODOROVA, S. (2008). *Combination of space geodetic techniques for global mapping of the ionosphere*. Ph.D. thesis, Vienna University of Technology, Austria.
- TODOROVA, S., SCHUH, H. AND HOBIGER, T. (2007). Using the Global Navigation Satellite Systems and satellite altimetry for combined global ionosphere maps. *Adv. Space Res*, 42, 727 – 736.

- TOLMAN, B., HARRIS, R., MUNTON, D., LITTLE, J., NELSEN, S. AND RENFRO, B. (2004). The GPS toolkit: Open source GPS software. In *16th International Technical Meeting of the Satellite Division of the Institute of Navigation*, Long Beach, California.
- TSAI, L. (2012). Ionospheric Sounding Lab. Website, <http://isarncu.ncu.edu.tw/en-us/index.html>.
- TSAI, L. AND TSAI, W. (2004). Improvement of GPS/MET ionospheric profiling and validation using the chung-li ionosonde measurements and the iri model. *J Terr Atmos Ocean Sci TAO*, 15, 589–607.
- TSAI, L., CHANG, K.K. AND LIU, C. (2011). GPS radio occultation measurements on ionospheric electron density from low earth orbit. *Journal of Geodesy*.
- TUCKER, A. AND FANIN, B. (1968). Analysis of ionospheric contributions to the doppler shift of CW signals from artificial ssatellites. *J. Geophys. Res.*, 73, 4325–4334.
- UCAR (2011). Cosmic program official. Website, <http://www.cosmic.ucar.edu/about.html>.
- VANÍČEK, P. AND KRAKIWSKY, E. (1982). *Geodesy: The Concepts*. Noth.Holland Publishing Company, Inc. - Amsterdam . New York . Oxford.
- VITMO VIRTUAL IONOSPHERE, M.O., THERMOSPHERE (2012). IRI 2012 online computation and plotting. Website, http://omniweb.gsfc.nasa.gov/vitmo/iri_vitmo.html.
- WALKER, J. (1988). *Fourier Series*. Encyclopedia of Physical Science and Technology, Oxford Univ. Press, University of Wisconsin Eau Claire, Eau Claire, WI 547024004.
- WARE, R., EXNER, D., FENG, M., GORBUNOV, K., HARDY, K., HERMAN, B., KUO, Y., MEEHAN, T., MELBOURNE, W., ROKEN, C., SCHREINER, W., SOKOLOVSKIY, S., SOLHEIM, F., ZOU, X., ANTHES, R., BUSINGER, S. AND TRENBERTH, K. (1996). GPS sounding of the atmosphere from low earth orbit: preliminary results. *Bull. Am. Meteor. Soc*, 77, 19 – 40.
- WELLS, D. (1974). Doppler satellite control. Tech. Rep. 29, UNB, Fredricton.
- WHITTEN, R. AND POPPOFF, I. (1971). *Fundamentals of Aeronomy*. John Wiley and Sons, Inc.
- WICKERT, J., REIGBER, C., BEYERLE, G., KÖNIG, R., MARQUARDT, C., SCHMIDT, T., GRUNWALDT, L., GALAS, R., MEEHAN, T., MELBOURNE, W. AND HOCKE, K. (2001). Atmosphere sounding by GPS radio occultation: First results from champ. *Geophys Res. Lett.*, 28, 3263 – 3266.

- WICKERT, J., BEYERLE, G., KONIG, R., HEISE, S., GRUNWALDT, L., MICHALAK, G., REIGBER, C. AND SCHMIDT., T. (2005). GPS radio occultation with champ and grace: A first look at a new and promising satellite configuration for global atmospheric sounding. *Annales Geophysicae*, 23, 653 – 658.
- WIJAYA, D. (2010). *Atmospheric correction formulae for space geodetic techniques*. Shaker verlag, Technical University of Graz.
- WOODEN, W. (1984). NAVSTAR Global Positioning System overview. In *the pacific congress on marine technology*, pp. OST3/10, Honolulu, Hawaii.
- YIN, P. AND MITCHELL, C.N. (2011). Demonstration of the use of the doppler orbitography and radio positioning integrated by satellite (doris) measurements to validate GPS ionospheric imaging. *Advances in Space Research*, 48, 500 – 506.
- ZUMBERGE, J., HEFLIN, M., JEFFERSON, D., M.M. WATKINS, M.M. AND WEBB, F. (1997). Precise point processing for the efficient and robust analysis of GPS data from large networks. *J. Geophys. Res.*, 102, 5005–5017.

Acknowledgments

I would like to express my sincere appreciation to the following individuals:

My thesis supervisor, Prof. Dr. Dr. h.c. Harald Schuh, for his continuous support and guidance through all my studies at Vienna University of Technology. He gave me time and freedom to evolve my ideas further and let me attend several scientific meetings to share my findings and to gain ideas from a broader scientific community. Without him, I couldn't have accomplished my research and studies in Vienna. My thesis co-supervisor, Prof. Dr. Michael Schmidt, for his constructive guidance and valuable conducts through my studies as a doctorate student, and for his precious revisions on this dissertation. During my studies in Vienna, he patiently spent a lot of time through teleconference or during my visits to his institute in Munich, discussing my problems and advising me through. Prof. Dr. Manuel Hernández Pajares for his supportive comments and encouraging suggestions. He always found time for answering my questions and provided helpful answers. During my visits to his institute, he and his colleagues at gAGE/UPC, made my stay in Barcelona a very pleasant one and always had a spare minute to answer my questions or to provide guidance towards my research. Prof. Dr. Robert Weber, for spending some time and answering my questions over GNSS related issues. Prof. Dr. Johannes Böhm, for all his support during my stay and study in Vienna. Although he had a lot of work to do himself, but he always provided his kind assistance to solve my scientific and organizational problems, whenever I asked him to. Prof. Dr. Lung-Chi Tsai from the Ionolab of Taiwan National University, for providing TEC information as well as F2-peak parameters from the F/C RO data. We also had fruitful discussions about the F/C mission in his visits to Vienna during EGU. I would like to express my deep gratefulness to Dr. Dudy D. Wijaya for spending time, having fruitful discussion about 3D and 4D modeling of the electron density. The idea of applying ray-tracing technique to the upper atmosphere, which was a key for solving the problem of integrating electron content along the ray-path, came from these discussions. Moreover, he kindly provided the Matlab codes for applying ray-tracing technique, implemented within this research. I would also like to take the opportunity to thank my friends, as well as my former and current colleagues at IGG of Vienna University of Technology, for their gracious help. I experienced such a great time studying in Vienna with them.

I wish to thank my family for their encouragement and for putting up with me through all this time, and the last but not least, my heart-felt gratitude goes to my very dear wife Farzaneh, who bore all the difficulties during this time and never gave up supporting me. No doubt her endurance has been the most encouraging.

I'm grateful to the Austrian Science Fund (FWF), which funded this research. Thanks to the IGS and to ADSCentral at GFZ Potsdam, for the free supply of GNSS and altimetry data. I am also thankful to the providers of the open-source Generic Mapping Tools (GMT) and the GPS Toolkit (GPStk) software.



This study was accomplished under two projects, namely, project COMBION (P19564-N10) from 2007 to 2010, and continuation project MDION (P22203-N22) from 2010 to 2013, funded by the Austrian Science Fund (FWF).

Author's Declaration

Parts of the work accomplished for this thesis has been published or is currently under review in form of four papers, namely

- Alizadeh, M.M., Wijaya, D., Hobiger, T., Weber, R. and Schuh, H. (2013). Ionospheric effects on microwave signals. In J. Böhm and H. Schuh, eds., *Atmospheric Effects in Space Geodesy*, Springer Verlag. ISBN: 978-3-642-36931-5.
- Böhm, J., Salstein, D., Wijaya, D. and Alizadeh, M.M. (2013). Geodetic and atmospheric background. In J. Böhm and H. Schuh, eds., *Atmospheric Effects in Space Geodesy*, Springer Verlag. ISBN: 978-3-642-36931-5.
- Alizadeh, M.M., Schuh, H., Todorova, S. and Schmidt, M. (2011). Global ionosphere maps of VTEC from GNSS, satellite altimetry, and Formosat-3/Cosmic data. *J. Geod.*, 85, 975-987.
- Alizadeh, M.M., Schuh, H., Todorova, S. and Weber, R. (2010). GPS precise point positioning for assessing GNSS and satellite altimetry combined global ionosphere maps. In *Proceedings of Geomatics Conference 89*, National Cartographic Center (NCC), Tehran, Iran.

While I have tried to cite the plots and segments following these publications, where appropriate, the main parts of the text have been rewritten and expanded from the papers, and I have not cited such text in detail. Contributions from co-authors are also noted in the text, and also acknowledged in the acknowledgments.

Curriculum Vitae

Curriculum Vitae

Personal information

Surname/ First name Alizadeh Elizei / Mohamad Mahdi
 Address(es) Strasse des 17. Juni 135, 10623 Berlin, Germany
 Telephone +49 (0) 30 – 314 29496
 Fax +49 (0) 30 – 314 21973
 Email mahdi.alizadeh@mail.tu-berlin.de
m.alizadeh@email.com
 Nationality Iranian
 Date of birth 4th January, 1975
 Gender male



Current occupation

Post-Doc. Research assistant (TVöD 13/3)
 Satellite Geodesy Group, Dept. of Geodesy and Geoinformation Science
 Technical University of Berlin (TUB), Berlin, Germany.

Education and training

Dates	March 2007 – February 2013
Title of qualification awarded	Doctorate in Technical Sciences (Dr. Techn.)
Principle subjects	Thesis title: "Multi-dimensional modeling of the ionospheric parameters, using space geodetic techniques" (achieved excellent mark)
Name of organization	Research Group Advanced Geodesy, Dept. of Geodesy and Geoinformation Vienna University of Technology, Vienna, Austria.
Dates	1998 – 2001
Title of qualification awarded	Master of Science in Geodesy Eng.
Principle subjects	Thesis title: "Assessment and Correction of Ionospheric Effects on GPS Observations, using a Global Electron Density Model". <i>(with grade point of 19.25 out of 20)</i>
Name of organization	K.N.Toosi University of Technology , Tehran – Iran
CGPA	17.50 <i>(from 20)</i>
Dates	1993 – 1997
Title of qualification awarded	Bachelor of Science in Surveying Eng.
Name of organization	K.N.Toosi University of Technology , Tehran – Iran
CGPA	16.10 <i>(from 20)</i>

Academic Achievements

- Best geodesist of the year award, Institute of Geodesy and Geophysics, Vienna University of Technology, Vienna – Austria, December 2011.
- Best paper award at the Geomatic-89 National conference, held by the Iranian National Cartography Center (NCC), Tehran – Iran, May 2010.
- Achieving first rank among Geodesy Eng. MSc. students graduating in summer 2001; Dept. of Geodesy & Geomatics, K.N.Toosi University of Technology.
- Proclaimed as the best student, presenting highest effort and achievement during the Bachelor graduation camp (Field surveying, Hydrography, Underground surveying), K.N.Toosi University of Technology, summer 1997.
- 1st place in the first scientific competition for bachelor students, held by the extra-curricular activities, scientific branch, K.N.Toosi University of Technology, 1996.

Occupational Career	
Dates	March 2013 – cont.
Occupation or position held	Post-doctorate research assistant
Main activities and responsibilities	<ul style="list-style-type: none"> • Principle scientist of project “SCH2010”, funded by the Austrian Science Fund (FWF), Project leader: Prof. Dr. Harald Schuh • Writing and preparing proposals for the satellite Geodesy Research Group to be applied for at the German Research Fund (DFG)
Name and address of employer	Satellite Geodesy Research Group, Dept. of Geodesy and Geoinformation Science, Technical University of Berlin (TUB), Germany.
Dates	March 2008 – February 2013
Occupation or position held	PhD candidate, Research assistant
Main activities and responsibilities	<ul style="list-style-type: none"> • Principle scientist of the project “MDION”, funded by the Austrian Science Fund (FWF), multi-dimensional modeling of the ionosphere using space geodetic techniques. (project leader: Prof. H. Schuh, duration: Sept. 2010 – Aug. 2013) • Principle scientist of the project “COMBION”, funded by the Austrian Science Fund (FWF), combining different space geodetic techniques for global modeling of the ionosphere. (project leader: Prof. H. Schuh, duration: March 2008 – Aug. 2010)
Name and address of employer	Advance Geodesy Research Group E-128/1, Institute of Geodesy and Geophysics, Vienna University of Technology, Austria. – Under supervision of Prof. Dr. Harald Schuh
Dates	April 2004 – May 2006
Occupation or position held	Project manager
Main activities and responsibilities	<ul style="list-style-type: none"> • Managing a research team carrying out feasibility study and evaluation of employing GPS for vehicle locating system. • Implementing Automatic Vehicle Locating system (AVL) as a pilot project.
Name and address of employer	Satellite Positioning and Navigation division, SON Computer Company; No. 30 Bakhshi-Movagharst, North Mofattehst, Tehran – Iran.
Dates	September – December 2005
Occupation or position held	Independent consultant
Main activities and responsibilities	<ul style="list-style-type: none"> • Feasibility study and implementing Satellite Tracking System for company’s Navigation fleet.
Name and address of employer	Logistic division of Supplying Automotive Parts Company (SAPCO) – Irankhodro, Tehran – Iran.
Dates	April 2002 – November 2003
Occupation or position held	University assistant – member of faculty scientific staff
Main activities and responsibilities	<ul style="list-style-type: none"> • Teaching “satellite Geodesy” and “Technical Language” course for surveying Bachelor student. • Presenting GPS practical course for surveying Bachelor students at their graduation summer camp. • Organizing and running a two day workshop on applications of GPS at the third festival of civil engineering students.
Name and address of employer	Azad University – South Tehran branch, Tehran – Iran.
Dates	September 2001 – September 2003
Occupation or position held	Visiting Lecturer
Main activities and responsibilities	<ul style="list-style-type: none"> • Teaching “Technical Language” course for surveying Bachelor students.
Name and address of employer	Iran University of Science and Technology (IUST).

Membership	<ul style="list-style-type: none"> Proposed member of International GNSS Service (IGS) – Ionosphere working group; June 2010. Member of International Association of Geodesy (IAG) - Ionosphere Modeling and Analysis Study Group (SG-4.3.1); since May 2009. Member of International GNSS Service (IGS) - Bias and Calibration Working Group; since March 2009. Member of International Committee on Global Navigation Satellite System (ICG) - Working Group A; since December 2008. Member of European Geosciences Union (EGU); since 2008. Member of American Geophysical Union (AGU) – Geodesy section; since 2008.
Projects	<ul style="list-style-type: none"> Co-author of project proposal “Multi-Resolution Ionosphere Model in Near Real-Time (MuRIM-RT)”, bilateral project between institutes of GFZ Postdam, and DGF Munich, submitted at the German DFG funding, July 2012. Author of project proposal “Multi-Dimensional Ionosphere, (MDION)”, Accepted and approved by the Austria's central funding organization for basic research (FWF) – December 2009. Convener of IONO Workshop, an International Workshop on Ionosphere. Held at Institute of Geodesy and Geophysics, Vienna University of Technology. July 2009. Co-author of project “Balkan Geodetic Observing System, (BALGEOS)”, bilateral project between Austria and Balkan countries; accepted by the Austrian Federal Ministry of Science and Research - February 2008.
Publications& Presentations	<p>Author or co-author of more than 30 publications and presentations. (listed in the attachment)</p>
Personal skills and competences Mother tongue Other Languages Organizational skills and competences	<p>Persian</p> <p>English: excellent GRE: 1030 – General test – (October 2005) Verbal: 300 – Quantitative: 730 – Analytical writing: 3.0 TOEFL: 570 – Paper based exam – (October 2004) Section1: 59 – Section2: 62 – Section 3: 50 - TWE score: 3.5 IELTS: 7.0 – (December 2001) Listening: 7.5 – Reading: 6.5 – Writing: 7 – Speaking: 7</p> <p>German: moderate Successfully passed A2 in “Common European Framework of Reference for Languages”, with excellent mark (July 2010).</p> <ul style="list-style-type: none"> Giving lecture at 2nd TRANSMIT summer school (Threats to different systems due to propagating ionization fronts and irregularities in the ionosphere), held by German Aerospace Center (DLR), September 10-14, 2012, Neustrelitz, Germany. Reviewer of several papers for different international journals. e.g. Journal of Geodesy and Advances in Space Research, (May 2010 – continued)

Computer skills
and competences

- Teaching assistant (while studying at MSc. degree), presenting following courses:
 - “Adjustment & Test” forgeomatics BSc students at K.N.Toosi University of Technology. (*September 1998 – April 2001*)
 - “Technical Language “ forgeomatics BSc students at K.N.Toosi University of Technology. (*January – April 2001*)
- After graduation from MSc.:
 - Teaching assistant in “GPS and its application in GIS & RS “ , at a joint program of K.N.Toosi University and Netherlands’ ITC university. The course was offered in English. (*September 2001*)
 - Teaching assistant in “Introduction to photogrammetry “ , at a joint program of K.N.Toosi university and Netherlands’ ITC university. The course was offered in English. (*October 2001*).
 - Presenting “Elementary & Advanced GPS” course at Irans’ Remote Sensing Center. (*August 2001*).
- Team work: Main developer and manager of the team designing website for the Geodesy & Geomatics Engineering department at K.N.ToosiUni. of Tech. (*February – December 2000*).
- Programming skills: C++ , Fortran, MATLAB.
- Operating system: Microsoft Windows, LINUX.
- Graphic Software: Photoshop, 3D Studio, AutoDesk Animator, AutoCAD, Macromedia Flash, Corel Draw.
- Web Design: HTML source code developing, Microsoft FrontPage, Microsoft Vizact.
- Other Software Packages: e.g.: Bernese GPS Software Ver. 5.0, 3SPak GPS Software, GPPS, Geogenious, SDR Map, Surfer, competent with most Microsoft Office programs

References:

- O. Univ. Prof. Dr. Dr. h.c. Harald Schuh harald.schuh@tuwien.ac.at
Department of Geodesy and Remote sensing, Deutsches GeoForschungsZentrum (GFZ), Potsdam, Germany.
- Priv. Doz. Dr. Michael Schmidt schmidt@dgfi.badw.de
Deutsches Geodätisches Forschungsinstitut (DGFI), Munich Germany.
- A.O. Prof. Dr. Manuel Hernandez-Pajares manuel@ma4.upc.edu
Research group gAGE, Technical University of Catalonia (UPC), Barcelona, Spain.
- Univ. Prof. Dr. techn. Johannes Böhm johannes.boehm@tuwien.ac.at
Institute of Geodesy and Geophysics, Vienna University of Technology, Vienna, Austria.

Publications

- Alizadeh M.M., Wijaya D., Hobiger T., Weber R., Schuh H.: "Ionospheric effects on microwave signals", In: Böhm J., Schuh H. (eds): Atmospheric Effects in Space Geodesy. Springer Verlag, ISBN: 978-3-642-36931-5, 2013.
- Boehm, J., Salstein, D., Wijaya, D. and Alizadeh, M.M., "Geodetic and atmospheric background", In J. Boehm and H. Schuh, (eds.): Atmospheric Effects in Space Geodesy, Springer Verlag, ISBN: 978-3-642-36931-5, 2013.
- Alizadeh M.M., "Multi-dimensional modeling of the ionospheric parameters using space geodetic techniques", PhD Thesis, Vienna University of Technology, Vienna, Austria, February 2013.
- Alizadeh M.M., Schuh H., Todorova S., Schmidt M., "Global Ionosphere Maps of VTEC from GNSS, Satellite Altimetry and Formosat-3/COSMIC Data", Journal of Geodesy (2011) vol.85, pp: 975-987, doi: 10.1007/s00190-011-0449-z, 2011.
- Alizadeh M.M., Schuh H., Todorova S., Weber R., "GPS Precise Point Positioning for Assessing GNSS and Satellite Altimetry Combined Global Ionosphere Maps", Proceeding of Geomatic-89 National Conference held at National Cartographic Center, Tehran – Iran, May 2010.
- Schuh H., Alizadeh M.M., Pashova L., "BALkanGEodetic Observing System, a scientific challenge for the balkan countries (BALGEOS)", Scientific report of the project funded by the Austrian Federal Ministry of Science and Research in the framework of its South Eastern European science cooperation initiative, "Research Cooperation and Networking between Austria and South Eastern Europe", Published by BALGEOS consortium, 1113 Sofia, Bulgaria, July 2009.
- Alizadeh M.M., Aghanajafi C., "The Effect of High Temperature Plasma on GPS Satellite Signals", Transaction of International Journal of Engineering Science, Iran University of Science and Technology. No.3, Vol. 13, Summer 2002.
- Alizadeh M.M., Aghanajafi C., "The Effect of Radiation on GPS Satellite Signals using a Global Electron Density Model", Proceeding of Ninth Asian Congress of Fluid Mechanics, May 27-31, 2002, Isfahan – Iran.
- Alizadeh M.M., Aghanajafi C., "Evaluating Ionospheric Delay on GPS Satellite Signals using the IRI-Model", Geomatic Conference-81, April 2002, National Cartographic Center, Tehran – Iran.
- Alizadeh M.M., Aghanajafi C., "Effect of Radiation Heat Transfer on GPS Satellite Signals", Proceedings of 2nd Conference of Satellite Based Positioning System: Oct. 2001. Tehran – Iran.
- Alizadeh M.M., Aghanajafi C., Ebadi H., "Evaluating the effect of TEC on GPS Observations using Two Frequency Measurements", Proceedings of 2nd Conference of Satellite Based Positioning System: Oct. 2001. Tehran – Iran
- Alizadeh M. M. "Assessment and Correction of Ionospheric Effects on GPS Observations, using a Global Electron Density Model", MSc Thesis dissertation, Supervisors: H. Ebadi, C. Aghanajafi, M. Najafi Alamdari – KNTU University of Technology, Faculty of Geodesy and Geomatics Engineering, Tehran – Iran, July 2001.

Oral & poster presentations

- Alizadeh M.M., Schuh H., "Multi-dimensional model of ionosphere/plasmasphere electron density using various space geodetic techniques", Oral presentation, International Association of Geodesy (IAG) scientific assembly, 1 – 6 September 2013, Potsdam, Germany.
- Alizadeh M.M., Schuh H., "Combined global VTEC maps from GNSS, satellite altimetry and Formosat-3/Cosmic", Poster presentation, International Association of Geodesy (IAG) scientific assembly, 1 – 6 September 2013, Potsdam, Germany.
- Alizadeh M.M., Schuh H. Schmidt M., Limberger M., "Combining space geodetic techniques for multi-dimensional modeling of the ionosphere", Oral presentation given by Marco Limberger, Asia-Pacific Radio Science Conference, 3 – 7 September 2013, Taipei, Taiwan.
- Alizadeh M.M., Schuh H., Schmidt M., Liang W. „Global 3D modeling of electron density using space geodetic techniques“, Poster presentation, presented by Wenjing Liang, International Beacon Satellite Symposium, 8 – 12 July 2013, Bath, UK.
- Alizadeh M.M., Schuh H., Schmidt M., "Three-dimensional reconstruction of Ionosphere/Plasmasphere using GNSS measurements", Poster presentation, EGU General Assembly, 7-12 April 2013, Vienna, Austria.
- Alizadeh M.M., Schuh H. and Schmidt M., "Global multi-dimensional modeling of ionospheric electron density using GNSS measurements and IRI model", Oral presentation, presented by H. Schuh at the American Geophysical Union 2012 fall meeting, 3-7 December 2012, San Francisco, USA.
- Alizadeh M.M., and H. Schuh, "Ionospheric impact on VLBI and comparison with other space geodetic techniques", Oral lecture at 2nd TRANSMIT summer school held by German Aerospace Center (DLR), 10-14 September 2012, Neustrelitz – Germany.
- Alizadeh M.M., H. Schuh, and D. Wijaya, "Global multi-dimensional model of F2 peak density and height using GNSS measurements and IRI model", Oral presentation: 39th COSPAR Scientific Assembly, 14-22 July 2012, Mysore – India.
- H. Schuh, M.M. Alizadeh, C. Tierno Ros, S. Todorova, "Remote sensing the ionosphere by means of space geodetic techniques", Oral presentation: 39th COSPAR Scientific Assembly, 14-22 July 2012, Mysore – India.
- Alizadeh M.M., H. Schuh, and M. Schmidt, "Global 4D modeling of electron density from GNSS, using spherical harmonics", Poster presentation: EGU General Assembly 2012, 22-27 April 2012, Vienna – Austria.
- Tierno Ros C., M.M. Alizadeh, H. Schuh, "Kriging Interpolationsmethode für Ionosphären-Modellierung über Österreich mittels GPS-Beobachtungen", Poster presentation: Geodätische Woche 2011, 27 – 29 September 2011, Nürnberg – Germany.
- Alizadeh M.M., Schuh H., Schmidt M., Hernandez-Pajares M., and Aragon-Angel A., "Calibrating GNSS VTEC Values by Satellite altimetry and Formosat-3/COSMIC Data using Parameter Estimation Technique", Poster presentation: EGU General Assembly 2011, 3 – 8 April 2011, Vienna – Austria.
- Alizadeh M.M., Schuh H. and Schmidt M., "Comparison of Electron Density Profiles from IRI with Combined Global Models from Space Geodetic Techniques" Oral presentation: COSPAR scientific assembly 2010, 18 – 25 July 2010, Bremen – Germany.
- Alizadeh M.M., Schuh H, Schmidt M., and Todorova S. "GNSS, Satellite Altimetry and Formosat-3/COSMIC for Determination of Ionosphere Parameters" Poster presentation: COSPAR scientific assembly 2010, 18 – 25 July 2010, Bremen – Germany.
- Alizadeh M.M., Schuh H, Todorova S., and Schmidt M., "Combining Space Geodetic Techniques for Global VTEC Modeling" Oral presentation: International Beacon Satellite Symposium 2010, 7-11 June, 2010, Barcelona – Spain.

- Schuh H, Alizadeh M.M., Todorova S., and Hobiger T., "Probing The Ionosphere By Means Of Space Geodetic Techniques", solicited presentation presented by M.M. Alizadeh: International Beacon Satellite Symposium 2010, 7-11 June, 2010, Barcelona – Spain.
- Alizadeh M.M., Schuh H, and Schmidt M., "Spherical Harmonics and Chapman Profile Approach for Modeling the Electron Density", Poster presentation: International Beacon Satellite Symposium 2010, 7-11 June, 2010, Barcelona – Spain.
- Alizadeh M.M., Schuh H., Todorova S., Weber R., "GPS Precise Point Positioning for Assessing GNSS and Satellite Altimetry Combined Global Ionosphere Maps", Oral presentation: Geomatic-89 National Conference, May 2010, Tehran – Iran.
- Alizadeh M.M., Schuh H., Schmidt M., "Multi-Dimensional Modeling of Electron Density using Spherical Harmonics and Chapman Function", Oral presentation: European Geoscience Union General Assembly 2010, 2 – 7 May 2010, Vienna – Austria.
- Alizadeh M.M., Todorova S., Schuh H., and Schmidt M., "Global Ionosphere Maps of VTEC from GNSS, Satellite Altimetry and FORMOSAT-3/COSMIC Data", Poster presentation: European Geoscience Union General Assembly 2009, 19 – 24 April 2009, Vienna – Austria.
- Alizadeh M.M., Weber R., Schuh H., "Regional Application of Combined Global Ionosphere Maps", Oral presentation: 1st IONO Workshop, Institute of Geodesy and Geophysics, Vienna University of Technology, 2,3 July 2009, Vienna – Austria.
- Alizadeh M.M., Todorova S., Schuh H., Schmidt M., "Towards 4D Ionosphere model Combining GNSS and Satellite altimetry with FORMOSAT-3/COSMIC", Oral presentation: Geodätische Woche 2008, 30 Sept – 2 October 2008, Bremen – Germany.
- Alizadeh M.M., Todorova S., Schuh H., Schmidt M., "Combining GNSS/Satellite Altimetry with Formosat-3/COSMIC data for modeling the Ionosphere", Poster presentation: COSPAR Scientific Assembly 2008, 13-20 July 2008, Montreal – Canada.
- Alizadeh M.M., Todorova S., Kudryashova M., Weber R., Schuh H. "Assessment of GNSS and Satellite Altimetry Combined Global Ionospheric Maps using Precise Point Positioning", Oral presentation: European Geoscience Union General Assembly 2008, 13 – 18 April 2008, Vienna – Austria.

Examiners



o.Univ.-Prof. Dr.-Ing. Dr. h.c. Harald Schuh

is currently director of Dept. 1 "Geodesy and Remote Sensing" at GFZ Potsdam, he is professor for "Satellite Geodesy" at Technical University of Berlin, and professor on-leave for "Higher Geodesy" at Vienna University of Technology. He has been Vice-President of the IAG since 2011, Elected Chair of the IVS since 2007, and the president of IAU Commission 19 since August 2009.



apl. Prof. Dr.-Ing. habil. Michael Schmidt

is a senior scientist at Deutsches Geodätisches Forschungsinstitut (DGFI), and a Professor at Technische Universität München (TUM). He is elected as the President of European Geosciences Union (EGU), Geodesy division, from April 2013. He is the chair of IAG Study Group Ionosphere Modeling and Analysis.



Univ. Prof. Dr. Manuel Hernández Pajares

is presently a Full Professor at the Technical University of Catalonia (UPC), Barcelona. He has been the chair and product coordinator of the IGS Ionosphere WG since 2002 until 2007, and the principal investigator of more than 20 national and international scientific projects.



Ao. Prof. Dipl.-Ing. Dr.techn. Robert Weber

is an Associate Professor at the Institute for Advanced Geodesy. He is the Chair of Satellite Geodesy Research Group and the interim Chair of Research Group Engineering Geodesy at Vienna University of Technology.

The more we learn,
the more we learn that there's more to learn ...